Exploring the molecular mechanisms of Ag(I) transporters involved in bacterial Ag(I) resistance

Ryan Mark Lithgo

MRes, BSc (Hons)

Doctor of Philosophy

University of Nottingham

School of Biosciences

October 2021

Supervisors: David Scott, Andrew Quigley

& Thomas Sorenson

Acknowledgments

Firstly, I would like to thank my supervisors Dr David J Scott, Dr Andrew Quigley and Dr Thomas Sorensen for providing me with the opportunity to do a PhD. Their guidance and supervision throughout the project has been a great learning experience, and without which I could not have progressed.

I would also like to give a special thanks to Dr Stephen Carr for allowing me to use his bench space and equipment. His help in teaching me crystallography cannot be under stated, I now have a much better understanding of getting from producing protein to determining its structure. In conjunction with this I would also like to thank Dr Gemma Harris for her help in using all the biophysical instruments at the RCaH.

I would like to thank the University of Nottingham BBSRC DTP and Diamond Light Source for providing the opportunity and funding for the PhD.

On a more personal level I would like to acknowledge all my friends at the Research Complex, without which the PhD would have undoubtably been more difficult. The laughs, experiences and memories will stay with me forever and helped in those tough times.

Finally, a special thanks to my family who have supported me in so many ways throughout my degrees and none more so than during the PhD. I could not have achieved any of this without their support, my only regret is that Nan never got to see me graduate.

Declaration

I hereby declare that the work conducted in this thesis was carried out by myself, under the supervision of Dr David Scott (University of Nottingham) and Dr Andrew Quigley (Membrane Protein Laboratory, Diamond Light Source), at the Research Complex at Harwell (Rutherford Appleton Laboratories).

No part of this work has been submitted for a degree or other qualification. All sources of information were correct at the time of writing, with sources acknowledged in the form of references.

COVID-19 Impact Statement

The COVID-19 pandemic occurred in the final 18 months of my PhD. Up to this point access to the labs and resources was readily available. The on-set of the pandemic caused a total shut down of the Research Complex at Harwell (RCaH) to any work other than on COVID-19. At this point of my research, I was finishing off the cloning and starting expression trials of the SilP and SilF constructs. However, as the labs were shut this worked was postponed until access back into the labs was granted in mid-June 2020.

Upon returning to the labs the cloning and expression trials could be conducted, however the work was now 3 months behind schedule. In addition to this the installation of a new Glacios Electron Microscope at the RCaH was delayed by 7 months. The microscope was to be used for assessing the quality of SilP on cryo-EM grids, the hope being that optimal conditions could be ascertained that would allow for access at EBIC on the Titan Krios microscopes (used for 3D reconstruction of the protein). The delay both in lab access and the installation of the Glacios microscope meant that structural work on SilP did not reach the level that we hoped.

A COVID-19 extension application was submitted to the BBSRC-DTP, along with the entirety of my cohort, and they were assessed on a case-by-case scenario. The application was declined; therefore, no funded extension was granted by the university, however a submission extension of 6 months was granted.
Diamonds annual review into my PhD granted a 3 month funded extension which was accepted by Nottingham University, however due to the time taken by Nottingham to accept this offer from Diamond I had found a job that meant the extension was not taken.

Abstract

Silver (Ag(I)) displays multiple antimicrobial properties that have led to its widespread use in the medical field. However, extensive use of Ag(I) has led to the emergence of bacterial resistance to Ag(I). Resistance to Ag(I) was inferred through the presence of plasmid pMG101 that contains a gene cluster, *sil*, which allowed bacteria to survive six times the normal lethal dose of Ag(I). The proteins of the *sil* system were given putative functions based on their sequence homology to the more extensively studied *cue* and *cus* systems, involved in copper homeostasis. To date only SilE has been characterised.

This work herein describes the functional and structural characterisation of three more of the proteins of the *sil* system; SilP, SilF and SilC.

Functional characterisation involved the use of a variety of biophysical and biochemical assays, with the former giving information on the oligomeric state of the proteins and the effects of metal binding. The biochemical assays showed that the proteins are able to bind or interact with Ag(I) and Cu(I), with preferential binding to Ag(I). SilP, a P-type ATPase, activity assays suggest a modified catalytic cycle that challenges the current cycles attributed to other P-type ATPases. Structural studies utilised x-Ray crystallography to produce atomic models for both SilF and SilC. While SilP was investigated using Cryo-Electron Microscopy, which showed the protein is dimeric on grids and a viable target for future work.

The functional and structural analysis within this thesis expands the limited understanding of the sil system and has significance for the future development of inhibitors of the proteins involved in bacterial silver resistance.

Table of Contents

List of Figures

List of Tables

List of Equations

Abbreviations

ADP	adenosine 5’-diphosphate
Ag(I)	silver (I)
ATP	adenosine 5’-triphosphate
AUC	analytical Ultracentrifugation
AKTA FPLC	AKTA fast protein liquid chromatography
bp / kbp	base pair / kilo base pair
c(s)	distribution of sedimentation coefficient function
CD	circular dichroism
CMC	critical micelle concentration
C-terminus	carboxy terminus
Cu(I/II)	copper (I/II)
CV	column Volume
Da, kDa, MDa	Daltons, kilo Daltons, Mega Daltons
DLS	dynamic light scattering
DNA	deoxyribonucleic acid
DNaseI	deoxyribonuclease I, from bovine pancreas
E.coli	*Escherichia coli*
et al	*et alia,* and others
g	centrifugal force
g, mg, µg	gram, milli-gram, micro-gram
HCl	hydrochloric acid
HEPES	N-(2-Hydroxyethyl)piperazine-N’-(2-ethanesulfonic acid)
IMAC	immobilised metal affinity chromatography
IPTG	Isopropyl-β-D-thiogalactopyranoside
K_{cat}	catalytic constant
K_d	dissociation constant
K_m	Michaelis constant
L, mL, µL, nL	Litre, milli-litre, micro-litre, nano-litre
M, mM, µM, nM	molar, milli-molar, micro-molar, nano-molar concentration (mol/L, mol/mL)
MWCO	molecular weight cut-off
m/z	mass to charge ratio

Ni^{2+}	Nickel (II)
ρ , ρ_0	solution , solvent density (g/mL)
PAGE	polyacrylamide gel electrophoresis
PBS	phosphate buffered saline
PCR	polymerase chain reaction
PDB	Protein Data Bank
PEG	polyethylene glycol
PEG-MME	polyethylene glycol monomethylether
pH	$-\log_{10}[H^+]$
P_i	inorganic phosphate
rpm	revolutions per minute
s	sedimentation coefficient (seconds, s / Svedbergs, S)
$s_{20,\,w}$	sedimentation coefficient, corrected to solvent conditions (viscosity and density of water at 20°C) Sedimentation coefficient corrected for non-ideality
S	Svedberg unit = 1×10^{-13} s
SDS	Sodium dodecyl sulphate
TAE	Tris acetate ethylenediaminetetraacetic acid
$\bar{v}$	partial specific volume (mL/g)
V_{max}	maximal velocity
v/v	volume to volume ratio
w/v	weight to volume ratio

Other abbreviations are appropriately defined in the text.

1 Introduction

Throughout history, metal ions have played a large role in our everyday life. The strength, malleability and aesthetics of metal ions have made them popular as materials for construction, weaponry, tools and jewellery. In an ionic form, metals have tremendous antimicrobial properties that have been utilised over centuries within the medical field. The applications of metals within medicine are wide ranging from the use of Ag(I) lined bandages for burns victims (Silver *et al.,* 2006), to more extreme treatments such as mercury fumigation as a treatment for syphilis between the 18th to the early 20th century (Zukerman, 2016). The antimicrobial properties of metal ions led to their addition in everyday products to help prevent infections such as laundry detergents, paints and deodorants (Mijnendonckx *et al.,* 2013). The use of metal ions declined throughout the 20th century as antibiotics were increasingly used, see Section 1.1, however as antibiotic resistance (AMR) emerged the use of metal ions was revisited once again (Huh & Kwon, 2011). The consequential excessive use of metal ions, leading to the same degree of AMR like antibiotics, has led to the emergence of bacterial resistance against several metal ions including Ag(I), Cu(I/II) and Zn(II) (Silver *et al.,* 1996). In order to better understand metal associated AMR, this research has investigated the structure and function of several of the proteins involved in bacterial resistance to Ag(I) (Silver, 2003). An understanding of the structural molecular basis of how these proteins function will overcome Ag(I) resistance.

1.1 Antibiotic Resistance in Bacteria

The emergence of antibiotics in the early 20th century was a game changer in the world of medicine. Antibiotics are naturally occurring chemical metabolites that are produced by bacteria to kill or inhibit the growth of other bacterial cells (Sengupta *et al.,* 2013). Their application within the medical field was famously made by Alexander Fleming through the discovery penicillin (Fleming, 1929). The discovery of penicillin led to the expansive growth of antibiotic discoveries as a 'magic bullet' for bacterial disease prevention/treatment (Hutchings *et al.,* 2019). However, the early optimism was off set as bacterial resistant to some antibiotics was discovered by the 1960's, the first identified was methicillin resistant *staphylococcus aureus* (MRSA), a penicillin-based resistance (Johnson, 2011). The emergence of antibiotic resistant bacteria, including penicillin based, was attributed to the early excessive and often misguided usage. In order to combat antibiotic resistance several antibiotics were classed as a last resort, this was due to laboratory studies showing it was difficult to induce resistance to them, vancomycin was one of these (Cunha, 1995). However, resistance has since been shown to some of these last resort antibiotics, vancomycin included, in many different bacterial species making the problem of antibiotic resistance a real medical problem (Pachori *et al.,* 2019 & Srinivasan *et al.,* 2002).

With the emergence of antibiotic resistance, metal ions have been proposed as an alternative and viable treatment/preventative measure to stop bacterial infection. However, the excessive use of metal ions has also led to the emergence of some bacterial resistance, the focus of this

research is looking at one of these resistance mechanisms to silver (Ag(I)).

1.2 Metal ions and Their General Biological Uptake in Bacteria

1.2.1 Cellular Requirements for Metal ions

Many metal ions have well known antimicrobial properties in excess, however there are several metal ions that are needed for biological functions termed 'essential'. Other metals ions that do not fall into this category are classed 'non-essential' metal ions. These non-essential metal ions are toxic if they enter the cell, disrupting many different cellular pathways and processes. Ag(I) is one such non-essential metal ion and, as will discussed later in this chapter, interacts with several cellular pathways leading to cell death.

In contrast to the 'non-essential' metal ions, 'essential' metal ions are needed by eukaryotic and/or prokaryotic cells for certain cellular process or pathways to function. The total number of metal ions included as 'essential' are debatable depending on the species, however the main elements included are; Na, K, Mg, Ca, Mn, Fe, Co, Cu, Zn and Mo (Bertini *et al.* 1994; Zoroddu *et al.* 2019). One example of an essential metal ion is that of iron, which has several oxidation states. Iron is used in a number of processes such as, photosynthesis and the production of ATP, through the formation of iron-sulfur clusters used in the electron transport chain (Bertini *et al.,* 1994; Xu *et al.,* 2013). However, although classed as 'essential', high concentrations of iron are toxic to the cell resulting in the production of reactive oxygen species through the Fenton reaction (Gonzalez-Fletcha *et al.,* 1995), see Figure 1.3.3. Due to the toxic effects of high metal ion concentrations, bacterial cells have

developed mechanisms for maintaining metal ion homeostasis. An example of metal ion control is copper homeostasis (Cu(I/II) in gram-negative bacteria, which involves several mechanisms of which the *cue* and *cus* systems are best known. These systems detect Cu(I/II) which leads to the expression of proteins which transport copper ions either into the periplasm or out of the cell altogether (Arguello *et al.,* 2013; Hernandez-Montes *et al.,* 2012).

1.2.2 Bacterial Cell Wall and Membrane Structure

Bacteria are single-celled prokaryotic organisms that differ from eukaryotic cells in both size and their cellular ultrastructure. Bacterial cells fall into two classes; Gram-positive and Gram-negative, based on the cells ability to take up the Gram stain (Gram, 1884).

Gram-positive bacteria contain an inner phospholipid membrane, similar to eukaryotic cells. In addition to this is a thick extracellular cell wall, comprised of a lattice of polyamino-sugar (peptidoglycan) chains anchored by lipoteichoic acid chains, separated from the cell membrane with a thin periplasm, see Figure 1.2.1.

The peptidoglycan chains are composed of alternating *N*-acetylglucosamine (GlcNAc) and *N*-acetylmuramic acid (MurNAc) monomers. MurNAc contains a linker region of 4 amino acids; L-alanine, D-glutamic acid, D-aminopimelic acid (DAP)/ L-lysine (the former being in Gram-negative and the latter in Gram-positive), and L-alanine (Silhavy *et al.,* 2010 & Waldemar *et al.,* 2008), see Figure 1.2.2. The linker region interacts with other MurNAc in opposite peptidoglycan chains to form a linker bond that gives the peptidoglycan structural rigidity (Beveridge, 1981).

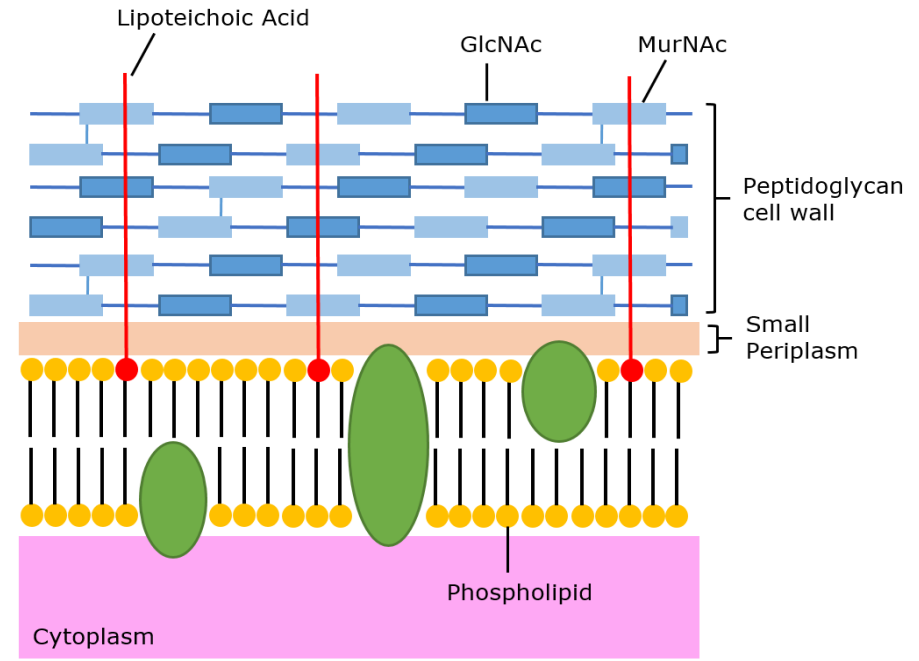

Figure 1.2.1: Structure of the bacterial membrane and large cell wall of gram-positive bacteria. There is a large peptidoglycan cell wall interconnected by amino-linkers and Lipoteichoic acids. The cell wall is separated by a small periplasmic region from the membrane.

The lattice structure of the peptidoglycan layer is also relatively porous to small molecules including metal ions (Waldemar *et al.,* 2008). In addition to peptidoglycan, the cell wall contains polyalcohol's (teichoic acids) which bind to the lipids of the membrane (lipoteichoic acids) and interact with the peptidoglycan chains. The interaction between the two molecules anchors the cell wall to the cell membrane and gives the cell wall rigidity, as well as an overall net-negative charge (Sonnenfield *et al.,* 1985). Figure 1.2.2 shows the structures of teichoic acid (**A**) and the linker region of MurNAc (**B**).

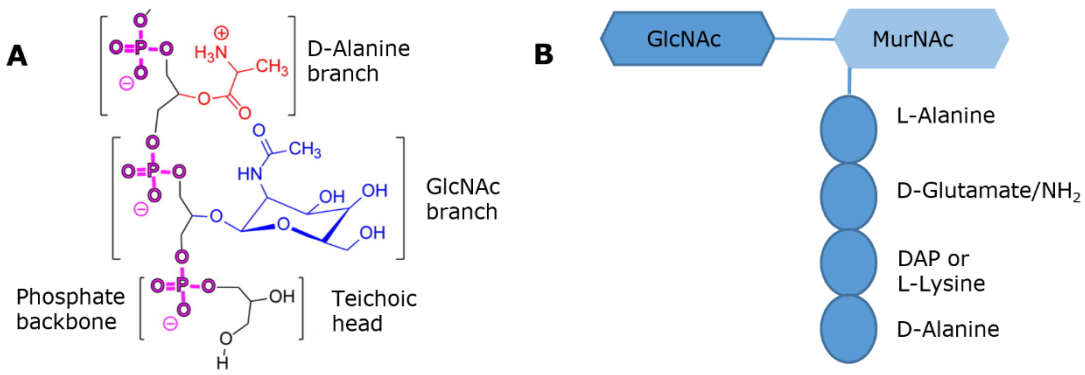

Figure 1.2.2: (A) Structure of teichoic acid linked to a D-Alanine and GlcNAc residues. The phosphate backbone is the main binding region for metal ions. **(B)** Amino branch of a MurNAc residue, the DAP/L-Lysine residue vary depending on bacteria type. These branches interconnect with one another forming a lattice that gives the peptidoglycan a rigid

Gram-negative cells, in comparison, do not have an extracellular cell wall but instead contain two phospholipid bilayers, creating an inner and outer membrane, with the space in between called the periplasm, see Figure 1.2.4. Within the periplasm a small cell wall is present, comprised of a few chains of peptidoglycan. The cell wall is not anchored by lipoteichoic acids like Gram-positive bacteria resulting in a less rigid structure.

The outer membrane (cell envelope) of Gram-negative bacteria encases the periplasm and cell wall. The outer membrane is composed of both phospholipids and lipopolysaccharides, in addition to outer membrane proteins such as porins. Porins are common to the outer membrane and allow small molecules to diffuse across the membrane (Vijayaraghavan *et al.,* 2008).

Lipopolysaccharides are important to bacteria as they interact with the extracellular region, their structure is broken down to three domains; Lipid-A, Core and O-antigen regions. The Lipid-A domain is normally composed of a glucosamine disaccharide that is phosphorylated, this in turn is covalently bound the core region. The core is composed of several

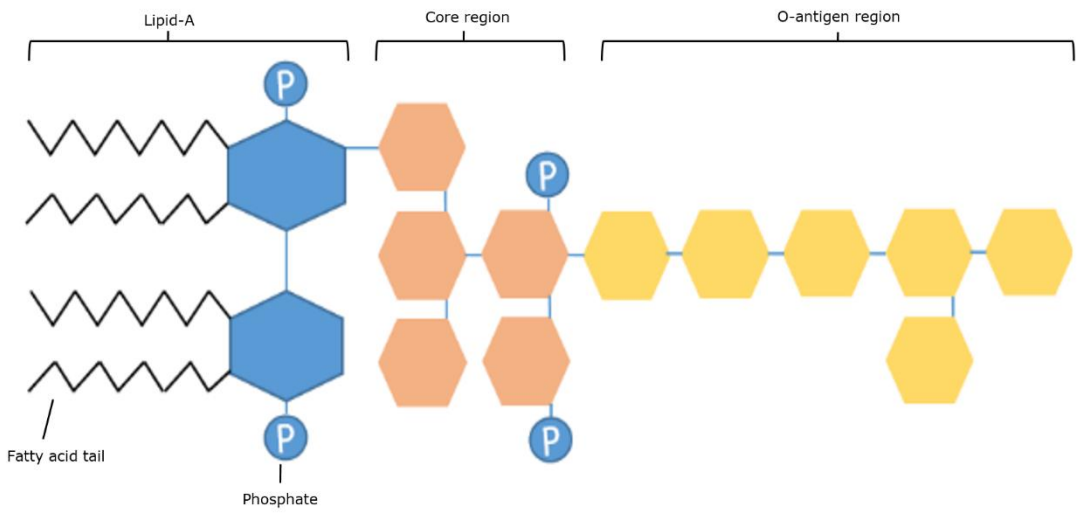

Figure 1.2.3: Structure of an average lipopolysaccharide. The Lipid-A region is a covalently bonded glucosamine disaccharide, connected to a Core region. The core varies in the number and type of sugars, however several of the monomers are phosphorylated. The O-antigen varies in the number of residues and a types depending on their signalling role.

covalently bound sugars such as heptose, some of which are phosphorylated, these join onto the O-antigen, which is a long polysaccharide chain involved in bacterial interactions and is what the immune system detects upon infection (Caroff *et al.,* 2003). Figure 1.2.3 shows the structural breakdown of an average lipopolysaccharide.

The components of the outer membrane are mainly polar or negatively charged, thus giving an overall net-negative charge which allows for interactions with extracellular material (Sonnenfield *et al.,* 1985). The structure of the inner and outer membranes of Gram-negative bacteria can be seen in Figure 1.2.4.

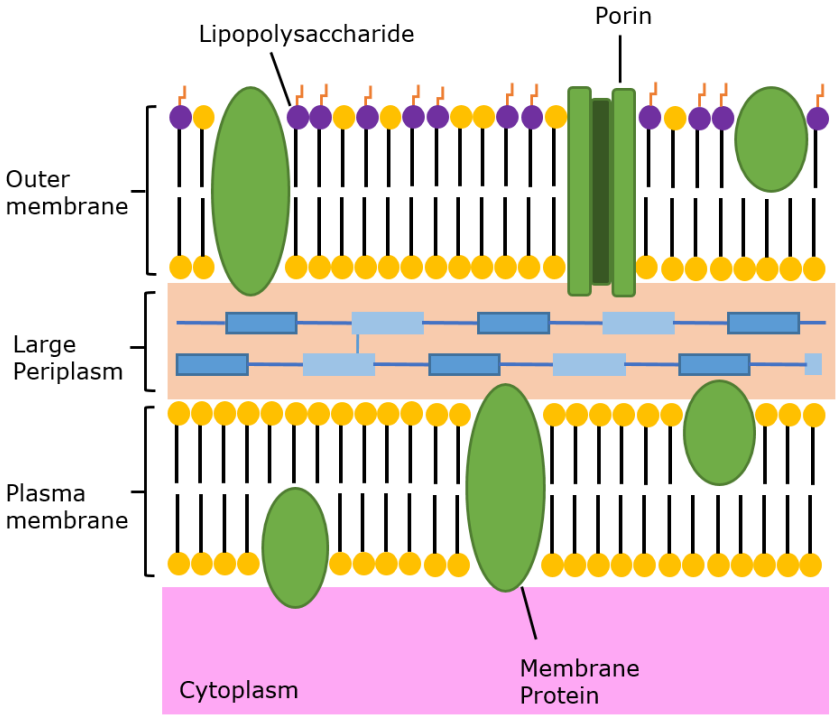

Figure 1.2.4: Structure of the bacterial membrane and cell envelope of gram-negative bacteria. There are two membrane regions with membrane bound proteins, including porins, divided by a large periplasmic region with a small peptidoglycan region.

1.2.3 Overview of Metal ion Uptake by Bacteria

The process by which metal ions are taken up by bacterial cells occurs through two main methods. The first is through an energy-independent method termed Biosorption, and the second is an energy-dependent process termed Bioaccumulation.

1.2.3.1 Biosorption

Biosorption is a metabolism-independent mechanism requiring no energy for the accumulation of metal ions by cells, this method of uptake has been observed by both living and dead cells (Oh *et al.,* 2009). External factors such as pH and metal ion type affect biosorption (Chen *et al.,* 2007). Several mechanisms as to how biosorption is carried out in cells have been identified including electrostatic interactions with the cell

wall/envelope, metal deposition, porins, binding to proteins with metal affinity, and ion exchange (Fomina and Gadd, 2014).

Electrostatic interactions between metal ions and either the cell wall (Gram-positive) or outer membranes (Gram-negative) of bacteria have been studied extensively. Section 1.2.2 showed that Gram-positive bacteria have a large cell wall comprised of peptidoglycans with amino acid linkers and interconnecting teichoic acids, resulting in an overall net-negative charge. Metal ion binding has been shown to occur with either the negatively charged carboxyl group of the glutamate in the peptidoglycan linker or the negatively charged backbone of the lipoteichoic acids. The affinity of the glutamate carboxyl for metal ions is higher than the lipoteichoic acid backbone, however this can vary depending on metal ion. It is suggested that the metal ions traverse the lipoteichoic acids backbone, additionally picking up any bound metal ions on the glutamate carboxyl group, by moving from one phosphate group to another along the backbone until it reaches the cell membrane where it aggregates into a metal deposit (Gadd, 1990; Thomas *et al.,* 2015).

In comparison, Gram-negative bacteria have a cell envelope composed of both phospholipids and lipopolysaccharides. The negatively charged phosphate groups of the lipopolysaccharides (see Figure 1.2.3) provide a metal binding region much like in lipoteichoic acids. In addition, the polar lipid heads of the membrane interact with metals, binding of the ion leading to a cascade effect whereby more metal ions bind resulting in a metal deposit (Beveridge *et al.,* 1985; Gadd, 1990).

Mullen *et al* (1989) showed deposition through the binding of Ag(I), Cu(II), Cd(II) and La(III) to both Gram-positive and Gram-negative bacteria. Ag(I) deposition, through aggregation, occurred both at the cell

wall/membrane and in cases the cytoplasm. The aggregation of metal ions has been shown to disrupt the membrane and create membrane pores, though which metal ions can enter the cell. This has been observed in several metal types including Ag(I) and Ni(II) (Afzal *et al.,* 2017; Feng *et al.,* 2000).

Similar to the production of cell pores through metal accumulation, porins are another way in which metals can enter the cell. Porins are found in the outer membrane of Gram-negative bacteria. They are comprised of β-barrel, typically as a trimer, embedded in the outer membrane with a hydrophilic channel that allows for the passive diffusion of small molecules into and out of the periplasm (Ma *et al.,* 2009), see Figure 1.2.5.

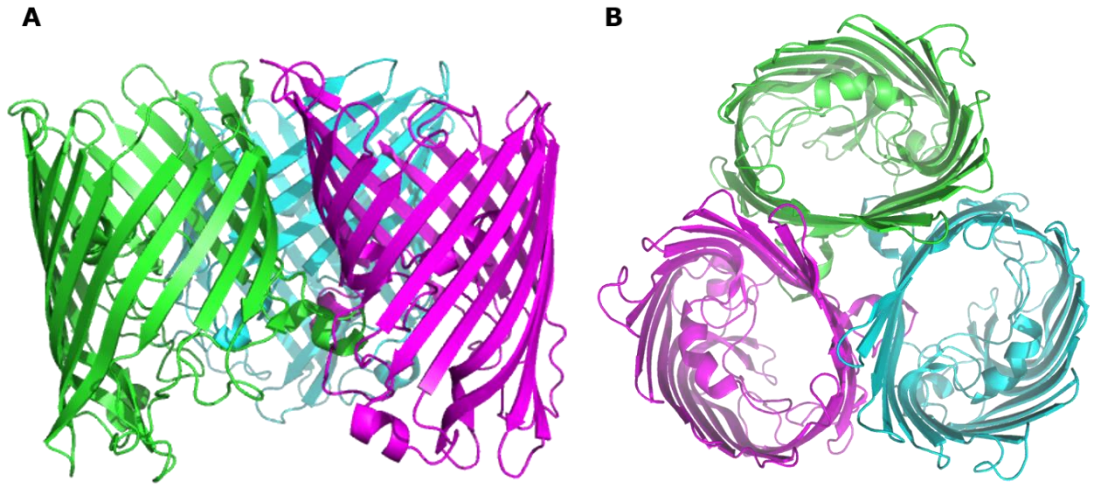

Figure 1.2.5: Structure of a typical porin, OmpF (PDB; 1OPF). The structure shows the trimer formation that the proteins adopt within the membrane both side on **(A)** and from above **(B)**.

There are many types of porins with different size channels that allows for an array of molecules including metals to diffuse through (Hancock, 1984; Vergalli *et al.,* 2019). Once the metal has passed through the porin it enters the periplasm where it is either actively taken up by proteins or pumped into the cytoplasm (Section 1.2.3.2), or the metal

ions interact with the phospholipid inner membrane causing membrane disruption as with the outer membrane.

Biosorption can also occur through the presence of metal ion binding proteins within the membrane, as well as extracellular proteins such as siderophores which bind iron ions and transport them into the cell through porins (Kramer *et al.,* 2019). The binding of metal ions to these proteins can occur on the cell surface or in the periplasm (Gram-negative) or cytoplasm (Gram-positive). Binding of metal ions can be specific or generic depending on the protein, specific binding usually occurs when metals are 'essential' to the cell. Whereas non-specific binding is usually observed in 'non-essential' metal binding.

Overall biosorption occurs down a chemical potential gradient, whereby it is a non-equilibrium process trying to achieve equilibrium. The major drawback of the process is that in most cases it does not allow for any specificity of metal ion, which can be deleterious to the cell.

1.2.3.2 Bioaccumulation

The process by which metal ions are actively taken up by cells is termed bioaccumulation, the process is a metabolism dependent mechanism by which membrane proteins either pump or facilitate the movement of metal ions across the membrane. Membrane pumps most frequently use an energy source, typically in the form of ATP, to actively pump metal ions across the membrane. Additionally, there are proton gradient driven channel proteins that bind to metal ions. The proton gradient allows metal ions to cross the membrane without the need for an energy source such as ATP (Diep *et al.,* 2018). Both processes are observed in Gram-positive/negative bacteria, although in Gram-negative bacteria if no energy driven proteins are present then porins facilitate the passage of

metal ions into the periplasm where there are energy driven pumps (Diep *et al.,* 2018).

Once in the cytoplasm of the cell the metal ions are either compartmentalised or taken up by metal ion binding proteins. In both cases the aim is to minimise the number of free metal ions present within the cell, thus reducing the toxic effect on the cell (Gadd, 1990). Figure 1.2.6 shows an overview of the methods of bioaccumulation.

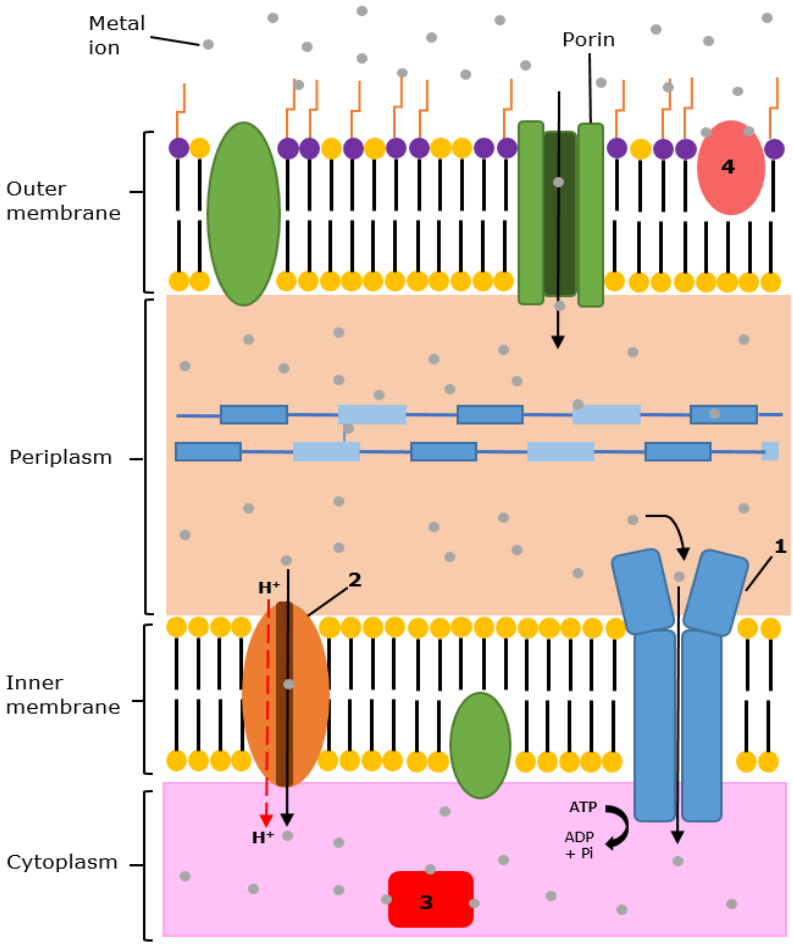

Figure 1.2.6: Overview of how bioaccumulation is achieved in bacteria. **(1)** Metals that have made into the periplasmic space can be actively pumped across the membrane using proteins that utilise ATP. **(2)** Metals can also be transferred across the membrane using a proton channel, this process requires a proton gradient. **(3)** Metals that make it into the cytoplasm after bioaccumulation are often taken up by metal binding proteins. **(4)** Metals binding to membrane proteins and accessing the periplasm through porins.

The dependence of a metabolism-based energy source means that the process of bioaccumulation is carried out by living cells only, in contrast to biosorption which is carried out by living and dead cells (Kadukova *et al.,* 2004). Bioaccumulation as a process allows for the possibility of high metal ion concentrations within the cell, going against a concentration gradient. However, high concentrations of metals ions within cells are generally highly toxic and so are not commonly found (Vijayaraghaven *et al.,* 2008). Bioaccumulation is a slower process than biosorption as it requires an energy source. The process can be affected temperature, metabolic state of the cell, presence of inhibitors and abundance of an energy source (Gadd, 1990). Overall, bioaccumulation is a useful mechanism for bacteria to take up essential metal ions when their presence in the environment may be limited.

1.3 Antimicrobial Properties of Silver and Ag(I) Resistance

Ag(I) is a metal which has extensive uses within the medical field due to its far reaching antimicrobial properties. This section explores the uses of Ag(I) within medicine and the toxic effects it has on bacteria.

1.3.1 Use of Ag(I) Within Medicine

Ag(I) has many uses within the medical field all of which are harnessing their antimicrobial properties. The main use of Ag(I) at present is in hospital burns wards as a precautionary treatment, with it added to creams or lining bandages. In both cases Ag(I) is added in the form of Ag(I) sulfadiazine, this is a stable metal compound that is non-toxic to humans at the medical concentrations used (Wright *et al.,* 1998). The UK

alone spent £25 million on Ag(I) containing bandages and creams in 2009 (NHS National Prescribing Centre, 2009).

In addition to this Ag(I) is commonly used to coat pieces of medical equipment such as catheters, as well as medical implants such as heart valves. The addition of Ag(I) is to prevent bacterial biofilms from forming which can lead to infection and possible sepsis (Cook *et al.,* 2000 & Tobin *et al.,* 2003).

Ag(I) compounds are not only found in hospitals as a preventative treatment. Dentistry uses Ag(I) as an amalgam, along with other metals such as mercury. However, with the development of different artificial materials the use of Ag(I) amalgams has reduced over the years, primarily due to possible metal toxicity issues (Bharti *et al.,* 2010). Other areas where Ag(I) is used is in linings of athletic socks, and as additives to deodorants and paints.

1.3.2 Mechanisms of Ag(I) Toxicity Within Bacteria

There are many different cellular pathways and processes that are affected by Ag(I) ions, all of which lead to eventual cell death. Figure 1.3.1 shows an overview of the different antimicrobial properties of Ag(I).

Ag(I) ions are strong electron receivers and readily interact with electron donors such as sulphur thiol groups: due to this Ag(I) readily binds to thiol rich proteins (Gordon *et al.,* 2010). A major group of thiol rich proteins within bacteria are those involved in respiration and the electron transport chain, any disruption of which is lethal to the cell (Figure 1.3.1-**1**).

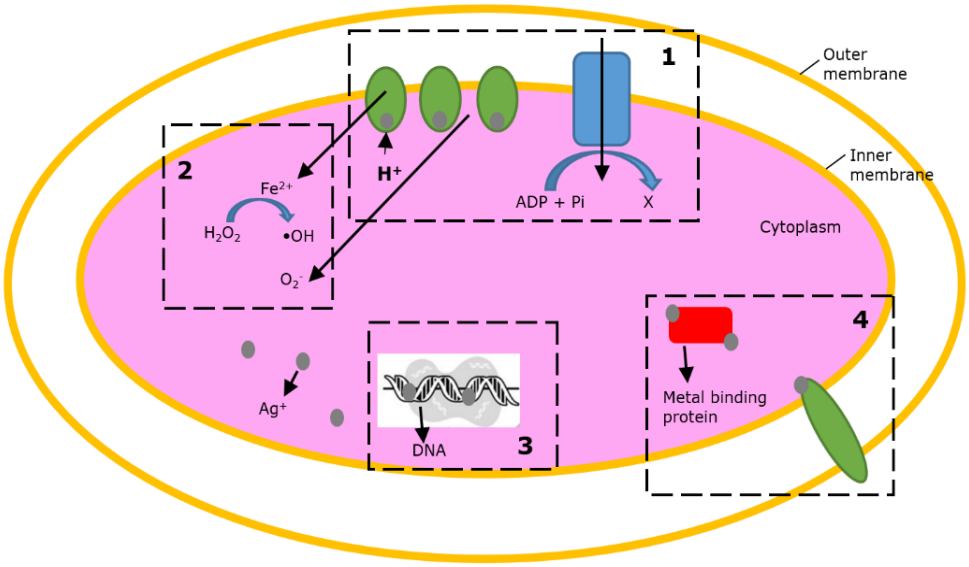

Figure 1.3.1: Diagram of the different antimicrobial mechanisms Ag^+ exert on bacteria. **(1)** The disruption of cell respiration and electron transport chain. The binding of Ag(I) inhibits the transferal of electrons and the pumping of protons, thus disrupting the proton motive force and stopping ATP synthesis. **(2)** The binding of Ag(I) to the electron transport proteins also created ROS species and liberates iron (Fe(II)) aiding the formation more ROS. The ROS removal enzymes are also inhibited by Ag^+ thus ROS concentrations increase. **(3)** Ag(I) binds to DNA forming pyrimidine dimers that reduce protein expression and transcription. **(4)** Ag(I) bind to other proteins within the cell disrupting or inhibiting their function.

The electron transport chain (ETC) utilises a proton gradient, which a membrane bound ATP synthase uses for the production of ATP (Anraku, 1988). Binding of Ag(I) has been observed with complex I of the ETC, NADH ubiquinone oxidoreductase, which contains an iron-sulphur (Fe-S) cluster used in electron transferal. The binding of Ag(I) to complex I inhibits the transferal of electrons to complex II, thus shutting down the system (Figure 1.3.1-**1**). The shutting down of the ETC results in a loss of the proton motive force, which results in the lack of ATP production

(Dibrov *et al.,* 2002). This can lead to disruption of the cell membrane which facilitates proton leakage and potentially allow more Ag(I) ions to enter the cell (Schreurs *et al.,* 1982; Semeykina *et al.,* 1990).

Possibly the biggest impact of Ag(I) in bacterial cells is the resulting production of reactive oxygen species (ROS) (Figure 1.3.1-**2**). These are molecules naturally produced by the cell, as a result of aerobic respiration. The most common types are superoxide (O_2^-), hydroxyl radical •OH and hydrogen peroxide (H_2O_2) (Gonzalez-Fletcha *et al.,* 1995).

ROS are highly toxic to cells, interacting with proteins and enzymes, often rendering the latter inactive, additionally they increase cell membrane permeability, interrupt the ETC and damage to DNA (Storz & Imlay, 1999 & Yin *et al.,* 2020). ROS are normally removed from bacteria through molecules such as superoxide dismutase (SOD), which as its names suggests catalyses O_2^- into a non-harmful alternative (Wang *et al.,* 2018). Enzymes such as SOD usually contain numerous thiol group, which are essential for the enzymes activity, this is problematic as they are targeted by Ag(I) ions rendering the enzyme inactive (Park *et al.,* 2009). The inability to remove ROS results in increased concentrations within the bacteria that leads to more damage and eventual cell death.

The build-up of ROS molecules has also been shown to disrupt Fe-S clusters within proteins through superoxide interactions, leading to iron leakage within cells. The presence of iron within the cytoplasm can lead to the production of more ROS molecules, specifically hydroxyl radicals, through the Fenton reaction involving the catalytical breakdown of hydrogen peroxide (see Figure 1.3.2) (Gordon *et al.,* 2010; Hayyan *et al.,* 2016).

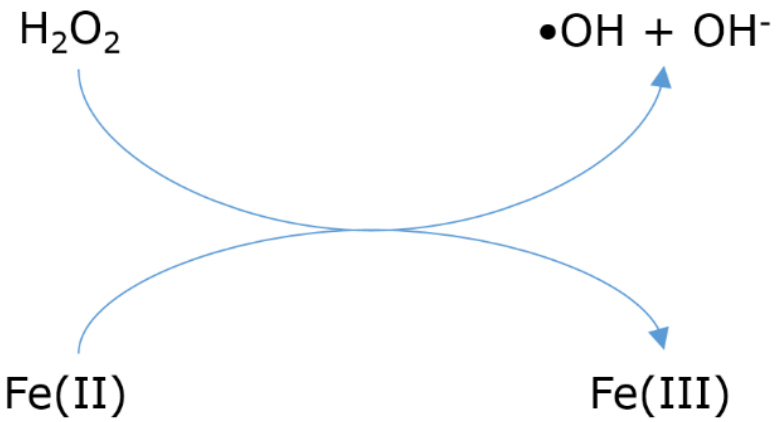

Figure 1.3.2: Diagram of the production of the ROS hydroxyl radical through the Fenton reaction. Iron(II) (Fe(II)) catalyses the degradation of hydrogen peroxide (H_2O_2) into a hydroxyl radical (•OH) and a hydroxyl molecule (OH^-). The process also creates Iron(III) (Fe(III)).

More recent studies have shown that Ag(I) interrupts several proteins involved in glycolysis and the TCA cycle, it should be noted that bacteria do not have a complete TCA cycle similar to eukaryotes however is relatively similar. Both systems are involved in the production of ATP/GTP and NADH which is important for the electron transport chain which is the main energy source for cells (Krebs & Johnson, 1980). Ag(I) has been shown to bind to 3 enzymes involved in glycolysis, the main being glyceraldehyde-3-phopshate dehydrogenase (used to make NADH), in addition several of the TCA enzymes were inactivated by the presence of Ag(I) (Wang *et al.,* 2019).

Finally the interaction Ag(I) is not limited to proteins, modifications of DNA through the presence of Ag(I) have been recorded (Figure 1.3.1-**3**). Ag(I) has been shown to interact with both the phosphate backbone and the nucleoside residue of DNA, with the latter interaction more

preferential (Mijnendonckx *et al.,* 2013). The most common interaction is through the formation of guanine pyrimidine dimers, occurring between two adjacent guanine bases. The formation of these dimers inhibits the sequential transcription of the DNA both for protein expression and more importantly DNA replication, thus with this inhibition cells cannot replicate for cell growth. Additionally, expression of ROS degrading proteins is also hindered (Arakawa *et al.,* 2001; Russell & Hugo, 1999).

1.3.3 Emergence of bacterial Ag(I) resistance

Although Ag(I) is an effective antimicrobial agent and is commonly used within the medical field, the extensive use of Ag(I), like antibiotics, has seen the emergence of Ag(I) resistance in some bacterial strains. This resistance falls into two categories; exogenous (external horizontal acquisition) and endogenous (mutational).

In terms of exogenous mechanisms for resistance to Ag(I), the main source is through the pMG101 plasmid. This was first recorded in Gram-negative *Salmonella* bacteria found in a US hospital burn ward in the 1960's, the resistant bacteria killed three patients through septicaemia (Jelenko, 1969). The ward was closed for decontamination, however it was found that the *Salmonella* had transferred the resistance into *E.coli*. Analysis of the *E.coli* found the plasmid pMG101, which inferred resistance to over six times the normal lethal dose of Ag(I). The plasmid also conferred resistance to Hg(II), tellurite and several antibiotics including ampicillin and chloramphenicol (Gupta *et al.,* 1999; McHugh *et al.,* 1975). To date the pMG101 plasmid, and thus the *sil* genes, have been identified in *Salmonella, Escherichia coli*, *Klebsiella, Acinetobacter. Enterobacter* and *Pseudomonas* (Finley *et al.,* 2015).

The region of the pMG101 plasmid that contained the Ag(I) resistance proteins was termed the *sil* gene cluster. The operon was found to contain nine open reading frames (ORF) in three transcriptional regions that were very similar to other metal resistance operons such as the *cus* and *cue* copper systems and the cadmium/zinc Czc system (Gupta *et al.,* 2001; Randall *et al.,* 2015 & Hotton *et al.,* 2021).

In addition to the exogenous method of resistance, through the pMG101 (*sil*) plasmid, bacteria have been shown to become resistant to Ag(I) through endogenous methods. Studies by Li *et al.* showed that under silver stress several strains of *E.coli* showed a reduction in the expression of OmpF or OmpC. These are outer membrane porins that would allow the passive diffusion of Ag(I) into the periplasm of bacteria which can then make its way into the bacterial cytoplasm. The reduced expression though led to the ability of these bacterial cells to withstand up to 64x the normal lethal dose of Ag(I) (Li *et al.,* 1997).

There is evidence to suggest that a combinatorial method of resistance occurs using both exogenous and endogenous resistance methods. Randall *et al.* showed that bacteria can obtain the pMG101 plasmid, however the *sil* system is inactive. Activation occurs when a a missense mutation within the SilS (sensor kinase) protein activates the expression of the rest of the proteins within the system (Randall *et al.,* 2015 & Elkrewi *et al.,* 2017).

Finally, in conjunction with exogenous and endogenous methods of resistance, bacteria has metal homeostasis mechanisms such as the *cus* and *cue* systems. These are chromosomal systems that regulate Cu(I) within the cell, however there is extensive evidence that they interact

and regulate low levels of Ag(I) (Staehlin *et al.,* 2016; Randall *et al.,* 2015).

1.4 The *sil* gene cluster

Many of the proteins within the sil system have not been studied extensively since its emergence, however through sequence homology many of the open reading frames have been given putative roles based on their homology to the copper *cue* and *cus* systems (Gupta *et al.,* 1999). The *cue* and *cus* systems, as stated earlier in section 1.2.1, are chromosomally located and are responsible for maintaining the copper homeostasis of Gram-negative bacteria (Outten *et al.,* 2001). Figure 1.4.1 shows an overview of the *cue* and *cus* systems within gram-negative bacteria, with the proposed roles of the sil proteins shown in Figure 1.4.2.

The *cue* system is primarily used by bacteria in anaerobic conditions and is activated by the binding of Cu(I) to CueR which is a transcriptional activator (Outten *et al.,* 2000; 2001). The activation of CueR upregulates the expression of two further proteins; CopA a P1B-type ATPase which actively pumps Cu(I) ions into the periplasm using ATP, and CueO a periplasmic multi-copper oxidase which chelates Cu(I) ions and oxidises them to less toxic Cu(II) ions (Gonzalez-Guerrero & Arguello, 2008; Gourdon *et al.,* 2011; Grass & Rensing, 2001; Singh *et al.,* 2004).

The *cus* system has a similar initiation process to the *cue* system, however instead of a single activator protein there is a two component regulation system, CusRS. CusS is an inner membrane sensor kinase that detects and binds periplasmic Cu(I), whereupon it phosphorylates and

activates CusR (Affandi *et al.,* 2016; Chen *et al.,* 2020). CusR is a response regulatory protein that upon activation binds to the *cus* operon and upregulates the expression of the CusCFBA proteins (Munson *et al.,* 2000). The CusCBA proteins form a resistance-nodulation-cell division (RND) complex that is responsible for exporting Cu(I) ions out of the cell. The complex is composed of CusA an inner membrane efflux pump that is proton driven, CusB a membrane fusion protein and CusC an outer membrane protein factor (Long *et al.,* 2012; Nies, 2003). CusF is a small periplasmic Cu(I)/Ag(I) chelating metallochaperone that delivers periplasmic Cu(I) to the CusCBA complex (Xue *et al.,* 2008). Overall, both the *cue* and *cus* systems lead to the controlled homeostasis of Cu(I) ions.

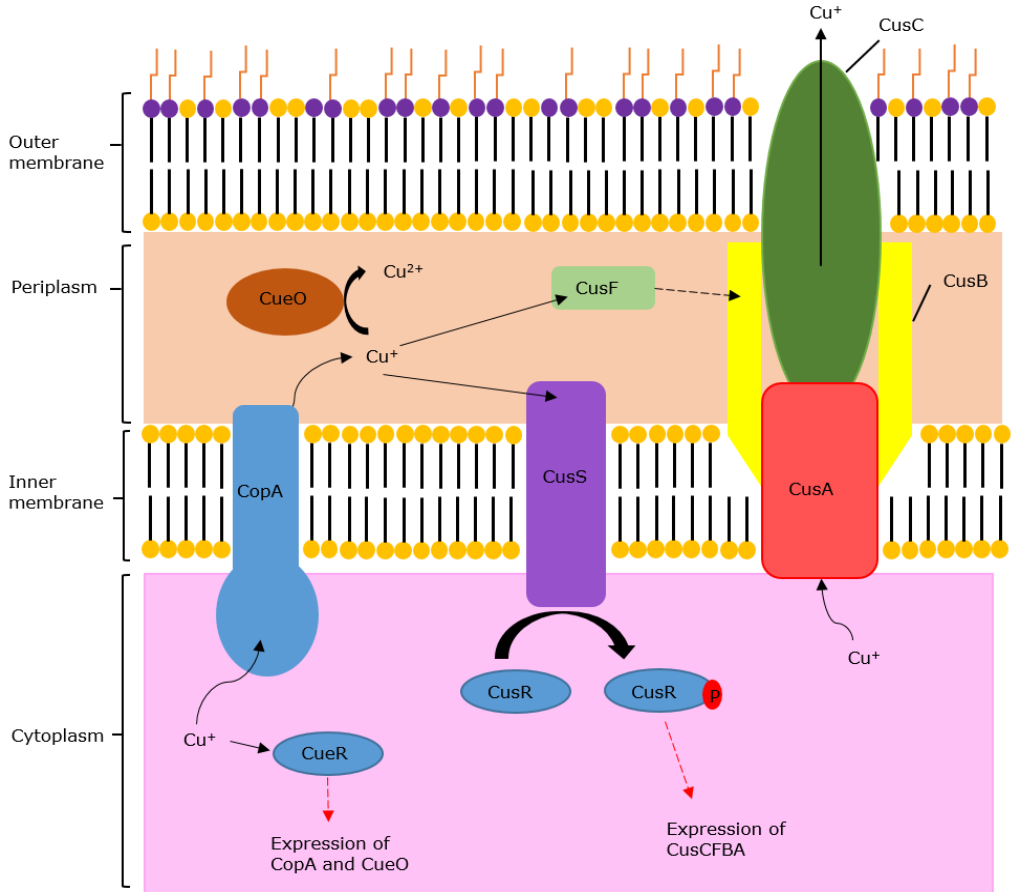

Figure 1.4.1: Overview of the inter-connecting *cue* (left) and *cus* (right) systems. The *cue* system includes the response regulator CueR, the ATPase CopA and the periplasmic oxidase CueO oxidising Cu(I) into Cu(II). The *cus* system shows the two component system CusRS, with the latter activating CusR for expression of CusCFBA. The CusCBA complex is shown spanning the periplasm with Cu^{+} entering through CusA and by CusF.

Due to the high degree of sequence homology between the *cue* and *cus* systems and the *sil* system, seven of the nine open reading frames have been given putative functions. As in the *cus* system there is a proposed two component translational regulatory system of SilS and SilR, the former a sensor-histidine kinase detecting periplasmic Ag(I) and the latter a response regulator protein promoting expression of the other *sil* genes at one of three transcriptional sites (Brown *et al.,* 1995). Upstream of the SilR site there is SilE, a 143 amino acid periplasmic protein that

has been shown to bind up to eight Ag(I) ions (Asiani *et al.,* 2016). Downstream of SilR are the remaining six reading frames given the names SilABCFGP. The ORF's for SilCBA have high sequence homology to the CusCBA complex, with 71%, 67% and 87% similarity respectfully (Gupta *et al.,* 1999). It is therefore assumed that these proteins form an Ag(I) exporting RND complex, with SilA the inner membrane efflux protein, SilB a membrane fusion protein and SilC an outer membrane protein factor (Silver, 2003). As in the *cus* system there is a proposed small periplasmic Ag(I) chelating chaperone protein termed SilF that is expressed with SilCBA, it is believed to deliver Ag(I) ions to the SilCBA complex (Mealman *et al.,* 2011). The last two translatable ORF's have been termed SilG and SilP, with the formers role not yet known. SilP is P_{1B}-ATPase, sharing a high homology to CopA of the *cue* system (Hobman *et al.,* 2014). It has therefore been proposed that SilP actively exports Ag(I) ions from the cytoplasm into the periplasm using ATP as an energy source (Alquethamy *et al.,* 2019; Gupta *et al.,* 1999). Figure 1.4.2 shows an overview of the *sil* system, with proposed roles for each protein.

The research within this investigation looks at three of the *sil* proteins; the ATPase efflux pump SilP, the periplasmic chaperone SilF and the outer membrane factor SilC.

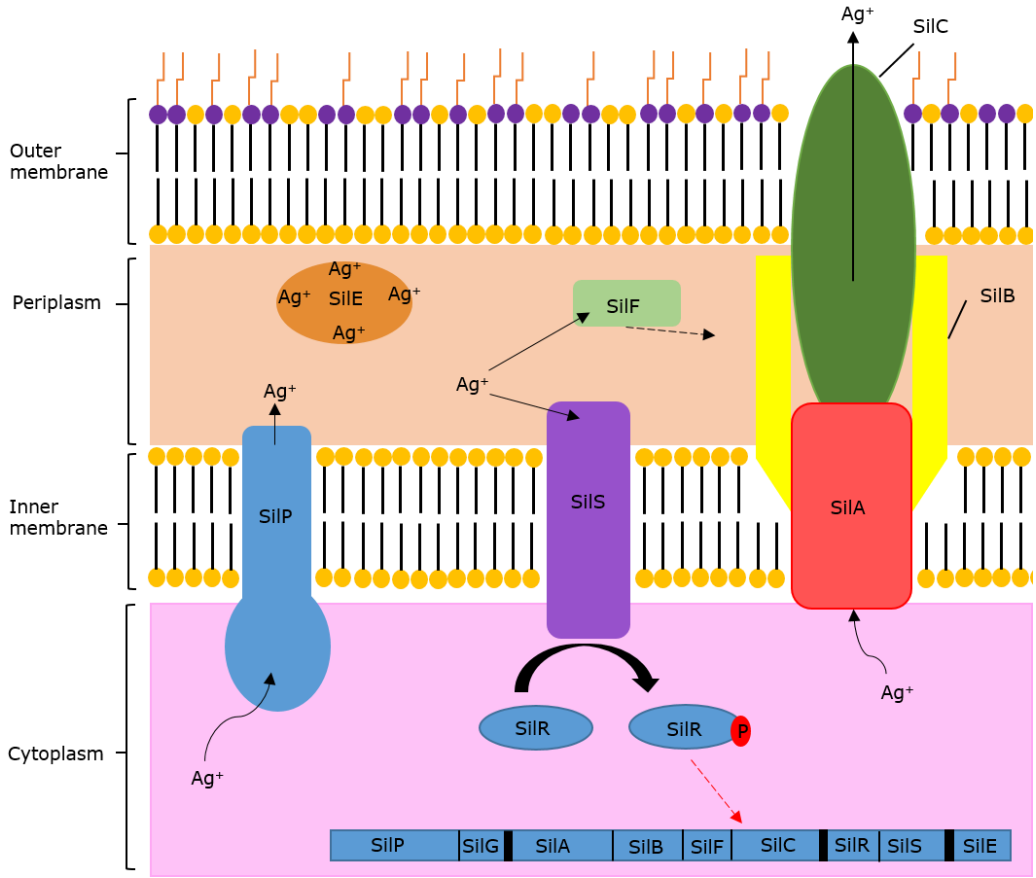

Figure 1.4.2: Overview of the sil system. The system is very similar to both the *cue* and *cus* systems. The two component regulatory system can be seen (central) upregulating the expression of the *sil* genes at the three transcriptional sites (highlighted in thick black lines). Cytoplasmic Ag(I) ions are exported into the periplasm by the ATPase SilP, SilE and SilF chelate these ions. The SilCBA complex (right) can be seen exporting Ag(I) ions out of the cell completely

1.5 SilP – Inner Membrane P1B-ATPase

The SilP gene encodes for 824 amino acid protein with a molecular weight of approx. 88kDa. Homology modelling of the gene indicates that the protein is a member of the P-Type ATPase superfamily (Silver *et al.,* 1999). P-type ATPases are phosphoenzyme protein pumps that use ATP to actively export a range of biological molecules, mainly ions and lipids, they are found in both eukaryotic and prokaryotic cells.

The nomenclature of P-type ATPases is indicative of the protein phosphorylation that occurs during its Post-Albers catalytic cycle (Axelsen & Palmgren, 1998; Palmgren & Nissen, 2011). The P-Type ATPase superfamily is subdivided into five main classes, which are subdivided further. The main functions of the different classes (and sub-classes) are as follows; P1 ATPases export transition and metal ions, with P1A exporting the former and P1B, which SilP belongs to, the latter (Thever & Milton, 2009). P2-ATPases are involved in Ca^{2+} and Na^{+}/K^{+} exportation with the best known sarco(endo)plasmic reticulum Ca^{2+}-ATPase (SERCA). P3-ATPases are involved in H^{+} exportation, P4 ATPases are lipid flippases and P5 ATPases have not been given putative roles as of yet (Lutsenko & Kaplan, 1995; Okamura *et al.,* 2003). In all cases it is believed that the catalytic cycle of all P-type ATPases follows the Post-Albers cycle, in which different conformations are adopted as ATP and the ligand bind, the process of which results in hydrolysis of ATP and the exportation of the ligand (Bublitz *et al.,* 2011), further detail on this is given in Section 1.5.5.

P-type ATPases have highly conserved structures comprising of four domains; actuator (A), phosphorylation (P), nucleotide binding (N) and the 8-10 transmembrane (TM) domain. P1B-ATPases contain an additional N- or C-terminal metal binding domain (HMBD) (Lutsenko & Kaplan, 1995; Solioz & Vulpe, 2006; Silver *et al.,* 1993). Each domain will be explored at greater depth later in the chapter. To date there are only two P1B-ATPase structures, CopA (PDB; 3RFU) a Cu(I) exporting ATPase and ZntA (PDB; 4UMV) a Zn(II) exporting ATPase, see Figure 1.5.1 below (Gourdon *et al.,* 2011; Wang *et al.,* 2014).

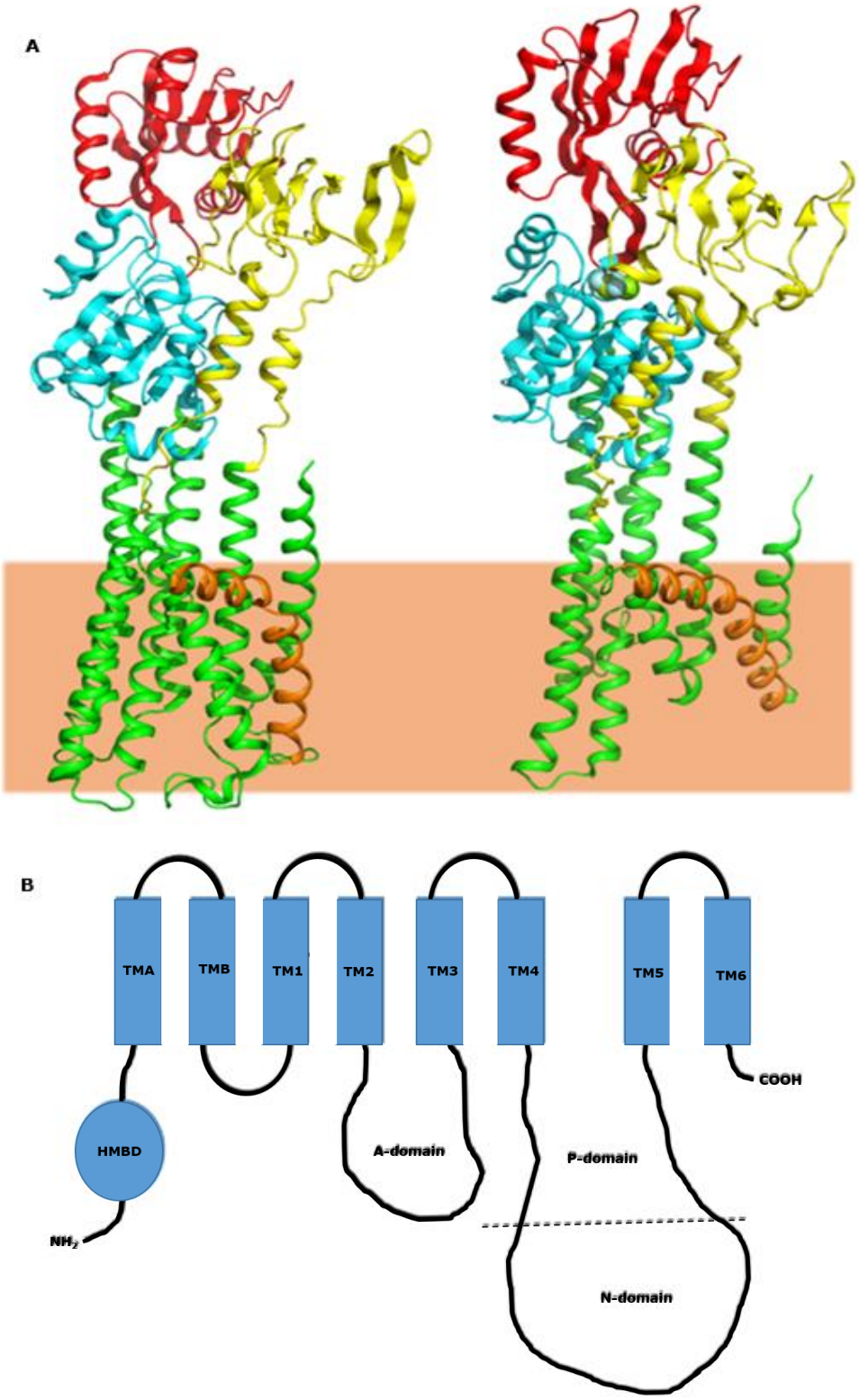

Figure 1.5.1: A) Structures of CopA (PDB: 3RFU) left and ZntA (PDB: 4UMV) right both in there catalytic E2 state. Both structures are without the HMBD, however contain all the other highly conserved core P-type ATPase domains; A- (Yellow), P- (Cyan), N- Red and the TM regions (Green with kinked TMB in orange). The inner membrane is shown in Peach. **B)** Overview of predicted SilP structure.

Between the P1B-ATPases there are several highly conserved motifs within the different domains that are essential for protein activity. However, as alluded to earlier in the chapter, there are sub-families within P1B-ATpase family. The first sub-family is $P1B_{(I)}$ this is a family which notionally only exports monovalent metal ions, CopA, and supposedly SilP, belong to this sub-family (Gupta *et al.,* 1999). A common characteristic of this family is the presence of cysteine and histidine rich HMBD's. The other sub-family is $P1B_{(II)}$ which notionally interact with divalent metal ions, ZntA belongs to this sub-family (Arguello *et al.,* 2003; Smith *et al.,* 2014, 2017; Sitsel *et al.,* 2015; Zhitnitsky *et al.,* 2014). Table 1-1 shows the motif differences between $P1B_{(I/II)}$-ATPases.

Table 1-1: Comparison of important motifs determined for either ATPase activity or for metal ion transport between $P1B_{(I/II)}$-ATPases.

Domain Motifs	$P1B_{(I)}$ (CopA/SilP)	$P1B_{(II)}$ (ZntA)
A Domain		
TGE	✓	✓
P Domain		
DKTGT	✓	✓
TGD(N/S)	✓	✓
GDGxNDxAP	✓	✓
N Domain		
HP	✓	✓
GxGxxG	✓	×
HMBD		
CxxC / GMxCxxC	✓/×	✓/✓
TM (TMA, TMB, TM1-6)		
CPC	✓	✓
YN	✓	×
MALSS	✓	×

Sequence alignment (Figure 1.5.2) of SilP to CopA and ZntA shows the highly conserved motifs are maintained across the family see Figure 1.5.2 (Gupta *et al.,* 1999).

Figure 1.5.2: Sequence alignment of SilP (E.coli) to CopA (3RFU) and ZntA (4UMV) structure sequences. Domains are coloured as follows; HMBD (orange), A- (yellow), P- (cyan), N- (red), TM-MA/MB (light green), TM-1-6 (dark green). Conserved and important motifs are highlighted in pink.

1.5.1 Catalytic Post-Albers Cycle

The catalytic cycle of SilP, and that of all P-type ATPases, is thought to follow that of the Post-Albers cycle (Bublitz *et al.,* 2011). The cycle describes that the ATPase exists in two main enzymatic states (E1 and E2), with several different phosphate-bound intermediate states. Progression through the cycle results in conformational changes that ultimately lead to exportation of the ligand of choice (Albers, 1967; Post *et al*, 1972). The cycle was originally based on the exportation of Na^+/K^+ ions by Post and Albers separately, however Ca^{2+} exportation in SERCA1 has also been observed (de Meis & Vianna, 1979; Sorensen *et al.,* 2004).

As stated, there are several proposed states involved in the Post-Albers catalytic cycle. The first state, E1, is bound to ATP and has high affinity for the specific cytoplasmic ion of choice, the binding of which results in a conformational change (E1.Ion) in which the ATP is hydrolysed, and the protein becomes phosphorylated at the aspartate of the DKTGT motif (E1P or E1P.Ion) (Andersson *et al.,* 2014; Lutsenko *et al.,* 2001). The new E1P state releases ADP, due to low affinity, and another conformational change occurs (E2P or E2P.I) opening a pathway for the ions to exit. The E2P state has a low affinity for the metal ions of choice but a greater affinity for a counter ion, which leads to the metal ion replacement with the counter ion (E2P.X). The presence of the counter ions result in the dephosphorylation of the ATPase and another conformational change ending in the E2 state. The E2 state has a high affinity for ATP, which binds in nucleotide binding domain and results in the conformational change to the E1 state and the cycle restarts (Bublitz

et al., 2010 & 2011; Mattle *et al.,* 2013). Figure 1.5.3 illustrates the proposed Post-Albers cycle for SilP exporting Ag(I).

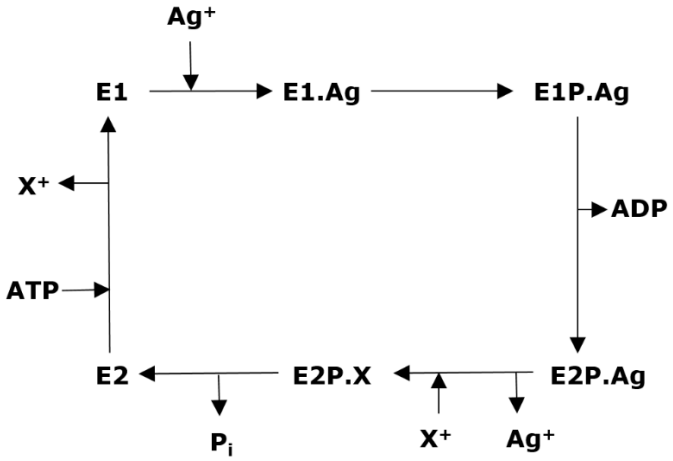

Figure 1.5.3: Proposed Post-Albers cycle for SilP. Binding of Ag(I) to ATP bound E1 SilP results in the hydrolysis of ATP and the phosphorylation of the protein, which itself results in a conformation change releasing ADP. Further conformational results in Ag(I) being released and counter ions replacing them which leads to ATP binding and the cycle restarts.

The majority of structural information regarding the Post-Albers cycle, was conducted on SERCA1 with several of the catalytic states solved, however it may vary between the sub-families with metal ions adopting a slightly different method (Olesen *et al.,* 2004 & 2007; Sorensen *et al.,* 2004; Toyoshima *et al.,* 2002). From these structures it has been shown that the main structural changes occur within the P, N and A domains, with the latter two showing the greatest degree of conformational change as they are catalytic heart of the reaction (Andersson *et al.,* 2014). The only structure of a P1B-ATPase at present is the copper (Cu^+) exporting ATPase CopA, this was captured in the E2 state (Gourdon *et al.,* 2011). Figure 1.5.4 shows a basic catalytic cycle of SERCA1, the changes are thought to be the same as in SilP.

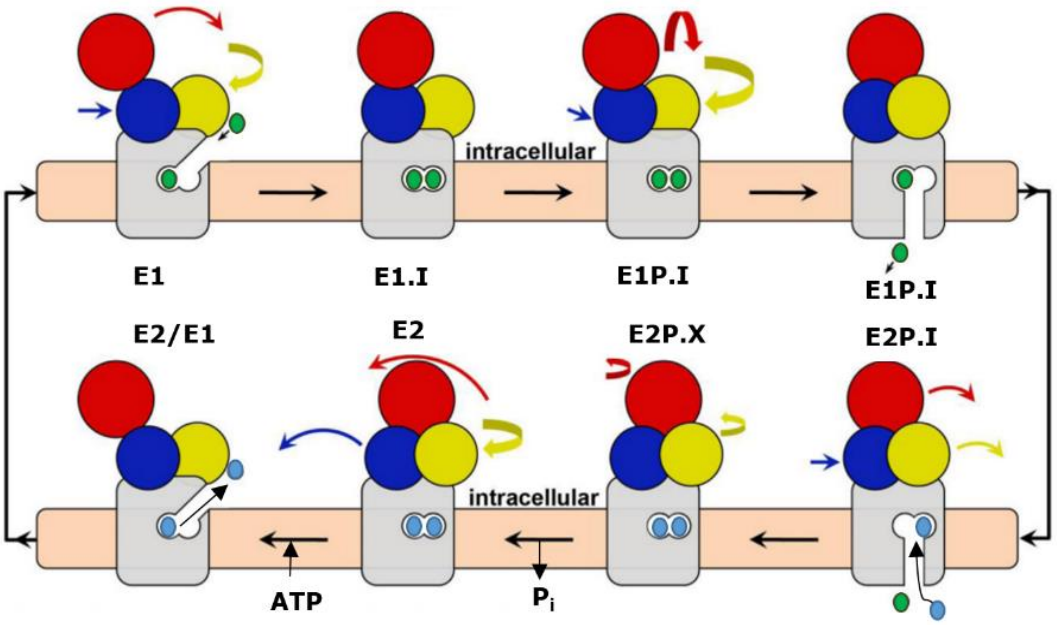

Figure 1.5.4: Supposed catalytic cycle of SilP based on the SERCA cycle. The figure shows the proposed conformational changes that may occur and the exportation of metal ions from the ATPase. A-domain (Yellow), P-domain (Blue), N-domain (Red), modified from Andersson et al 2014.

Overall SilP is a multi-domain P1B-ATPase that exports Ag(I) from the cytoplasm into the periplasm. Previous studies of homologs to SilP indicate that large conformational changes occur throughout the catalytic cycle, which result in the exportation of Ag(I). Previous studies of Ag(I) resistance are limited due to the difficulty of the protein purification and the addition of Ag(I), due to this the theories and limited evidence of Ag(I) exportation are derived from the homologs of SilP, CopA and ZntA.

1.5.2 SilP Nucleotide Binding Domain (N-Domain)

As mentioned earlier in the chapter, P1B-type ATPases have a core structure of 5 domains of which SilP is no exception.

The nucleotide binding domain (N-domain) is where ATP binds to the protein. It is positioned on the large cytoplasmic loop in between the TM4 and TM5 region. The N-domain is flanked at its N- and C-terminal ends

by the two halves of the P-domain (see Figure 1.5.1-B), with these hinge regions important for conformational changes (Gourdon *et al.,* 2011 & Toyoshima & Nomura, 2002).

The N-domain does not seem to have much sequence conservation across the P-type ATPase family, however structural conservation can be observed (Sazinsky *et al.,* 2006a). Structural comparisons of several P-type ATPase N-domains, including CopA and ZntA, show a six stranded anti-parallel β-sheet, with a set of two α-helices on either side (Gourdon *et al.,* 2011; Sazinsky *et al.,* 2006a; Wang *et al.,* 2014), see Figure 1.5.5. It is believed that this structure will also be adopted by SilP.

The N-domain contains two motif regions that are highly conserved within P1B-ATPases; **HP** and **GxGxx(G/A)**, these motifs are thought to be crucial for ATP binding to the domain (Okkeri *et al.,* 2002, Solioz *et al.,* 1996). The motifs have been shown to form a cleft region whereby interactions with the histidine and second glycine of the HP and GxGxx(G/A) motifs interact with the adenosine head of ATP primarily (Dmitriev *et al.,* 2006; Morgan *et al.,* 2004; Sazinsky *et al.,* 2006a). Reduced ATP binding affinity was observed when the histidine was mutated out of the sequence of CopA (Dmitriev *et al.,* 2006).

Both the motifs are observed in the SilP sequence and may be an area of mutagenesis for later activity studies.

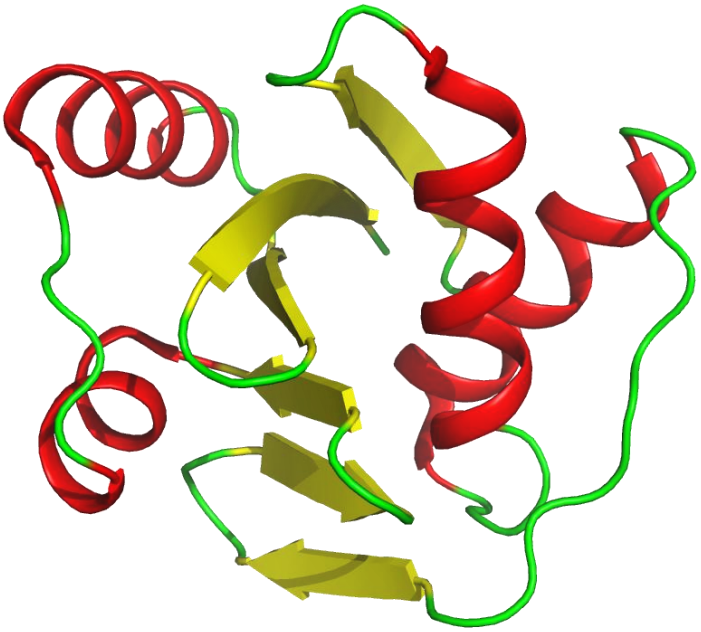

Figure 1.5.5: Structure of the CopA N-domain from *A.fulgidus* (PDB; 2B8E) showing the six β-stranded core with two pairs of flanking α-helices.

1.5.3 SilP Phosphorylation Domain (P-Domain)

Arguably, the most important domain for P-Type ATPases is the phosphorylation domain (P-domain), where ATP hydrolysis occurs. Much like the N-domain the sequence homology of the P-domain is low across the P-type ATPase family, however structurally is highly conserved with a core six stranded parallel β-sheet flanked on either side by three α-helices (Sazinsky *et al.,* 2006a), see Figure 1.5.6. The P-domain occurs on the large cytoplasmic loops between TM4 and TM5, however the domain is split into two sections occurring at the N- and C-termini of the loop with the N-domain occurring in the middle (Gourdon *et al.,* 2011; Wang *et al.,* 2014), refer to 1.5.1-B.

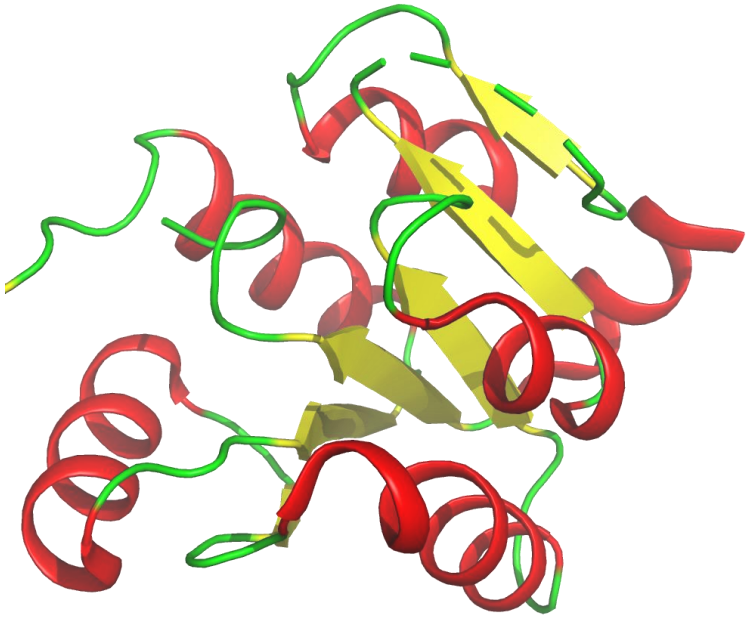

Figure 1.5.6: Structure of *A.fulgidus* CopA P-domain (PDB; 2B8E). The six central parallel β-strands (Yellow) can be seen in with the two sets of three α-helices (Red) either side.

Although sequence homology is low across the P-type ATPase family, there are several highly conserved important motifs. The two main conserved motifs are; **DKTGT**, **TGD(N/S)** and **GDGxNDAP** (Palmgren & Nissen, 2011; Solioz & Vulpe, 1996), see Figure 1.5.2 and Table 1-1. All three motifs form a catalytic crevice with one side of the crevice containing the DKTGT motif and the other side containing the other two motifs (Lutsenko *et al.,* 2007; Sazinsky *et al.,* 2006a).

Extensive studies of the P2-ATPase SERCA showed that during catalysis a conformational change in the N-domain brings the ATP into the P-domain crevice, with the γ-phosphate of the ATP next to the DKTGT motif. In addition, a Mg^{2+} is utilised for phosphorylation, being held in place with the first threonine of the DKTGT and the aspartate of the GDGxNDAP motifs (Palmgren & Nissen, 2011). The Mg^{2+} ion facilitates a rotameric change in the aspartate of the DKTGT motif, the new position of the side chain carboxyl group leads to the hydrolysis of ATP whereby the γ-

phosphate binds to the aspartate (Moller *et al.,* 1996; Sazinsky *et al.,* 2006a; Sorensen *et al.,* 2004; Toyoshima *et al.,* 2004a; Zhitnitsky *et al.,* 2014). Figure 1.5.7 shows the P-domain motifs of SERCA with ATP bound. Studies have shown that knocking out the aspartate residue of the DKTGT motif results in an inactive protein (Okkeri *et al.,* 2002), highlighting the importance of the motif to the protein.

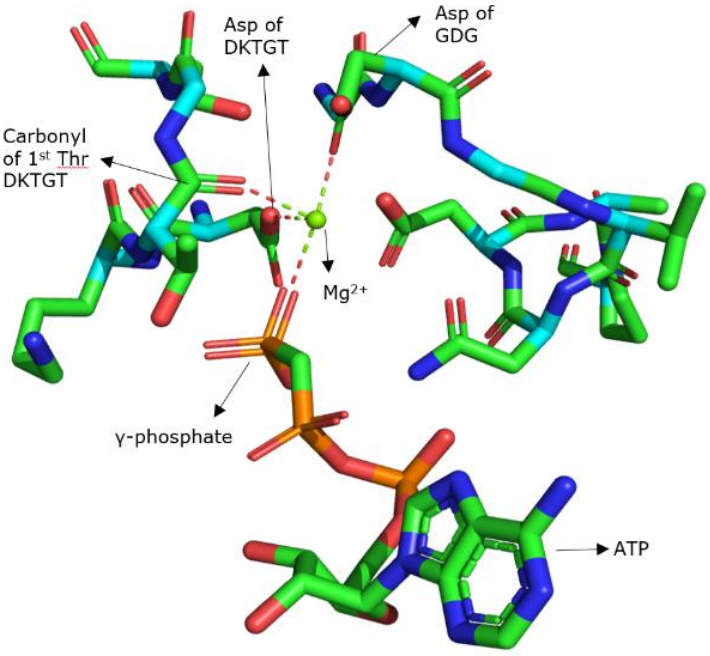

Figure 1.5.7: P-domain of SERCA (PDB; 7BT2) with ATP bound. The γ-phosphate of ATP is within close proximity to the aspartate residues of the DKTGT motif. There are several hydrogen bond interactions with the Mg^{2+} ion involving both the DKTGT and GDGxNDAP motifs. Hydrolysis of ATP results in the binding of the γ-phosphate to the aspartate residue.

1.5.4 SilP Actuator Domain (A-Domain)

The final main catalytic domain is the actuator domain (A-domain), this domain is responsible for the dephosphorylation of the protein, acting as a phosphatase domain (Palmgren & Nissen, 2011). The A-domain is typically a ten stranded anti-parallel β-sheet with coiled loop at the N-

terminal end and a α-helix at the C-terminus, see Figure 1.5.8 (Gourdon *et al.,* 2011; Sazinsky *et al.,* 2006b).

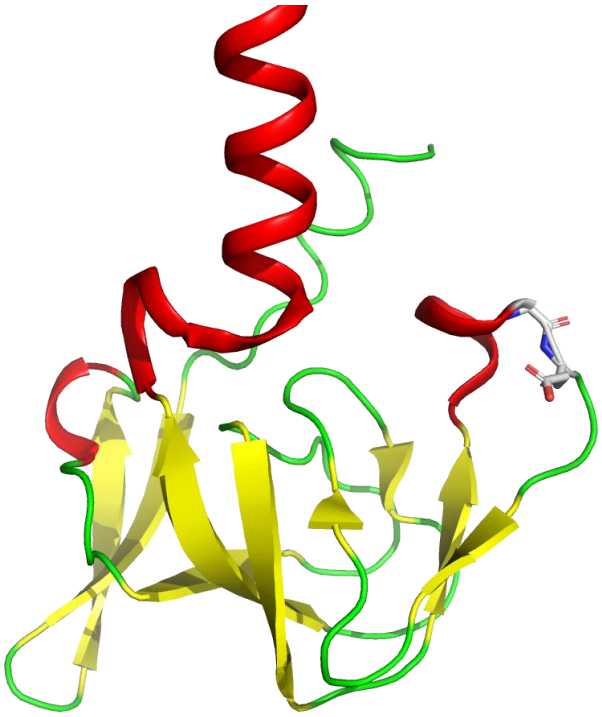

Figure 1.5.8: Structure of the A-domain from *A.fulgidus* CopA (modified from PDB; 2HC8). The conserved loop TGE motif is shown as stick structures to the right of the protein.

The coiled loop and α-helix are long and relatively flexible, the latter being important to facilitate conformational changes needed during catalysis (Palmgren & Nissen, 2011; Sazinsky *et al.,* 2006b). Studies of SERCA have shown that there is additional limited interaction between these two structures and the P-domain, which stabilise the structure during dephosphorylation (Toyoshima *et al.,* 2004b). It is feasible to assume that this proposed interaction may occur within the SilP as well.

The A-domain contains a single highly conserved motif, **TGE** which is located on a solvent accessible loop (see Figure 1.5.8). The position of the motif has been suggested to allow interaction with the DKTGT side of the catalytic cleft within the P-domain. The glutamate of TGE is thought

to facilitate the dephosphorylation of the aspartate residue, evidence of this has been seen in the SERCA ATPase (Bublitz *et al.,* 2011; Olesen *et al*., 2004; Sazinsky *et al.,* 2006b). Evidence of the A-domain being involved with the dephosphorylation of P1B-ATPases has not been seen yet, however it is thought to be similar as the SERCA mechanism.

1.5.5 SilP Metal Binding Domain (HMBD) and Transmembrane Region (TM)

The HMBD is a feature that seems exclusive to the P1 ATPase family, with the majority occurring within the P1B-ATPases perhaps unsurprisingly considering they bind to metal ions (Solioz and Vulpe, 1996). HMBD's are found at both the N- and C-termini of the proteins, within prokaryotes typically having them at the N-terminus. The number of HMBD's seems to vary between P1B-ATPases, with different species version of the same protein containing different numbers as well (Arguello, 2003).

Although no structure of a HMBD in a full length P1-ATPase protein has been solved, a structure of a truncated HMBD on its own, derived from CopA has been solved. The structure shows that the HMBD adopts a ferredoxin like βαββαβ conformation (Fu *et al.,* 2013; Jones *et al.,* 2003). HMBD's fall into two main sub-classes, I and II, with sub-class I having a higher number of histidine residues whereas sub-class II does not (Gupta *et al.,* 1999). SilP falls into the sub-class I category as it contains a **H_5DH_2** motif within its HMBD, CopA also has numerous histidine residues (See Figure 1.5.2). Both sub-classes also show high conservation of a CxxC motif which is heavily linked to metal binding, sub-class II HMBD's however have a GMx region at the N-terminus of this motif which is

thought to aid in cation specificity, see Table 1-1 (Arnesano *et al.,* 2002; Lutsenko & Kaplan, 1995).

The role of the HMBD within P1B-ATPases is highly debated with no structural evidence available to suggest a role. The ability to bind metals, and its location at the N-terminus, has led to speculation that it is involved in metal ion transference to the protein for exportation. However, several studies have shown that P1B-ATPases lacking a HMBD have only shown a slight reduction in activity and metal ion exportation (Arguello *et al.,* 2007; Borjigin *et al*., 1999; Gonzalez-Guerrero *et al.,* 2008). The lack of inhibition, with regard to metal ion exportation, has led to the speculation that the HMBD actually provides more of a regulatory role, possibly interacting with the A-domain (Hatori *et al.,* 2008; Mandal & Arguello, 2003). Additional research has shown that CopA receives Cu(I) ions through an additional protein, CopZ, at its transmembrane regions, highlighting that P1B-ATPases have alternative routes for acquiring metal ions (Mattle *et al.,* 2013; Gonzalez-Guerrero *et al.,* 2008).

The transmembrane region of P1B-ATPases is similar to other P-type ATPases with one major exception. P1B-ATPases contain two α-helices (TMA & TMB) that are unique to this sub-family, with the latter having a ~90° kink halfway down, see Figure 1.5.1-A (Lutsenko *et al*., 2007). The TM region plays an essential role within the P1B-ATPase as they are directly involved in the movement of metal ions. As a result, there are several highly conserved residues that occur within the TM helices; **CPC** (TM4)**, YN** (TM5) and **MxxS** (TM6) (Arguello, 2003; Solioz & Vulpe, 1996).

The residues CP of the CPC motif are highly conserved, with the latter cysteine shown to vary between the sub-classes, as a results P1B-ATPases are often referred to as CPX-ATPases (Solioz & Vulpe, 1996). The three sets of motifs are believed to make two TM metal binding sites (TM-MBS), with the CPC motif forming the main TM-MBS and the other two forming the second TM-MBS. In both TM-MBS there are thiol containing residues which are able to coordinate the metal ion, in the case of Ag(I) sulphurs are especially prevalent at coordinating (Loftin *et al.,* 2005 & Nies, N.H., 2003). Mutations within one of the cysteine's of the CPC motif have been shown to stop metal binding and inhibit ATPase activity within CopA, however the protein was able to bind ATP suggesting that the lack of CPC stops conformational changes to allow ATP hydrolysis (Mandal & Arguello, 2003). The latter two motifs are believed to form a hydrophilic channel that enables the metal ions to leave the TM region and exit the protein into the extracellular area (Arguello, 2003; Mandal *et al.,* 2004).

The P1B-ATPase TMB contain a 'kink' halfway up the helix forming a platform that is adjacent to the membrane surface (see Figure 1.5.1-A). This platform is believed to be involved in some sort of metallo-protein docking, be it through the HMBD or through an additional protein (Gourdon *et al.,* 2011; Wang *et al.,* 2014). There is evidence of CopA receiving Cu(I) from the cytoplasmic CopZ without the presence of the HMBD, suggesting that the protein delivers Cu(I) through another mechanism possibly utilising the TMB kink platform.

1.6 SilF - Periplasmic Metallochaperone

The gene encoding SilF was not originally designated a putative role based on the wrong assignment of its nucleotide starting sequence, originally giving a 96 amino acid protein when in actuality it was 119 amino acids (Gupta *et al.,* 1999; Randall *et al.,* 2015). The eventual correct amino acid sequence indicated SilF was a close homolog to CusF, showing 50% sequence homology. The protein CusF belongs to the copper *cus* system and is expressed within the CusCFBA operon. CusF is a small periplasmic metal chaperone that has been shown to bind to both Cu(I) and Ag(I) ions (Kittleson *et al.,* 2006). The structure of CusF has been determined in both its apo and holo forms with both Cu(I) and Ag(I) (Loftin *et al.,* 2005; Xue *et al.,* 2008). CusF adopts a five stranded β-barrel with two large extended loops at either end of the barrel, one of these loops contains the metal binding site, see Figure 1.6.1

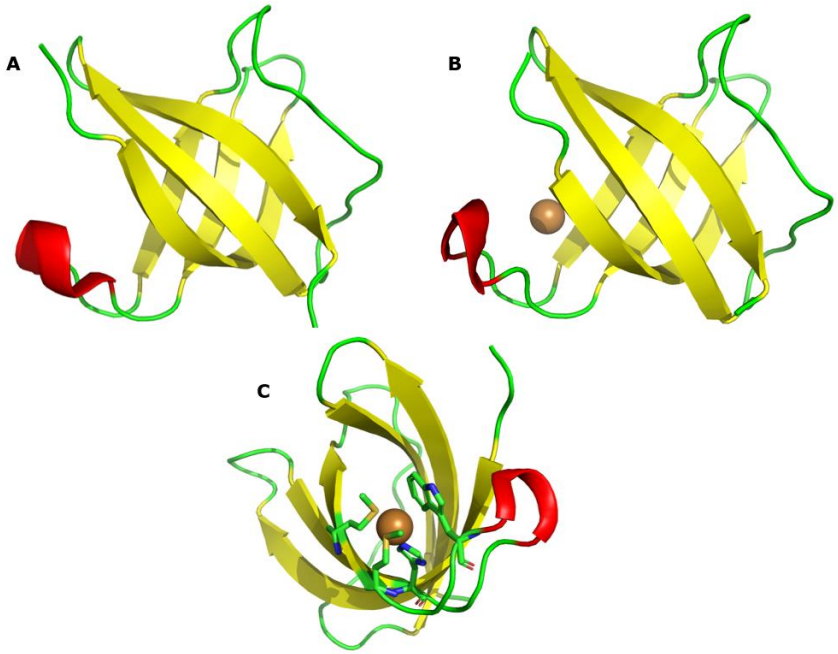

Figure 1.6.1: (A) Apo structure of CusF (PDB; 1ZEQ) with its secondary structure coloured. **(B)** Structure of Cu(I) bound CusF (2VB2). **(C)** The metal binding site of CusF with all coordinating residues illustrated as stick models.

The CusF structure shows that the metal binding site is made up of two coordinating methionine's and a histidine residue, with the thiol groups of the methionine's providing the main coordination (Franke *et al.,* 2003; Xue *et al.,* 2008). In addition, a nearby tryptophan residue is also shown to coordinate the metal ions, this is thought to occur through a π-cation bond, originating from the aromatic indole ring of the tryptophan (Xue *et al.,* 2008).

Sequence alignment of CusF and SilF, using Clustal Omega (Sievers *et al.,* 2011) show that the residues of the metal binding site are highly conserved, suggesting the same mechanism is observed and the SilF may bind both Ag(I) and Cu(I), see Figure 1.6.2 for the sequence alignment.

```
CusF      MKKALQVAMFSLFTV---IGFNAQANEHHHETM----SEAQPQVISATGVVKGIDLESKKI     54
SilF      MRNSLKAVLFGAFSVMFSAGLHAET--HQHGDMNAASDASVQQVIRGSGVVKAIDMNSKKI     59

CusF      TIHHDPIAAVNWPEMTMRFTITPQT----KMSEIKTGDKVAFNFVQQGNLSLLQDIKVSQ-     110
SilF      TISHEAIPAVGWPAMTMRFTFVNADDAIDAINALKTGNHVDFSFIQQGNISLLKSINVTQS     119
```

Figure 1.6.2: Sequence alignment of CusF and SilF. The metal binding residues are highlighted in green, the conserved primary MxM motif can be seen. Highlighted in yellow are the proposed signal peptide sequences for delivery to the periplasm as according to SignalP v.5.

Functionality characterisation of CusF showed that the protein, as in the structures, bound to both Cu(I) and Ag(I) at a 1:1 ratio of protein:ion, supporting the one metal binding site observed in the structure. Isothermal calorimetry (ITC) studies showed CusF had a higher affinity to Ag(I) over Cu(I), with dissociation constants (Kd) of 495 nM and 39 nM for Cu(I) and Ag(I) respectfully (Kittleson *et al.,* 2006). It is logical to assume SilP, with its high sequence homology, shows a similar binding

preference and affinities. Especially with regard to Ag(I) considering it is part of a Ag(I) resistance mechanism.

The binding of CusF to either Cu(I) or Ag(I) results in high periplasmic concentration of either ion, all be it bound to a protein reducing its toxicity to the cell. Metal ions, bound to CusF, are thought to be exported out of the cell through interactions with CusB, of the CusCBA complex. Studies have shown interactions between CusF and CusB, however no conclusive evidence of metal ion transferal. Analysis of the structures of both CusF and CusB have shown a possible metal ion transference pathway, utilising methionine residues to coordinate the metal (Bagai *et al.,* 2008). Mutagenesis of the identified methionine residues on both CusF and CusB showed a marked reduction in Cu(I) transference and subsequent exportation out of bacterial cells. (Franke *et al.,* 2003; Kittleson *et al.,* 2006; Mealman *et al.,* 2012).

Structures of CusF have shown the metal bound state of the protein and indications of interactions with CusB in offloading the metal ion, however the mechanism by which CusF acquires the metal ion is not known. The presence of Cu(I) within the periplasm is brought about through the P1B-ATPase CopA, this gives rise to two possibilities of CusF metal ion uptake. The first possibility is that CusF is merely a periplasmic chelating metallo-chaperone that binds to free Cu(I)/Ag(I) in the periplasm. The second possibility is that CusF interacts directly with CopA facilitating ion transferal. A computational study by Padilla-Benavides *et al.,* (2014) showed the possibility of CusF docking to the kinked TMB region of CopA. Experimental data suggested that a weak interaction may occur, however further data was required for conclusive evidence. It is plausible to

assume that a similar interaction may occur between SilF and SilP, this is one of the many aspects of SilF that will be investigated.

1.7 SilC – Outer Membrane Factor

The final component of the *sil* system to be examined in this work is the outer membrane factor SilC. The gene of *SilC* encodes for a 461 amino acid protein that is homologous to the CusC outer membrane protein that is present within the *cus* system.

CusC is a component of the larger CusCBA complex, a resistance-nodulation-cell division (RND) efflux pump, the complex is formed of several oligomers of each component protein. CusA, a inner membrane proton driven efflux pump forms a trimer, CusB is a membrane fusion protein, which forms a hexamer, and CusC is trimeric, forming a single α/β-barrel channel that is positioned in the outer membrane. Overall, the complex has a 3:6:3 conformation of CusA:CusB:CusC (Long *et al.,* 2012; Nies, 2003).

CusC falls into the family of outer membrane factor (OMF) proteins which forms a trimer that has a porin like head, embedded in the outer membrane, and a α-helical barrel tail extending into the periplasm (Franke *et.al.,* 2003 & Kulathila *et al.,* 2011). The porin head is typically comprised of a 12 stranded β-barrel interconnecting through hydrogen bonding of the peptide backbone. The α-helical barrel is comprised of up to 12 α-helices divided into coiled-coil pairs (Koronakis *et al.,* 2000; Kulathalia *et al.,* 2011). Figure 1.7.1 shows the structure of CusC, a typical OMF protein. Studies of CusC have shown no evidence of enzymatic activity, nor any direct metal ion interaction within CusC. The

width observed for the α/β-barrels is uniform along the length of the protein, ~30 Å, which is wider than would be expected if a direct interaction was to be observed. In addition the length of the protein, connecting the CusAB proteins, suggests that that CusC, and to that extent SilC, facilitates the passive diffusion of the metal ion through the protein channel (Koronakis *et al.,* 2000).

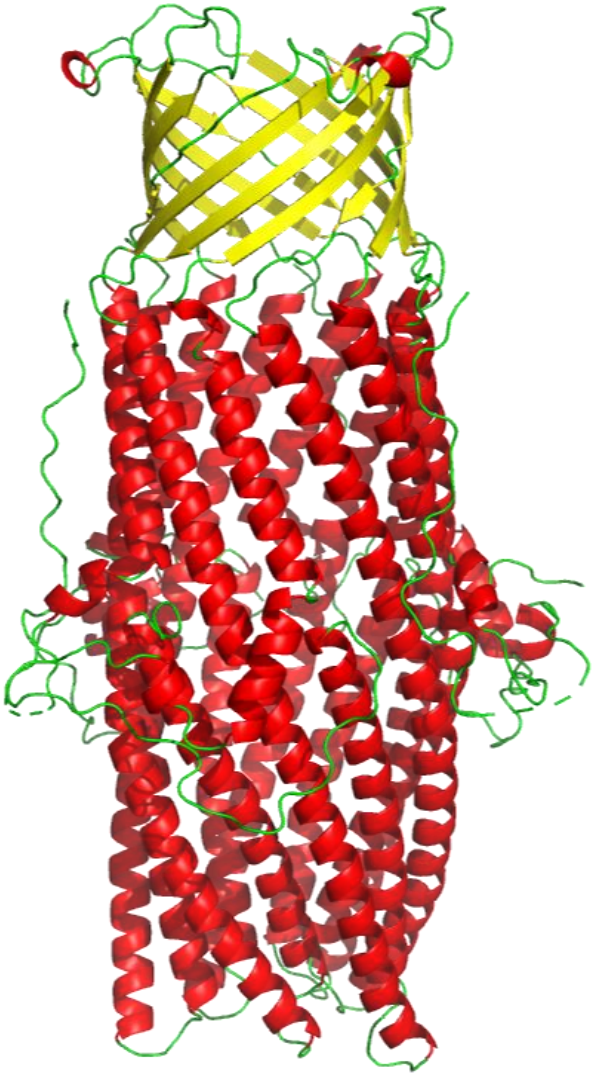

Figure 1.7.1: Structure of CusC (PDB; 3PIK) trimer showing the 12 stranded β-barrel head (Yellow), which is embedded in the outer membrane, along with the α-helical barrel tail (Red) which extends into the periplasm.

Outer membrane factor proteins are very common, with typical examples including TolC and OprM, the former involved in the transport of antibiotics and other toxic molecules (Higgins *et al*., 2004). All of these proteins have be shown to form a complex with an inner membrane efflux pump and a membrane fusion protein, SilC is believed to be no exception to this. The exact method by which the proteins interact with each other is based on the heavily studied TolC-AcrAB system (Du *et al.,* 2004).AcrB (inner membrane efflux pump) and AcrA (membrane fusion protein) readily form a complex, with TolC only interacting in the presence of the substrate (Su *et al.,* 2012 & Zgurskaya & Nikaido, 2000). Upon substrate binding the periplasmic end of the TolC α-barrel directly interacts with the top of the AcrA channel, with the interactions occurring through hydrogen bonding of the TolC coiled-coil loops and the loops of the AcrA α-helical channel, see Figure 1.7.2. The sequences of the coiled-coil loops vary between different OMF's, this is believed to allow for specificity. Studies whereby CusC was substituted with TolC showed that there was no activity within the complex (Franke *et al,* 2003), it was theorised that this lack of interaction was a result of the different amino acids in the coiled-coil loop regions. Hopefully by obtaining the structure of SilC it will be possible to see if there is a substantially different interaction site as well.

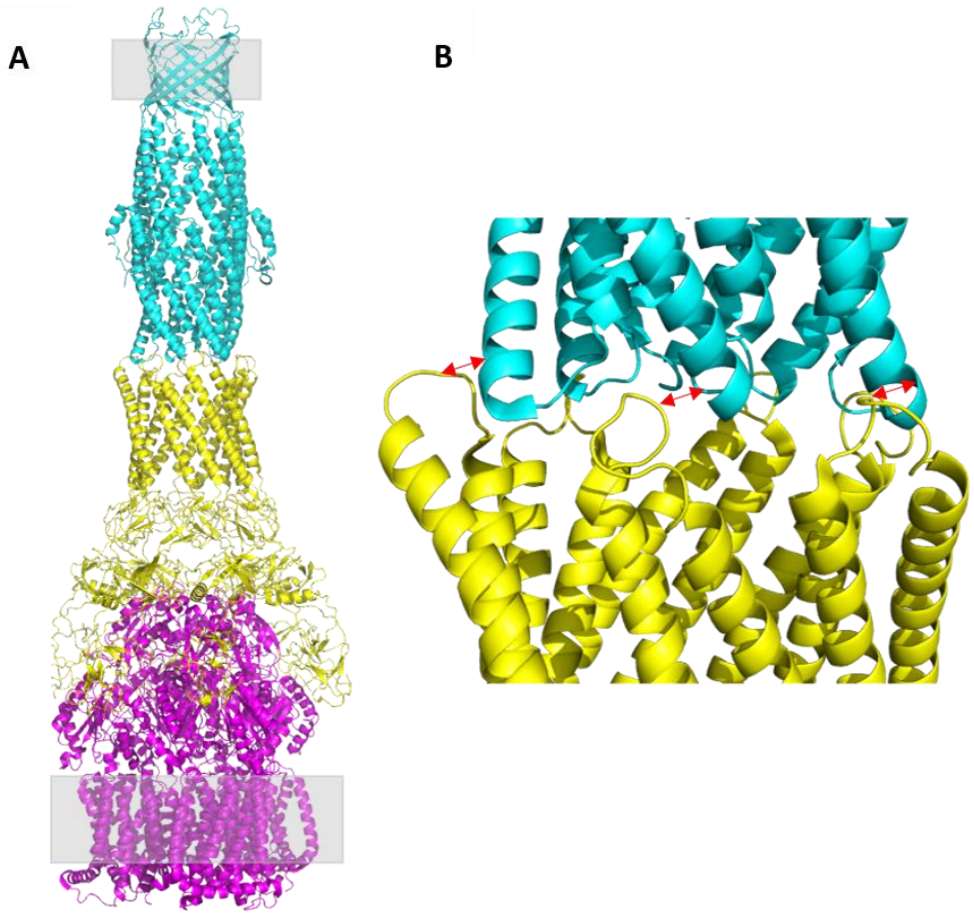

Figure 1.7.2: (A) TolC (Cyan), AcrA (Yellow) and AcrB (Magenta) complex, with membranes shown in Grey, showing the interaction sites within the complex. **(B)** Interface between TolC and AcrA showing the interactions between the loops of AcrA and the coiled-coils of TolC (arrows).

1.8 Project Aims

The emergence of bacterial metal resistance, in the case of this project Ag(I), in the medical field is an alarming one, especially when coupled with the already extensive antibiotic resistance as this is seen as another preventative treatment. Understanding the mechanisms of how bacteria achieve resistance to Ag(I), through the sil system, is a vital step in the ladder of developing inhibitors that will disrupt this system. The ability to

disrupt this system will allow the continuation of Ag(I) as a preventative treatment for bacterial infections.

In this research three proteins will be investigated: SilP, SilF and SilC. Structural and functional characterisation of each of these proteins will shed light on how they function and the role they play in the sil system.

1.8.1 Chapter Overviews

Chapter 3 looks at the characterisation of the inner membrane P1B-ATPase SilP. The chapter addresses the difficulties in expression and purifying SilP and how they were overcome to produce a pure functional protein, as determined through ATP assays. The structural characterisation of SilP reached a point whereby 2D classifications were produced but further data collection is required for an atomic resolution model.

Chapter 4 addresses the expression, purification and biophysical characterisation of the periplasmic metal chaperone SilF. The chapter looks primarily at the binding of SilF to metals, namely Ag(I) and Cu(I), with ITC showing the strong binding affinity of SilF to both metal ions but with a preference for Ag(I).

Chapter 5 is a continuation of Chapter 4, however the primary focus is the structural characterisation of the protein through X-Ray crystallography. Successful high-resolution structures of SilF in its apo and holo bound forms (Ag(I) and Cu(I)) were achieved, highlighting the binding mechanism of the protein. The structures showed that different binding mechanisms occurred for each metal, supporting the findings of Chapter 4.

The final chapter, Chapter 6, looks at the biophysical and structure determination of the outer membrane factor SilC. SilC is part of the SilCBA complex is responsible for exporting Ag(I) out of the cell altogether. SilC has a close homolog, CusC, which through determining the atomic structure, SilC is shown to have a similar conformation as well. Differences within the structures leads to speculation of how the system is more catered to Ag(I). The determination of SilC also gives a footing for determining the whole SilCBA complex as well, which ultimately leads to a better understanding of the system.

By investigating the functionality of the proteins within the sil system, and any atomic resolution structures, it is hoped that the molecular mechanisms that give rise to silver resistance will be better understood.

2 General Methods

All chemical and reagents were purchased from Merck unless stated.

2.1 Bacterial Cells and Growth media

2.1.1 Bacterial Strains

Several strains of *E.coli* were used throughout the project for both cloning and expression studies. Table 2-1 below lists the strains used.

Table 2-1: Sil constructs and vectors previously cloned by OPPF.

Strain	Genotype	Source
Top10	F- *mcrA* Δ(*mrr-hsd*RMS-*mcr*BC) Φ80*lac*ZΔM15 Δ *lac*X74 *rec*A1 *ara*D139 Δ(*araleu*)7697 *gal*U *gal*K *rps*L (StrR) *end*A1 *nup*G	Thermo Fisher
Stellar	F–, endA1, supE44, thi-1, recA1, relA1, gyrA96, phoA, Φ80d lacZΔ M15, Δ (lacZYA - argF) U169, Δ (mrr - hsdRMS - mcrBC), ΔmcrA, λ–	Takara
BL21 (DE3)pLysS	F–, ompT, hsdSB (rB–, mB-), dcm, gal, λ(DE3), pLysS, Cmr	Promega
Rosetta (DE3)pLysS	F– ompT hsdSB(rB– mB–) gal dcm (DE3) pLysSRARE2 (CamR)	Novagen
Lemo21 (DE3)pLysS	fhuA2 [lon] ompT gal (λ DE3) [dcm] ΔhsdS/ pLemo(CamR) λ DE3 = λ sBamHIo ΔEcoRI-B int:(lacI:PlacUV5:T7 gene1) i21 Δnin5 pLemo = pACYC184-PrhaBAD-lysY	Thermo Fisher
C41 (DE3)	F – ompT hsdSB (rB- mB-) gal dcm (DE3)	Thermo Fisher
C43 (DE3)	F – ompT hsdSB (rB - mB -) gal dcm (DE3)	Thermo Fisher

2.1.2 Growth Media

Luria-Bertani (LB) (Bertani, 1951) Agar plates were prepared using autoclaved LB media and Bacto-Agar cooled to ~40 °C, 25 ml of the agar, containing relevant antibiotics (1:1000), was poured into petri dish and left to set. Set plates were kept refrigerated at 4 °C.

LB Broth was prepared by mixing 25 g FORMEDIUM powdered medium (Formedium, UK) with 1 L of reverse osmosis (RO) water and then autoclaved at 121 °C for 15 minutes. The media was stored at room temperature if being used within a few days, otherwise stored at 4 °C.

Power Prime Broth, a higher yielding media than TB, was prepared by mixing 52 g of Power Prime powdered media (Molecular Dimensions Inc) with 1 L of RO water and 4 ml Glycerol. The media was autoclaved at 121 °C for 15 minutes and stored until use.

Terrific Broth (TB) (Tartoff & Hobbs, 1987) was prepared by mixing 47.6 g of MELFORD TB media powder (Melford, UK) with 1 L RO water and 4 ml Glycerol, the media was then autoclaved at 121 °C for 15 minutes and then stored until use.

2.2 DNA Transformation and Vectors

2.2.1 Transformations

Commercial competent Top10 *E.coli* cell aliquots were defrosted on ice, before addition of 1 µL of 100 ng/µL plasmid DNA and incubated on ice for 30 minutes. The cells were heat shocked at 42 °C for 35 seconds using a pre-heated water bath, after which 300 µL of LB media was then

added to the cells and left to recover at 37 °C for 1 hour. 200 µL of cells were pipetted on the agar plate (Section 2.1.2) and left to air dry. Plates were sealed with Para film and left overnight at 37 °C. Plates that had colonies were then stored at 4 °C until needed, however were kept no longer than 2 weeks.

2.2.2 Cloning and expression vectors

Previous work on the *sil* genes resulted in most of the genes being cloned into vectors designed by the Oxford Protein Production Facility - OPPF (now Protein Production UK (PPUK), RCaH, Harwell Campus, Oxfordshire, UK). OPPF vectors are designated pOPINX, with X denoting the different tags present. All the vectors contain carbenicillin resistance for selection. Table 2-2 lists the vectors used in this project.

Table 2-2: Vectors used throughout the project, supplied by PPUK.

Vector	Tag/s	N/C terminal	Cleavage site (1 or 2)
pOPINE	6His	C	-
pOPINE-GFP-8His	GFP-8His	C	3C
pOPINEneo (1 or 2)	8His	C	3C or TEV
pOPINEneo-GFP (1 or 2)	GFP-8His	C	3C or TEV
pOPINEneo-GFP-StrepII	GFP-8His-StrepII	C	3C
pOPINF	6His	N	3C

2.3 *sil* expression construct cloning

Previous work on proteins from the *sil* operon led to the cloning of several *sil* proteins. The cloning was conducted by PPUK (formerly OPPF), Dr Karishma Asiani and Dr David Casa-Mao. Table 2-3 below shows the

previous constructs used in this project that have been cloned using the OPPF infusion method (Berrow *et al.,* 2007).

Table 2-3: Sil constructs and vectors previously cloned by OPPF.

Protein Description	Abbreviation	Vector
SilP Full length, *Klebsiella pneumoniae*	kp-SilP	pOPINE-GFP-His8 (1)
∆150 N-terminal truncated SilP , *Klebsiella pneumoniae*	Δkp-SilP	pOPINE
HMBD (first 150 amino acids of kp-SilP)	HMBD	pOPINEneo-6His (1)
SilC Full length, *Salmonella typhimurium*	SilC	pOPINE

2.3.1 New Constructs and Primers for Cloning

2.3.1.1 New constructs for *sil* gene overexpression

As stated in Section 2.3 several previous *sil* constructs were cloned. In addition to the previous constructs in Table 2-3 several new constructs were designed. These were two new SilP species variants and a new protein, SilF, with variants again from two species. Each of these genes were cloned into different vectors with different tags, this is summarised in Table 2-4. The sequences for the genes were obtained from Uniprot and synthesised by Twist Bioscience (San Francisco, USA). Expression constructs were made in gene fragments, with a maximum length of 1300 bp per fragment. SilF genes were synthesised within single fragments, however SilP genes had to be split in half to fit due to its

greater size with each half ~1500 bp. This necessitated an extra step in the cloning protocol where the SilP fragments were amplified by PCR then ligated to each other before further ligation into the vector of choice.

Table 2-4: List of new species variants of SilF and SilP that were to be cloned as part of this project. Vectors with a 1 or 2 denote a 3C-protease (1) or TEV (2) cleavage site

Species	Protein	Code	Vector	Uniprot
Klebsiella pneumoniae	SilF Full length (M1)	kp-SilF1	pOPINF	R4WBT7
	SilF Full length (M1)	kp-SilF2	pOPINE	
	SilF Trunc (V38)	kp-SilF1Δ	pOPINF	
	SilF Trunc (V38)	kp-SilF2Δ	pOPINE	
E.coli	SilF Full length (M1)	ec-SilF1	pOPINF	AOA3TOVB72
	SilF Full length (M1)	ec-SilF2	pOPINE	
	SilF Trunc (V38)	ec-SilF1Δ	pOPINF	
	SilF Trunc (V38)	ec-SilF2Δ	pOPINE	
E.coli	SilP Full length (M1)	ec-SilP1	pOPINEneo-3C-GFP(1)	AJT46594
	SilP Full length (M1)	ec-SilP2	pOPINEneo-TEV-GFP(2)	
	SilP Full length (M1)	ec-SilP3	pOPINE	
	SilP Trunc (T154)	ec-SilP1Δ	pOPINEneo-3C-GFP(1)	
	SilP Trunc	ec-SilP2Δ	pOPINEneo-	

	(T154) SilP Trunc (T154)	ec-SilPΔ	TEV-GFP(2) pOPINE	
Flavobacterium	SilP Full length (M1)	fb-SilP1	pOPINEneo-3C-GFP(1)	KVV14976
	SilP Full length (M1)	fb-SilP2	pOPINEneo-TEV-GFP(2)	
	SilP Full length (M1)	fb-SilP3	pOPINE	
	SilP Trunc (A93)	fb-SilP1Δ	pOPINEneo-3C-GFP(1)	
	SilP Trunc (A93)	fb-SilP2Δ	pOPINEneo-TEV-GFP(2)	
	SilP Trunc (A93)	fb-SilP3Δ	pOPINEneo	
	SilP Trunc (M160)	fb-SilP4Δ	pOPINEneo-3C-GFP(1)	
	SilP Trunc (M160)	fb-SilP5Δ	pOPINEneo-TEV-GFP(2)	
	SilP Trunc (M160)	fb-SilP6Δ	pOPINEneo	

2.3.1.2 Primers for Cloning SilF and SilP

The new construct sequences were inputted into the OPPF OPTIC server (www.oppf.rc-harwell.ac.uk/OPPF/public/services/bioinformatics.jsp).

The server forms a library of constructs whereby the Infusion primer sequences can be designed based on the construct DNA sequence. Primer design entailed selecting the construct DNA of interest and the desired vector. Once selected primers were designed upon the 'nearest

neighbour' melting temperature (Kibbe, 2007), most primers were designed to be ~24 bp with a melting temperature between 70 – 74 °C, optimal for PCR. The melting temperature relates to the annealing part of the primer. The primers also contained an additional Infusion sequence on the 5' ends of the primers for vector insertion. Table 2-5 lists the primers used for cloning.

Table 2-5: List of primers used for cloning of new SilF and SilP constructs, with melting temperatures and clonal uses labelled. Infusion sequence are in lowercase.

Primer Name	Sequence (5' – 3')	Tm (°C)	Cloning use
F001	aagttctgtttcagggcccgATGCGTAATTCACTT AAAGCCGTTTTATTTG	74	kp-SilF1 & ec-SilF1 forward
F002	aggagatataccatgCGTAATTCACTT AAAGCCGTTTTATTTG	74	kp-SilF2 & ec-SilF2 forward
F010	aagttctgtttcagggcccgATGGTACAGCAGGTT ATCAGGGGCTC	72	kp-SiF1Δ & ec-SilF1Δ reverse
F011	aggagatataccatgGTACAGCAGGTTATCAG GGGCTC	72	kp-SiF2Δ & ec-SilF2Δ reverse
F013	aggagatataccatgCTTCAGATATGCATAAGG AGAGTTAC	72	ec-SilP1 & 2 forward
F021	aggagatataccatgATACATCACTATCAAATAA GCGGCATG	74	fb-SilP1 & 2 forward
F025	aggagatataccatgGCAGAAGGCAAATA TTACTGCCC	68	fb-SilP1Δ & 2Δ forward
F029	aggagatataccatgATGCAACCGTCAGC AAGCGAAGAC	74	fb-SilP3Δ & 4Δ forward
R001	ATGGTCTAGAAAGCTTTAggattgcgtaacgtt aatgcttttg	70	kp-SilF1 reverse
R002	GTGATGGTGATGTTTggattgcgtaacgttaat gcttttg	70	kp-SilF2 reverse
R007	ATGGTCTAGAAAGCTTTAggattgcgtaacg ttaatgcttttaag	74	ec-SilF1 & 1Δ reverse
R008	GTGATGGTGATGTTTggattgcgtaacgttaat gcttttaag	74	ec-SilF2 & 2Δ reverse

R013	TACAGGTTCTCGTTTCCtttcccgagcctg acacttttcag	72	ec-SilP1 & 1Δ reverse
R014	CAGAACTTCCAGTTTtttcccgagcctgac actttcag	72	ec-SilP2 & 2Δ reverse
R021	TACAGGTTCTCGTTTCCaattttagctgaa cgcaaacgcaaag	72	fb-SilP1 & 1Δ & 3Δ reverse
Sp1A rev	GCCATTCTCTGGATGGGGGCACGCGAACG	68	ec-SilP 1st fragment reverse
Sp1B for	GATGCACAGCGTTCGCGTGCCCCCATCC	68	ec-SilP 2nd fragment forward
Sp2A rev	GCATCAGTAACCATTTGTACAATTTGGGCAAGC	62	fb-SilP 1st fragment reverse
Sp2B for	CAGATACGTTGCTTGCCCAAATTGTACAAATGG	63	fb-SilP 2nd fragment forward

2.3.2 Polymerase Chain reaction (PCR)

Cloning followed the OPPF (PPUK) method of In-Fusion, this involved an in-house PCR method utilising Phusion Flash polymerase (Thermoscientic F-458L). SilP samples had an additional prior PCR step where each half of the gene was amplified first (following the protocol below) then the whole gene amplification.

PCR reactions were carried out in 25 µL volumes in a 96 well plate, consisting of in the following order:

- 12 µL 2x Phusion Flash Master Mix
- 8.5 µL Sterile Water
- 1.5 µL (10 µM) Forward Primer (see Table 2-5)
- 1.5 µL (10 µM) Reverse Primer (see Table 2-5)
- 1 µL (10-20 ng/µL) Template DNA (gene fragment)

If samples did not amplify particularly well then DMSO was added (end concentration 5 %).

Samples were sealed with a foil seal and placed into a thermo cycler for PCR amplification. Thermo cycler stages consisted of:

Step 1: 98 °C – 10 secs

Step 2: 98 °C – 2 secs

Step 3: 66-72 °C – 5 secs (based on Tm of primers)

Step 4: 72 °C – 20-30 secs based on template length (extension time based on 15 s/kbp)

Step 5: 72 °C – 2 minutes

(Steps 2-5 were repeated 29 times)

Step 6: 4 °C - Hold

The sizes of the amplified samples were analysed using an Invitrogen 1.2% Agarose E-Gel or a 1 % Agarose gel for amplification confirmation. The 1% agarose gels were prepared by dissolving 1 g of agarose in 100 mL of TAE buffer using a microwave to heat the sample until all agarose crystals were dissolved. Prior to gel setting (~40 °C), 10 µL SYBR safe stain was added to a final concentration of 1 %, whereupon the gel was poured into the gel tank with a 10 well-comb added in. Samples were prepared by mixing 5 µL of sample with 5 µL of 5 x loading dye, these were loaded into each well. An additional 5 µL of 1Kb Plus DNA Ladder (Thermo Fisher) was loaded into lane 1 of the gel. Gels were covered with TAE buffer and run for 1 hour at 110 V. Gels were imaged under UV light to check bands of the correct size were present. Once correct sizes of amplified fragments were confirmed samples were used immediately for vector ligation or were frozen (at -20 °C) for later usage.

2.3.3 PCR Clean-Up and In-Fusion Ligation

Purification of amplified fragments was performed using two methods: gel purification and PCR clean-up kits. The choice of clean-up was based on the PCR fragment intensity from the agarose gel. If the product band was not intense then PCR clean-up was performed as it did not lose as much product as gel purification.

Gel purification involved using a kit from NEB (New England Biolabs, UK). PCR samples were run down another 1% agarose gel (as in section 2.3.2) and the correct band was excised from the gel. The protocol within the kit was followed; the resulting purified DNA (without agarose) was measured on a nano-drop at 260 nm to check the concentration and purity.

PCR clean-up using a NEB Monarch PCR Clean-up kit that works in a similar to a standard mini-prep kit. Remaining PCR samples cleaned up following the in-kit protocol with concentration and purity assessed on the nano-drop at 260nm wavelength.

Ligation of PCR products, into specific vectors of choice, was conducted using the In-Fusion enzyme (Takara, France). 10 µL of linearised pOPIN vector (100 ng) was mixed with PCR product (100 ng) in a 96 well PCR plate, the samples were made up to a total volume of 10 µL. 2.5 µL of In-Fusion ligation enzyme was added to the samples and then sealed, the PCR plate was incubated at 42 °C for 30 minutes. After ligation time elapsed, circular DNA was transformed into Stellar™ competent cells (Section 2.2.1), plasmids were extracted by mini-prep (details below) and sent for sequencing.

Cellular plasmid DNA was extracted from competent cells using a Qiagen Mini-Prep kit (Qiagen, UK). Mini-preps followed the kit protocol, with DNA

elution's measuring approx. 100ng/µL. Purified DNA was sent for sequence verification using Source Bioscience (Source Bioscience, Oxford), samples were 5 µL at 100 ng/µL. All pOPIN vectors used for cloning contained a T7 forward primer, with the reverse primer being either EGFP-nRev (constructs containing GFP) or TriEx Down (constructs with no GFP)

2.3.4 Sequence Verification

DNA sequencing was conducted using Source Bioscience (Oxford, UK), with results returned within 24 hours. Nucleotide sequences returned from Source Bioscience were compared to the anticipated sequence for confirmation of successful cloning. See Table 2.6 below for successfully cloned sequences.

Table 2-6: Successfully cloned constructs verified through sequencing.

Species	Construct	Designated Name	Vector
E.coli	SilP trunc	ec-SilP2Δ	Eneo-TEV-GFP
E.coli	SilP trunc	ec-SilP1Δ	Eneo-3C-GFP
Flavobacterium	SilP FL	fb-SilP2	Eneo-TEV-GFP
Flavobacterium	SilP FL	fb-SilP1	Eneo-3C-GFP
Flavobacterium	SilP FL	fb-SilP	Eneo
Flavobacterium	SilP trunc A93	fb-SilP1Δ	Eneo-TEV-GFP
Flavobacterium	SilP trunc A93	fb-SilP2Δ	Eneo-3C-GFP
Flavobacterium	SilP trunc A93	fb-SilPΔ	Eneo
Flavobacterium	SilP trunc M140	fb-SilP4Δ	Eneo-3C-GFP
Flavobacterium	SilP trunc M140	fb-SilP6Δ	Eneo

Salmonella	SilP FL	SilP-A12	Eneo-3C-GFP
Salmonella	SilP FL	SilP-TEV	Eneo-TEV-GFP
K. pneumoniae	SilF FL	kp-SilF1	pOPINF
K. pneumoniae	SilF FL	kp-SilF2	pOPINE
K. pneumoniae	SilF Trunc	kp-SilF1Δ	pOPINF
K. pneumoniae	SilF Trunc	kp-SilF2Δ	pOPINE
E.coli	SilF FL	ec-SilF1	pOPINF
E.coli	SilF FL	ec-SilF2	pOPINE
E.coli	SilF Trunc	ec-SilF1Δ	pOPINF
E.coli	SilF Trunc	ec-SilF2Δ	pOPINE

2.4 SilF Protein Expression and Purification

2.4.1 Expression

Transformation of cells containing the relevant SilF expression plasmid were prepared as in section 2.2.1. A single colony from this plate was picked and placed into LB media containing relevant antibiotics at a 1:1000 dilution, either carbenicillin 50 mg/mL stock and/or chloramphenicol 35 mg/mL stock was used. The volume of the inoculant depended on final total number of litres of culture that was to be expressed: 10 mL inoculant per 1 L of final culture was used as standard. The cultures were left at 30 °C in a shaking incubator set to 190 rpm overnight. The overnight culture was added to either LB or TB media containing relevant antibiotics, and left at 37 °C shaking at 180 rpm until an optical density (OD_{600nm}) of between 0.6-0.8 (LB) or 1.2-1.4 (TB) was attained. Once the desired OD was achieved 1 ml of 1 M IPTG (final [1 mM]) was added and the temperature of the incubator reduced to 22.5

°C and left overnight. Cells were harvested using a Beckman high capacity standing centrifuge (Avanti J-26 XPI, Beckman Coulter, US), with a JLA8.1 rotor. Cells were centrifuged at 6238 *g* for 10 minutes, the resulting pellet was collected and placed into 50 mL falcon and frozen -80 °C unless being used straight away.

2.4.2 Protein Purification

Cells were re-suspended in **Lysis Buffer A** until fully in solution with large particulate removed using a sieve, where upon they were passed through a Constant System Cell Disruptor (Constant Systems Ltd, UK) at 28 kpsi for two rounds at 4 °C. Lysates were clarified by centrifugation using a Beckman Avanti J-26 XPI floor standing centrifuge with a JA25.50 rotor, cells were subjected to 53,000 *g* for 30 minutes.

> **Lysis Buffer A:** 50 mM HEPES (pH 7.8), 300 mM NaCl, Roche protease cocktail inhibitor tablet (Roche, USA) (1 tablet per 100 mL), DNaseI (10 µg/mL) and Lysozyme (0.1 mg/mL).

Proteins containing a 6-His or 8-His tag were purified first using affinity chromatography methods using 1 or 5mL HisTrap Ni^{2+} Sepharose columns (Cytiva, Belgium). HisTrap columns were pre-equilibrated with 5 column volumes (CV) Lysis Buffer A containing imidazole between 20 mM (lysozyme, DNaseI and protease inhibitor tablets were not added). Lysate supernatants were pooled together and imidazole (pH7.5) was added to a final concentration of 20 mM, the pooled lysates were then passed through the HisTrap using a peristatic pump at a flow rate of 3 mL/min. Columns were then washed with **Wash Buffer 1** for a total of 20 CV.

Wash Buffer 1: 50 mM HEPES (pH 7.8), 300 mM NaCl, 30 mM imidazole.

Elution of the bound protein was carried out using a gradient elution of imidazole (0-750 mM), using Buffer A1 and B1 (below) on an AKTA Pure FPLC (fast protein liquid chromatography) system (GE Life Science, UK). Gradient elutions were carried out over 20 CV with 3 mL fractions collected. Absorbance values were taken at 280 nm to ascertain when protein eluted.

Buffer A1: 50 mM HEPES (pH7.8) & 300 mM NaCl

Buffer B1: 50 mM HEPES (pH7.8), 300 mM NaCl & 750 mM imidazole.

Fractions containing eluted protein were run down a ready-made 4-12% Biorad sodium dodecyl sulphate – polyacrylamide gel electrophoresis (SDS-PAGE) gel (Biorad UK) at 300V for 15 minutes, the gel was stained with InstantBlue (Abcam, UK) dye to visualise the separated proteins.

Expressed SilF protein that contained a cleavable His-tag which was cleavable using Human Rhinovirus (HRV) 3C protease, hereafter 3C protease. Samples were placed into dialysis tubing (Spectrum Spectra/Por 3.5 kDa molecular weight cut-off (MWCO)) and submerged in dialysis buffer, consisting of Buffer A1 with 1 mM β-mercaptoethanol and 1 mM DTT added. 3C protease was added to the sample at a 1:100 ratio, samples were left overnight at 4 °C stirring gently.

SilF that was either straight from affinity chromatography or dialysis was concentrated to a volume of 350 µL using Amircon Ultra Centrifugal filters with 3 or 5 kDa MWCO. Any precipitants in the retained protein

samples were removed through centrifuging the sample at 13 krpm for 10 minutes on a small benchtop centrifuge at 4 °C.

Samples were then loaded using an AKTA Pure (GE Life Science, UK) purifier onto a pre-equilibrated size exclusion chromatography (SEC) column. A Superdex 75 10/300 GL or HiLoad 26/60 Superdex 75 (GE Healthcare, UK) were used depending on volumes and concentration of protein. Both columns have a resolution of 3–75 kDa, pre-equilibrated with SEC Buffer 1 or 2.

SEC Buffer 1: 25 mM HEPES (pH 7.8), 150 mM NaCl

SEC Buffer 2: 20 mM HEPES (pH 7.8), 30 mM KNO_3

SEC columns were run at flow rate of 0.5 mL/min with 0.5 mL fractions collected, over a total volume of 1.2 CV (~26 mL). Absorbance readings were taken at 215 nm and 280 nm, measuring the protein backbone and aromatic residues respectively, to monitor protein elution. Fractions containing desired 280nm absorbance values and correct predicted elution volumes were analysed by SDS-PAGE analysis to confirm size and purity of the samples. Fractions containing the desired protein were pooled and concentrated, with the concentration measured on the nano-drop with the extinction co-efficient (ε/1000) and the molecular weight. For SilF the ε/1000 was 5.5 and the Mw was 9.1 kDa.

Characterisation or structural studies were carried out immediately, otherwise the protein was snap frozen in liquid nitrogen and stored at -80 °C.

2.5 Inner Membrane, SilP, Protein Expression and Purification

The methodology of purification for SilP involved initial small-scale expression, purification and detergent screening prior to large-scale purification.

2.5.1 Small Scale Expression and Purification

The 12 constructs of the new cloned SilP (Section 2.3 & Table 2-6) variants were transformed into 5 different E.coli strains; LEMO21, Rosetta, C41, C43 and BL21-pLysS cells following the method outlined in section 2.2.1.

A 24 deep well block containing 700 µL TB media were then inoculated with a single colony from each construct cell line, with respective antibiotics added in and left to incubate overnight at 220 rpm at 37 °C. From these 150 µL was then placed into 3 mL of TB media (with antibiotic) in a different 24 deep well block, cells were left at 37 °C for 3-5 hours then induced with 1 M IPTG to a final concentration of 1 mM. The temperature was then reduced to 20 °C and left to shake overnight. The cells were then pelleted by centrifuging the blocks at 300 rpm for 10 minutes, after which cells were stored at -80 °C until needed.

Purification of the small-scale expression was conducted using a standard method employed by the Membrane Protein Laboratory at Diamond, outlined below, using n-Dodecyl-β-D-Maltopyranoside (DDM) and n-Dodecylphosphocholine (Fos-Choline-12) (Anatrace, USA).

Frozen cells were re-suspended in 1 mL Lysis Buffer in a 24-well block and sonicated using a Vibra-Cell ultrasonic liquid processor (VC 505)

(Sonics, USA) with a 24-probe head at maximum frequency with 15s on and 30s for a total on time of 90 seconds.

> **Lysis Buffer:** 20 mM HEPES (pH 7.8), 500 mM NaCl, 10% glycerol & 10 mM imidazole, DNaseI (0.1 µg/mL) & lysozyme (0.1 mg/mL).

Lysed cells were then split in half (450 µL each) and placed into two new 96 deep well blocks, one for DDM and the other Fos-choline. To each well 50 µL of 10 % detergent (DDM or Fos-Choline-12) was added and left to solubilise shaking at 800 rpm for 1 hr. The blocks were centrifuged for 30 minutes at 3500 *g* using a Beckman Benchtop Allegra X-14 with a SX4750 rotor (this centrifuge and rotor was used for all steps with a 96 deep well block involved). After pelleting of insoluble material the lysate was added to a 96 deep well filter plate (Generon, UK). Each well had 100 µL of 50% suspension TALON resin (Takara Bio, USA) added (pre-equilibrated with lysis buffer). Blocks were left to incubate for 1hr at 4 °C to enable binding to the beads.

After incubation the lysate was drained off by centrifuging the blocks at 300 rpm for 3 minutes. The remaining TALON resin, with bound protein, was washed 3 times with 500 µL of Wash Buffer and drained off by centrifuging.

> **Wash Buffer:** 20 mM HEPES (pH 7.8), 500 mM NaCl, 10% glycerol, 25 mM imidazole & 3x critical micelle concentration (CMC) detergent.

After washing, 50µL of Elution Buffer was applied to each well and a collection plate was placed under the filter block. The blocks were then incubated for 30 minutes before centrifuging at 300 rpm for 3 minutes to elute the protein.

Elution Buffer: 20 mM HEPES (pH 7.8), 500 mM NaCl, 10% glycerol, 500 mM imidazole & 3x CMC detergent

From the eluted samples 35 µL of each was placed into high recovery vials for Fluorescence-detection Size Exclusion Chromatography (FSEC), with the remaining 15 µL was added to 15 µL SDS-dye and frozen for gels at a later date.

FSEC is a method by which a protein that has been labelled with a fluorophore (in this research we used GFP) is tracked through SEC using fluorescence optics, as opposed to the traditional 280 nm absorbance optics. Using fluorescence optics only protein containing the fluorophore is seen on the FSEC trace, this gives a quick determination of a proteins presence and also an indication to its state in solution (i.e. aggregated or monodispersed) (Kawate and Gouaux, 2006). FSEC was conducted on Shimadzu Prominence HPLC system (Shimadzu, Japan) using a Superdex 200 10/300 column pre-equilibrated with FSEC Buffer, over a period 20 mL volume (1 CV) with a flow rate of 1.0 mL/min, collecting at 280 nm and 510 nm for GFP fluorescence.

FSEC Buffer: 20 mM HEPES (pH7.8), 150 mM NaCl, 0.03% DDM

2.5.2 Small Scale Detergent Screen

The 16 best expressing SilP constructs from the various *E. coli* cell strains identified from the expression trials, based on their FSEC profile and yields, were expressed again in their desired cell lines. A single colony from the transformation plates were added into 10 mL TB media a left to incubate shaking overnight at 37 °C. Inoculation of 50 mL LB media for each construct was conducted using 500 µL of the overnight, with the relevant antibiotic added. Cells were grown at 37 °C to an OD_{600} of 0.5

whereupon they were induced with IPTG to a final concentration of 1 mM, cells were left to grow overnight at 20 °C before being pelleted in a Beckman Avanti J-26 XPI centrifuge using a JA25.50 rotor. Cells were re-suspended in 25 mL of Lysis Buffer from section 2.5.2.

From the 25 mL resuspension sample 3 mL was placed into each well of a 24 deep well block row (4 blocks in total as 16 constructs). Samples were then sonicated using the same setting as section 2.5.2. Once lysed, using all of the wells of a single row, 950 µL of lysate was placed into each well of a 96 deep well block row (1-12). Each well had 95µL of 10% detergent added, based on the format below in Table 2-7, for solubilisation and left to 1 hour shaking.

Table 2-7: Detergent screen layout based on a 96 well block with 12 columns.

Well No.	Detergent	Detergent Abbreviation
1	n-Dodecyl-β-D-Maltopyranoside	DDM
2	n-Dodecyl-β-D-Maltopyranoside + CHS*	DDM+CHS
3	n-Decyl-β-D-Maltopyranoside	DM
4	n-Decyl-β-D-Maltopyranoside + CHS*	DM+CHS
5	n-Octyl-β-D-Glucopyranoside	OG
6	Lauryl Maltose Neopentyl Glycol	LMNG
7	Octyl Glucose Neopentyl Glycol + CHS*	OGNG+CHS
8	n-Dodecyl-N,N-Dimethylamine-N-Oxide	LDAO
9	Octaethylene Glycol Monododecyl Ether	C12E8
10	Polyoxyethylene(9)dodecyl Ethe	C12E9
11	5-Cyclohexyl-1-Pentyl-β-D-Maltoside	CYMAL5
12	n-Dodecylphosphocholine	Fos-Choline 12

*CHS – Cholesterol hemisuccinate

After solubilisation, samples were centrifuged at 3500 *g* for 30 minutes to pellet any insoluble material using the benchtop centrifuge as in section 2.5.2. The remaining protocol followed section 2.5.2 with each respective detergent used for washes and elution's.

Samples were again taken for FSEC analysis, being run in with the same parameters as section 2.5.2. The same FSEC Buffer was the same for each detergent (DDM used as the detergent CMC component), this was due to the inability to use multiple buffer lines for each of the 12 detergents.

2.5.3 Large Scale Expression

Based on the expression and purification screening of previous section (define) a large-scale expression and purification of SilP was conducted with the *E.coli* truncated (T154) pOPINEneo-3C-GFP-8His construct used in LEMO21 (DE3) cells.

LEMO21 (DE3) cells containing the relevant expression plasmid were prepared as in Section 2.2.1. A single colony was picked and placed into LB media containing relevant antibiotics, volume depended on number of litres required (10 mL inoculant per 1 L scale up). Samples were left overnight to incubate at 30 °C and shaking at 190 rpm. 1 L of TB media was inoculated with 10 mL from the overnights, relevant antibiotics were added to a 1:1000) dilution and L-Rhamnose was added to an end concentration of 1 mM. Cells were grown at 37 °C, shaking at 210 rpm, until an OD_{600nm} of between 1.2-1.4 was achieved upon which 1 mL of 1 M IPTG was added. Cells were left at 37 °C for 4 hours then harvested. 1 mL of media was removed prior to harvest for GFP count measurements to determine the level of expression. Cells were harvested at 4800 *g*

using a Beckman standing centrifuge, with a JLA8.1 rotor. The resulting pellet was collected and placed into 50 mL falcon and placed into -80 °C storage unless being used straight away.

2.5.4 Quantification of Protein Expression and Concentration using GFP fluorescence

Cells that contained GFP-tagged protein were measured for the amount of GFP present to get an initial expression confirmation and concentration determination. Briefly, 1 mL of cell cultures was taken and centrifuged at 13,000 rpm on a bench top centrifuge for 1 minute, after which the supernatant was removed. The cell pellet was resuspended in 200 µL of phosphate buffered saline (PBS) buffer, the resulting resuspended solution had 100 µL pipetted into clear flat bottom 96-well plate. GFP fluorescence was measured using a SpectraMax M2 plate reader (Molecular Devices) using an excitation wave of 488nm and recorded the emission from the GFP at 512nm. Using the GFP count from the spectra max the concentration of GFP and thus protein could be calculated using Equation 2.1 below.

$$\left(\frac{\text{GFP count}}{12000}\right) \times 0.03\ (\text{mg/mL}) \times \text{Volume of source (mL)} = [\text{GFP}]\ (\text{mg/mL}$$

$$\frac{\text{Mw of protein (kDa)}}{\text{Mw of GFP (kDa)}} \times [\text{GFP}]\ (\text{mg/mL}) = [\text{Protein}]\ (\text{mg/mL})$$

Equation 2-0-1: Where (12000) fluorescence of GFP at 0.03mg/mL, (0.03mg/mL) concentration of pure GFP.

2.5.5 Purification

2.5.5.1 Lysis and membrane preparation

Expression cells, directly from cell harvest or from -80 °C storage, were resuspended in Lysis Buffer B until fully in solution, approximately 50mL per 10g pellet.

> **Lysis Buffer B:** 50 mM HEPES (pH 7.8), 300 mM NaCl, Roche protease cocktail inhibitor tablet (1 per 100 mL), DNaseI (10 µg/mL) and Lysozyme (0.1 mg/mL).

The re-suspended solution was placed into a Constant System Cell Disruptor, using a sieve to remove large particulates, and subjected to two rounds of high pressure (28 kpsi). Lysates were centrifuged at 132,000 *g* for 1 hour 30 minutes using a Beckman Optima L-100 XP Ultracentrifuge in order to pellet cellular membranes.

Membrane pellets were collected and re-suspended in lysis buffer, without DNaseI and lysozyme added, using a handheld homogeniser with 50mL buffer for homogenising. Re-suspended membranes were either snap frozen and stored at -80 °C for future solubilisation or immediately solubilised in detergent.

Solubilisation of SilP involved incubating re-suspended membranes with 1% LMNG (end concentration) in a broad beaker with a magnetic stirring rod, rotating at 300 rpm for 1-2 hours. After solubilisation samples were centrifuged at 132,000 *g* for 1 hour in the ultracentrifuge as before to remove and insoluble material. The soluble supernatant was then applied to a Strep-Tactin XT Superflow GFP nanobody column affinity column.

2.5.5.2 Affinity Chromatography and SEC

SilP constructs containing GFP tags were purified using affinity chromatography methods. Initial purification methodology followed those outlined in section 2.4.2, however protein yield and purity was considerably lower. A new method was used for purification which utilised biotinylated GFP antibody (here after nanobody) that has a high affinity for GFP (Zhang *et al.,* 2020).

The nanobody contains a 15 amino acid 'Avi-tag' sequence (GLNDIFEAQ**K**IEWHE) which is identified by the enzyme BirA, this enzyme ligates a molecule of biotin to the lysine residue thus biotinylating the protein (Fairhead & Howarth, 2015). The biotinylated protein can bind to Strep-Tactin XT resin as the strep resin has high affinity for biotinylated molecules. Once the nanobody is bound to the column and immobilised the protein sample supernatant can be passed over the column with the nanobody binding to the GFP-tagged protein thus purifying it.

The method below outlines how the purification was conducted.

Strep-Tactin XT resin was placed in a gravity flow column and equilibrated with 5 CV of Wash Buffer 2.

> **Wash Buffer 2:** 50 mM HEPES (pH 7.8), 300 mM NaCl, detergent 3x CMC

A GFP-nanobody containing solution was passed over the resin to allow binding to the nanobody, this was repeated several times to ensure saturation of resin.

Solubilised SilP was passed over the column to allow binding of the protein, once bound the column was washed with 10 CV Wash Buffer 2.

The protein was then eluted with Elution Buffer 1 to a total volume of 2 CV.

> **Elution Buffer 1:** 50 mM HEPES (pH7.8), 300 mM NaCl, 100 mM Biotin, detergent (3x CMC). Adjust pH after addition of biotin.

The eluted protein was then dialysed overnight against Elution Buffer 1 without the biotin added, as to remove the biotin, with Human Rhinovirus (HRV) 3C protease added to cleave the GFP-6His tag.

After dialysis, the protein sample applied to a reverse IMAC column (Histrap) to remove the His-tagged GFP and 3C-protease. The flow through was collected and the column was washed with 10 CV Wash Buffer 3, before eluting the bound protein with 3 CV Elution Buffer 2.

> **Wash Buffer 3** 50 mM HEPES (pH 7.8), 300 mM NaCl, 10 mM imidazole, detergent (3x CMC)

> **Elution Buffer 2:** 50 mM HEPES (pH 7.8), 300 mM NaCl, 500 mM imidazole, detergent (3x CMC)

Samples of each stage were run down an SDS-PAGE gel to track the protein and confirm cleavage had occurred. Fractions containing cleaved SilP were pooled and concentrated to a volume of 300µL using a Amircon 50kDa MWCO spin concentrator. Samples of SilP used for biophysical and activity assays purposes continued to SEC, however samples for structure determination were purified further using a sucrose gradient.

Sucrose gradient purification entailed applying 300 µL to a sucrose gradient, composed by mixing 10% & 30% sucrose on a Biocomp piston gradient fractionator/gradient station Model 152/153 (Biocomp, Canada). Samples were then ultracentrifuged it at 115,000 *g* in a swing bucket

SW50.50 for 16hrs, using a Beckman Benchtop Optima Max-XP ultracentrifuge (Hauer *et al.,* 2015). The sample was then collected through fractionation using 280nm to ascertain where the protein elutes. The fractions were applied to an SDS-PAGE gel to determine where SilP eluted before concentrating further for SEC.

SilP SEC was conducted on a Superdex 200 10/300 GL (GE Healthcare, UK), pre-equilibrated with SEC Buffer 2.

> **SEC Buffer 2:** 25 mM HEPES (pH7.8), 150 mM NaCl, detergent (3x CMC)
>
> **SEC Buffer for structure determination using Cryo-EM contained no LMNG CMC**

SEC columns were run at 0.4 mL/min with 0.2 mL fractions collected over a total of 1.2 CV. Absorbance readings at 215 nm and 280 nm were taken to monitor protein elution. Fractions containing 280 nm UV absorbance were analysed on an SDS-PAGE gel for confirmation and purity checks. Fractions containing SilP were concentrated using a Amircon 50 kDa MWCO spin concentrator to concentrate the protein to desired concentration, samples were centrifuged in a Beckman Allegra X-14 benchtop centrifuge. The protein was either used immediately or frozen for future use.

2.6 Outer Membrane protein SilC: Protein Expression and Purification

2.6.1 Large Scale Expression

Transformed C43(DE3) *E.coli* cells containing the relevant expression DNA were prepared as in section 2.2.1. The remainder of expression and harvest was the same as in section 2.5.4 with one change, there was no Rhamnose added to the samples as the C43 cells do not require this. Cells were used immediately after harvest or frozen and stored at -80°C.

2.6.2 Purification

Cell pellets were re-suspended in **Lysis Buffer C** (50 mL per 10g pellet).

> **Lysis Buffer C:** 20 mM HEPES (pH 7.5), 50 mM NaCl, Roche protease cocktail inhibitor tablet (1 per 100 mL), DNaseI (0.1 µg/mL) and Lysozyme (0.1 mg/mL)

Re-suspended cells were passed twice through the cell disruptor at 28kpsi. Lysates were clarified at 132,000 *g* for 1 hour 15 minutes in an Ultracentrifuge as in Section 2.5.5.

Membrane pellets were re-suspended in Lysis Buffer C, without DNaseI and lysozyme, using a handheld homogeniser with 50 mL buffer used for homogenising. After resuspension, samples were made up to the same volume as used for lysis and N-lauroylsarcosine was added into a final concentration of 0.5%. N-lauroylsarcosine solubilises the inner membrane component only, resulting in the insoluble outer membrane pelleting. Solubilisation was conducted for 30 minutes at 4 °C after which the sample was centrifuged as before at 132,000 *g* but for 45 minutes in the ultracentrifuge. After ultracentrifugation, the pelleted outer membranes were re-suspended in **Binding Buffer 1** to a volume of 400 mL, with LDAO added to an end concentration of 1%.

Binding Buffer 1; 20 mM Tris (pH 8), 300 mM NaCl, 10 mM Imidazole, 10% glycerol.

The outer membrane solubilisation was left for 1 hour at 4 °C, after which another 45 minute ultracentrifugation was conducted at 132,000 *g* to remove any insoluble material.

The supernatant was poured off and run over a 10 mL Ni^{2+} Histrap column, pre-equilibrated with Binding Buffer 1. After binding the column was washed with 20 CV **Wash Buffer 4,** followed by an imidazole gradient elution with **Elution Buffers 3 and 4** over a 20 CV duration ending in 100% Elution Buffer 4.

Wash Buffer 4; 20 mM Tris (pH 8), 300 mM NaCl, 20 mM Imidazole, 10% glycerol, 0.1% LDAO.

Elution Buffer 3; 20 mM Tris (pH 8), 300 mM NaCl, 20 mM Imidazole, 10% glycerol, 0.1% LDAO.

Elution Buffer 4; 20 mM Tris (pH 8), 300 mM NaCl, 500 mM Imidazole, 10% glycerol, 0.1% LDAO.

Samples were collected in 2.5 mL fractions, with UV absorbance recorded at 215 and 280 nm. Fractions containing protein were analysed on an SDS-PAGE gel. Fractions of SilC were buffer and detergent exchanged using a PD10 column (following the kit protocol) (Cytiva, UK), pre-equilibrated with **SEC Buffer 3** with 1% DDM used as opposed to the 0.03% used for SEC. The DDM increase was to facilitate efficient exchange.

SEC Buffer 3; 10 mM sodium-acetate (pH 5), 100 mM NaCl, 10% glycerol, 0.03% DDM.

After buffer exchange samples of SilC were concentrated to 300 µL for SEC using a Amircon 30kDa MWCO spin concentrator. SilC was applied to a Superdex 200 10/300 GL (GE Healthcare, UK), pre-equilibrated with SEC Buffer 3, and run at 0.4 mL/min with 0.2 mL fractions collected over a total of 1.2 CV. Absorbance readings at 215 and 280nm were recorded to evaluate protein elution. Fractions containing 280 nm UV absorbance were analysed on an SDS-gel for confirmation and purity checks. Fractions containing desired protein were pooled and concentrated as before using a spin concentrator to a desired concentration. The protein was either used immediately for biophysical or structural characterisation or stored at -80°C.

2.7 Biophysical Characterisation Methods

2.7.1 Buffer Viscosity and Density Measurements

Buffer densities and viscosities were measured using an Anton Paar Dual DMA 5000M machine, 10 mL of buffer was injected into the instrument whereby several density and viscosity measurements were automatically conducted. Densities were calculated using pulse excitation waves with values given in g/cm^3, viscosities values were determined using the in-line rolling ball technique with values given in mL/g.

2.7.2 Size Exclusion Chromatography & Multi-Angle Laser Light Scattering (SEC-MALLS)

Size exclusion chromatography with multiangle laser light scattering (SEC-MALLS) was carried out using an AKTA Pure25 (GE Healthcare) fitted with DAWN HELEOS-II 18 angle light scattering detector and a

Optilab T-rEX refractive index monitor (both Wyatt Technologies). Proteins were applied to either a Superdex S75 10/300 or Superdex S200 10/300 increase columns (GE Healthcare) pre-equilibrated with respective protein SEC buffers. Samples were prepared to 1.0 mg/mL (SilC & SilP) or 2.5 mg/mL (SilF) and of 100 µL of protein was injected onto the column. UV absorbance, refractive index (RI) and light scattering (LS) values were collected and analysed Astra v7 (Wyatt, California, USA).

Membrane protein analysis for SilP and SilC used an additional method for molecular weight determination called conjugate analysis, supplied through Astra v7. Conjugate analysis uses all three detection systems whereby the UV absorbance measures the concentration of the protein component, RI optics determine the overall concentration of the sample, using the dn/dc of the protein and detergent, therefore by subtracting the protein concentration from the overall concentration you get each component concentration (detergent and protein). Light scattering is used to determine the overall and component molecular weights using an extension of Equation 2-2 (Slotboom *et al.,* 2008. & Wyatt Technologies, UK).

$$I_{\,scattered} = M_w \,.\, c \,.\, \left(\frac{dn}{dc} \right)^2 P(\theta)$$

Equation 2-0-2: Where $I_{scattered}$ is the light scattering, M_w is the molecular mass of the molecule, c is the concentration of the molecular component, dn/dc is the refractive index increment of the molecule to that of the solvent and P(θ) the degree of scattered light as a function of angle (multi-angle light scattering (MALS)).

2.7.3 Analytical Ultracentrifugation (AUC)

Analytical Ultracentrifugation (AUC) is a quantitative technique for measuring solutions of macromolecules. AUC works on the principle that under a centrifugal force, molecules with different molecular weights and shapes separate and sediment through a solvent at different rates. The rate of sedimentation is largely affected by the mass of the molecule (Svedberg *et al*., 1926). There are two types of AUC measurements: sedimentation velocity (SV) and sedimentation equilibrium (SE). Experiments in this project focus on SV runs only.

2.7.3.1 Sedimentation Velocity (SV)

Sedimentation velocity involves the application of a large centrifugal force to a macromolecular solution over a period of ~18 hours through high rotor speeds, the sedimentation is tracked using absorbance or Rayleigh interference optics.

The rate of sedimentation, divided by the force applied, is termed the sedimentation coefficient (*s*). Sedimentation coefficients are dependent upon the size and shape of the macromolecule. Generally, the larger the macromolecule the faster it sediments, thus possessing a larger sedimentation coefficient (Svedberg *et al.*, 1926). The Svedberg equation in Equation 2-3 shows the relationship between molar mass and sedimentation coefficient.

$$s = \frac{v}{\omega^2 r} = \frac{M(1 - \bar{v}\,\rho_0)}{N_A f}$$

Equation 2-0-3: where (*s*) sedimentation coefficient, (v) boundary terminal velocity, (ω) angular velocity (radians/second), (r) radius from the centre of rotation,(M) molar mass, ($\bar{v}$) partial specific volume, (ρ_0) solvent density, (N_A) Avogadro's number and (f) frictional coefficient.

In monodisperse solutions the rate of sedimentation should be uniform as the macromolecules are the same size, shape and molecular weight. However, in polydisperse systems the molecules have different masses, size and shape which result in a range of different sedimentation rates.

Sedimentation velocity data was analysed using the computer programme SEDFIT (Schuck, 2000). This aims to determine the distribution of sedimentation coefficients, c(S), that best fits the Lamm equation (2-4) (Lamm, 1929) which defines the transport of

$$\frac{dc}{dt} = D\left[\left(\frac{d^2c}{dr^2}\right) + \frac{1}{r}.\left(\frac{dc}{dr}\right)\right] - s\omega^2.\left[r\left(\frac{dc}{dr}\right) + 2c\right]$$

Equation 2-0-4: Where; (D) diffusion coefficient, (c) concentration, (r) radial position and (t) time (s).

macromolecules through the solution:

The c(*s*) analysis incorporates the effects of diffusion within the algorithm. The impact of diffusion on a system is more prominent on a solution of small proteins than large proteins (Schuck, 2000). The diffusion coefficient is determined by finding the frictional ratio of the macromolecule. The frictional ratio is the frictional coefficient of the observed macromolecule to that of a perfect sphere of the same molecular weight (Brown *et al.*, 2006). With the addition of the diffusion coefficient more defined peaks are often observed, however it can also lead to over-sharpening of some peaks (Schuck, 2000). The addition of diffusion within the calculation also results in c(*s*) distributions being able to estimate the weight average molar mass by transforming c(*s*)

distributions into c(M) vs M plots. This is applicable for systems that are monodispersed, but gives incorrect values of M for polydisperse systems.

2.7.3.2 AUC Experimental method

Sedimentation velocity analytical ultracentrifugation (SV-AUC) were performed using a Beckman-Coulter Optima Analytical Ultracentrifuge (Beckman-Coulter, USA). Sample cells were comprised of a two channel 12mm epoxy resin centrepiece with two sapphire windows on either end, enclosed within an aluminium case and tightened to a torque of 130lb (Figure 2.7.1 shows an AUC cell).

AUC for SilF followed similar sample preparation methods between each other, however with slight differences.

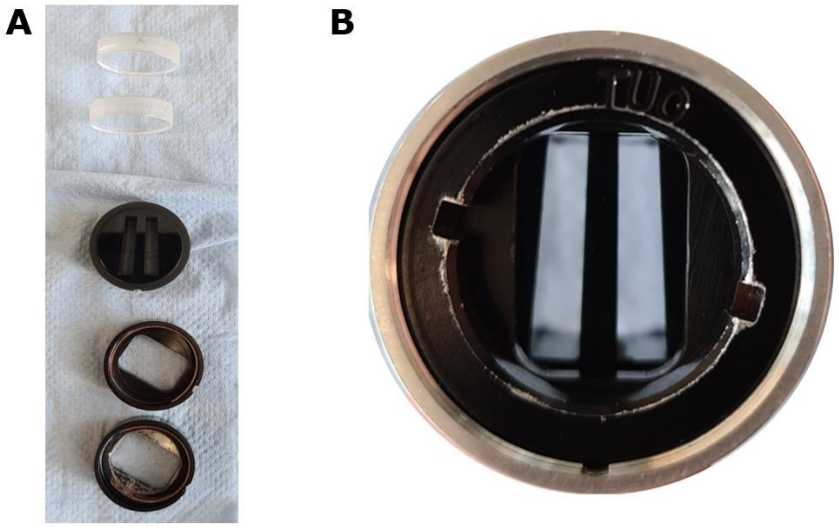

Figure 2.7.1: (A) Components of the AUC cell; x2 sapphire windows, centrepiece and window cases. **(B)** Assembled AUC cell looking down the cell with the 2 sectors.

Samples of apo ec-SilF1Δ were prepared to 3.0, 2.0, 1.0, 0.5 & 0.25 mg/mL in SEC Buffer 1, along with Ag(I) (5.0, 2.0 & 1.0 mg/mL) and Cu(I) bound (2.0 and 1.0 mg/mL) gradient series. The Cu(I) series was prepared in a nitrogen glove box to reduce oxidation of Cu(I) to Cu(II). Apo and holo bound runs were conducted separately.

To one sector of the cell 400 µL of buffer was added and to the other 396µL of sample was added. Once filled, the sample injection ports were sealed with aluminium screws. The cells were then placed and aligned into either an 8 hole An-50Ti or 4 hole An-60Ti rotor and placed within the AUC. Absorbance and Interference optical systems were then moved into place and the centrifuge was closed. The air within the sample chamber was removed using vacuum pump, upon which the AUC was allowed to equilibrate to the desired experimental temperature before the main method was implemented.

The main method consisted of both optical systems taking regular readings, approximately every minute, with the samples being spun between 40-50 krpm over a 18 hour period.

2.7.4 Nano-Differential Scanning Fluorimetry (nano-DSF)

Stability of proteins was determined using nano-DSF and was carried out using a Nanotemper Prometheus NT.48 (Nanotemper Technologies, UK).

Nano-DSF works using the intrinsic fluorescence intensities of aromatic residues within protein, primarily tryptophan residues. Denaturing the protein changes the environment around these residues and as such they change fluorescence as the protein denatures and unravels. The relationship between the fluorescence intensity changes and temperature indicate the melting temperature (T_m) of the protein (Wen *et al.,* 2020).

The Prometheus measures the fluorescence of tryptophan residues at two wavelengths 330 nm (fluorescence of buried tryptophan's) and 350 nm (fluorescence wavelength of surface tryptophan's). As the protein denatures there is normally a shift in the 330/350 ratio. Using the Prometheus the point at which the protein starts to unfold and when it is

fully unfolded are calculated based on the change of this ratio. The data is given in a graphical view showing the onset and inflection (T_m) points.

Thermal assays involved initial sample screening of proteins at several concentration, 0.1, 0.5 & 1.0 mg/mL. Duplicates of each sample concentration were placed into 10 µL glass capillaries, through capillary action, and placed into the Prometheus. Discovery scans were conducted to identify sufficient excitation intensities for reasonable sample signal to be measured. Once an excitation intensity and concentration was identified a standard run was conducted, with a temperature gradient ranging between 20 °C - 95 °C with a 1 °C/minute increase.

Samples of SilC, SilP and SilF were prepared to 1.0 mg/mL. SilF samples were prepared in two batches; The first batch was prepared with no metal and Ag(I) (end [5 mM]) added in, with the samples dialysed into water (based off the ITC studies). The second batch of SilF had no metal and Cu(I) (end [5 mM]) added, both were prepared in 1 M NaCl, this was to aid Cu(I) solubilisation. Sample capillaries with Cu(I) were prepared in a glove box with wax sealed ends to prevent the oxidation of Cu(I).

Once run, sample inflection points and melting temperatures were calculated, using the first derivative of the 330/350 ratio plot.

2.7.5 Isothermal Titration Calorimetry (ITC)

ITC experiments were conducted using a MicroCal PEAQ-ITC calorimeter (Malvern Panalytical, UK) in an anaerobic glove box to ensure that Cu(I) did not become oxidised and also to ensure changes in environment were kept minimised between different metal measurements. Purified ec-SilF1Δ was dialysed into either only water or 1 M NaCl, samples were placed in refrigerator within the glovebox to de-gas. Purposes of water

was for solubilisation of Ag(I) and 1 M NaCl for Cu(I) solubility, further reasoning is explained in section 4.7.3.

Dialysed samples were centrifuged in an Eppendorf benchtop centrifuge for 10mins at maximum speed to remove any precipitated material. ec-SilF1Δ samples were prepared to 25 μM and placed into the ITC cell to a volume of 200 μL. Titrant samples of Ag(I) and Cu(I) were prepared to 250 μM in their respective buffers and placed in the titrant well. ITC measurements were conducted at 25 °C, with 1 μL injections occurring every 60 seconds to a total of 39 injections. The stirring rate of the sample well injector syringe was set to 750 rpm. Repeats of each condition were carried out so that 5 data sets per sample were acquired. Blank runs were conducted where by Ag(I) and Cu(I) were titrated into buffer only. These readings were subtracted from the SilF with metal runs to correct for any titrant anomalies. Data analysis was carried out using Malvern Panalytical's built in software.

2.7.6 Circular Dichroism (CD)

SilF samples were prepared to a concentration of 5 mg/mL in CD Buffer 1;

CD Buffer 1: 20 mM HEPES (pH 7.8), 30 mM KNO_3,

Additionally, samples of SilF with a 1:10 molar ratio of Cu(I) and Ag(I) were prepared in CD buffer 1.

CD experiments were performed on B23 beamline (Diamond Light Source, UK), using a B23 nitrogen-flushed ChirascanPlus CD spectropolarimeter (Applied Photophysics Ltd, Leatherhead, UK) (Hussain *et al.,* 2012). Due to COVID19 restrictions these measurements were performed by beamline staff only. The samples were studied across two

regions: near-UV (250-330 nm) and far-UV (180-260 nm). The measurements were acquired using an integration time of 1 sec, cuvettes of 0.002 cm (demountable – for far-UV) and 0.2 cm path length cuvette (for near-UV) with 1 nm bandwidth at 25 °C. In total 4 repeats were acquired for each sample. The data obtained was processed using CDApps – for the far-UV region (Hussain et al., 2015) and OriginLab™.

2.7.7 Hydrogen Deuterium Exchange Mass Spectroscopy (HDX)

HDX was conducted on SilF samples only. Initial mapping of SilF (40μM) in buffer E (20 mM HEPES, 30 mM KNO_3, pH 7.8) was carried out by quenching the protein with 100 mM KH_2PO_4/K_2HPO_4, 2 M GuHCL, pH 2.08. 50 μL of sample was injected into a Waters HDX Manager with an immobilized pepsin column (2.1 × 30 mm; Waters), C18 trapping column (VanGuard ACQUITY BEH 2.1 × 5 mm; Waters), and analytical C18 column (1.0 × 100 mm ACUITY BEH; Waters). Mass spectrometer – Synapt G2-Si. Mobile phases were 0.1% formic acid in H2O (A) and 0.1% formic acid in ACN (B), such that their pH was 2.55. Protein was applied to the pepsin and trapping columns in 100 μL/min buffer A and eluted from the analytical column according to the following elution profile using H_2O/ACN (+0.1% formic acid v/v): 1 – 7 minutes 97% water to 65% water, 7 -8 minutes 65% water to 5% water, 8 – 10 minutes held at 5% water.

Sample preparation of SilF in its apo, Ag(I) and Cu(I) bound states for labelling experiments were conducted in the same manner as mapping, however sample buffer E was made in D_2O instead of H_2O and quenching occurred after 30s, 5 minute and 30 minutes.

Peptide sequences were assigned from MSE fragment data with Protein Lynx Global Server (Waters) and DynamX (Waters). Labelling data was acquired as for sequencing, except the mass spectrometer acquired MS scans only.

2.7.8 ATPase Assays

ATP assays were conducted with SilP constructs, using the Promega ADP-Glo assay (Promega, USA) following the manufacturer's instructions. All reaction steps were conducted in an anaerobic glove box as some reactions had Cu(I) added.

A calibration curve for the kit was first prepared. Samples of ultra-pure ATP and ADP were made up in Kinase Buffer to a concentration of 1 mM:

> **Kinase Buffer:** 40 mM Tris (pH 7.5) 20 mM MgCl2 0.1 mg/mL BSA

Using the ADP and ATP a concentration range was prepared within a 96 plate (A1-12), with each well made to 100 µL giving a 1 mM stock. See Table 2-8 for the layout and components.

Table 2-8: Components of the ADP/ATP calibration curve, each % value is also the volume in µL of each component.

ADP %	100	80	60	40	20	10	5	4	3	2	1	0
ATP %	0	20	40	60	80	90	95	96	97	98	99	100

Once each concentration was prepared 10 µL from each well was placed into another row and 90 µL of Kinase Buffer added, this made a 100 µM stock. This process was repeated again two more times, each time taking

10 µL from the new stock, giving an overall concentration range of 1 mM, 100 µM, 10 µM and 1µM.

SilP reactions mixtures were set up in Eppendorf's to a total volume of 15 µL, composed of 10 µM SilP, ATP (ranging from 1 µM – 5 mM), Kinase Buffer. A separate reaction was conducted with the same conditions but with Cu(I) added to a final concentration of 200 µM. Reactions were allowed to persist for 30 minutes before being separated into 5 µL aliquots (giving triplicates of each [ATP]) and placed into a Corning 384 white microplates (Corning, USA), as this would maximise luminescence readings. In addition, the ADP/ATP controls were also aliquoted out into separate rows. Each aliquot then had 5 µL of ADP-Glo reagent added to stop any kinase activity and deplete any ATP still present within the mixture, leaving only ADP. This reaction was left for 40 minutes at room temperature before 10 µL of Kinase detection buffer was added and left for 2hrs. This reagent converts ADP back to ATP and, along with a luciferase and luciferin, adds a fluorophore to the ATP which will be used for luminescence readings.

Luminescence readings were measured on a CLARIOstar-Plus (BMG LABTECH, UK), with a wide range of wavelengths to ensure maximum luminescence signal was recorded.

Luminescence readings were plotted out in excel and compared to the control ADP/ATP measurements to determine ATP consumption.

2.8 Protein Crystallisation

2.8.1 Screening Trays

Initial screening trays were set up for purified protein to identify conditions that formed protein crystals. Specific conditions for SilF protein preparation are outlined in Section 5.3.1/2 and for SilC Section 6.5.1

Throughout the project two main types of 96-well plates were used, CrystalQuick-X (2 drop) (Grenier Bio-One Ltd, UK) and SWISSCI 3 Lens (3 drop) (SWISSCI Ltd, UK). These plates all incorporate the sitting drop method of protein crystallisation, whereby a drop of protein and matrix (at a given ratio) are mixed and placed on a column in a reservoir of matrix, see Figure 2.8.1.

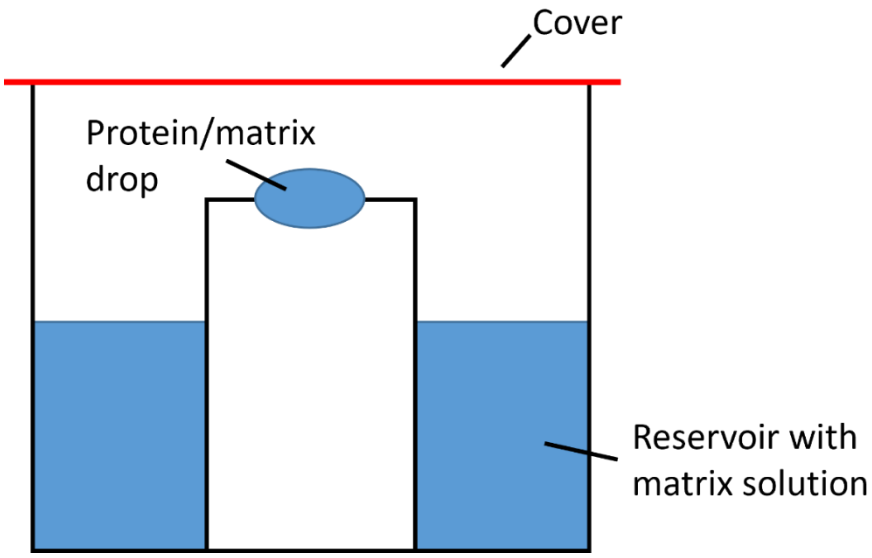

Figure 2.8.1: Sitting drop technique for crystallography. A column whereby the protein/matrix drop sits in the middle of the matrix

Trays were prepared using the Hydra dispenser (Art Robbins Instruments, USA) to automatically dispense a set quantity of matrix solution into the wells within the trays. For CrystalQuick-X plates this was

40 µL and for Swissci plates it was 60 µL. Several different screening matrix solutions were used throughout the project provided from Hampton Research (UK) or Molecular Dimensions (UK). The only Hampton Research screen used was the Index screen (D'Arcy *et al.,* 2003). From Molecular dimensions several screens were used; JCSG+ (McPherson, A., 2001), SG1 (Fazio *et al.,* 2014), Morpheus II (Gorrec, F., 2015), MemGold (Newstead *et al.,* 2008), MemGold2 (Parker, J. & Newstead, S., 2012), MemStart/MemSys (Iwata, S., 2003) & MemChannel (Parker, J. & Newstead, S., 2016). For SilC all Mem-based screens were used for screening, whereas JCSG+, SG1+ and Morpheus II screens were used for SilF.

Protein screens were prepared using the in house Mosquito LCP dispenser (SPT Labtech) which was humidity controlled (to 50%) to reduced sample evaporation. When using CrystalQuick-X plates a 1:1 ratio of protein:matrix was dispensed with 100 nL of each component used respectively. However, when using 3 drop Swissci plates a 2:1, 1:1 and 1:2 ratios (protein:matrix) was used, with a total drop volume of 150 nL dispensed. Screens were sealed with non-stick adhesive clear crystal covers (Molecular Dimensions, UK) and placed into a RockMaker R1-1000 imager (Formulatrix, USA), stored at 20 °C or 4 °C. SilF plates were only stored at 20 °C in either the Rockmaker image or an anaerobic glove box if Cu(I) was used. Whereas SilC plates were stored at both temperatures. Plates were imaged, using both UV and visual optics, on a pre-sequenced set of days based on a Fibonacci sequence.

2.8.2 Crystal Mounting, cryo-protection and cryo-cooling

Crystals that formed in given conditions were imaged using UV optics to assess if the crystals were protein or not. Crystals that were protein were mounted in preparation for imaging.

Before mounting, cryo-protecting conditions were identified and prepared, these depended on the crystallisation conditions. Table 2-9 below shows the additional cryo-protectant added to the crystals that were collected off.

Table 2-9: Cryo-protecting conditions used

Protein	Commercial screen & well	Crystallisation condition	cryo-protectant [Final]
ec-SilF1Δ apo	SG1 E4	2 M Ammonium sulphate, 0.1M sodium HEPES pH 7.5	5% glycerol
ec-SilF1Δ apo	SG1 G3	0.01 M Zinc sulphate heptahydrate, 0.1 M MES pH 6.5, 25% v/v PEG 550 MME	10% glycerol
ec-SilF1Δ Ag(I)	SG1 D10	0.2M $LiSO_4$, 0.1M Bis Tris pH 6.5, 25% w/v PEG 3350	15% glycerol
ec-SilF1Δ Ag(I)	SG1 G9	0.2M Ammonium tartrate dibasic, 20% w/v PEG 3350	20% glycerol
ec-SilF1Δ Cu(I)	SG1 C4	0.2 M potassium sodium tartrate tetrahydrate & 20% w/v PEG 3350	25% glycerol

SilC	MemChannel B12	0.1 M $MgCl_2$•$6H_2O$, 0.1M sodium citrate (pH 5), 11% PEG 4000	20% glycerol
SilC	MemGold F2	0.12 M Lithium sulphate, 0.02 M Tris (pH 7.5), 0.1 M sodium citrate (pH 5) & 20% v/v PEG 300	n/a

Trays containing crystals were imaged under a light microscope, crystal wells were unsealed using a scalpel and 1 µL of cryo-protectant was placed either into an empty adjacent well or onto a glass cover. Hampton Research mounted CryoLoops (0.05, 0.1, 0.2 or 0.3 mm) (Hampton Research, UK) were used for SilF crystals and MiTeGen MicroLoops LD (20, 35 & 50 µM) (MiTeGen, USA) were used to mount SilC crystals. Crystals were taken from the crystalising condition and placed into the cryo-protectant solution for approximately 1 minute then extracted and plunge frozen into a storage puck in liquid nitrogen.

2.8.3 A Brief Crystallography Background

This is a brief introduction to X-Ray crystallography and some terminology. Further details about specific steps in the data analysis are explained below in section 2.8.6.

Protein crystals form through the ordered regular array or protein molecules (and thus atoms) coming together and forming crystal contacts (McPherson & Gavira, 2013). Passing X-Rays through the regular array of atoms gives X-Ray scattering, which in turn gives a 2D diffraction pattern which gives information on the arrangement of

molecules within the crystal. Using the 2D diffraction patterns the unit cell of the protein crystal can be determined, that is unit by which the crystal is made of through translation along its 3 axis (vectors a, b & c with angles α, β & γ). The unit cell is comprised of a asymmetric unit, this is the is smallest portion of the unit cell that, when crystal symmetry is applied, can describe the entire unit cell (Krissinel, E. & Henrick, K., 2007), see Figure 2.8.2.

The unit cell dimension's and symmetry vary between crystals and are determined through the diffraction patterns. Further processing by indexing, integrating, scaling and merging the diffraction data results in the determination of electron density maps. Molecular replacement of the electron density maps with a model (with reasonable homology to your protein) yields a model which represents your data (see section 2.8.5). Further model modifications and refinements (process of measuring the agreement of your model to the experimental data) eventually yield a completed structure.

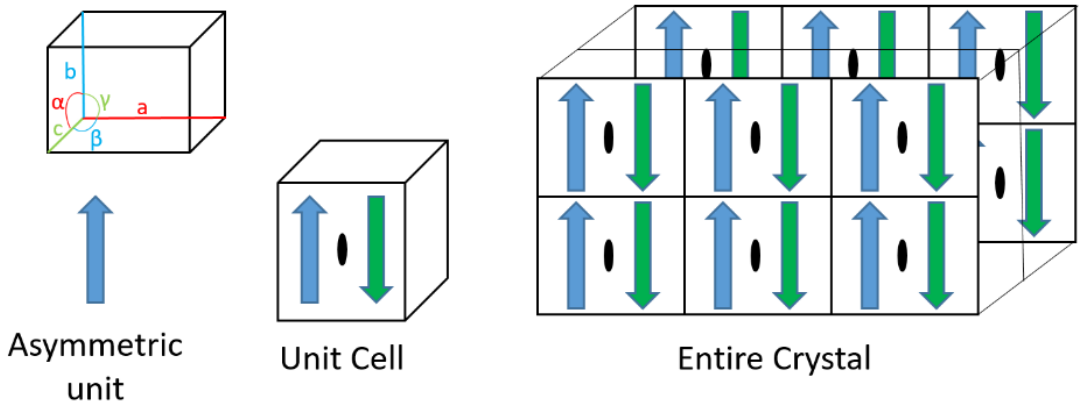

Figure 2.8.2: Description of the composition of a typical protein crystal. The asymmetric unit is the smallest portion of the crystal, which through the rotation and translation, using the symmetry operators allowed by the crystal symmetry makes up the unit cell. The unit cell is the portion of the crystal having the full symmetry of the crystal system, which when translated in 3D will generate the complete crystal.

2.8.4 Imaging and Data Collection

X-ray data collection of crystals were conducted at Diamond Light Source (UK) on Beamlines I04 or I24 (Microfocus MX) either in person or remotely. Samples were loaded automatically onto the beamline from the storage pucks. Initial screening of the crystals was conducted by centering the crystal so that it stays in the beam the entire time (360°). Prior to taking the test shots several variables were inputted, the Ω-start (starting°), Ω-oscillation (always 0.5°) and the Ω-delta (always 45°), along with the projected resolution and number of images (3). Finally, the transmission and exposure time were set, in both cases for screening the exposure time was 0.1 seconds. Transmission power for screening of SilF crystals was conducted at 10% while for SilC this was increased to 100%. Depending on the beamline a Eiger2 XE 16M (I04) or a Pilatus3 6M (I24) detector was used. Screening shots that diffract enter the automatic processing pipeline at Diamond, this utilises Mosflm (Powell *et*

al., 2017) and EDNA (Incardona *et al.,* 2009). Mosflm is a programme which indexes and integrates 2D diffraction images which gives an indication on the space group and unit cell dimensions. EDNA also gives an indication on the space group of the crystal and based on this suggests data collection strategies for several different parameters.

Data collection for diffracting crystals followed one of the collection methods suggested by EDNA, this included several parameter adjustments. In most cases the Ω-start (starting°) differed from the screening, Ω-oscillation varied between 0.1-0.15° and the Ω-delta was always set to 0°, the number of images to be taken is typically over 1800 (>180 ° of data) and the beam intensity is a percentage of the beam strength used for screening.

2.8.5 Data Processing

Data acquired from the beamline automatically entered the Diamond processing pipeline, which attempts to reduce the diffraction data to a set of structure factor amplitudes using various software packages; autoPROC, fast_dp, Dials and XDS. This software performs all steps of data reduction (indexing, integration, scaling and merging) to, hopefully, produce an mtz file suitable for use in structure solution.

Indexing identifies maxima on the diffraction image and uses their relative positions to determine the unit cell parameters and predict the space group of the crystal. The observed data points are compared to predicted spots for the given space group and unit cell (Evans, P., 2006; Ewald, P.P., 1969; Kabsch, W., 1988 & Steller *et al.,* 1997). The positions of the spot predictions are then refined to improve agreement

with the observed spots, this is important for integrating as it gives a more defined region of the spot (Powell, 2017).

Once indexed the data is integrated, this involves measuring the intensities of the spots arising from x-ray diffraction and also the x-ray background resulting from random scattering of x-rays (Battye *et al.,* 2011). Background intensities are subtracted from the diffraction spots to give a true intensity value for the given diffraction spot, since there is background noise behind the diffraction spot itself. This process, in conjunction with the averaging of multiple measured data spots, allows more accurate measurement of weaker reflections.

Finally, the integrated data is scaled and merged, a process which takes all the measured intensities from the data and puts them on a uniform scale. Variance in intensities of the diffraction spots can be affected by several factors including crystal morphology. Placing the data intensities on a normalised scale enables averaging of symmetry related spots, which theoretically should have identical intensities, to produce the final merged data set (Evans, R. & Murshudov, G.N., 2013 & Powell, 2021). The scaled and merged data is then exported , ready for use in molecular replacement and refinement.

This process is routinely carried out automatically during data collection and works well for standard cases, however manual processing is required for more challenging cases (Powell, H.R., 2017). The structure determination of SilC described herein nicely illustrates the benefits of manual intervention during the data processing when automated procedures produce an incorrect solution.

The mtz files containing the reduced diffraction data were analysed using the programme Matthews in the CCP4i software suite (Winn *et al.,* 2011).

This determines the Matthews coefficient (Matthews, B.W., 1968), which represents the ratio of the volume of the asymmetric unit to the protein molecular weight (Da). The Matthews coefficient estimates the number of protein molecules within the asymmetric unit and the associated solvent content, the lower the solvent content the more densely packed the asymmetric unit which indicates more protein molecules (Kantardjieff & Rupp, 2003; Matthews, B.W., 1966 & 1968). Knowing the number of molecules within the asymmetric unit aide's molecular replacement in Phaser, since it narrows down the number of molecules that need to be found (McCoy *et al.,*2007).

Molecular replacement is the process by which a known structure is used to solve the unknown structure of your data, this is carried out in Phaser within CCP4i. Models used for MR usually have a high percentage homology to the unknown structure. Within Phaser a homology of >40%, between the known and unknown structures, usually yields a correct solution however this is not always the case (McCoy *et al.,* 2007), see below. Models used for SilF and SilC were CusF (PDB; 2VB2) and CusC (PDB; 3PIK) respectively.

MR works by overcoming the phase problem within crystallography. X-ray diffraction data gives information on the intensity of a photon for a given spot, however no information of the phases of the photons is given. MR is a way of estimating the phases for a given spot, which leads to the determination of structure factors and thus a model solution.

MR works by using a previously determined homologous model (i.e. >40% sequence identity), whereby the position of the residues in the model should be similar to those of the unknown structure being solved. Using the model, the phases can be applied to the unknown structure

from the data collection, with the phases of the model used as estimations. However, although not identical to the model, the phases are usually close enough (if a highly homologous model) to the true values of the observed data, allowing for a feasible solution to be found. The model is applied to the experimental data in a number of and positions orientations, by rotation and translation functions of the model, within the unit cell until predicted diffraction matches the observed using a maximum likelihood analysis. The phases from the model, combined with the observed diffraction data, are then used to produce initial maps for the structure. The structure within the maps can be modified and refined to best fit the data present (Evans and McCoy, 2008). Phaser is the widely used programme for MR, which uses the maximum likelihood method outlined above to determine the phases for the experimental data based on solved models (McCoy *et al.,* 2007). Once a suitable solution is determined structure factors are output along with modified electron density maps which can be analysed in Coot prior to refinement in either Refmac5 or Phenix (Liebschner *et al.,* 2019 & Murshudov *et al.,* 2011).

Coot is currently the favoured programme for modelling protein structures. It is both a building and validation programme that measures and optimises many parameters including, B-factors (positional uncertainty of a residue/atom) and geometry of coordinates (bond lengths, angles, chirals, planes and torsion angels) (Emsley & Cowtan, 2004). Using coot, the model is interactively modified to give an optimal fit of the structural model to best represent the electron density maps. Coot has options for many adjustments to be made to the model including residue mutations, rotamer optimisation, addition of non-

protein ligands (if present), etc. However, with the ability to make adjustments to the model, overinterpretation of the data can also occur. Attributing electron density to a known atom or molecule aids refinement of the model, however this can have a detrimental effect (overinterpretation) if an atom/molecule is attributed to density that isn't there, this may instead be noise, which leads to the building of the wrong model.

Following modifications, the model is then refined using either Refmac5 or Phenix_refine, both refinement programmes use maximum likelihood analysis to drive the refinement process. Refinement analyses the model in coot and tries to maximise the agreement between the structure factors of the model (F_{calc}) to the experimental amplitude data (F_{obs}). Both programmes have a number of parameters that are iteratively taken into account when refining including; atomic coordinates, twinning (if applicable), B-factors, bulk solvent correction (background scattering from disordered solvent), occupancies etc. (Murshudov *et al.,* 1996 & 2011). The refined model should have an improved set of structure factors that better represent diffraction from the crystallised protein. The agreement between the structure factors and the observed data is monitored through the *R* factor (the normalised linear residual calculated from the observed and model data), and *R*-free (*R* value calculated using 5-10% of x-ray data that is omitted from the refinement process), Figure 2.8.3.

$$\frac{R = \sum_{hkl} ||F_{obs}| - |F_{calc}||}{\sum_{hkl} |F_{obs}|}$$

Equation 2-0-5: Equation for calculating R during refinements.

The values for Rfree can give an indication of over fitting during refinement, this is due to the Rfree data does not have any bias from the model. Typically the Rfree will be higher than the R value but both should reduce if refinement is correct (i.e. not over interpreting the data or overfitting the model). However, a decrease in R and an increase in Rfree suggests that the model is either over fitted or the changes to the model are incorrect (Brunger, A.T., 1992).

Initial rounds of refinements were conducted using Refmac5, where typically 15 cycles were run to give a reasonable model, which was manually edited in coot. Further refinement cycles were conducted either in Refmac5, with the number cycles guided by convergence of the LLG values (log-likelihood gain; a measure of the improvements of the model to the data) or in Phenix_refine where 3 cycles were always used. The 3 cycles within Phenix are macrocycles, with many different refinement parameters built into each step. A structure is deemed solved when the LLG and LLGfree converge, this is not necessarily the point at which the R and Rfree no longer change, however it is most often the case that they are also minimised.

Post-refinement models were analysed with MolProbity, a model validation programme, either via the online server (Williams *et al.,* 2018) if refined using Refmac5, or if using Phenix it is automatically outputted (Chen *et al.,* 2010). MolProbity looks at many parameters within the model such as the all-atom contacts, distribution of rotamers, Ramachandran plot and Cβ deviations (Williams *et al.,* 2017). If any interatomic clashes or geometric outliers are identified they are highlighted for correction in coot. After any changes are made to the model further cycles of refinement are performed before subsequent

validation. The process of model changes, refinement and validation are continued until all the electron density has been interpreted, and validation indicates no geometric outliers persist in the model.

2.9 Negative Staining and Cryo-EM

2.9.1 Negative Stain Grid Preparation and Imaging

Negative staining was carried out using Agar Scientific Carbon Film 300 Mesh Cu grids. Grids were glow discharged under a vacuum using a Quorum GloCube (Quorum Technologies Ltd, UK) for 1 minute, this was to make the grids hydrophilic.

Initial negative stain screening involved using kp-SilP construct solubilised in DDM (3x CMC 0.03%) and LMNG (no added CMC) detergents at concentrations of 0.05 and 0.01 mg/mL. Samples of SilP were applied to grids to a volume of 5 µL, for 30 seconds then blotted, blotting consisted of gently placing filter paper along the edge of the grid until all excess solution was absorbed. Grids were subsequently washed twice with 5 µL of water for 10 seconds each then blotted, a 10 µL uranyl acetate (end concentration 0.2%) stain was finally applied for 1 minute then blotted in the same manner as earlier. Grids were air dried for a couple of minutes before placed in a grid holder. Sample grids were stored at room temperature until imaged.

Imaging was conducted using a JEOL JEM-2100 200 kV Transmission Electron Microscopy (TEM) microscope (Lanthanum hexaboride emission gun and EDS detector. Sample grids were placed into a vacuum chamber before an electron beam was passed through. Micrographs were shown on screen and searched as to find areas of interest with homogenous

non-aggregated protein. Once areas of interest were found an automatic imaging programme was initiated. The programme consisted of moving the grid along a given axis (X or Y) at 50 μm intervals. Between each interval movement images were taken after 2 minutes equilibration time, as to stop drift occurring, for a total of 60 images.

2.9.2 Cryo-Grid Preparation

Cryo grid preparation involves applying a few microlitres of sample to glow discharged grids and blotting off the excess liquid, this produces a thin film of protein containing liquid on the grids. The grids are plunge frozen at a high speed into liquid ethane, this sudden freezing causes the ice to vitrify. Vitrification is important for Cryo-EM as the vitrified ice is glass like and does not destroy the protein, in comparison conventional freezing causes ice crystals to form which interact and denature protein.

Samples preparation used QuantiFoil 300 mesh Au QuantiFoil R1.2/1.3 grids, these were different to those used in negative stain. Grids were glow discharged using a Quorum GloCube before protein samples were applied. Grids were glow discharged at 30KeV for 30s twice before use.

Following glow discharge a single grid was placed into a Vitrobot mark IV (ThermoFisher Scientific). The Vitrobot enables various parameters such as blot time and force to be adjusted for optimisation reasons, it also enables vitirifcation of the samples through rapid plunge freezing.

Samples of ec-SilP1Δ were applied to a volume of 4 μL at 0.8 mg/mL, the general rule is to use 10X the concentration used for negative stain as more sample is likely to be lost in Cryo-EM prep. After sample application grids were blotted to remove excess liquid, using the Vitrobot filter pads. Blotting and blot forces were varied until an optimal condition was

identified, the optimal condition was 2 seconds blot with a blot force 2 setting. Following blotting the samples were auto plunge frozen into liquid ethane, after which the samples were stored in an EM grid box in liquid.

2.9.3 Clipping, Screening and Data Collection of Grids

Prior to imaging the frozen sample grids were clipped, this is needed so that the grids can be easily handled and stored while imaging takes place. Before any clipping a clipping station was cooled down using liquid nitrogen, with the station sat in a pool of liquid nitrogen. Once cooled down clipping grids were placed on top of the station to cool down, as were the C-clips. Once cooled down clipping grids were placed in the grid holder and the sample grids were taken out of their grid box positions and placed on the clipping grid. C-clips were then inserted as to lock the sample grid into position, the clipped grid was then returned to the grid box for imaging.

Grids were imaged either on the Glacios microscope (Research Complex at Harwell & Diamond Light Source, UK) housed at eBIC (Diamond Light Source, UK) or at Leicester on the Titan Krios microscope (Midlands Regional Cryo-EM Facility, Leicester, UK) by local contacts. The Glacios has a 200kV X-FEG emission gun and a Flacon4 electron detector, whilst the Titan Kiros has a 300kV Schottky X-FEG emission gun and a Gatan K3 electron detector.

Grids were imaged remotely using NoMachine and TeamViewer for both microscopes. To set up both screening and collection methods on the microscope the programme EPU (ThermoFisher Scientific, UK) was used, this is an easy to use interface that controls the microscope.

Screening consisted of making initial grid atlas's to get an overview of the grid quality and ice thickness, this was made at low magnification as to not damage the grids with the electron beam. Once an atlas was made, higher resolution screening was conducted inspecting individual grid squares and holes. Grid holes with sufficient particle distribution and ice quality were saved in the atlas map for data collection, this process continued until a sufficient number of grid squares/holes were identified.

Data collection was then conducted based on the saved grid squares/holes from screening. Setting up data collection followed a similar process to screening with additional methods such as setting up number of images, dosage, and area of hole to collect off. Data collection typically ran for 24-48hrs. Micrographs from data collection were transferred for data processing.

2.9.4 Data Processing

Data analysis of micrographs was conducted using Relion 3.1 was conducted to get 2D classes and potential 3D model. Relion is a programme uses Bayesian analysis to compares the observed data collected to that expected, iteratively analysing the data by taking into account many parameters to improve the agreement between the observed and expected data (Scheres, S.H.W., 2019). Relion 3.1 is a user friendly interface programme, with each step leading to the next for ease of processing.

The first step of data analysis is the importing of micrographs into Relion 3.1, with several parameters such as electron dosage, voltage and pixel size also inputted. Following the addition of the micrographs motion correction and contrast transfer function (CTF) estimations are made.

Motion correction takes into account the movement of proteins within the ice when an electron beam is applied, due to the heat from the beam slightly melting the ice. As each micrograph is actually a series of several images, rather than a single 2D image, comparisons between each image can find consistent features which it can focus on and correct for any variation. CTF estimation corrects for the image distortion that occurs within the micrographs due to the interaction between the beam and the grids.

The next step is automatic particle picking, the step involves picking reference particles from several micrographs before applying it to all other micrographs. The loaded images have particles selected with a given box size, the box size is typically slightly larger than the estimated longest dimension of the protein of interest. Typically, a good micrograph will have hundreds of particles to pick, this is repeated for approximately 10 micrographs. After picking particles from the reference micrographs rudimentary 2D classes automatically generated, generated by features that are commonly seen in the particles. Selecting the 2D classes that look like protein particles they can be used as a reference for Relion 3.1 to apply to the remaining micrographs, resulting in thousands to millions of particles being picked. The particles that are picked from the remaining micrographs are then extracted, with the particle size increased to 3X the box size, as to get maximum information. The extracted particles are then used to make much more defined 2D classes, typically showing several different orientations of the protein. 2D classification used a maximum-likelihood approach to give 2D classes that have minimal signal to noise. 2D classes that were of sufficient quality were then taken to 3D model building, whereby the different

orientations of the proteins are amalgamated together to give an overall 3D model. However, within this project this step was not achieved as samples were not of sufficient quality to allow for this.

3 Inner Membrane P_{1B}-ATPase SilP

3.1 Introduction

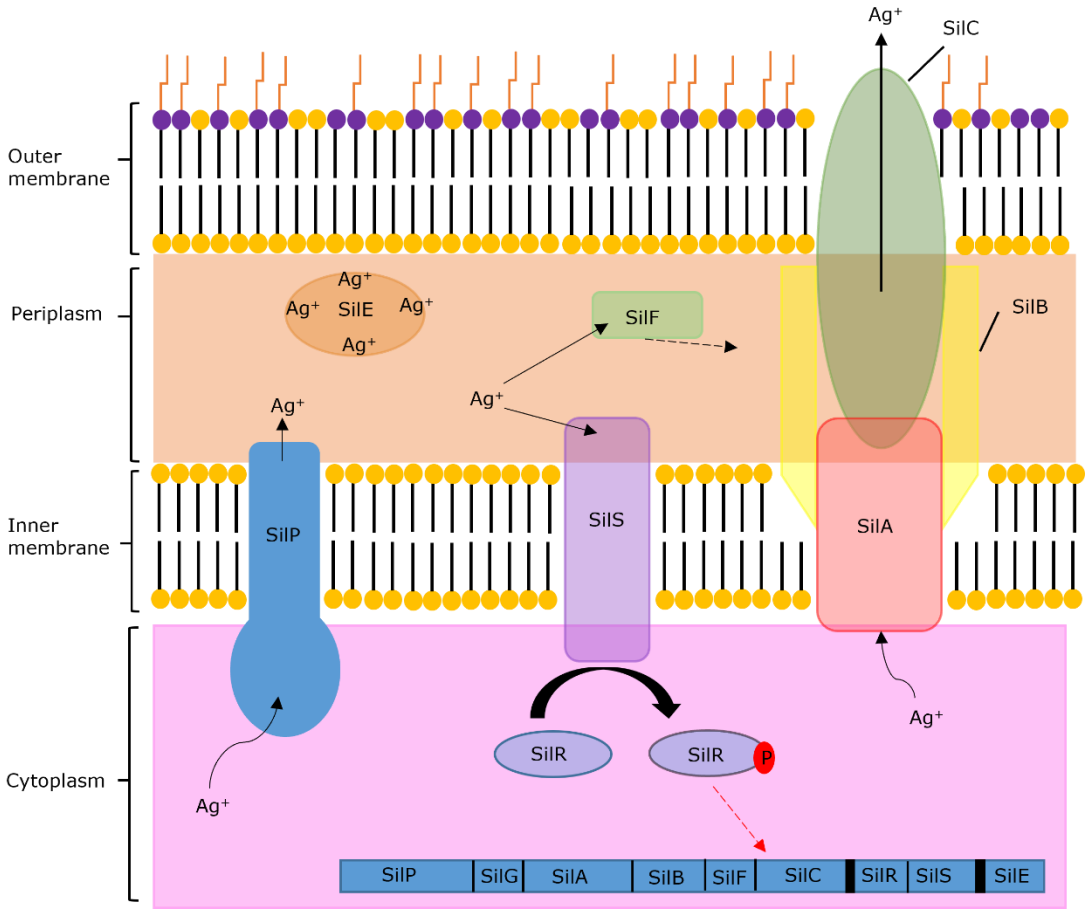

Figure 3.1.1: Sil system overview with SilP highlighted (Blue) showing its suggested role within the system.

SilP is an integral component of the sil family of proteins involved in bacterial Ag(I) resistance (Figure 3.1.1). Through homology modelling to the copper homolog, CopA, SilP is an inner membrane P_{1B}-ATPase metal ion exporting efflux pump. The primary function of CopA is to export Cu^+ ions, although it has been shown to additionally export Ag(I), from the bacterial cytoplasm to the periplasm using the hydrolysis of ATP to drive the catalytic cycle. It is surmised that SilP serves the same purpose within the *sil* system, primarily exporting Ag(I) into the cytoplasm, although possibly Cu^+ as well.

SilP is made of 5 domains; Heavy Metal Binding Domain (HMBD), Nucleotide binding domain (N-domain), Phosphorylation domain (P-domain), Activator (A-domain) and a transmembrane region (TM) (Andersson *et al.*, 2014).

The catalytic mechanism of SilP, from the CopA homolog, follows the Post-Albers cycle (Section 1.1) (Albers, 1967). The cycle consists of several steps (E1, E1P, E2P, E2 etc.) which adopt different conformations that facilitate catalysis and transportation of metal ions.

3.2 Aims

An atomic resolution structure of SilP, coupled with an analysis of the biophysical and biochemical properties of SilP will provide an in depth model that can be used to better understand the role of SilP within the sil system. The specific aims of this chapter are to:

I. Express and purify SilP constructs in quantities commensurate with conducting structural, biophysical and functional analysis.
II. Obtain a structure of SilP in one or several of its catalytical states using Cryo-EM analysis.
III. Conduct biochemical characterisation of SilP in its apo and metal bound states.

3.3 Cloning of SilP

Section 2.3 detailed previous work on the *sil* genes resulting in the production of three SilP over-expression constructs from *Klebsiella pneumoniae*, full length SilP with c-terminal GFP (kp-SilP) and a HMBD-less SilP with c-terminal GFP tag (Δkp-SilP). These versions have previously been produced by Dr David Casas-Mao (Casas-Mao PhD thesis Nottingham, 2018).

In addition to previously cloned constructs, two new constructs of SilP were cloned. Homology modelling of the *Klebsiella pneumoniae* sequence provided many other bacterial variants of SilP. Different variants were chosen based on the differing % identity to the search sequence as well as their evolutionary distance from the *Klebsiella pneumoniae* species. Eventually the *E.coli* and *Flavobacteria* bacterial species were chosen. The *E. coli* variant was chosen as the protein will be expressed in an *E. coli* system which may aid expression and protein folding (although codon optimisation reduces this impact), in addition the protein maintains the natural His-tag region in the HMBD which may be of interest. The *Flavobacterium* variant was chosen as it had a lower sequence identity to the *E. coli* and *Klebsiella pneumoniae* variants. The sequence also does not contain the natural His-tag in the HMBD and thus it will be a good comparison for identifying metal binding.

Cloning of these constructs was carried out in two rounds, owing to the gene being cheaper to synthesise in two halves as opposed to once single gene by Twist Bioscience.

The new SilP genes were too large for synthesis on a single fragment, therefore the genes were divided in half with an overlapping region which could be used to join the two halves together (~24 bp). The gene

fragments also contained a 15 bp generic nucleotide sequence either side of the gene section which was removed through PCR. PCR was carried out using the method outlined in section 1.3.2, using the primers for each respective construct in Table 2-5. The PCR products were analysed on a Invitrogen 1.2 % Agarose (GP) E-Gel containing SYBR safe stain to

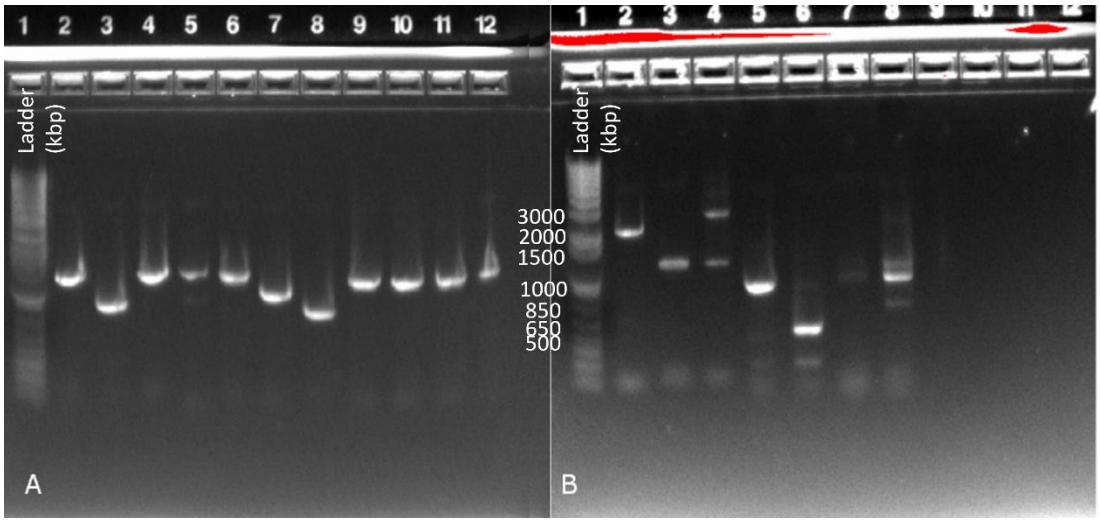

Figure 3.3.1: E-Gel UV fluorescence images of each SilP half fragment after the 15 bp generic sequence has been removed. **(A)** SilP fragments of *E.coli* and *Flavobacterium* homologs. **(B)** Final SilP *Flavobacterium* variants. See Table 2-5 for the primers and expected Mw's.

view the results of the PCR (Figure 3.3.1).

As shown in Figure 3.3.1 the gene fragments were successfully amplified, with all the bands occurring around the 1500 bp mark for the full-length constructs and lower bands for the truncated constructs. Additional purification of amplified samples was not conducted as there was minimal contaminants. Additionally, the ladder did not show anticipated separation between the different markers, this was attributed the ladder being of considerable age.

The second round of PCR amplification allowed for the gene halves of each construct to anneal (due to the overlapping regions incorporated into the fragments) and amplify the combined gene. The method used was the same as before, however the template DNA this time was each SilP half. The annealing temperatures of the primers were kept the same as before, the resulting PCR product were analysed on a 1% agarose gel, see Figure 3.3.2.

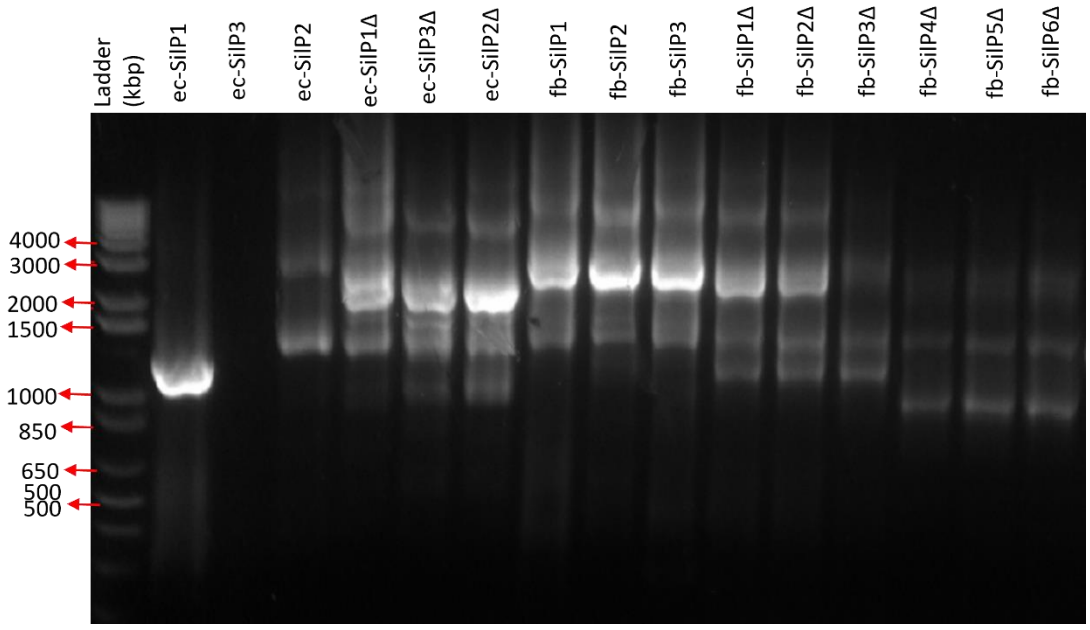

Figure 3.3.2: 1% Agarose gel of the PCR annealing of the SilP fragments from *E.coli* (ec) and *Flavobacterium* (fb). Lane 1 is the ladder (in kbp), with the other lanes labelled with the respective constructs. Full length constructs are approx. 3000bp with the truncations ranging

The results of the agarose gel showed what looked like a 50/50 split of samples that appear to have annealed and amplified compared to those that appeared unsuccessful. Fully annealed constructs had bands between 2000-3000 bp, whilst those that didn't work showed weak bands around the 1000 – 1500 bp marks. Gene fragments that had produced a full-length product, based on the correct band being present

on the agarose gel, were gel extracted using a QiaQuick gel extraction kit; the kit protocol was followed as outlined in Section 2.3.3.

The concentrations of the amplified fragments from the extraction were measured using the Nano-drop (260 nm) and all measured between 20-50 ng/µL. Cloning ligation followed the protocol outlined in Section 2.3.3, with the amounts of insert varied depending on their concentration. The ligated vector was transformed into STELAR competent cells for over expression of the plasmid, which was extracted using the mini-prep method and subsequently sequence verified (see Section 2.3.4). All clonal DNA concentrations from the mini-prep measured in excess of 150 ng/µL. Sequence verification confirmed that 9/15 constructs were successfully cloned. The verified sequences are outlined in Table 3-1 below.

Table 3-1: Cloned constructs of *E.coli* and *Flavobacterium* that have been sequence verified.

Protein	Code	Vector	Verified presence	Label for storage	Used in screening
SilP Full length (M1)	ec-SilP1	pOPINEneo-3C-GFP(1)	Yes	-	No
SilP Full length (M1)	ec-SilP2	pOPINEneo-TEV-GFP(2)	No	A1	No
SilP Full length (M1)	ec-SilP3	pOPINE	No	-	No
SilP Trunc (T154)	ec-SilP1Δ	pOPINEneo-3C-GFP(1)	Yes	C1	Yes
SilP Trunc (T154)	ec-SilP2Δ	pOPINEneo-TEV-GFP(2)	Yes	B1	Yes

SilP Trunc (T154)	ec-SilP3Δ	pOPINE	No	-	Yes
SilP Full length (M1)	fb-SilP1	pOPINEneo-3C-GFP(1)	Yes	D1	Yes
SilP Full length (M1)	fb-SilP2	pOPINEneo-TEV-GFP(2)	Yes	A2	Yes
SilP Full length (M1)	fb-SilP3	pOPINE	Yes	B2	Yes
SilP Trunc (A93)	fb-SilP1Δ	pOPINEneo-3C-GFP(1)	Yes	C2	Yes
SilP Trunc (A93)	fb-SilP2Δ	pOPINEneo-TEV-GFP(2)	Yes	D2	Yes
SilP Trunc (A93)	fb-SilP3Δ	pOPINEneo	Yes	A3	Yes
SilP Trunc (M160)	fb-SilP4Δ	pOPINEneo-3C-GFP(1)	Yes	B3	Yes
SilP Trunc (M160)	fb-SilP5Δ	pOPINEneo-TEV-GFP(2)	Yes	C3	Yes
SilP Trunc (M160)	fb-SilP6Δ	pOPINEneo	Yes	D3	Yes

3.4 Small Scale Expression and Detergent Screening of SilP constructs

3.4.1 Small Scale Expression and Purification

E.coli and *Flavobacterium* constructs of SilP, that were successfully cloned and verified in the previous section, were expressed on a small scale to ascertain their expressibility and respective yields. Small-scale expression and purification followed the method outlined in Section 2.5.1

using *E. coli* strains: Rosetta, LEMO21, BL21-pLysS, C43 and C41. Following extraction and purification in DDM, the constructs were analysed through in-gel fluorescence and FSEC (see Section 2.5.1 for method). The results of the in-gel fluorescence can be seen in Figures 3.4.1 and 3.4.2, with the former figure a coomassie stained gel showing all the proteins present in the purification.

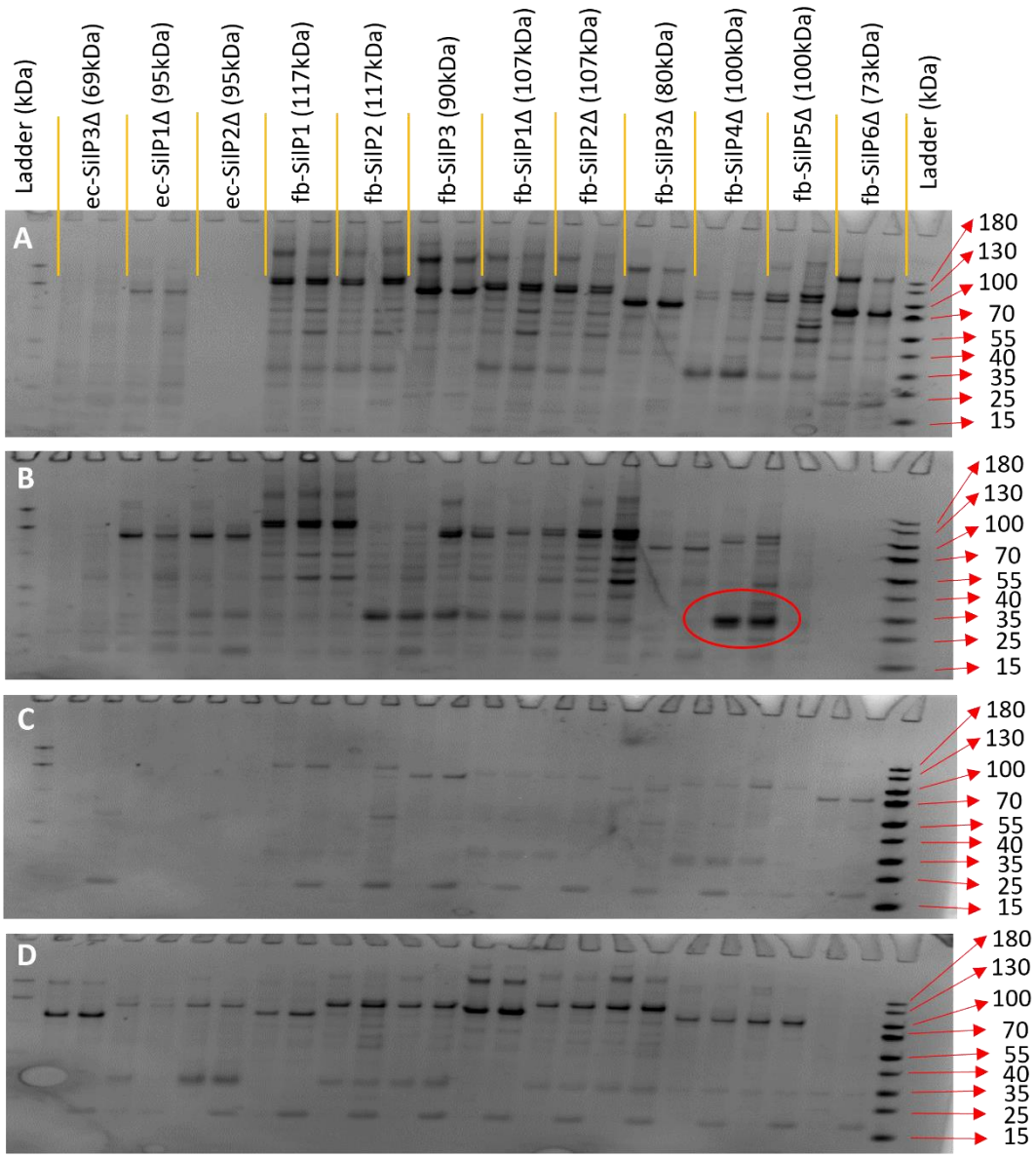

Figure 3.4.1: Coomassie stained gel of various *E.coli* and *Flavobacterium* constructs of SilP cloned retrieved from IMAC purification, see Table 3-1. Constructs are labelled in each lane with their expected Mw. Constructs were grown in Rosetta **(A)**, LEMO21 **(B)**, C43 **(C)** and BL21-pLysS **(D)**. Compared to the in-gel fluorescence (Figure 3.4.2) more bands can be seen in each lane showing the contaminants brought through, as well as the free GFP (highlighted with Red circle). Constructs of SilP that did not contain a GFP tag can be seen in this gel.

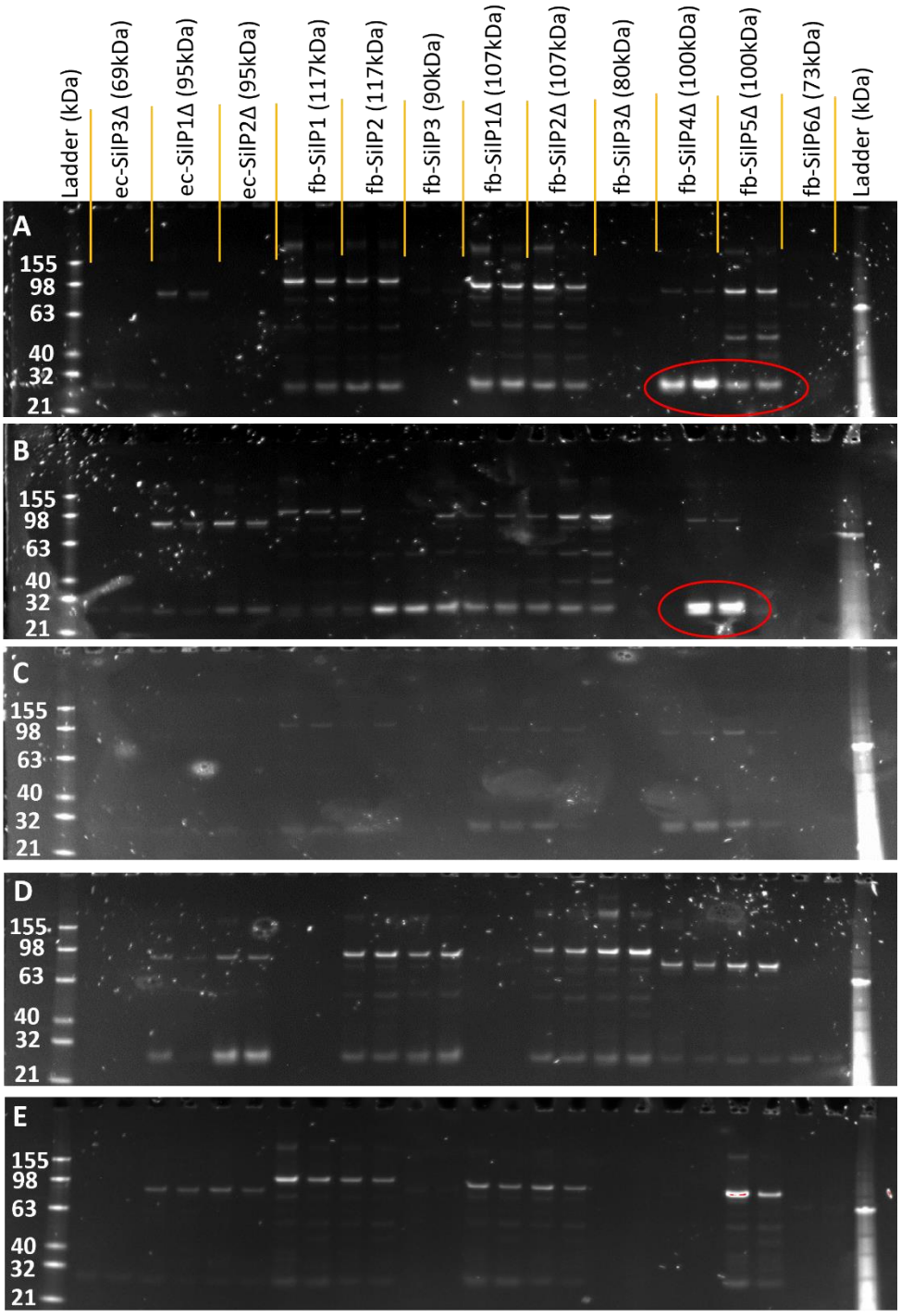

Figure 3.4.2: GFP in-gel fluorescence gels of various *E.coli* and *Flavobacterium* constructs of SilP cloned, following the layout as Figure 3.4.1 with Rosetta **(A)**, LEMO21 **(B)**, C43 **(C)**, BL21-pLysS **(D)** and C41 **(E)**. Most constructs showed expression in at least one cell line. Many of the constructs showed SilP degradation with a GFP band appearing at approximately 27 kDa (Red circle).

Both gels show that many of the constructs express well, with intense bands on the Coomassie stained and in-gel fluorescence gels. The in-gel

fluorescence gels also show that many of the constructs show degradation of SilP, resulting in free intact GFP as evident from a band appearing at 27 kDa.

The fluorescence values for most of the proteins indicates a good level of expression, fluorescence values above 100,000 were deemed to be of good as it was above background levels. Full-length constructs of SilP, from both species, eluted at 8.5 mL with truncated versions eluting slightly later at approximately 9.0 mL. The FSEC profiles showed two monodisperse peaks one for the SilP constructs, and the other eluting at 10.5 mL for free GFP, which corroborates with the gel images.

Based on both the FSEC data and in-gel fluorescence gels 12 constructs, were selected based on their FSEC profile and band intensities on the gels, see Table 3-2 for the chosen constructs.

Table 3-2: Constructs of SilP with the best expression levels. Constructs will be used for a 12 detergent screen. (*) denotes non-GFP protein

Cell type	Construct	Fluorescence count
Rosetta	FL fb-SilP1	40 000
	FL fb-SilP2	50 000
	FL fb-SilP3	38 000 *
	Trunc (A93) fb-SilP1Δ	80 000
	Trunc (A93) fb-SilP2Δ	40 000
	Trunc (A93) fb-SilP3Δ	78 000 *
	Trunc (M160)fb-SilP5Δ	90 000
LEMO21	Trunc (T154) ec-SilP2Δ	550 000
	Trunc (T154) ec-SilP1Δ	500 000
C41	Trunc (T154) ec-SilP1Δ	1 250 000
	FL fb-SilP3	500 000 *
	Trunc (M160) fb-SilP5Δ	2 000 000

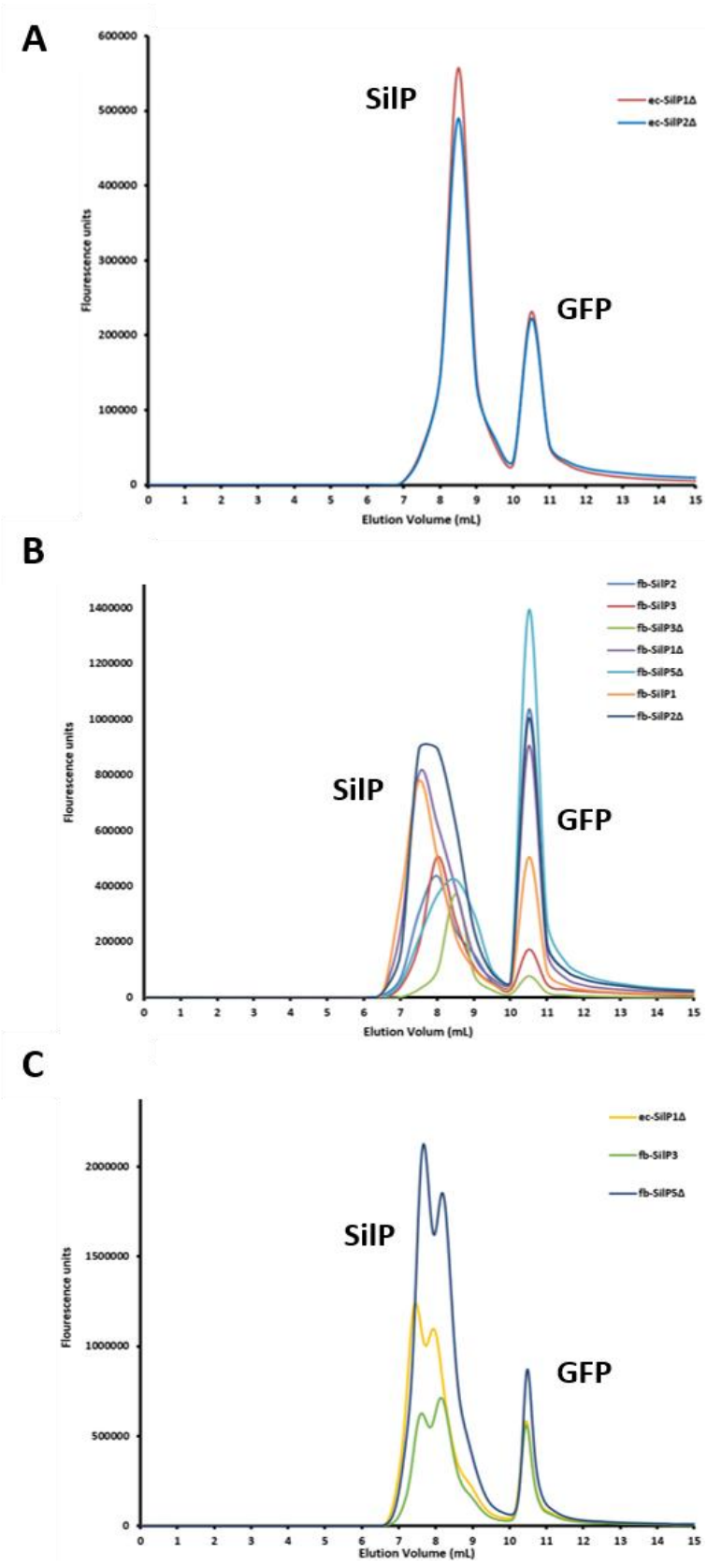

Figure 3.4.3: FSEC traces of the 12 best constructs from different *E.coli* strains. Constructs were picked based on the fluorescence values and trace profile. **(A)** LEMO21 cell line, **(B)** Rosetta cell line and **(C)** C41 cell line.

3.4.2 Detergent Screening of SilP constructs

The 12 constructs identified from Section 3.4.1 were expressed again but purified using the method outlined in Section 2.5.2, this method solubilised expressed SilP protein in 12 different detergents. The aim of the screen being to identify the detergent that gives the best protein yield and stability, as assessed through in-gel fluorescence and FSEC.

The in-gel fluorescence gels (Figure 3.4.4) of the detergent screen showed that most of the constructs expressed and purified well, with bands appearing at the correct molecular weights (somewhere between the 98 and 155 kDa marker). The gels showed that there was some degradation of SilP in some constructs, with free GFP present (Figure 3.4.4 panels A1, B2, C2, D2 and F2), as observed before, however this was to a lesser extent with 5 out of the 12 constructs showing degradation. The coomassie stained version of these gels (Figure 3.4.5) show that other than the expected protein and any degraded GFP, the samples were clean with some limited lower molecular weight contaminants. These gels also show more clearly the expression level of the non-GFP tagged constructs (Panels B1, C1 & E1).

From both sets of gels (Figures 3.4.4 and 3.4.5) two of the constructs (fb-SilP1 and 2) did not express at all, with no expected protein band or only a GFP band present, this was shown in both the in-gel and coomassie stained gels. The remaining samples for each construct were analysed by looking for the brightest intensity band, with the correct Mw, on both gels. For each construct a single detergent was selected, this is shown in Figure 3.4.6, and applied to the FSEC column for further characterisation.

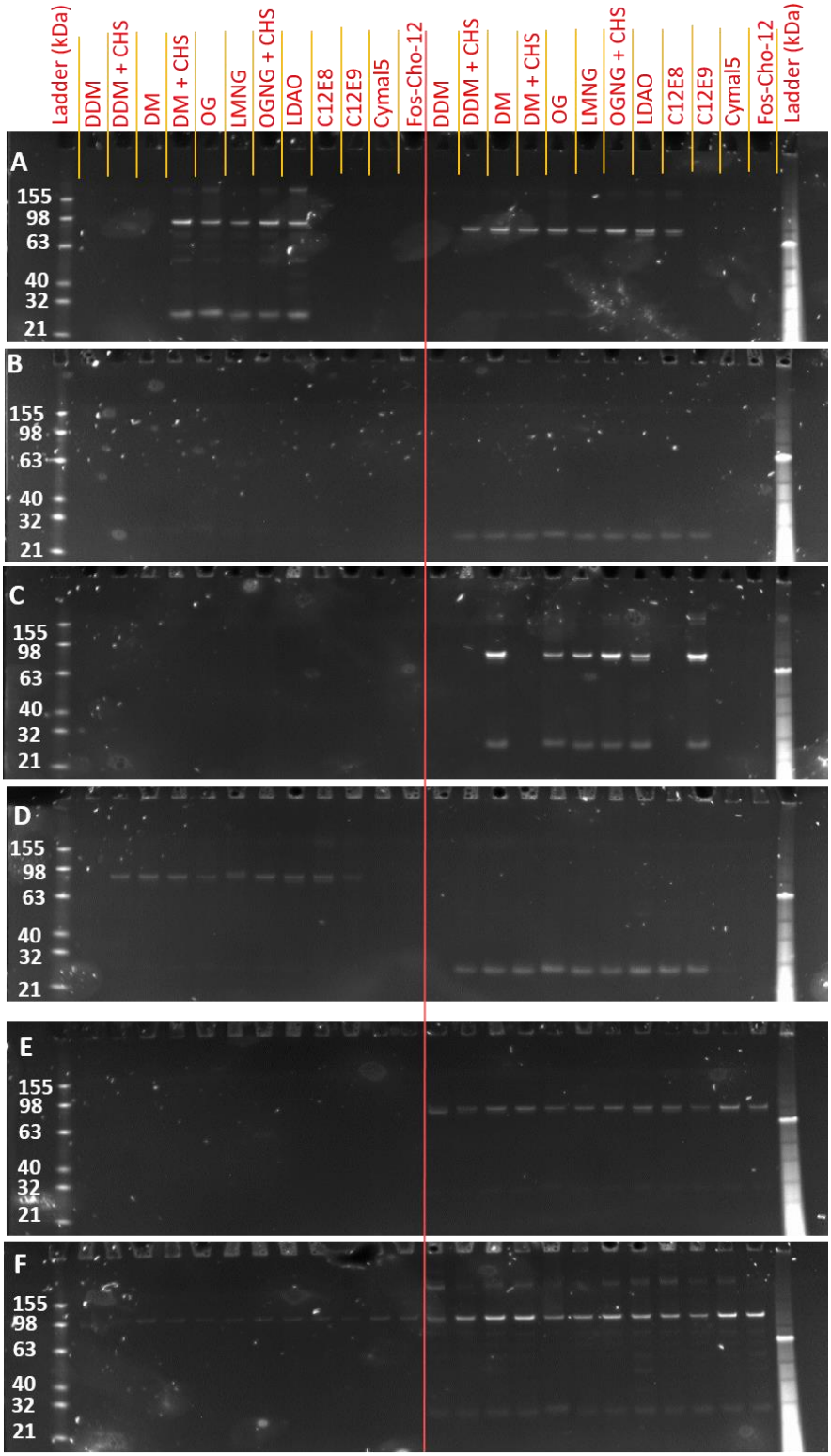

Figure 3.4.4: GFP in-gel fluorescence gels of SilP constructs in different detergents from optimised *E.coli* strains (L-LEMO21, R-Rosetta and C-C41). Left and Right side of each gel respectively; **(A)** L ec-SilP2Δ (95kDa) & R fb-SilP2Δ (95kDa), **(B)** R fb-SilP3 (90kDa) & R fb-SilP2 (117kDa), **(C)** C fb-SilP3 (90kDa) & L ec-SilP1Δ (95kDa)**, (D)** R fb-SilP1Δ (95kDa) & R fb-SilP5Δ (100kDa)**, (E)** R fb-SilP3Δ (80kDa) & C ec-SilP1Δ (95kDa) and **(F)** R fb-SilP1 (117kDa) & C fb-SilP5Δ (100kDa).

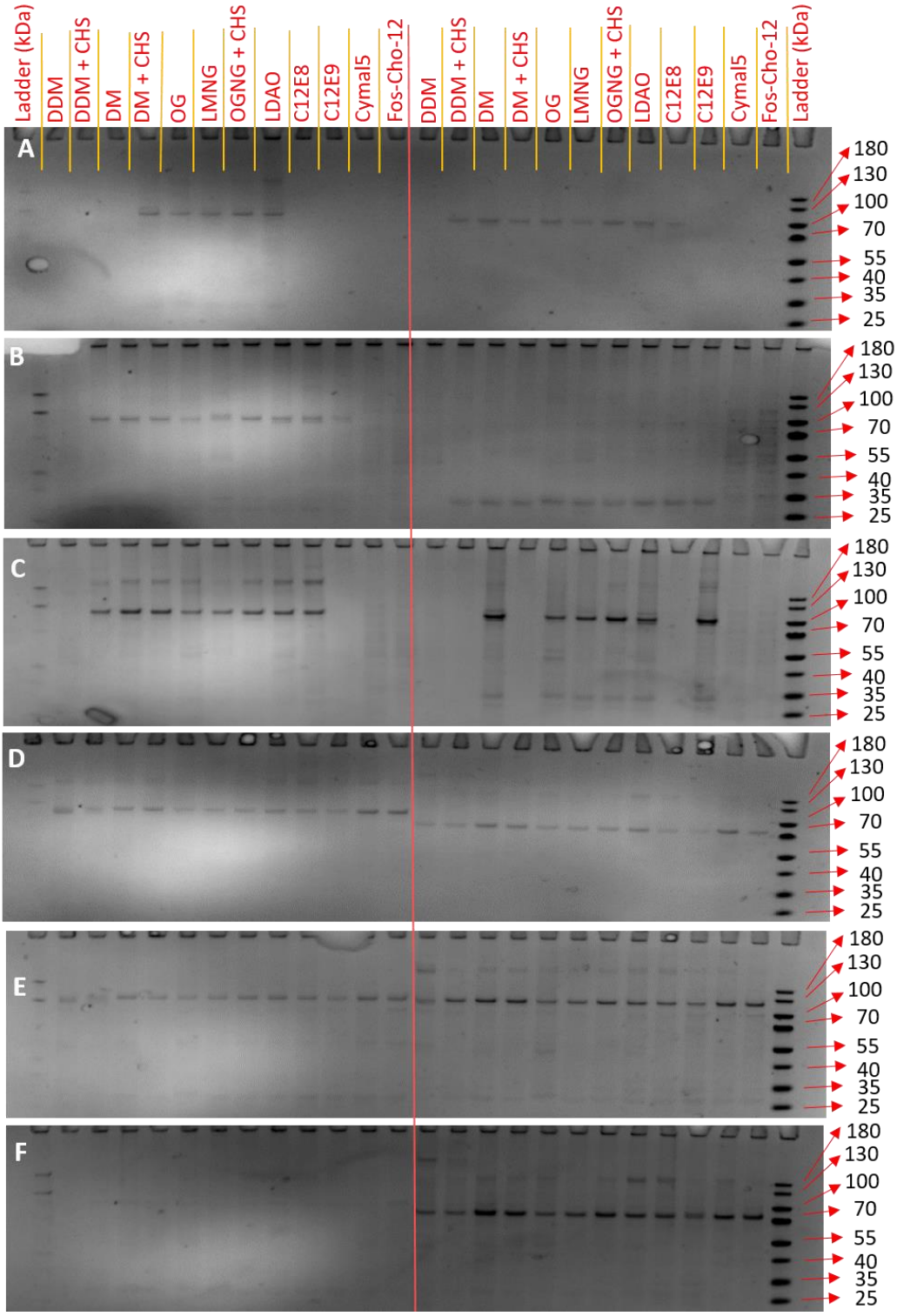

Figure 3.4.5: Coomassie stained versions of the GFP in-gel fluorescence gels from Figure 3.4.4. Showing the different cell line expressed constructs (L-LEMO21, R-Rosetta and C-C41) and the detergent screen. Left (L) and Right (R) side of each gel respectively; **(A)** L ec-SilP2Δ (95kDa) & R fb-SilP2Δ (95kDa), **(B)** R fb-SilP3 (90kDa) & R fb-SilP2 (117kDa), **(C)** C fb-SilP3 (90kDa) & L ec-SilP1Δ (95kDa)**, (D)** R fb-SilP1Δ (95kDa) & R fb-SilP5Δ (100kDa)**, (E)** R fb-SilP3Δ (80kDa) & C ec-SilP1Δ (95kDa) and **(F)** R fb-SilP1 (117kDa) & C fb-SilP5Δ (100kDa).

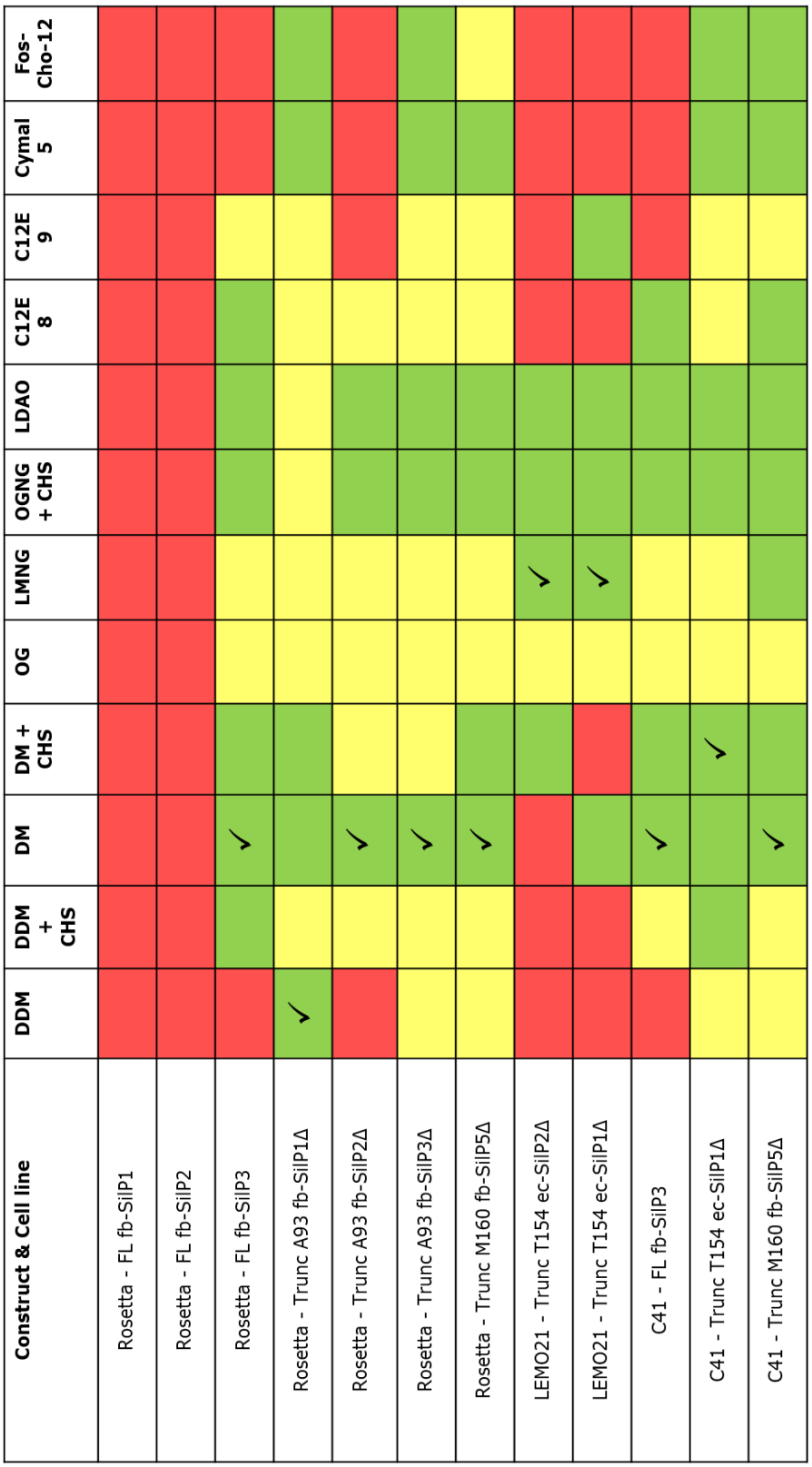

Figure 3.4.6: Colour chart of the detergent screen for each construct. Colours denote the amount of expression of a given construct, no expression (Red), limited expression (Yellow) and over expression (Green). Expression was denoted based on the band intensity from both gels. The best detergent for each construct were assigned a tick and subsequently analysed with FSEC.

The FSEC GFP-profiles (Figure 3.4.7) of the selected constructs and their respective detergents, based on Figure 3.4.6, showed two monodisperse peaks; one for the SilP construct and the other for free GFP. As in Figure 3.4.3, the free GFP peak eluted at 10.5 mL for all constructs.

As all the constructs were truncated forms (Mw between 100 or 107 kDa) of *E.coli* or *Flavobacterium* homologs of SilP the elution peaks were consistent, with elution occurring between 8-9 mL (peaks labelled SilP in Figure 3.4.7). All SilP constructs, except Rosetta fb-SilP2Δ and C41 SilP1Δ, showed sharp monodispersed peaks, indicating single monodispersed protein. The two constructs, Rosetta fb-SilP2Δ and C41 SilP1Δ (Figure 3.4.7 panels B & C respectfully), showed a broader shouldered peak. The main peak eluted between 8.5 mL as the other constructs, however had an earlier shoulder peak between 7.0 mL. The earlier peak suggests the presence of a larger protein component possibly a dimer, see Section 3.8.2 for further discussion.

Based on the FSEC profiles the construct ec-SilP1Δ in LMNG was selected for further expression and characterisation. Selection of the construct was based off the high fluorescence values (~280,000 units) indicating good expression, a value below ~70,000 units is considered low expression. In addition, the presence of less free GFP suggests a more stable protein that doesn't degrade.

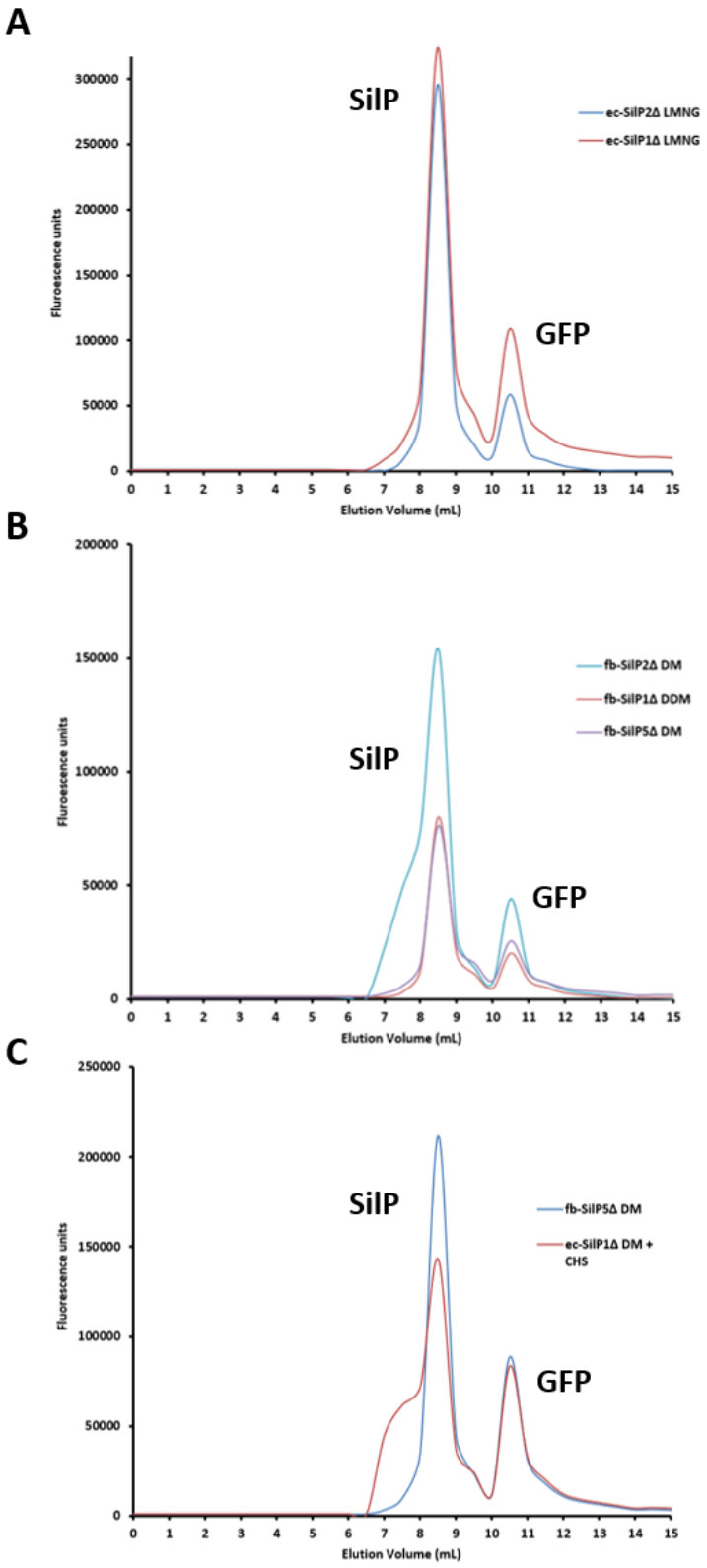

Figure 3.4.7: FSEC fluorescence traces for the selected constructs and their best detergents, based off Figure 3.4.6. Constructs grown in LEMO21 **(A)**, Rosetta **(B)** and C41 **(C)** cells showed for the most part 2 main peaks. Peak 1 (8.5 mL) elutes at the volume corresponding to Mw of the truncated SilP constructs. Peak 2 (10.5mL) is indicative of free GFP.

3.4.3 Large Scale Expression of ec-SilP1Δ

The expression plasmid of ec-SilP1Δ with a C-terminal GFP-6xHis-tag was transformed in LEMO21 *E.coli* cells (according to Section 2.2.1). Expression followed the protocol outlined in Section 2.5.3. Cell pellets were either used for purification straight away or were stored at -80 °C.

3.4.4 Large Scale Purification of ec-SilP1Δ

Cells containing ec-SilP1Δ were lysed and membranes prepared using the 2 or 3 stage method outlined in Section 2.5.3.

The initial affinity chromatography step is uniform to both the 2 or 3 step purification method. The binding of ec-SilP1Δ to the Strep-Tactin XT GFP nanobody column was successful with the column turning green as the sample bound. The subsequent elution, 3C-protease cleavage and reverse Ni^{2+} IMAC proved successful in obtaining a cleaved clean ec-SilP1Δ. Samples of each step were taken and analysed on a SDS-PAGE gel (Figure 3.4.8) to ascertain the presence of ec-SilP1Δ and if the GFP has been cleaved off. The SDS-PAGE gel showed ec-SilP1Δ was present, with a band around the 100 kDa MW marker. After the addition of the 3C-protease and reverse IMAC, a band for the cleaved ec-SilP1Δ was evident at the 75 kDa MW marker. The purity of the protein at this point was >90%.

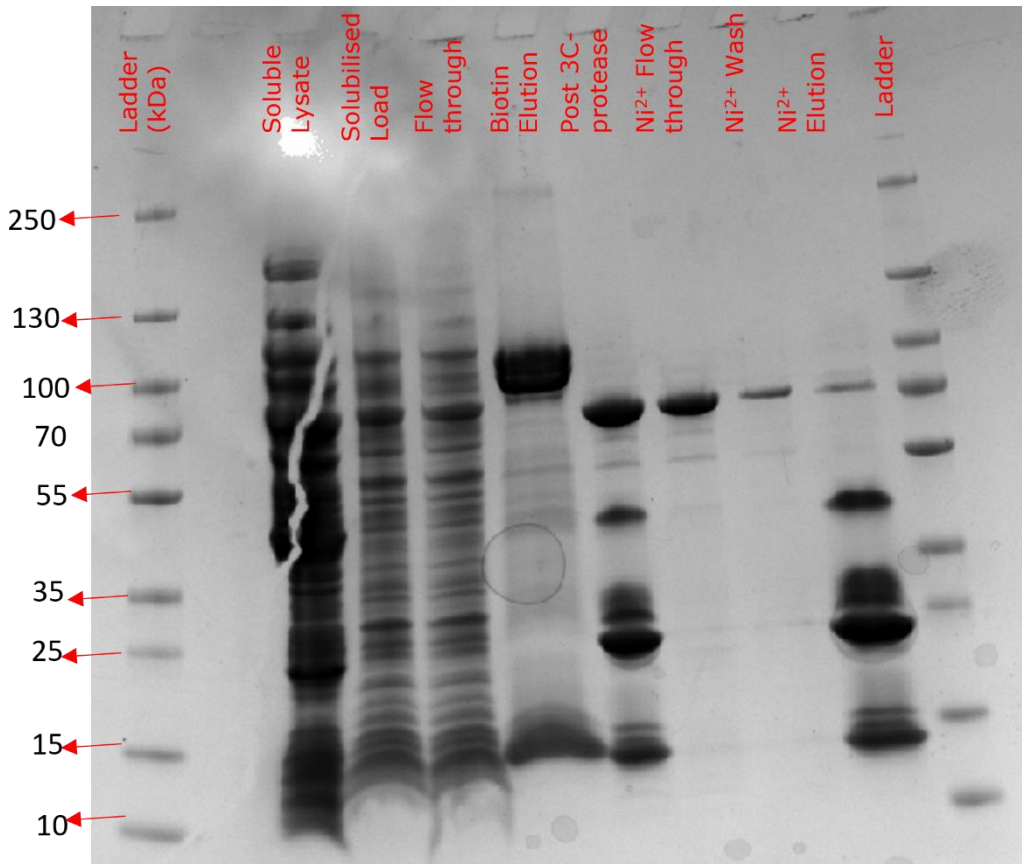

Figure 3.4.8: SDS-PAGE gel of ec-SilP1Δ after each step of the affinity chromatography purification. Initially there are a lot of contaminants in the sample, however after the GFP nanobody elution step and the subsequent cleavage and reverse IMAC steps the ec-SilP1Δ samples are >90% pure. Clean, cleaved, ec-SilP1Δ can be seen in the Ni^{2+} flow through and wash lanes.

Following the nanobody purification step, ec-SilP1Δ in most cases was subjected to a sucrose gradient clean-up to remove the excess LMNG micelles. The results of the gradient clean up gave identical bands on a SDS-PAGE gel as the reverse IMAC Ni^{2+} flow through and elution fraction in Figure 3.4.8. As there is no method for determining if the detergent micelle has been removed it is assumed.

Following either reverse IMAC or a sucrose gradient, samples of ec-SilP1Δ were applied to a SEC column using the method outlined in Section 2.5.5. The 280 nm absorbance profile (see Figure 3.4.9-A below)

showed a large initial peak (Peak 1) at 10 mL which suggests a large protein or protein complex was present. Based on the SDS-PAGE from previous steps it was hypothesised that this was a dimer as the Mw of a protein eluting at that volume would be >200 kDa. The main peak (Peak 2) of interest occurred at approximately 11.5 mL, this elution point is indicative of a protein with a Mw of ~150 kDa of which ec-SilP1Δ would be by taking the detergent micelle into account. There was also evidence of lower molecular weight contaminants through the broad peak base. Fractions from Peaks 1 and 2, as well as some later eluting fractions, were analysed down a SDS-PAGE gel (Figure 3.4.9-B). Fractions from peak 1 were shown to be composed primarily of ec-SilP1Δ, with a band at 75 kDa, however there were faint bands higher up at ~250 kDa which may support the dimer prediction. Peak 2 (11.5 mL) showed only the presence of ec-SilP1Δ with a single band at 75 kDa. Fractions from the later trailing peak showed some ec-SilP1Δ but mainly contaminants that had been brought through. The concentration of the fractions corresponding to monomeric ec-SilP1Δ were measured on the nano-drop and ranged between 0.4 mg/mL on the trailing sides and 0.8 mg/mL at the apex fractions, the overall purity of ec-SilP1Δ was >95% based off the SDS gel.

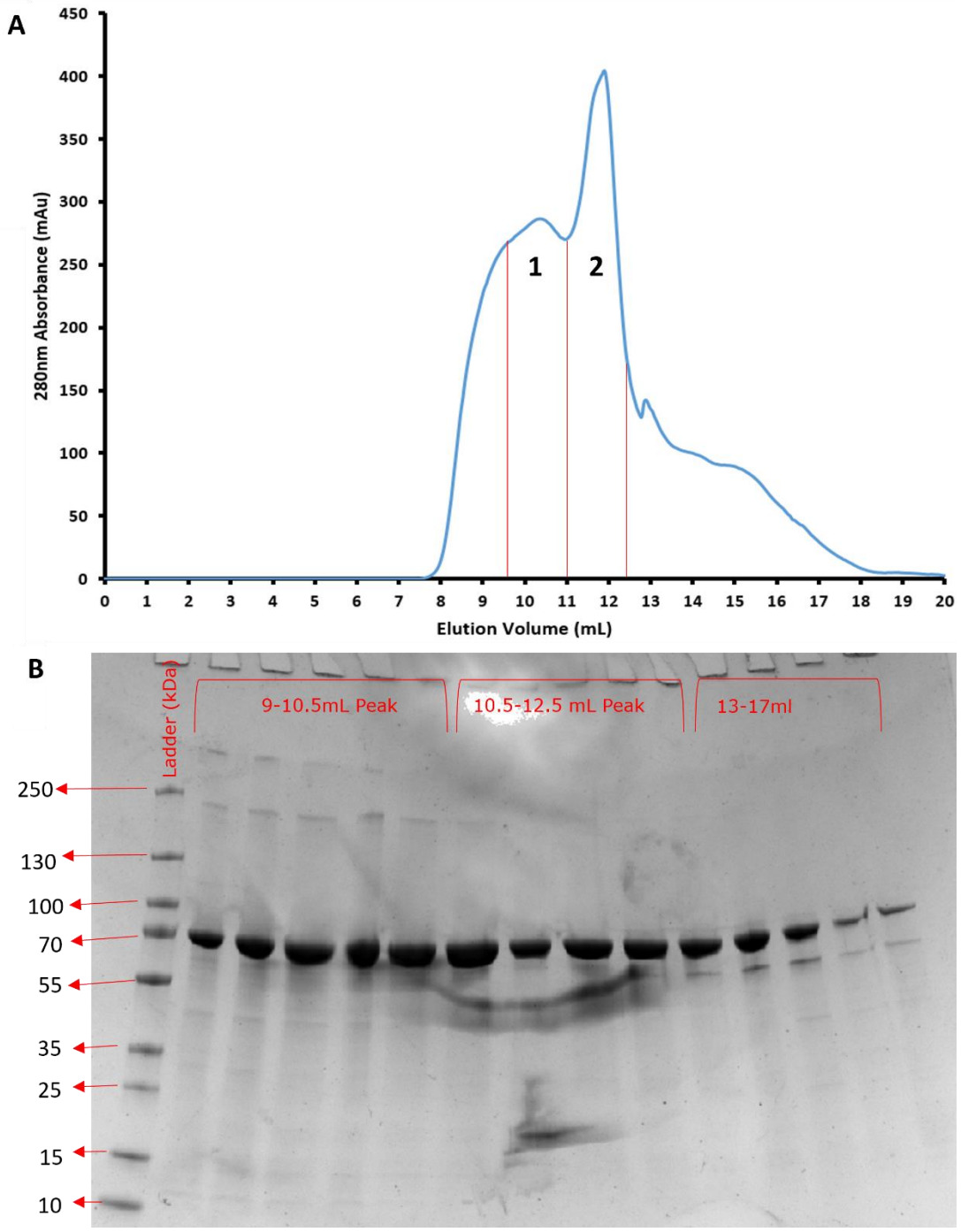

Figure 3.4.9: (A) Absorbance (280 nm) profile of ec-SilP1Δ after SEC was conducted. An initial broad peak between 10 mL suggests the presence of a dimeric ec-SilP1. The main peak at 11.5 mL indicates the presence of monomeric ec-SilP1Δ. **(B)** SDS-PAGE gel of the peaks from the ec-SilP1Δ SEC. the initial broad peak shows the presence of ec-SilP1Δ suggesting higher a Dimer was present. The main peak shows clean ec-SilP1Δ at a reasonable band intensity indicating a good yield of protein.

3.5 Biophysical Characterisation

3.5.1 SEC-MALLS determination of the oligomeric state of ec-SilP1Δ

Following expression and purification ec-SilP1Δ, characterisation was conducted using SEC-MALLS with the method outlined in Section 2.7.2. From the purification the main peak corresponding to ec-SilP1Δ was injected onto the column for analysis. Figure 3.5.1 shows the Rayleigh scattering, UV absorbance (280 nm) and molecular weight estimations for the ec-SilP1Δ sample.

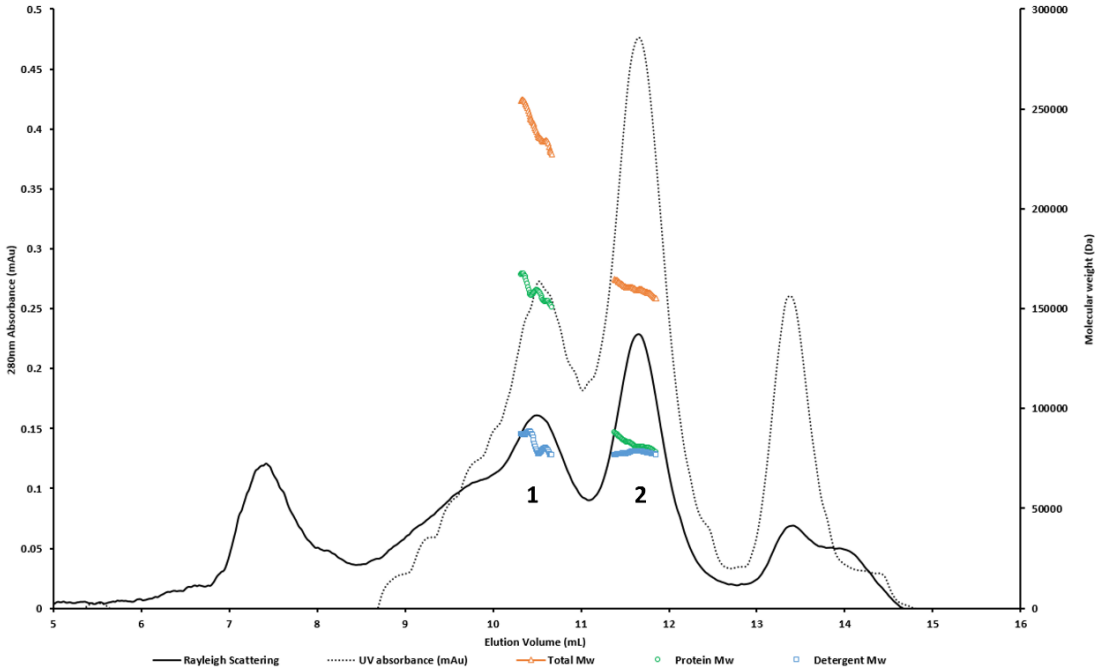

Figure 3.5.1: SEC-MALLS profile of ec-SilP1Δ with Rayleigh Scattering and UV 280 nm traces shown. Overall Mw (Orange), protein Mw (Green) and detergent Mw's (Blue) are shown for each peak using conjugate analysis.

The results from the SEC-MALLS with all optical data sets showed that there were four main peaks. A void volume peak (7.5 mL for a S200 10/300 Superdex column) suggested aggregated material was present. The next peak (peak 1) eluted at 10.5 mL which is consistent with Peak 1 seen during purification (Figure 3.4.9-A). The second peak of interest

elutes at 11.5 mL which is again consistent with that seen during purification, indicating the presence of monomeric ec-SilP1Δ. The final peak 3 is a broader peak with 2 apexes.

Molecular weight estimations of peaks 1 and 2 utilised conjugate analysis, a method for distinguishing between two components of a single peak (see Section 2.7.2 for more information). In the case of SilP the two components were the protein itself and the detergent LMNG. Through conjugate analysis the overall molecular weight of peak 1 was estimated to be 238 kDa, with the protein Mw component estimated to be 149.3 kDa and a detergent Mw of 89 kDa. Using the actual Mw of ec-SilP1Δ (75 kDa) this suggests that the peak corresponds to a dimer of ec-SilP1Δ. Peak 2 on the other hand had an overall Mw estimation to be 159.9 kDa, with a protein Mw of 76.6 and a detergent Mw of 83.2 kDa. These molecular weights suggests that monomeric ec-SilP1Δ is present. The molecular weight estimations from conjugate analysis are presented in Table 3-3.

Table 3-3: SEC-MALLS Mw estimation using conjugate analysis of the two main peaks of interest (Peak 1 and 2). Molecular weight estimations indicate the presence of monomeric and dimeric ec-SilP1Δ.

SEC-MALS Output	Peak 1 (Dimer)	Peak 2 (Monomer)
Co-polymer Mw (kDa)	238 (±0.70%)	159.9 (±0.40%)
Protein Mw (kDa)	149.3 (±0.80%)	76.6 (±0.44%)
Detergent Mw (kDa)	89 (±2.30%)	83.2 (±1.05%)
Polydispersity (Mw/Mn)	1.005	1.001

3.5.2 Nano-DSF Stability Assay

The stability of ec-SilP1Δ was assessed through nano-DSF, using the method outlined in Section 2.6.3 with a protein concentration of 1.0 mg/mL. The results of the assay based on the 330/350 nm ratio can be seen in Figure 3.5.2 and Table 3-4.

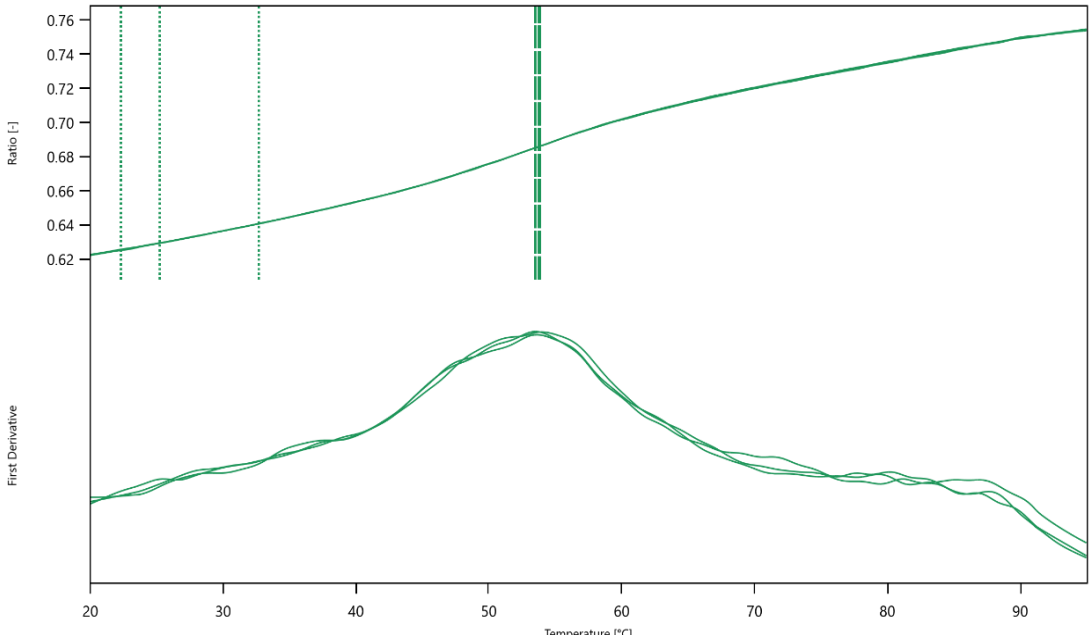

Figure 3.5.2: Nano-DSF of ec-SilP1Δ showing the 330/350 ratio with the T_m shown to be 53.7 °C

Table 3-4: Onset and T_m of ec-SilP1Δ based off the results from the nano-DSF. The low onset temperature suggest that the protein may be unstable.

ec-SilP1Δ Sample	Onset Temperature (°C)	Melting Temperature, T_m (°C)
1	25.2	53.9
2	23.5	53.5
3	22.3	53.7
Average	23.7	53.7

The results of the assay show that ec-SilP1Δ had an early onset temperature of 23.7 °C suggesting that the protein may be unstable. Based on the 330/350 nm ratio the T_m was shown to be 53.7 °C ±0.2 °C.

3.6 Activity Assays of SilP

Activity assays of ec-SilP1Δ in LMNG utilised the end point ADP-Glo Assay Kit (Promega, UK), see Section 2.7.8 for the methodology.

Assays were carried out in both the presence and absence of Cu(I), with assays containing Cu(I) conducted under anaerobic conditions in a glove box to stop oxidation of Cu(I) to Cu(II). Luminescence readings were converted into ADP usage, using the calibration curve, and plotted in

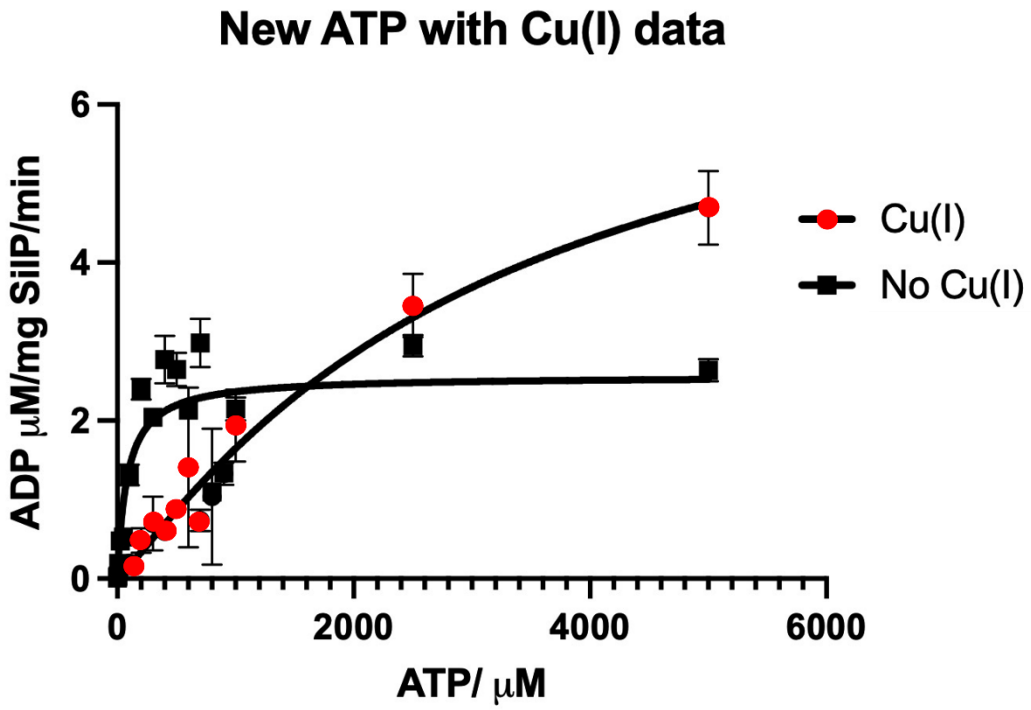

Figure 3.6.1: ADP-Glo assay results of ec-SilP1Δ with (Red circle) and without Cu(I) (Black square), showing the amount of ADP produced per mg of ec-SilP1Δ per minute. Data was fitted using the equations in Equation 3.1(A-C), giving the fitted curves seen above.

Prism with the plot shown in Figure 3.6.1.

Initial data analysis used the Michaelis-Menten model to determine the V_{max} of both conditions (Equation 3.1A). Once the V_{max} was determined the K_{cat} (turnover number) was determined using an extended form of the previous equation (Equation 3.1B). Following on from this the

A $$Y = (V_{max} \times X) / (K_m + X)$$

(Where Y is enzyme velocity, X is [substrate], V_{max} is maximum velocity and Km is [Substrate] at ½ V_{max}.)

B $$Y = ((Et \times K_{cat}) \times X) / (K_m \times X)$$

(Where Y is enzyme velocity, X is [Substrate], K_{cat} is turnover number, K_m is the [Substrate] at ½ V_{max} and Et is the [enzymatic catalytic sites].

C $$Y = (V_{max} \times X^h) / (K_{half}^h + X^h)$$

(Where Y is enzyme velocity, X is [substrate], V_{max} is maximum velocity, K_{half} is the [Substrate] that produces half-maximal enzyme

Equation 3-1: (A) The Michaelis-Menten equation used for determining the velocity of a reaction. **(B)** Extension if the Michaelis-Menten equation used for determining the turnover number (K_{cat}) of reaction. **(C)** Equation used for allosteric sigmoidal models, of which SilP is believed to adopt.

sigmoidal fitting of the data was also calculated following Equation 3.1C

The data from the assay shows that apo ec-SilP1Δ reached a maximum saturation point, with approximately 2.3 μM of ADP produced per mg of ec-SilP1Δ per minute. Whereas in the presence of Cu(I) the reaction, although not reaching a maximum, showed an approximate 2-fold increase in the amount of ADP produced. Using Prism to plot and extrapolate the data, a V_{max} of ~7.6 μM of ADP produced per mg of ec-SilP1Δ per minute was determined. This shows that the protein is roughly 2.5x as active when the target ligand is present.

Additionally, the K_m ([substrate] at ½ V_{max}) from the data shows that ATP affinity is weaker in the Cu(I) addition data, however as the data is incomplete this is an estimation. The catalytic rate for both runs were the same with a K_{cat} of ~1.03 ATP/min turnover, suggesting that although in the presence of Cu(I) the amount of ATP turnover is greater, the rate at which it converts ATP is the same as when Cu(I) is not present. Tabe 3-5 shows the data from the data interpretation.

Table 3-5: ADP-Glo assay result for SilP with and without Cu(I) present.

	Apo-SilP	SilP + Cu(I)
V_{max} (μM ADP/mg SilP/min	2.316	7.630
K_{cat} (ATP/s^{-1})	1.026	1.030
K_m (μM)	84.4	7900

3.7 Towards the determination of ec-SilP1Δ structure using Cryo-EM

The ability to express ec-SilP1Δ to a level and purity, >1 mg at 95% purity, allows for structural analysis to be conducted. The recent advances of Cryo-EM, through the production of better detectors, made it a better method for trying to solve a structure of ec-SilP1Δ as opposed to crystallography which is inherently difficult for inner membrane proteins.

3.7.1 Negative Stain Imaging and 2D classification

Negative stain grids of ec-SilP1Δ in DDM and LMNG were prepared with subsequent imaging and data collection conducted using a JEOL JEM-2100 TEM microscope, see Section 2.9.1 for the method.

Initial imaging of grids of ec-SilP1Δ at 0.01 mg/mL in DDM showed micrographs (Figure 3.7.1 C & D) that contained particles (white blobs with black outline) that measured roughly 20 nm in size. Particle density was low and there was evidence of aggregation with large blobs present, there was also evidence of detergent micelles with small circular particles present (Figure 3.7.1-D).

In comparison the micrographs of ec-SilP1Δ in LMNG at 0.05 mg/mL were much better (see Figure 3.7.1-**A/B**), there was a higher number of particles that appeared to be mainly homogeneous with limited aggregation. The particles measured roughly 20 – 30 nm in size and there appeared to be a number of different shaped particles suggesting different orientations.

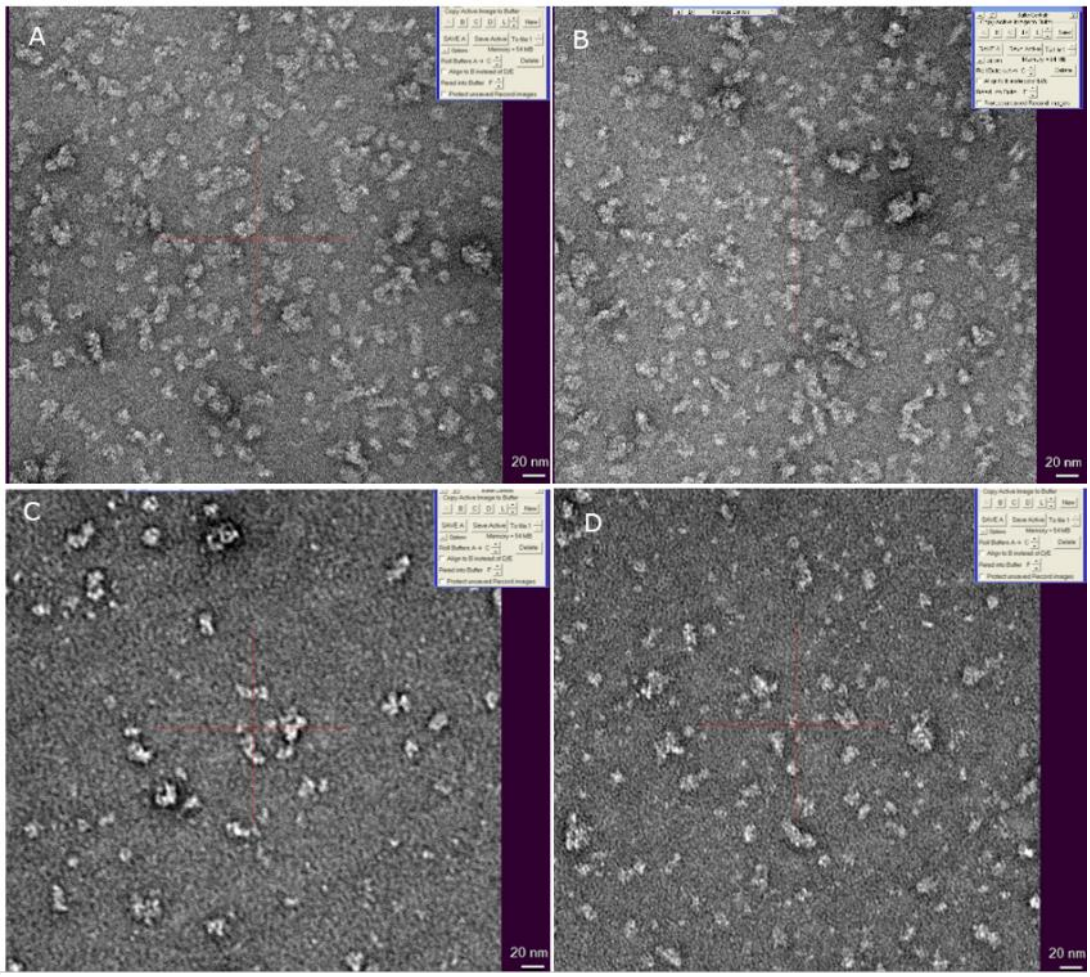

Figure 3.7.1: Negative stain images of ec-SilP1Δ in LMNG at 0.05 mg/mL (**A** & **B**) and DDM at 0.01 mg/mL(**C** & **D**). Particle distribution was better in LMNG than in DDM, with less aggregation also present.

Based on the imaging micrographs a data collection of the 0.05 mg/mL ec-SilP1Δ LMNG grid was set up with a 60 micrographs collected (see Section 2.9.1). The data collection micrographs were subsequently analysed in RELION3.1 which picked the individual particles in each micrograph, for these grids that was approximately 130 particles per micrograph. A total of ~8000 particles were correlated and compared to each other using RELION3.1, looking for common orientations, to produced 2D classifications. Figure 3.7.2 shows the 2D classification that Relion3.1 produced of ec-SilP1Δ from all the particles identified.

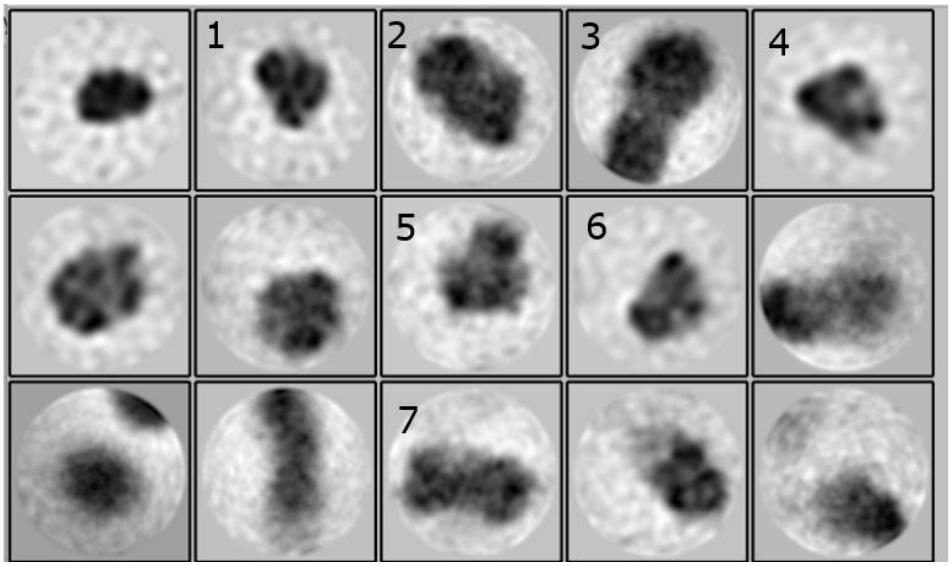

Figure 3.7.2: 2D classes of ec-SilP1Δ in LMNG. Images numbered are believed to be ec-SilP1Δ in different orientations. Numbered are the best 2D classes of what is believed to be ec-SilP1Δ illustrating different orientation.

The 2D classes produced by RELION3.1 showed several orientations of ec-SilP1Δ. Figure 3.7.2 panels 3 and 5 and 7 seem to show the best orientations with panel 3 showing what is believed to be a side on view, panel 5 a top-down view with possibly the 3 cytoplasmic domains (N, P and A, see Section 1.4) observable. Panel 7 possible shows another side view of the protein or potentially a top-down view of a dimer. Based on the particle distribution and the 2D classes that were produced further analysis of ec-SilP1Δ in LMNG was conducted with Cryo-EM grids prepared.

3.7.2 Cryo-EM Imaging and Data Collection/Analysis

Based on the particle distribution with the concentrations used in the negative stain images, Cryo-EM grids of ec-SilP1Δ were prepared as in Section 2.9.2 with a protein concentration of 0.8 mg/mL used. Grids were imaged using the Thermo Glacios Cryo-TEM microscope with a

Falcon 4 detector at EBic (Diamond Light Source), with the screening of several holes conducted (Figure 3.7.3-A/B). The samples appeared homogeneous on the grids with good particle distribution between each other. The shape of the samples different somewhat from the negative stain images in size with most of the particles having a size between 5-10 nm.

A data collection was set up over a 24 hour period with a total of 1500 micrographs recorded. As images were acquired they entered the automatic Relion3.1 pipeline on the eBIC servers. The pipeline automatically processes the micrographs, as was conducted for the negative stain grids, and produces 2D class averages (see Section 2.9.4 for method). Figure 3.7.3-C shows the 2D classes from the Cryo-EM grids of ec-SilP1Δ in LMNG. Observation of the 2D classes shows that there is a lot of spherical like particles which would suggest a top-down or bottom-up conformation, there is limited side on views of the product. This suggests that there is a lot of preferential orientation occurring within the sample. There is also evidence of dimers being present within the sample, based on SEC-MALLS this is to be expected. The dimers appear as two small spheres close to each other which would suggest they are in the same detergent micelle.

The presence of preferential orientation of the sample within the grid meant that no further analysis was conducted to produce a 3D model as there was not enough data.

Further sample production and grids were needed however, time constraints meant that this was not possible within the time allocation of the PhD.

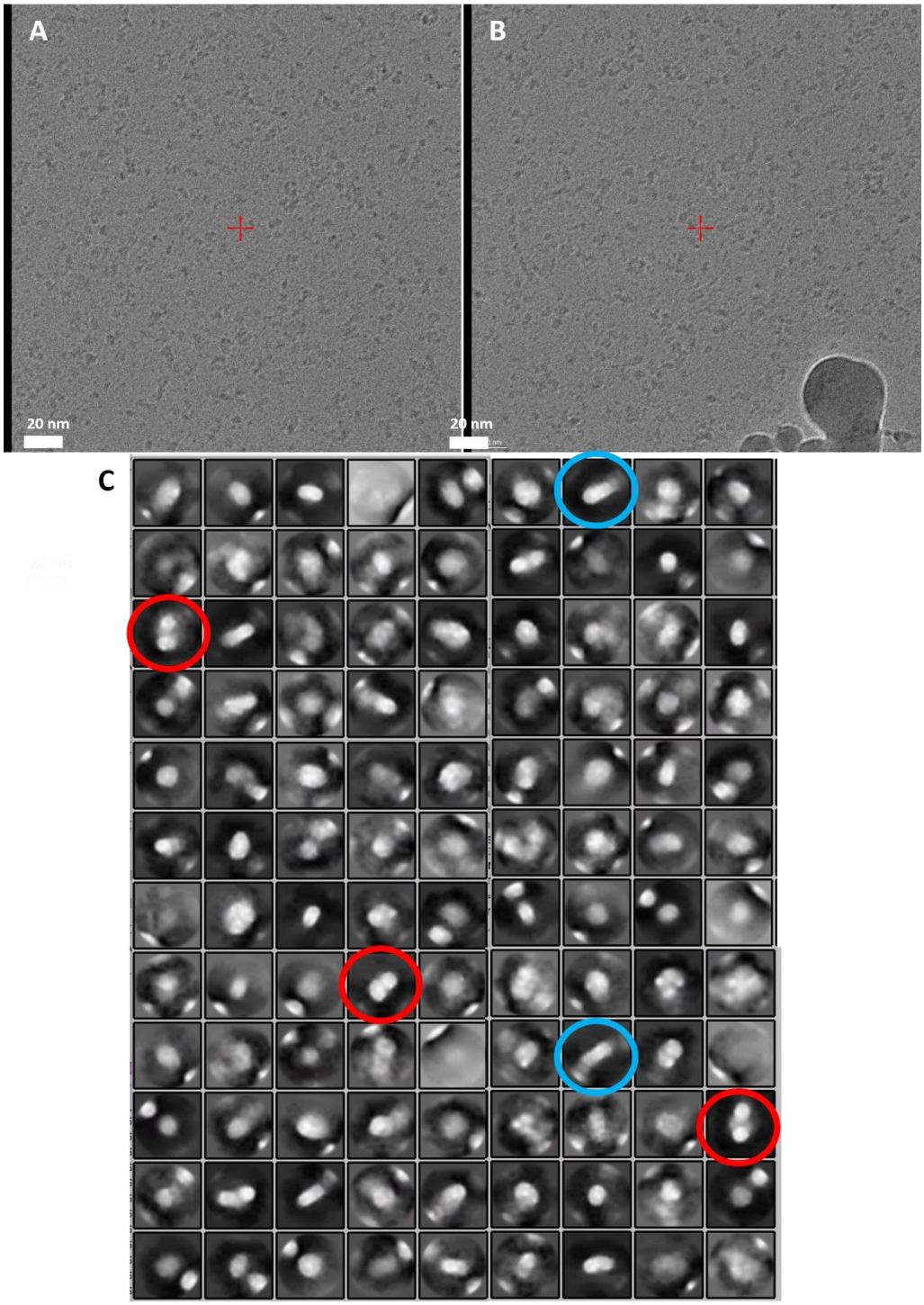

Figure 3.7.3: (A & B) Cryo-EM screening images of ec-SilP1Δ in LMNG from the Glacios TEM. Each panel shows a different grid hole take from different grid squares of a single grid. Panel **B** has a contaminant in the bottom right corner, the other panels show clean sample. **(C)** 2D classes of SilP1Δ in LMNG imaged on the Glacios TEM, classes were based ~800,000 particles. The classes show a lot of preferential orientation for a top-down / bottom-up view of the protein, with a few classes suggesting a side on view (circled Blue). There is evidence of SilP1Δ dimers being present (circled in Red) within the samples.

3.8 Discussion and Future Work

3.8.1 Cloning of SilP constructs

Previous purification and characterisation studies of SilP, from *Klebsiella pneumoniae*, by Dr David Casas-Mao (Casas-Mao PhD thesis, Nottingham, 2018) showed that the levels of expression and purity of the protein were low, with structural characterisation impractical. In order to overcome this issue, new constructs of SilP from different species were identified with the hope of finding a construct that expresses and purifies to a level where structure determination could be conducted.

Initially four species homologs of SilP were identified from *E. coli, Flavobacterium, Citrobacter* and *Salmonella enterica*. The sequences of the homologs were ~50% similar with the greatest variability in the N-terminal HMBD domain, see Figure 3.8.1. Comparing the new sequences to the original *K. pneumoniae* the two species chosen for gene synthesis were the *E.coli* and *Flavobacterium* homologs. The *E.coli* homolog had a very similar sequence to that of the original (94%) with the natural 8 His-tag in the HMBD. The other *Flavobacterium* homolog had 47% sequence identity to the original *K. pneumoniae* sequence, however the core motifs were conserved (see Section 1.4). The variation in the N-terminal HMBD domain sequence posed an interesting observation as it may show how the protein varies in its binding to Ag(I)/Cu(I), as the natural His-tag of the other homologs is theorised to be involved in metal binding (Gupta *et al.,* 1999).

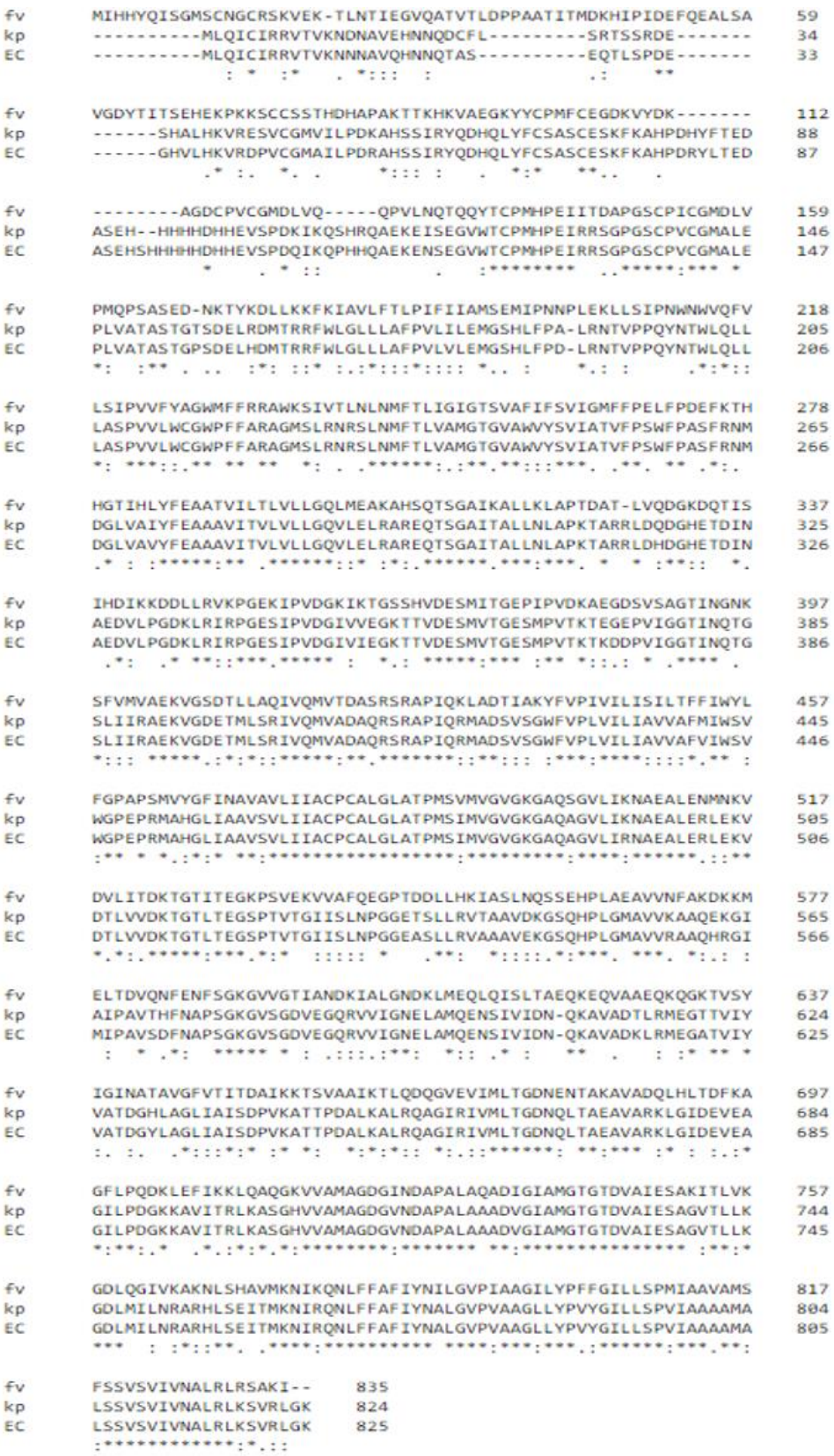

Figure 3.8.1: Sequence alignment of homologs of SilP from *E.coli* (**ec**), *Flavobacterium* (**fb**) and *Klebsiella pneumoniae* (**kp**). The sequence identity between *K.pneumoniae* and *E.coli* is high (~94%) with a lot of conserved regions between. Whereas the *Flavobacterium* sequence varies quite drastically to the other two homologs, with only a 47% identity.

The gene synthesis of the *E.coli* and *Flavobacterium* homologs, conducted by Twist Bioscience (USA), results in the overall gene (~2500 bp) was split into two halves (~1250 bp each) as this was cheaper than whole gene synthesis. Therefore, in order for cloning to be conducted an over lapping region of nucleotides, consisting of the construct sequence, between each half was added to each 3' end of one half and the 5' end of the other. The purpose of this was to allow the two halves to be amplified through PCR, subsequently mixing the two halves together the overlapping regions would act as internal primers that would join the two halves together through amplification. The method was not the ideal method for gene synthesis and cloning, with some constructs not successfully cloning (see Section 3.3). However, the constructs that were successfully cloned entailed each homolog, with at least a full length and truncated variant produced which could be subjected to small scale expression and detergent screening trials.

3.8.2 Expression, Purification and characterisation of SilP1Δ

Constructs of SilP from each homolog that were successfully cloned were subjected to a number of optimisation screens to produce the best quality and quantity of protein.

The first screen was based on cell strain expression, the aim being to find the *E. coli* cell strain that best expressed the proteins. The screen included a number of commercially available *E.coli* strains that are specialised for membrane proteins, this is achieved through the cells having more membranes than normally through the production of extra membrane organelles (Schlegel *et al.,* 2012).

In order to assess which cell strain best expressed, each construct was purified using Co^{2+} charged TALON resin as this has been used widely for protein characterisation (Grieben *et al.,* 2016 & Liu *et al.,* 2013). TALON resin was selected for two reasons; firstly Co^{2+} has a higher specificity for a His-tag than Ni^{2+}-NTA, which means less contaminants should be brought through. Secondly the affinity of Co^{2+} to a His-tag is lower than Ni^{2+}-NTA, therefore less imidazole needs to be added to the elution buffer which may be beneficial as imidazole can be denaturing to certain proteins (Chaga *et al.,* 1999 & Porath, 1992). The benefit of using TALON could be seen in the coomassie stained gels of the cell strain expression (Figure 3.4.2), whereby there was relatively little contaminant brought through the purification in comparison to the protein of interest.

From the screen the three main cell strains that were identified with the best expression were Rosetta (DE3), LEMO21 (DE3) and C41 (DE3). These strains are unsurprising as they are engineered for increased membrane protein expression (Schlegel *et al.,* 2012). Based off the screen the constructs and their respective cell strain were taken further for detergent screening trials.

Detergent screening utilised a screen of 12 detergents (see Table 1-6) which were selected based on a number of parameters such as harshness in extraction (i.e. amount of protein they solubilise), charge, micelle size and their common uses within membrane protein structure determination (Sjostrand *et al.,* 2017). Detergents such as DDM and DM are commonly used in structure determination, whilst detergents such as C12E8, C12E9 and LMNG have large micelles (between 50-90 kDa) but have very low CMC levels (between 0.001-0.005%) which is beneficial for Cryo-EM as it reduces the detergent background noise (Stetsenko & Guskov, 2017).

Fos-Cho-12 was used as a control as it is a harsh detergent which usually solubilises all membrane proteins. In addition to the properties and impact on the target protein, the range of detergents also screened for suitable detergents that would allow the cleavage of the GFP tag for any GFP tagged proteins as not all detergents are compatible with proteases (Vergis & Wiener, 2011).

The results of the screening showed that not all detergents were suitable for every construct, this was shown in the in-gel and Coomassie stained gels where no band was present for the protein (see Figures 3.4.4, 5 & 6). The detergents that did produce a band were mainly DDM, DM and LMNG, this is unsurprising as DDM and DM, as stated earlier, are commonly used detergents for structural biology of membrane proteins. Whereas LMNG, although not used as commonly, is rapidly becoming a detergent of choice for Cryo-EM structure determination owing to its low CMC (Bloch *et al.,* 2020 & Hauer *et al.,* 2015). As stated previously Fos-Choline-12 is used as a control due to its ability to solubilise virtually all membrane proteins, however in some of the screens there was no band present for this detergent. The lack of band suggests either that the protein was not solubilised by Fos-Cho-12, or more likely that the lysis and subsequent distribution of the lysates was not uniform resulting in the lack of extractable protein being present during solubilisation.

FSEC profiles for all the GFP-tagged constructs in their optimal detergent showed generally two peaks (Figure 3.4.7), an early eluting SilP peak (8.5 mL) and a later eluting GFP peak (~10.5 mL). The presence of a GFP peak suggests that all the constructs showed some form of degradation, which can be common for GFP-tagged proteins (Newstead *et al.,* 2007). This may suggest that the SilP is degrading through a

protease being present, even though protease inhibitors were added. If the GFP-tag is being cleaved then so is the His-tag, this would affect the purification method for the detergent screen and later large scall purification. However, as most constructs showed a correct Mw band on the gels, and the FSEC traces showed that the stable tagged protein was in greater concentration than the free GFP. The free GFP would also be removed through later purification steps. The FSEC traces for two proteins, Rosetta fb-SilP2Δ and C41 SilP1Δ, showed in addition to the GFP peak a shouldering effect on the early construct peak, edging towards an earlier elution volume. This earlier elution suggests the presence of a larger fluorescent protein, which given the size it is plausible to assume that this would be a dimer or some other higher oligomeric state of SilP. As seen in Section 3.5.1 this assumption was shown to be the case with the data from the SEC-MALLS.

Based on the FSEC profiles the *E.coli* construct ec-SilP1Δ showed the highest fluorescence count, with a sharp narrow peak at the correct elution volume (8.5 mL). Therefore, it was decided that this construct would be the main focus for the rest of project.

Large-scale expression of ec-SilP1Δ showed, through GFP counts (section 2.5.4), that approximately 3 mg of ec-SilP1Δ was expressed per 6L of TB media. The purification method for ec-SilP1Δ, using the GFP-nanobody Strep-Tactin XT yielded very clean protein. The high selectivity of the strep-tagged nanobody provided a clean basis for purification, and the high affinity of the nanobody for GFP furthered this giving a purity of 99% for the protein. As seen in Figure 3.4.8 the biotin elution fraction, which is where the bulk of the ec-SilP1Δ protein occurs after affinity chromatography, has a purity of ~80% with only low levels of

contaminants which are predominantly comprised of the purifying nano-body. The reminiscence of the contaminants are removed through reverse Ni^{2+} IMAC, this is achieved as the nanobody is his-tagged. The resulting protein is ~99% pure (Figure 3.4.8). Further purification through SEC showed, on the 280 nm absorbance profile, that two main peaks eluted (Figure 3.4.9-A). The first of these peaks eluted at 10 mL, this is a broad elution range however based on the elution volumes of controls for an S200 10/300 column suggests that the protein element would have an approximate Mw of 200-300 kDa. This suggests that, as in the Rosetta fb-SilP2Δ and C41 SilP1Δ FSEC traces, a dimer of ec-SilP1Δ maybe present. The main peak of interest which eluted at 11.5 mL has an elution volume indicative of a protein with Mw of ~150 kDa, of which monomeric ec-SilP1Δ would be with its LMNG detergent element. The purity of the ec-SilP1Δ after SEC, based on the SDS-PAGE gel (Figure 3.4.9-B), was high with an estimated purity of >90%. This was ideal for structure determination through Cryo-EM.

Subsequent analysis of the monomeric ec-SilP1Δ peak through SEC-MALLS (see section 3.5.1), showed again that two peaks eluted at the same volumes as the purification. Molecular weight estimations of these peaks showed that indeed there was evidence of the earlier peak corresponding to a ec-SilP1Δ dimer (protein Mw 149 kDa) and the later peak being monomeric ec-SilP1Δ (protein Mw 76 kDa). The data suggests that an equilibrium of monomer and dimer ec-SilP1Δ occurs within solution. It is suggestive that the ratio of the equilibrium is 2:1 of monomer:dimer, based on the absorbance of the monomer peak being twice that of the dimer peak.

Samples of ec-SilP1Δ that were intended for Cryo-EM analysis were additionally applied to a sucrose gradient. The purpose of this step was to separate out the components of the sample based on their Mw and size, with the main aim to remove the detergent micelle element of the LMNG solubilised ec-SilP1Δ. By removing the free detergent micelles the hope was to reduce the background noise that is often observed in membrane protein grids (Hauer *et al.,* 2015). The removal of LMNG was seen in determing the detergent concentration with the direct detect, as well as in the Cryo-EM grids, see Figure 3.7.3. The grids showed little evidence of free detergent micelles being present. LMNG was used for this reason as it can tolerate below CMC levels of detergent.

In addition to SEC-MALLS, ec-SilP1Δ was characterised using nano-DSF to determine its stability in solution. The results of the nano-DSF suggest that ec-SilP1Δ is an inherently unstable protein in detergent (specifically LMNG), based on the low onset temperature of 23.7 $^{\circ}$C. The low onset implies that the protein is starting to unfold at an early stage, of which there are several hypothesised reasons for. Firstly, the protein is theorised to be a flexible, based on homology and to the know CopA ATPase structure (see Section 1.4), therefore it could be that the protein flexibility is exposing tryptophan residues that can be buried in one conformation but not in another. Another possibility is that the protein is a dimer and that the application of a temperature gradient destabilises the dimer leading to monomeric ec-SilP1Δ. In dissociating any surface tryptophan's which may have been buried as a dimer contact point are now exposed and so register as a shift in the 330/350 nm ratio. Finally, the protein is simply unstable and requires little energy to start

unfolding. Based on the thermal profile and the single T_m (53.7 °C) it is more plausible that the third option is true, if one of the first two were true there would be at least two peaks on the profile. Therefore based on this result most other experiments were conducted at 4 °C to try and preserve the protein for longer periods of time. Additional nano-DSF measurements with the protein in amphipols, peptidiscs, etc. may show that the protein is more stable however due to time restraints this was not conducted.

In addition to the work conducted by myself in this chapter, additional screening for non-detergent based membranes was conducted by Dr Harish Cheruvara (MPL, Diamond Light Source ,UK) on ec-SilP1Δ. The new screen looked at alternative to detergents such as nanodiscs, amphipols, peptidiscs and SMALPS. Nanodiscs are derived from human serum lipoprotein A1, they are similar to the natural phospholipid bilayer and as such are believed to produce a more natural environment for the protein which can benefit activity (Denisov & Sligar, 2016 & Gibson *et al.,* 2009). They can range in size of diameters to accommodate different sized proteins. Amphipols are amphipathic polymers that interact with hydrophobic regions of membrane proteins, mainly those of the transmembrane region however it is not limited to those regions (Tribet *et al.,* 1996). Due to this it has been observed that amphipols can interrupt conformational changes and protein-protein interactions which inhibit activity (Picard *et al.,* 2006). Peptidiscs are a non-detergent based peptide, consisting of a short amphipathic bi-helical construct, several monomers wrap around the protein (Carlson *et al.,* 2018). Finally, SMALPs (styrene maleic acid lipid particles) are another polymer based

alternative to detergents. SMALPs, like amphipols, are amphipathic polymers that bind around the hydrophobic regions of the protein. In addition, unlike amphipols, they can be used to directly solubilise proteins without the initial detergent solubilisation step (Postis *et al.,* 2015).

Small scale screening of ec-SilP1Δ, following the method outlined in Section 2.5.2, was conducted using a variety of solubilising agents (see Table 3-6.

Table 3-6: Detergents and non-detergent based substitutes used for additional screening of ec-SilP1Δ by Dr Harish Cheruvara.

Well No.	Detergent	Detergent Abbreviation
1	n-Dodecyl-β-D-Maltopyranoside	DDM
2	n-Dodecyl-β-D-Maltopyranoside + CHS*	DDM+CHS
3	Lauryl Maltose Neopentyl Glycol	LMNG
4	Lauryl Maltose Neopentyl Glycol + CHS*	LMNG+CHS
5	Decyl Maltose Neopentyl Glycol	DMNG
6	n-Dodecylphosphocholine	Fos-Choline 12
7	Digitonin	Digitonin
8	glyco-diosgenin	GDN
9	Amphipol A8-35	A8-35
10	Non-Ionic Amphipol	NAPol
11	Peptidisc	NSPr
12	SMALPs	SMA

The results of the screening, through in-gel fluorescence, showed that in addition to the expected LMNG solubilised bands there were bands for the detergent substitutes (Figure 3.8.1). Of the non-detergents the amphipol (A8-35) and non-ionic Amphipol (NAPol) gave the greatest band intensity.

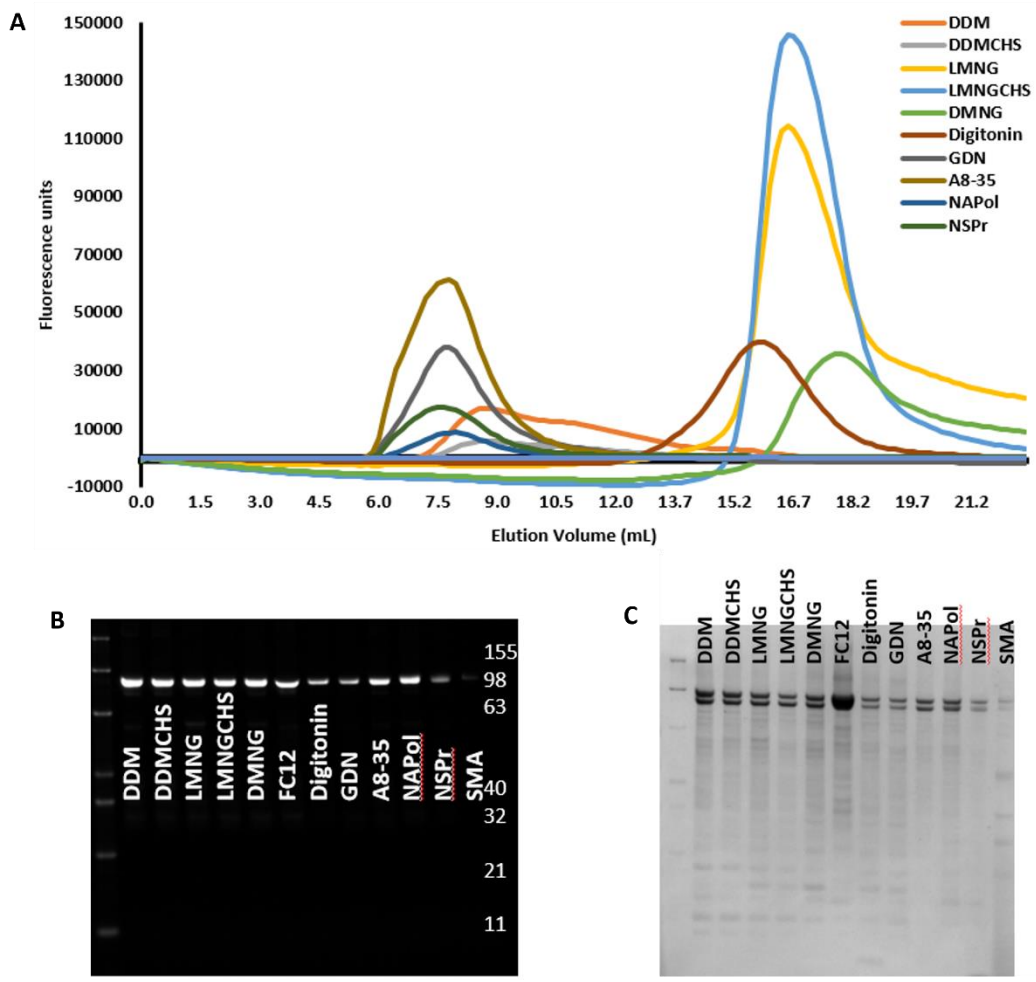

Figure 3.8.1: (A) FSEC fluorescence profiles from the screen showing that A8-35 (Gold) gave the greatest fluorescence count with no degraded GFP present. **(B & C)** (Left) In-gel fluorescence and coomassie stained gels from screen. The greatest band intensities for the non-detergents were A8-35 and NAPol. Overall, the band intensities were not as great as the detergents. Experiments and data analysis conducted by Dr Harish Cheruvara

The subsequent FSEC traces also showed that A8-35 had the greatest fluorescent count compared to the other samples, in addition it also had no peak at the free GFP elution volume. This observation was also seen for the nanodiscs and peptidiscs, suggesting that these non-detergent based surfactants stabilise the protein based off the lack of degradation. This finding is important going forward with Cryo-EM as it means other protein preps can be conducted to see how the protein looks on Cyro-EM grids on the Glacios. The sample of amphipol exchanged ec-SilP1Δ was applied to a cryo grid and imaged on the microscope, see section 3.8.4 for more details.

3.8.3 Activity of SilP1Δ

The production and purification of ec-SilP1Δ in LMNG to a high level, illustrates one membrane protein hurdle that has been overcome. However, as is often the case in structural biology determining the structure is not enough, functionality of the protein is also required. Many protein structures that have been solved, when later studied for their functionality have been shown to be inactive (Seddon *et al.,* 2004). Detergents, although membrane like in nature are not the same as the phospholipid bilayer, therefore ideal conditions for membrane proteins would be to reconstitute in liposomes as these are more membrane like (Shen *et al.,* 2013). With this said any functionality with regard to ec-SilP1Δ in LMNG will show that the protein is functional within the detergent and also any subsequent structural data will also have confidence that it is physiologically relevant.

Functionality of ec-SilP1Δ revolves around two mechanisms; 1) the turnover of ATP and 2) the successful transport of its target ligands,

Ag(I)/Cu(I). Due to time constraints (due to COVID19 restrictions) only the first mechanism was looked at, whereby ATP turnover of ec-SilP1Δ was investigated using the ADP-Glo assay kit (Promega, USA).

Two assays were conducted, one examining the ec-SilP1Δ basal ATP turnover and the second looking at ATP turnover in the presence of Cu(I). The addition of Cu(I) was used as the buffer conditions for the ADP-Glo kit were not Ag(I) friendly, the salt content of the buffer was NaCl which would cause Ag(I) to precipitate out of solution. However, based on the homology of SilP to CopA and studies of the other sil system protein, Chapter 4, providing evidence for Cu(I) binding, Ag(I) was substituted for Cu(I).

The results of the assay are initial and repeats and optimisation is heavily required. However, the initial data showed that apo ec-SilP1Δ followed a traditional enzyme kinetic trend, with a hyperbolic Michaelis-Menten graph plotted from the data. The V_{max} from the data suggested that 2.3 μM ADP/ mg ec-SilP1Δ/ minute was produced which compares well with literature values (Mandal *et al.,* 2002). The addition of Cu(I) to the reaction however did not give a traditional enzyme kinetic result, with the reaction not reaching saturation levels. However plotting the data and extrapolating in Prism, showed that the V_{max} was 7.63 μM ADP/ mg ec-SilP1Δ/ minute. This was 2.5x the V_{max} observed in the apo form, which suggests that there is more capacity for ATP turnover in the presence of Cu(I).

Although the data suggests that there is more capacity for ATP turnover when Cu(I) is present the K_{cat}, that is the number of molecules of ATP hydrolysed per second, is the same for both reactions at ~1 ATP/s^{-1}.

What this suggests is that SilP has the same turnover rate of ~1 ATP/s^{-1} regardless of Cu(I) being present, however the protein has a larger capacity to hydrolyse more ATP when Cu(I) is present. The turnover of ATP must be rate limiting and could be affected by the transport of Cu(I) through the protein. As we did not measure Cu(I) transport, only ATP turnover, we cannot comment on this and is mere speculation at this point.

The data also showed that differences in activity were not limited to just the V_{max}, the K_m (the substrate concentration that gives ½ V_{max}) also showed differences. Apo ec-SilP1Δ had a K_m of 84 μM whereas Cu(I) ec-SilP1Δ had a sigmoidal curve with a K_m of 7.9 mM. The differences in K_m suggest that Cu(I) ec-SilP1Δ has weaker binding to ATP compared to the apo protein.

The estimation of the K_m for the Cu(I) data is determined through extrapolated data which is missing higher ATP concentration data which may increase validity. However, with that said the fitted line through the data has a h (Hill slope) value attributed to this. The hill slope is a measure of allostery, amongst other things, a Hill slope value of 1 suggests a tradition Michaelis-Menten model. Whereas a Hill slope value >1 suggests a sigmoidal model and one where co-operativity (allostery) is involved.

Based on the data collected it is theorised that allosteric cooperativity is present within the system when Cu(I) is present (i.e. the protein has multiple conformations). The implication from this is that the conformation of apo ec-SilP1Δ is better suited for ATP turnover. Compared to the Cu(I) bound ec-SilP1Δ, which needs to undergo a conformational change before being able to hydrolyse ATP again. The

basis of the allosteric cooperativity is that the protein has a binding site for Cu(I) and ATP, which are linked to each other. The linkage is known as a heterotropic linkage (two ligands present), also known as heterotropic allosteric modulation (Hsu *et al.,* 1972).

Overall, the results from the activity assay show that the protein can turnover ATP, showing it is a functioning protein and that SilP seems to produce more ADP in the presence of Cu(I) than in its apo form. There are many possible explanations for this, and more data is required to make a better assumption. However, based on the results one possibility is that the Post-Albers cycle is slightly modified.

The expected Post-Albers catalytic cycle of ec-SilP1Δ, apo ec-SilP1Δ exists in the E2 state (high affinity to ATP) (Figure 3.8.2-**1**) and the addition of ATP results in the slow turnover of ATP (Figure 3.8.2-**2B**). However, with Cu(I) addition the protein is in a E1 state (Figure 3.8.2-**2A**) whereby it must go to an E2 state before binding ATP. However, with the data from the assays this is not necessarily observed. Apo ec-SilP1Δ gives a hyperbolic Michaelis-Menton curve with regard to ATP, implying that the protein is in one conformation. Whereas the addition of Cu(I) gives a sigmoidal curve which suggests that when Cu(I) binds there is a change from one conformation to another. This leads to two possibilities (1) that there is a conformational change that is not described by the standard Post-Albers scheme, or (2) that such an apparent drop in affinity at low Cu(I) concentrations is part of a discrimination mechanism that may favour Ag(I) transport over Cu(I). More experimentation is required to distinguish between these two hypothesis and what may actually be occurring.

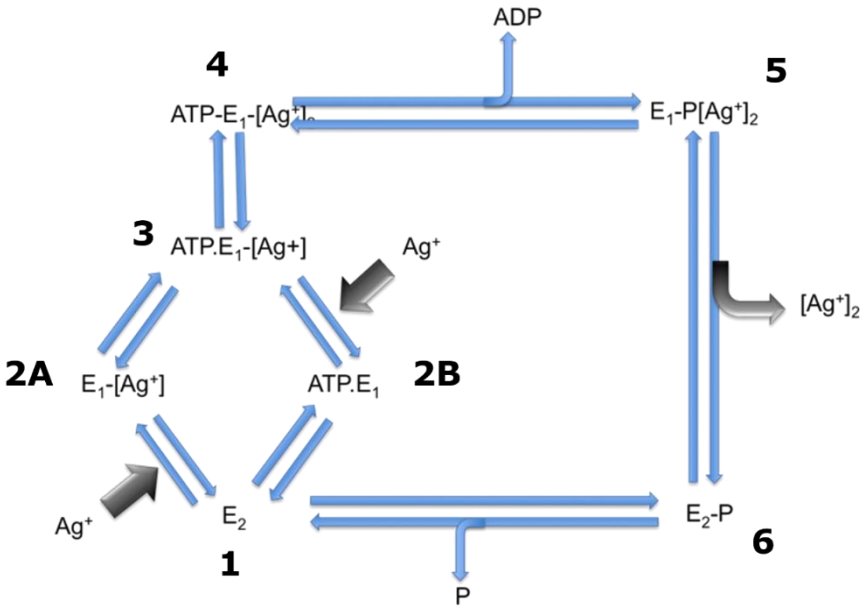

Figure 3.8.2: Anticipated Post-Albers cycle for P-type ATPases, showing the different catalytic states of the protein. This is the anticipated cycle for SilP, however the data from this work suggest SilP may have a modified version of this.

3.8.4 Structural Characterisation of SilP1Δ

Structure determination of ec-SilP1Δ proved unsuccessful in acquiring a atomic resolution of ec-SilP1Δ, however a lot of foundation work has been laid for future studies into the structure.

Sufficient concentrations of ec-SilP1Δ can be produced to a high level of purity, which gives a good starting point for grid preparation. The use of LMNG as the detergent of choice was highlighted in the negative stain images (Figure 3.7.1). The micrographs of the negative stain showed the stark difference between the use of LMNG and DDM, with the latter resulting in aggregation of the protein. The particles on the LMNG grid in comparison were of sufficient quality as to produce rudimentary 2D classes that can be used as a reference for Cryo-EM. However, it must be noted that although negative stain can give an indication to sample shape and size, the dehydrating nature of the uranyl based salts used

leads to non-physiological conditions occurring. What this can result in is the potential denaturing of the protein or the shape changes based on essential water molecules being replaced by salt molecules (Cizmar & Yuana, 2017). In the case of ec-SilP1Δ the negative stain images seem to show mainly intact protein, which resembles some plausible shape for ec-SilP1Δ (panels 3 and 5 of Figure 3.7.2). The 2D classes shows a molecule which looks mushroom like, that would correspond to the transmembrane region being the stalk and the cytoplasmic domains forming the head.

Following on from negative stain TEM of ec-SilP1Δ, Cryo-EM was conducted. A number of different grid preparation conditions were used to find an optimal condition for the protein, variables such as glow discharge, blot times and forces were all explored. Grids were imaged on the Glacios TEM at eBic which allowed examination of the grids to be conducted, looking at the grid condition (i.e. crack, broken grids, etc), ice thickness, particle distribution and homogeneity. Examining the grids showed that ec-SilP1Δ preferred thicker ice, as thinner ice presented a lot of preferential orientation. Therefore, in order to get thicker ice the glow discharge was increased to two rounds giving the grids more charge, as they hydrophobic initially, therefore more solution will enter the grid holes. In addition to this the blotting times were decreased so less solution was removed.

Imaging of the grids with the new condition (Figure 3.8.3) gave grids which had reasonably thick ice, that still gave good contrast. The particle distribution was also good with little aggregation observed. The particles were smaller (~5-10 nm) than those observed in the negative stain grids (~20 nm), suggesting that either these were not ec-SilP1Δ particles or,

and more likely, that the particles in the negative stain grids were not physiologically relevant and slightly denatured. However with this said there seemed to be no obvious LMNG detergent micelles present in the background, illustrating that low level CMC detergents are vastly beneficial for membrane protein Cryo-EM.

Although there were many homogeneous looking particles present, the particles appeared somewhat preferentially orientated within the ice with many small oblate particles present. The oblate particles are thought to be a top-down or bottom-up view of the particle, this assumption is based on the structure of the homolog CopA (PDB 3J09) which shows that the diameter of the protein is smaller than its length (Allen *et al.,* 2011). Additionally the 2D classes that were produced from the ~800,000 picked particles showed that this preferential orientation was wide spread, with the overwhelming majority of classes showing a similar shape. However, one note that was taken from the 2D classes was the presence of ec-SilP1Δ dimers. Figure 3.8.3 below shows a few of the 2D classes which illustrate the presence of dimers of ec-SilP1Δ. After the preferentially orientated monomers of ec-SilP1Δ these classes were the next most common.

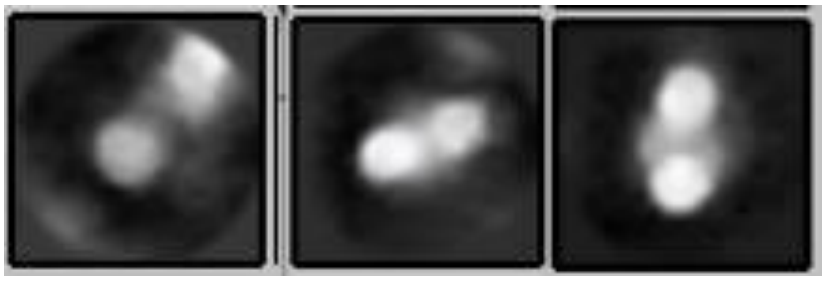

Figure 3.8.3: 2D classes of ec-SilP1Δ in LMNG imaged on the Glacios TEM. Shown are what appear to be dimers of ec-SilP1Δ within the same detergent micelle, the two more intense dots are believed to be a top-down view of ec-SilP1Δ while the less intense (fuzzier) portion id believed to be the LMNG detergent micelle.

The lack of side on orientations of ec-SilP1Δ means that a reasonable 3D model would not be feasible to produce, as not enough overall orientations would be present to produce a reconstituted map. Therefore, further data analysis of the stopped as the samples were not deemed of sufficient quality.

However, as suggested in Section 3.8.2, more grids were prepared with ec-SilP1Δ solubilised in amphipols (solubilisation by Dr Harish Cheruvara), again using the same grid preparation parameters as the LMNG girds. The grids were imaged and analysed by Dr Peter Harrison of MPL (Diamond Light Source, UK), on the 300 kV Titan Krios TEM microscope (Thermo Fishers Scientific, USA). Approximately 1 million particles were picked from the micrographs producing 2D classes shown in Figure 3.8.4.

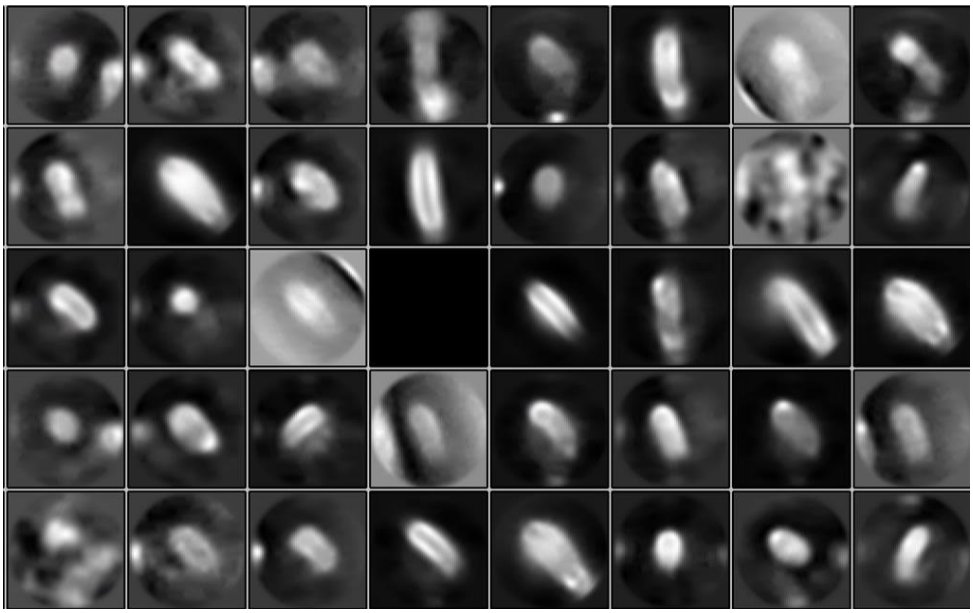

Figure 3.8.4: 2D classes of ec-SilP1Δ solubilised in amphipols. The particles show mainly elongated rods, indicating preferential orientation to a side on views of the protein. This is different to those observed in LMNG which showed a preference for a top-down orientation. 2D classes obtained by Dr Peter Harrison.

The particles shown in the 2D classes show predominantly rod like structures which suggest a side on view of the protein, however there is some evidence of top-down views of the protein as well. This is interesting as previously a top-down view of the protein was only observed in LMNG. The lack of variable orientations may also be a result of the amphipols constricting the conformation of the protein into an orientation that is favourable for a side on view.

Based on a number of orientations being present preliminary 3D models of ec-SilP1Δ were produced (Figure 3.8.5). The 3D models show rod like 'sausages' with little detail shown, such as domains. However, there is also a lot of missing density within the model, this is a result of a lack of all orientation being present within the particles. That said the protein models are approximately 120 Å in length, the SilP homolog, CopA, has a length of ~110 Å therefore the models corroborate with the expected model size. However, overall more data is needed in order to determine the structure to a respectable resolution. As with the LMNG samples thicker ice is expected to be able to produce more orientations of the protein which will allow for better structure determination.

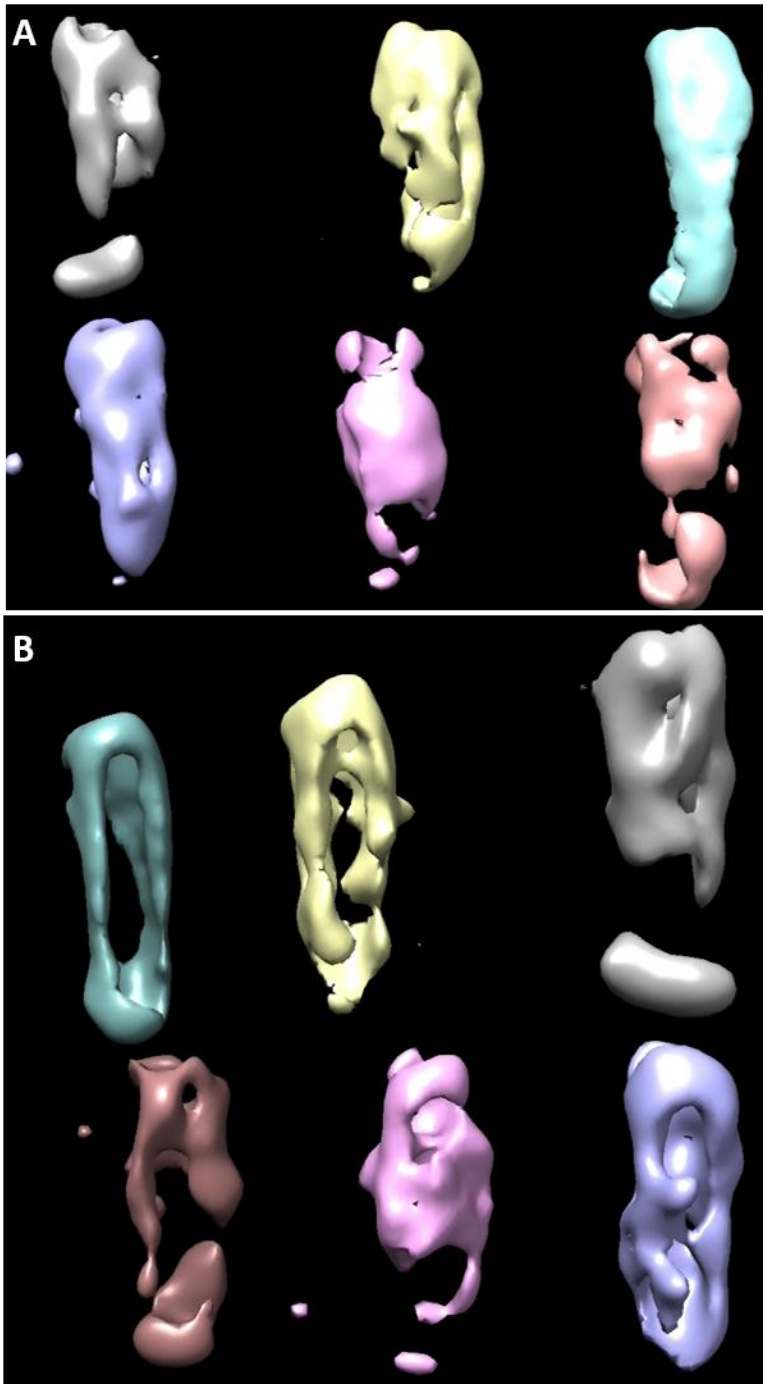

Figure 3.8.5: 3D models of ec-SilP1Δ in amphipols. **(A)** Forward facing 3D models of ec-SilP1Δ showing some complete density. **(B)** Side on view of the protein showing a lot of incomplete density, suggesting a lack of data to accurately fit. Model building conducted by Dr Peter Harrison.

3.8.5 Conclusion and Future Work

The extensive construct design and cloning of a variety of SilP homologs, has resulted in an optimal construct that can be produced and purified to a level that allows characterisation to be conducted.

Ec-SilP1Δ was shown to form dimers in solution in the detergent LMNG, the biological function of which is unknown. The purified protein was shown to be functional in LMNG as shown through ATP assays, which showed the protein turns over ATP in its apo state. However, the addition of metal ions (Cu(I)) showed a 2.5x increase in ATP turnover suggesting that metal ions stimulate the full function of the protein. The confirmation of activity is important as any structural information regarding ec-SilP1Δ in LMNG can be deemed physiologically relevant and not a structural artefact.

The structural characterisation of ec-SilP1Δ has reached a point whereby the protein has been preliminarily imaged using Cryo-EM techniques, giving rudimentary 2D classes and an idea of what the protein particles look like. However, a full atomic structure has not been solved whereby we can attribute how the protein functions, but have paved a way forward for future work into this protein.

Going forward with ec-SilP1Δ several directions need to be explored further. Firstly, looking at the activity of the protein, additional assays in the presence of Ag(I) need to be conducted to see if there is a difference in activity compared to when Cu(I) is present. This would give an idea of the protein's specificity to its main target ligand. Additionally looking at the activity of a full-length version of SilP, with the HMBD present. The HMBD is thought to provide a regulatory role (Hatori *et al.,* 2008; Mandal & Arguello, 2003) within the protein, therefore if its present it may increase ATP turnover more than in the truncated construct. Based on the activity results from the chapter an additional investigation would be to look *in vivo* studies of at substituting CopA with SilP to see if bacteria cells survive in Cu(I) rich environment. CopA is a P-type ATPase which is

involved in the *cue* system, close homolog to the *sil* system, therefore it is plausible that SilP may effectively substitute CopA allowing bacterial cells to survive in Cu(I) environments.

Secondly, going forward, optimisation of Cryo-EM grid preparation with samples of ec-SilP1Δ solubilised in either LMNG or amphipol. Based on the preliminary data collected in both conditions optimisation should be easy enough, varying primarily the glow discharge and blotting time should yield more favourable grids. Additionally adding in ligands that may stabilise the conformation of the protein, e.g., non-hydrolysable ATP analogues, may also improve data collection and analysis as a number of different possible conformations may no longer be present.

4 Characterisation of Periplasmic SilF

4.1 Introduction

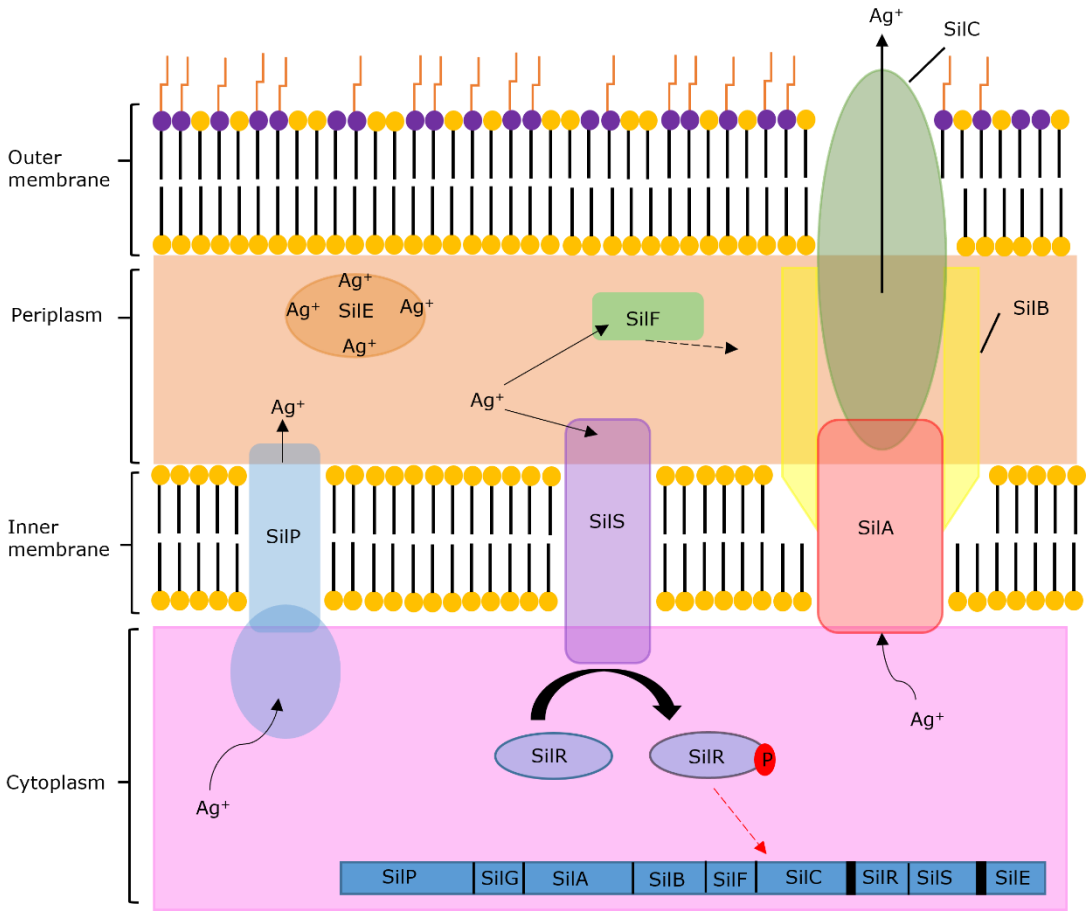

Figure 4.1.1: Sil system overview with SilF highlighted (Light Green) in the periplasm.

SilF is a small soluble periplasmic metalloprotein (~13 kDa) that forms one of the nine member proteins of the *sil* family of proteins involved in bacterial Ag(I) resistance. Nothing is known of SilF, other than its speculated function based on homology modelling to the copper chaperone CusF, which is a member of the *cus* operon involved in Cu(I) regulation in bacterial cells. Functional analysis of CusF have shown that the protein binds to both Cu(I) and Ag(I) within the periplasm and has been shown to interact with the CusB component of the CusCBA complex (Mealman *et al.,* 2011), a metal ion exporting RND transmembrane copper pump (Franke *et al.,* 2003). Based on the degree of homology

between SilF and CusF (~50%), it is anticipated that a similar function and ability to bind to both Ag(I) and Cu(I) ions will be shown during characterisation.

4.2 Aims

SilF is anticipated to be a key for the movement of Ag(I) and Cu(I) ions within the periplasm. To this end I will aim to:

I. Clone, express and purify SilF for biophysical and structural analysis.

II. Investigate the biophysical properties of SilF to aid structure determination and functional characterisation.

III. Investigate the binding capabilities of SilF to Ag(I) and Cu(I) and compare these to published values for the CusF system to identify any differences and try to explain these.

4.3 Cloning of SilF for protein over-expression

SilF construct design and production followed the In-Fusion method outlined in section 2.3.2. Products of the PCR were analysed on a 1% TAE agarose gel, following the method in Section 2.3.2. The results of the agarose gel can be seen in Figure 4.3.1. The full-length SilF fragments were sized at approximately the ~350 bp mark and the truncated fragments at ~250 bp, which corresponds to the expected size

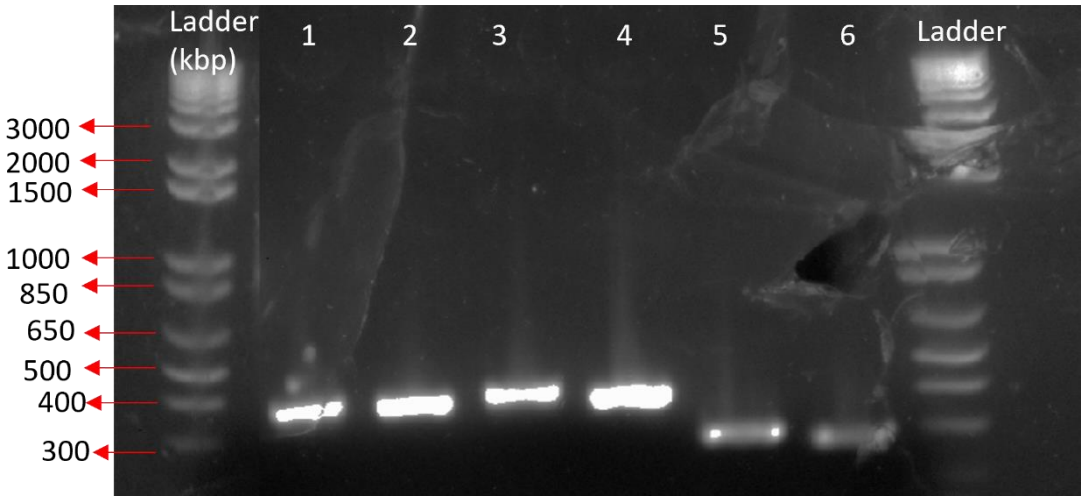

Figure 4.3.1: 1% Agarose gel of SilF PCR products. (Lane 1) 1kbp Invitrogen DNA Ladder, (Lanes 2-3) fb-SilF1/2 PCR fragments, (Lanes 4-5) ec-SilF1/2 PCR fragments and (Lanes 6-7) ec-SilF1/2Δ fragments.
of the fragments.

Gel fragments containing PCR products were excised and the DNA extracted using QIAquick Gel Extraction Kit protocol (Qiagen, UK). The final concentration of the purified DNA fragments were ~40 ng/μL. Each fragment was inserted into the respective vector using the Infusion ligation method described in Section 2.3.3. Bacterial colonies that grew had the plasmid DNA extracted using the mini-prep method outlined in

Section 2.3.4. After which the plasmid DNA was sequence verified, confirming that all constructs were successfully cloned.

4.4 Expression and Purification

4.4.1 Full Length ec-SilF1

N-terminally tagged full length ec-SilF constructs contained a natural N-terminal signal peptide that enables the protein to be transported to the periplasm, however the signal peptide is cleaved from the protein once in the periplasm. This cleavage removed the His-tag that was cloned into the protein for purification, therefore the protein could not be purified.

Plasmid DNA of ec-SilF1 (c-terminally tagged) was transformed into *E.coli* BL21(DE3) and subsequently expressed in TB media following the method outlined in section 2.4.1.

Cells containing ec-SilF1 were purified following the method set out in section 2.4.2, with an initial imidazole gradient used to elute the protein off a 5mL Ni^{2+}-Histrap FF column (Cytiva, UK). The protein eluted around 50 – 65 mL which corresponds to an imidazole concentration of between 300 – 400 mM. Figure 4.4.1 shows the absorbance trace from the imidazole gradient along with the SDS-PAGE gel of the fractions.

SDS-PAGE analysis (Figure 4.4.1-B) of the gradient fractions confirmed the presence of ec-SilF1 at around the 12 kDa mark, which is close the predicted molecular weight of 11.5 kDa. However, the gel showed prominent contaminant bands around the 75, 30 and 25 kDa marks.

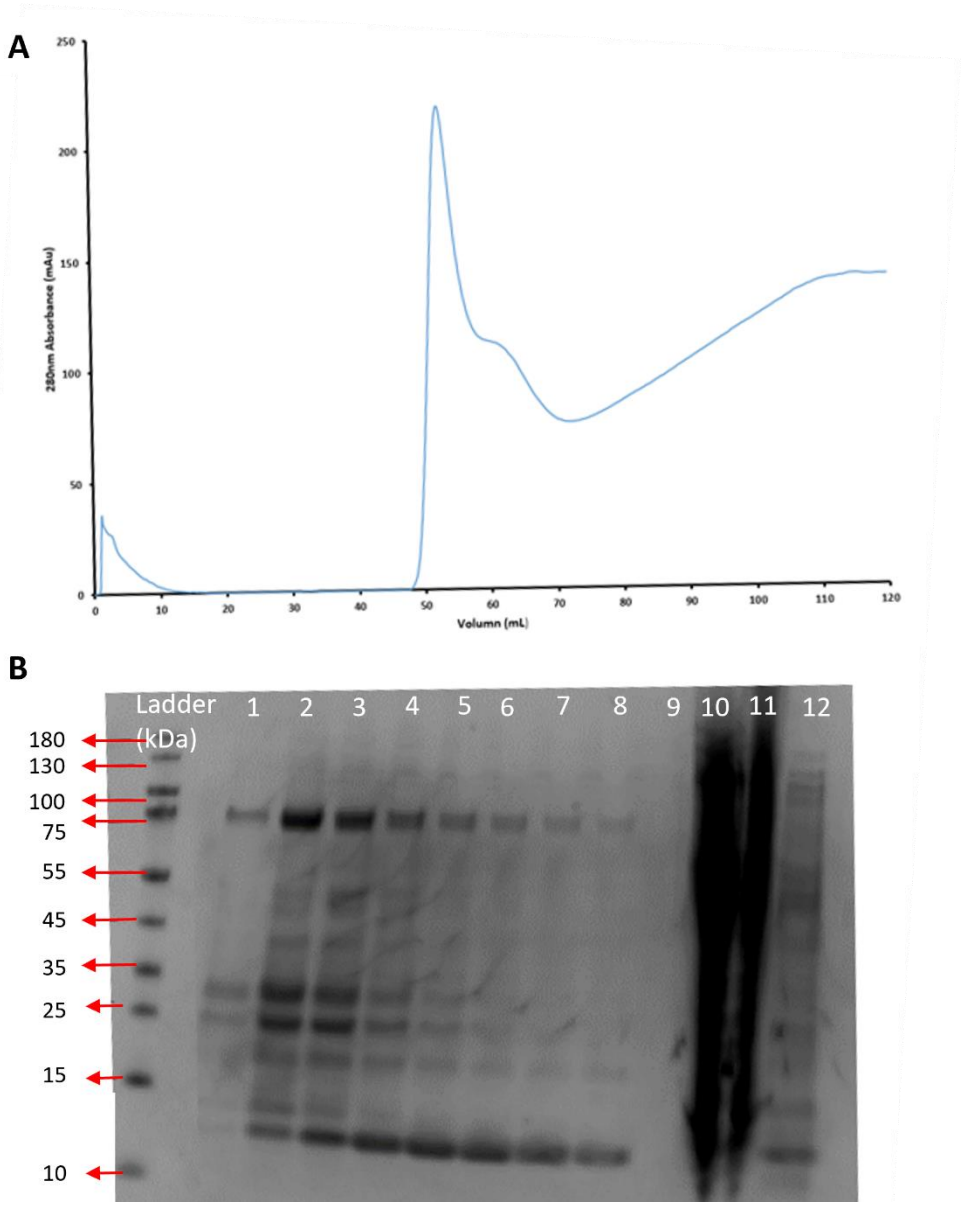

Figure 4.4.1: (A) Absorbance (280 nm) trace of ec-SilF1 following imidazole gradient. Bulk of protein eluted around 50 – 65 mL, evident through the drastic increase in 280 nm absorbance. This volume corresponds to an imidazole concentration of between 300 – 400 mM. Linear increase in absorbance afterwards is indicative of imidazole absorbance as the concentration increases. **(B)** SDS gel of ec-SilF1 from gradient elution. (1–4) Fractions from 50-55 mL, (5-9) fractions 56-75 mL, (10) Load, (11) Flow through & (12) Wash.

Fractions containing ec-SilF1 were pooled together and concentrated to 400µL, using a Amicon 3 kDa MWCO spin concentrator, after which they were applied to a SEC as outlined in Section 2.4.2. Figure 4.4.2 shows the AKTA 280 nm absorbance profile from the SEC run with several peaks present. Peak 4 (16 mL) corresponds to the elution point of a protein with a Mw of approximately 8 kDa, which although lower than ec-SilF1 is similar. Samples from each peak were analysed on a SDS-PAGE gel with Peak 4 showing the presence of SilF however there were large amounts of contaminants present. Fractions of ec-SilF1 were concentrated with a 4 mL 3 kDa MWCO spin concentrator to a volume of 1 mL (concentration 14 mg/mL) and frozen for storage.

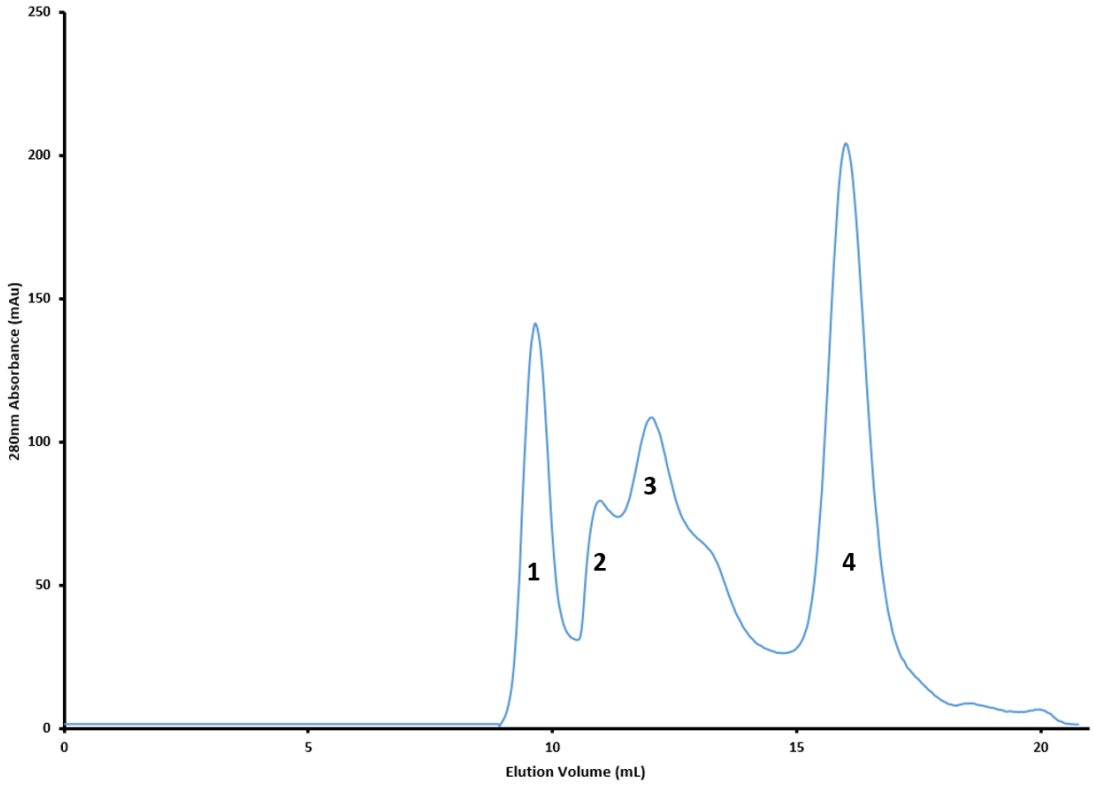

Figure 4.4.2: AKTA Absorbance (280 nm) trace of ec-SilF1 applied to a Superdex 75 10/300. Peaks 1 -3 are higher molecular weight contaminants that have been separated out. Peak 4 (16 mL) occurs at an elution volume indicative of a protein with a molecular weight similar to SilF (11.5 kDa).

4.4.2 Truncated SilF - ec-SilF1Δ

Expression of truncated *E.coli* SilF (ec-SilF1Δ) followed the method outlined in section 2.4.1. Cells containing expressed ec-SilF1Δ were purified following the method set out in section 2.4.2. As with the full-length protein (Section 4.4.1) the protein was purified with Ni^{2+}-IMAC, with the protein eluted using FPLC with an imidazole gradient on a AKTA Express (GE Lifescience, US) (see Section 2.4.2). The bulk of the protein eluted at an imidazole concentration ranging from 200–350 mM, based off 280 nm absorbance optics within the AKTA (Figure 4.4.3). The protein eluted at a similar imidazole concentration as the full-length protein.

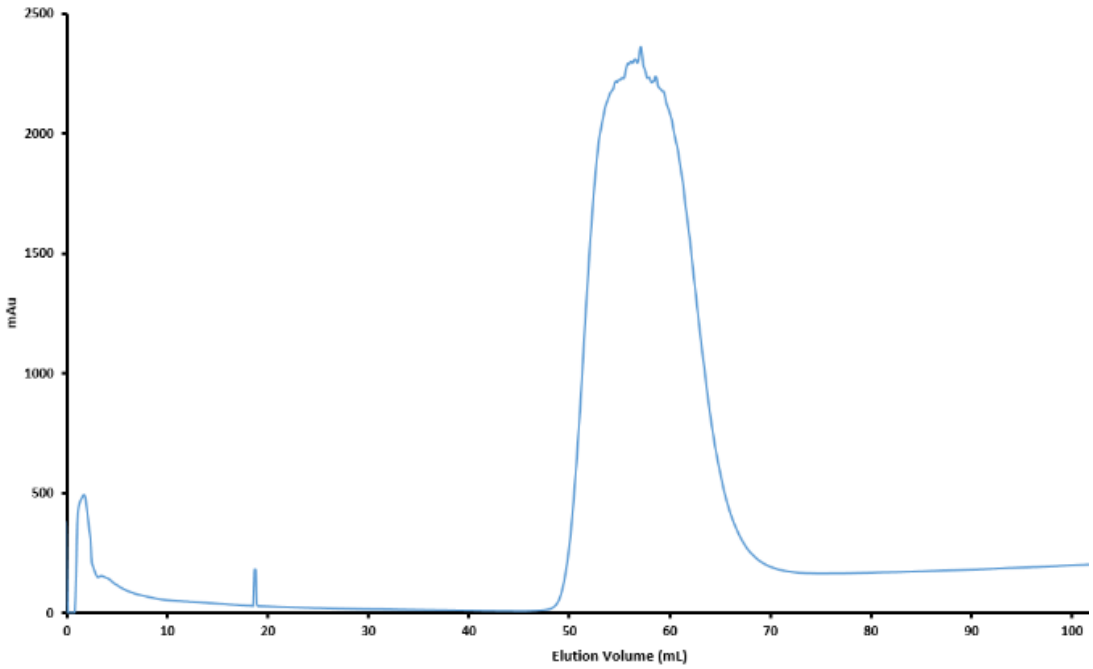

Figure 4.4.3: AKTA absorbance trace using UV 280 nm for Ni-IMAC gradient elution of ec-SilF1Δ. The protein eluted between 200-350 mM imidazole. The monodispersed peak has a very high absorbance indicating a high concentration of protein present.

SDS-PAGE analysis (Figure 4.4.4) of the fractions corresponding to the peak showed that the initial couple of fractions of the peak contained some ec-SilF1Δ, however there was a lot of contaminating proteins

present as well. Later fractions in comparison contained much less contaminating protein but a much higher concentration of ec-SilF1Δ, with intense bands at the correct Mw ~11 kDa. The fractions containing ec-SilF1Δ were pooled and concentrated to a final volume of 10mL, the sample was dialysed with 3C protease overnight (section 2.4.2).

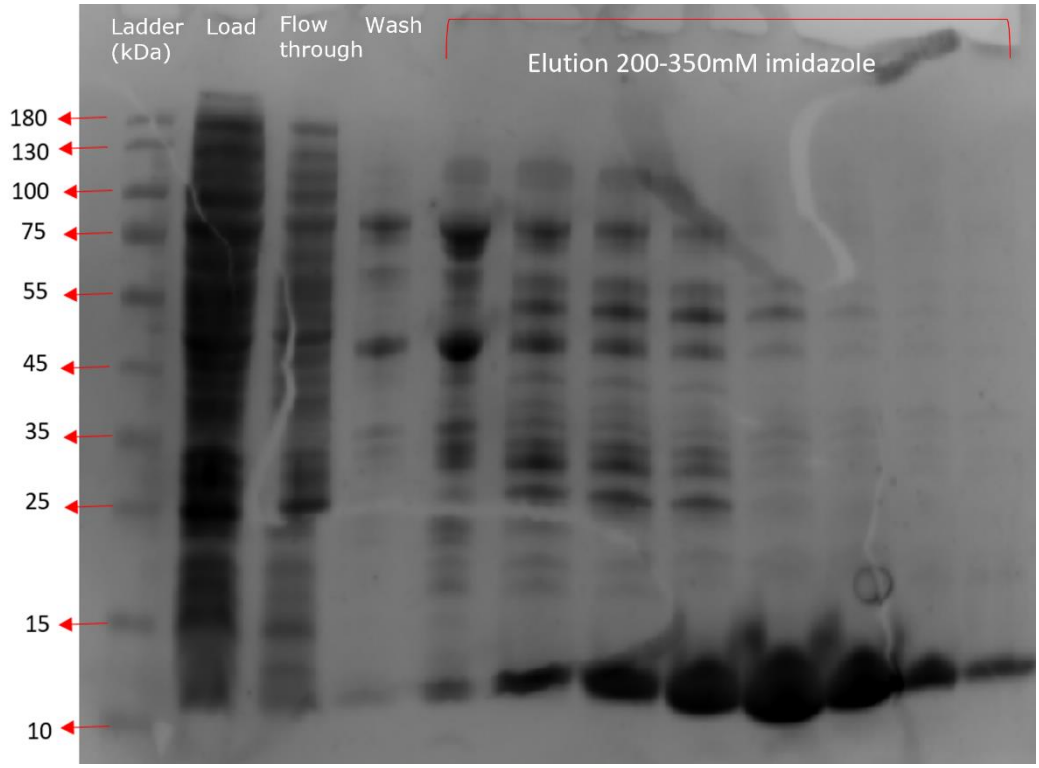

Figure 4.4.4: SDS gel of ec-SilF1Δ gradient elution based on Figure 4.4.4. (1) Ladder, (2) Lysate load, (3) Flow through, (4) Wash, (5-15) Fractions from 50 -70 mL.

After dialysis and 3C protease digestion the sample was subjected to a reverse IMAC HisTrap (see section 2.4.2), with confirmation of the protein being cleaved and its purity assessed through an SDS-PAGE gel (Figure 4.4.5). Cleaved samples of ec-SilF1Δ were present in the flow through and wash to a high degree of purity, with all contaminating proteins and 3C protease present in the elution. The flow through and wash were pooled and concentrated to 400µL before SEC (see Section 2.4.2). Figure 4.4.6A shows the 280 nm absorbance trace from the SEC

run, there is a single distinct peak at 15 mL with a high absorbance indicating the presence of ec-SilF1Δ. Several different fractions from the SEC run were analysed on a SDS-PAGE to ascertain the purity of the sample (Figure 4.4.6B).

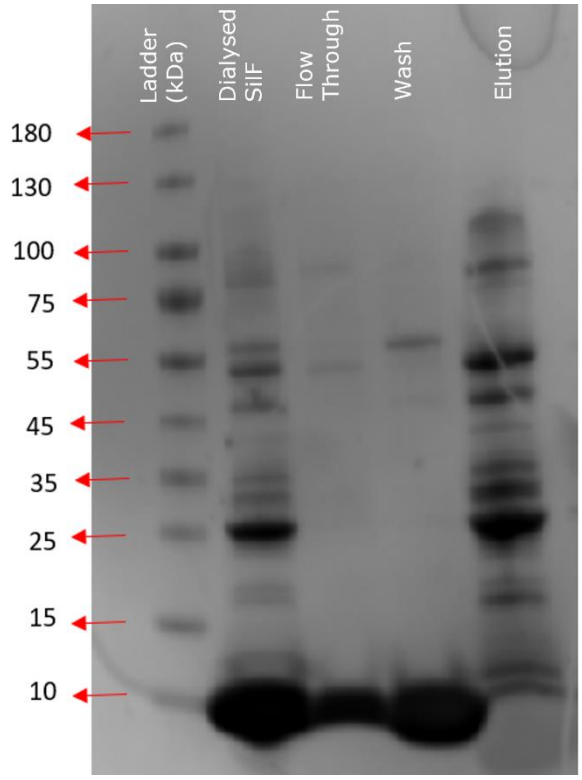

Figure 4.4.5: Reverse IMAC of ec-SilF1Δ. (1) Ladder, (2) Dialysed SilF with 3C protease, (3) Flow through, (4) Wash & (5) Elution.

The molecular weight of the protein was confirmed using intact mass spectroscopy, (Section 4.5.1). SDS-PAGE analysis showed that the fractions corresponding ec-SilF1Δ had a purity of ~95% (Figure 4.4.6-B). The high SEC 280 nm absorbance and band intensity on the SDS-PAGE gel suggested that the protein was heavily concentrated, further measurements using the nano-drop (with the corresponding 1 % ε_{280nm} (5.5 OD/mg) and Mw (9.1 kDa)) showed that the concentrations of each fraction, over the main peak, ranged from 25-36 mg/mL.

Based on high expression levels and purity of the samples, a decision to go with ec-SilF1Δ for the biophysical and structural characterisation was

decided. Fractions containing the protein were used either immediately for characterisation or stored at -80 °C for later use (if frozen glycerol was added to an end concentration of 10%).

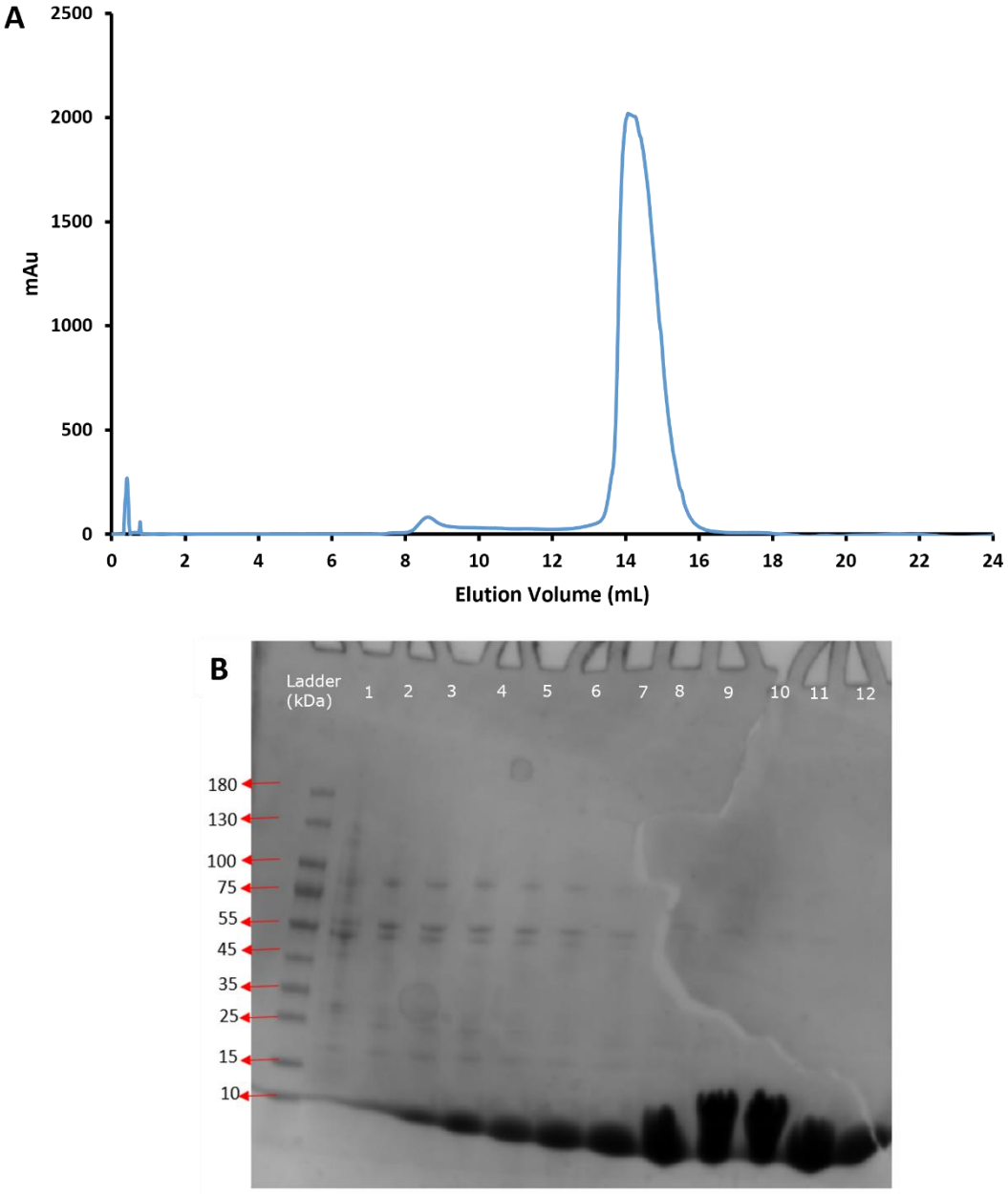

Figure 4.4.6: (A) 280 nm absorbance trace from SEC of ec-SilF1Δ using an S75 10/300 column. **(B)** SDS-PAGE gel of fractions from S75 SEC, (1-5) 8.5-12mL, (6-12) 13-16 mL, based on the 280 nm absorbace trace.

4.5 Biophysical Characterisation

4.5.1 Intact Mass Spectroscopy

Mass spectroscopy confirmed the presence of the protein and that it was cleaved. Samples of ec-SilF1Δ were injected into the mass spectrometer, following the method in Section 2.6.6 with 20 µL of protein at 50 µM, with the results shown in Figure 4.5.1.

The results of the mass spectroscopy showed that the main protein molecular weight was 9151 Da showing that the protein is cleaved. The calculated Mw is 5 Da lighter than the anticipated Mw of 9156 Da, this is discussed later in Section 4.7.2.

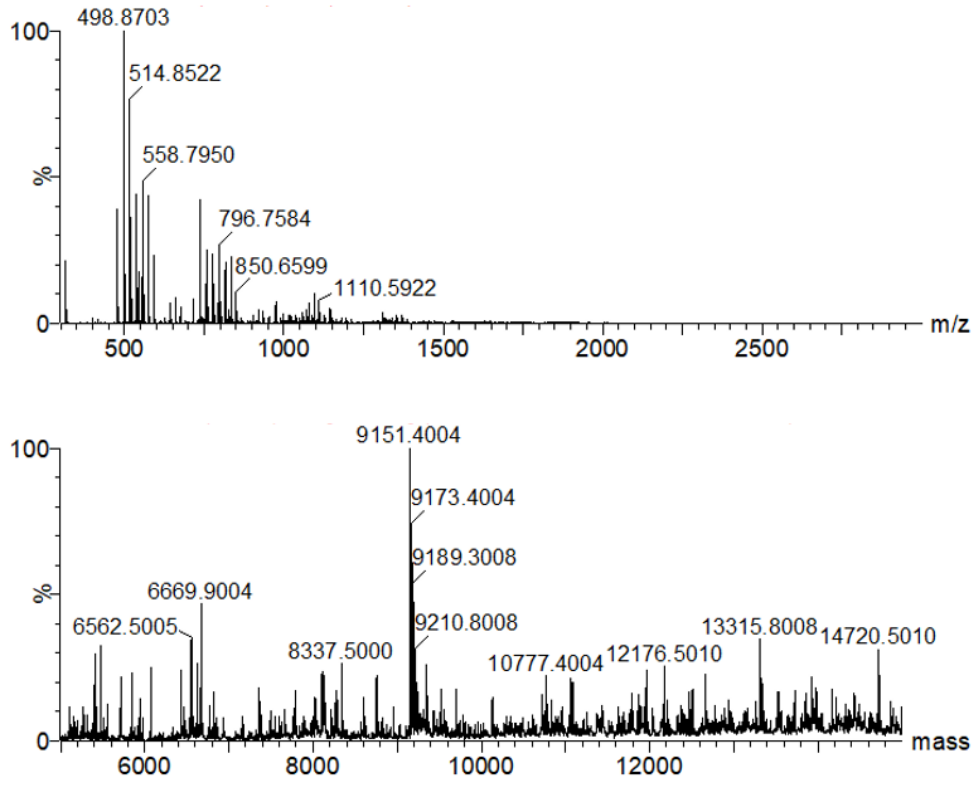

Figure 4.5.1: Mass spectroscopy data analysis of ec-SilF1Δ. (Top) Raw data from the ionisation of the protein. (Bottom) Calculated molecular weight of the protein, shown to be 9.151 kDa.

4.5.2 SEC-MALLS

SEC-MALLS analysis was carried out on ec-SilF1Δ to assess the molecular weight of the protein component and its oligomeric state. SEC-MALLS was conducted following the method outlined in Section 2.7.2, with 100 µL of 2.5 mg/mL ec-SilF1Δ applied to the Superdex 75 10/300 column. Measurements were made using UV absorbance (280 nm), light scattering and refractive index optics.

The spectra of all three measurements from SEC-MALLS (Figure 4.5.2) indicated that the sample was monodisperse with a singles peak at 15 mL, with no major measurable contaminants present. The elution point of SilF corroborates with the elution point on the SEC S75 10/300 column used during purification. The molecular weight of the protein component of the peak was estimated to be ~8.77 kDa (± 8.116%) (see Table 4.1) which is close to the anticipated 9.1 kDa.

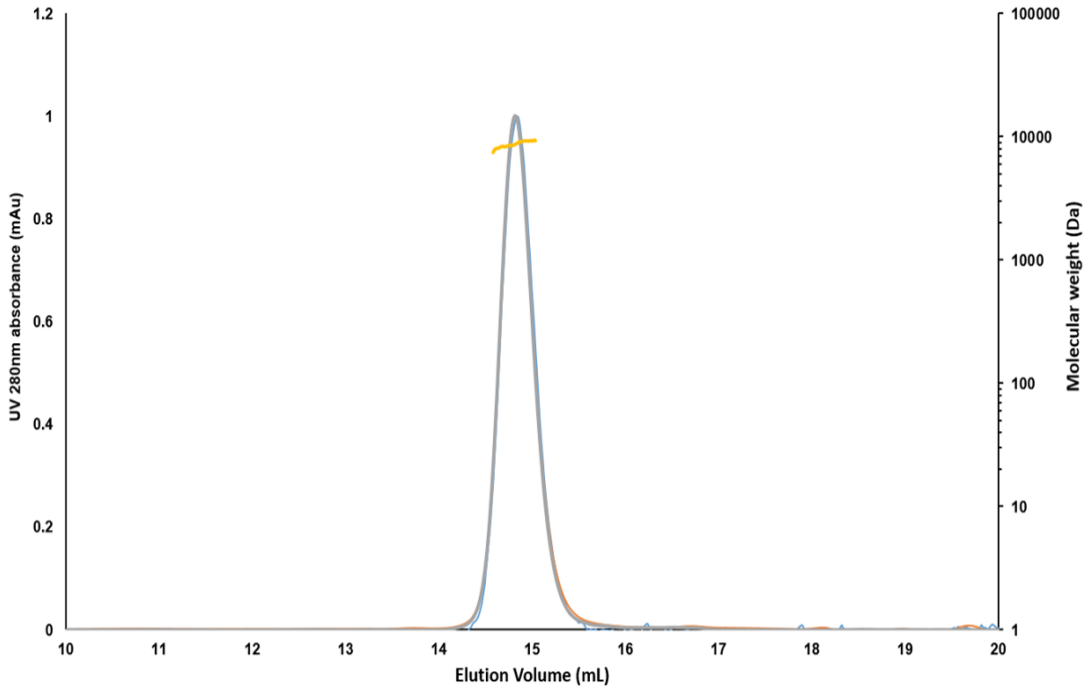

Figure 4.5.2: Data output from SEC-MALS; (Blue) Light Scattering, (Orange) Refractive Index, (Grey) UV & (Yellow) Mw estimation. The trace shows a monodispersed peak that had a Mw of approximately 8.7 kDa.

Table 4-1: SEC-MALLS statistics of ec-SilF1Δ.

SEC-MALLS Output	Values
Radius of hydration (rh(Q)z) (nm)	2.323 (±8.365%)
Average rh(Q) (nm)	1.884 (±1.670%)
Weight averaged Mw (g/mol)	8.769×10^3 (±8.116%)
Polydispersity (Mw/Mn)	1.003 (±4.398%)

4.5.3 Stabilisation studies of ec-SilF1Δ in the presence of metal substrate using nano-DSF

In order to ascertain the stability of SilF in solution a time and temperature course was applied to the protein using the Prometheus NT.48 nano-DSF. Assays were carried out on apo SilF and with the potential ligands Ag(I) and Cu(I) added in, the method is outlined in Section 2.6.3. Table 4-2 shows onset and melting temperature (T_m).

Table 4-2: Nano-DSF results for SilF in its apo state and holo bound state with Ag(I) and Cu(I).

Sample	Onset Temperature	Melting Temperature
Apo SilF (water)	57.1 °C (±0.7 °C)	72.7 °C (±0.3 °C)
Ag(I) SilF (water)	64.1 °C (±0.5 °C)	78.9 °C (±0.1 °C)
Apo SilF (1M NaCl)	56.4 °C (±0.2 °C)	65.4°C (±0.1 °C)
Cu(I) SilF (1M NaCl)	59.3°C (±0.6 °C)	67.3°C (±0.3 °C)

The T_m of both apo forms of ec-SilF1Δ show a large difference (see Table 4-2), with the 1 M NaCl condition having a 7.3 °C lower T_m suggesting either a destabilising effect or a different conformation of the protein. A similar observation is seen between the two metal ions, with Ag(I) having a T_m of 78.9 °C compared to 67.3 °C seen in Cu(I). However, both metal added samples of ec-SilF1Δ have a higher T_m than their apo counterparts, indicating that metal ion binding is occurring and that there is a form of stabilisation occurring resulting in an increased T_m.

4.5.4 Analytical Ultracentrifugation (AUC) of ec-SilF1Δ

SEC-MALLS data for ec-SilF1Δ showed that the protein is monomeric in solution. Additional conformation was sought using AUC to see if there is a change in the oligomeric state of ec-SilF1Δ in solution with the metal ion added in. Sedimentation velocity (SV) was performed, as outlined in 2.6.2. Samples of ec-SilF1Δ were sedimented at 50,000 rpm over 16 hours with absorbance (280 nm) and interference optics tracking progress.

Density and viscosity measurements were measured on the density meter (see Section 2.6.1), the density was 1.007590 g/cm^3 and the viscosity was 0.01032 poise. The partial specific volume ($\bar{v}$) of apo ec-SilF1Δ was calculated to 0.743 mL/g. Results of the data analysis, using SEDFIT (see Section 2.7.3.1), can be seen in Table 4-3 and Figure 4.5.3.

Table 4-3: Sedimentation coefficient values for ec-SilF1Δ in apo, Ag(I) and Cu(I) bound states

ec-SilF1Δ sample	Concentration (mg/mL)	Sedimentation coefficient (S)	Molecular weight (kDa)
Apo	2.0	1.159	9.03
	1.0	1.158	9.01
	0.5	1.156	8.91
	0.25	1.154	9.11
Ag(I)	5.0	1.330	9.71
	2.0	1.318	9.61
	1.0	1.302	9.24
Cu(I)	2.0	1.305	9.65
	1.0	1.301	9.32

Both apo and metal added samples of ec-SilF1Δ gave 2 peaks in their sedimentation coefficient distributions. The first peak (~0.1 S) is indicative of a salt peak resulting from the buffer components. The second peak is the protein peak. Apo ec-SilF1Δ gave a sedimentation coefficient range of 1.159 – 1.154 S, plotting the data and extrapolating back to zero concentration (S^0) for ec-SilF1Δ was shown to be 1.1543 S (see Figure 4.5.4 below). Extrapolating the data for Ag(I) bound ec-SilF1Δ a sedimentation coefficient of 1.294 S was calculated, whereas for Cu(I) as only 2 results were obtained an average was taken with the sedimentation coefficient being 1.303 S.

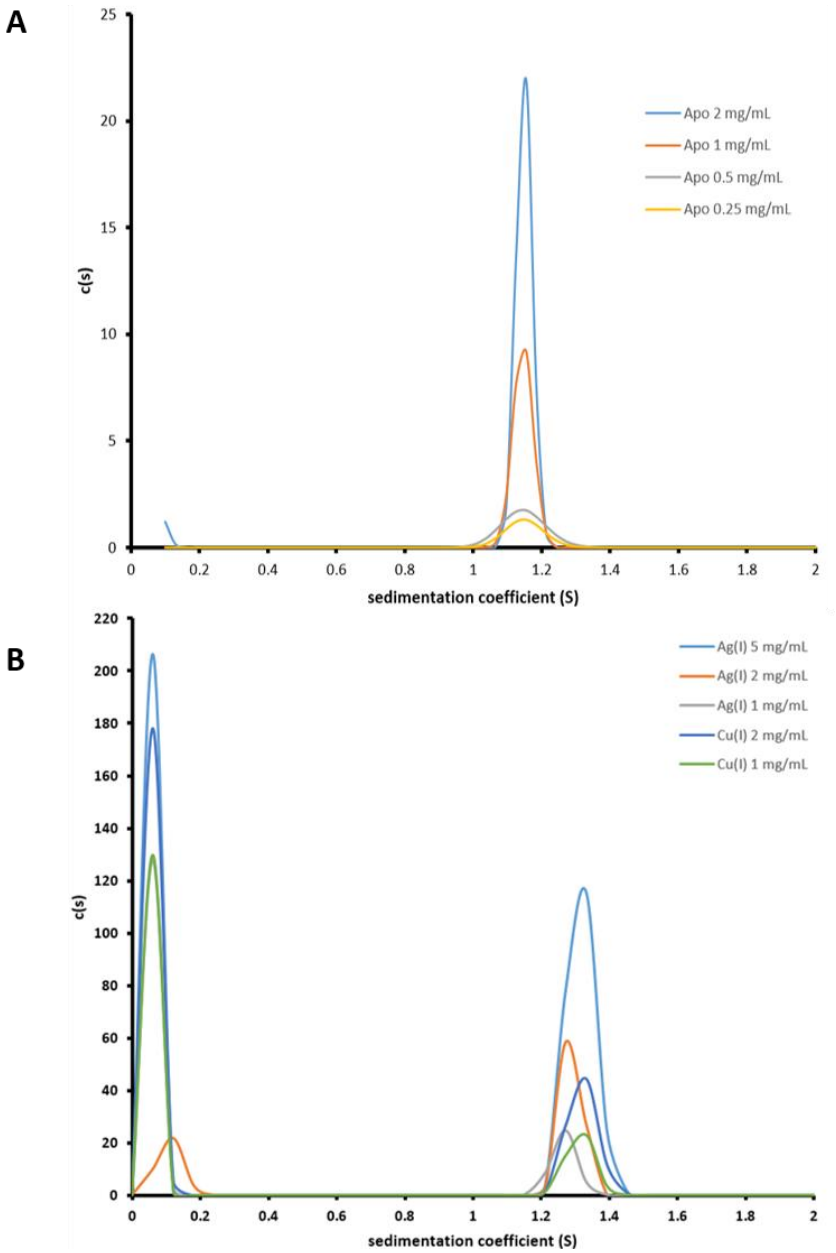

Figure 4.5.3: Sedimentation coefficient distribution of ec-SilF1Δ without metal **(A)** and with Ag(I) and Cu(I) added **(B)**, derived from SV absorbance data. Single homogenous peaks indicate monomeric ec-SilF1Δ in both conditions.

The molecular weight estimations of the apo protein peaks were reasonably close to the anticipated 9.1 kDa. The metal bound Mw's were slightly higher than anticipated, this is discussed later in section 4.7.2.

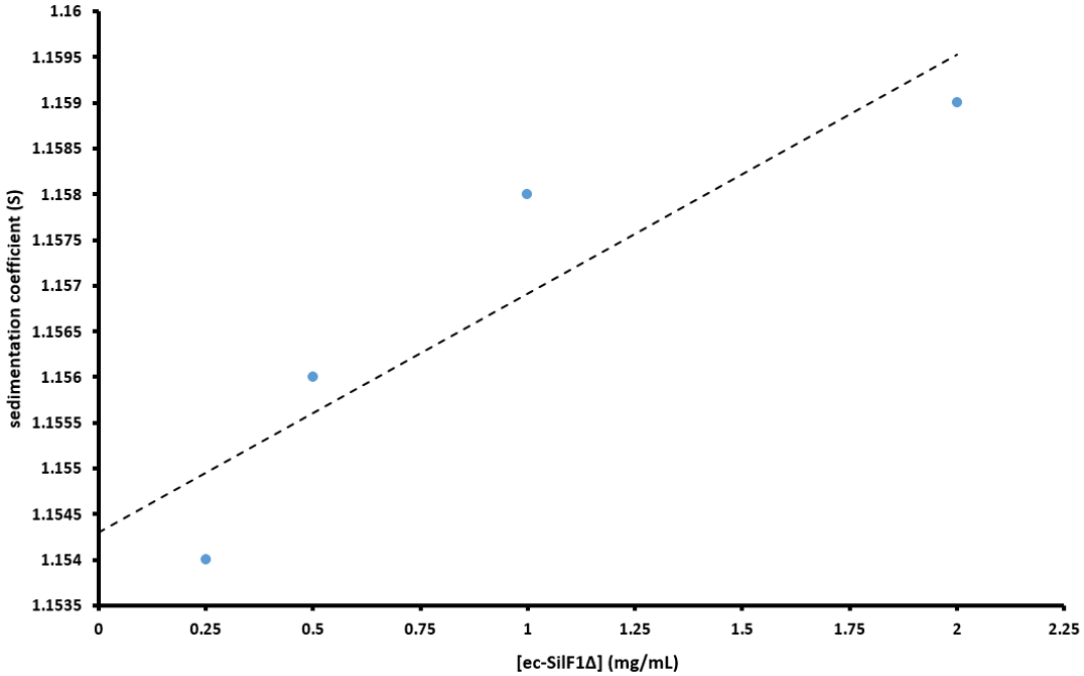

Figure 4.5.4: Sedimentation coefficient vs [ec-SilF1Δ] with extrapolation back to zero concentration to get the true sedimentation coefficient of ec-SilF1Δ, 1.1543 S.

4.6 Isothermal Titration Calorimetry (ITC) Binding Studies of SilF with Ag(I) and Cu(I)

In order to determine binding affinities of ec-SilF1Δ to Ag(I) and Cu(I) ITC was performed following the method outlined in section 2.7.5. The results can be seen in Table 4-4.

Table 4-4: ITC results of ec-SilF1Δ with Ag(I) and Cu(I), showing the dissociation constant (K_d), stoichiometry, enthalpy change (ΔH°), entropy change (ΔS°) and the free energy change (ΔG°).

Complex	**SilF + Ag(I)**	**SilF + Cu(I)**
K_d (nM)	7.55 (±1.25)	30.00 (±6.53)
Stoichiometry	0.987 (±0.026)	0.960 (±0.22)
Δ*H*° (kJ/mol)	-55.1 (±1.59)	-54.8 (±1.16)
Δ*S*° (kJ/mol)	-0.029	-0.034
Δ*G*° (kJ/mol)	-46.4 (±0.488)	-44.6 (±3.71)

The results showed that ec-SilF1Δ had a four-fold greater affinity to Ag(I) than Cu(I), with a K_d of 7.5 nM compared to 30 nM. In addition, both metals bound with a stoichiometry of 1:1 with ec-SilF1Δ, as expected from the structures of the metal ion bound proteins determined by X-ray crystallography (see Chapter 5).

The ITC isotherm measured Figure 4.5.5 shows one of the five repeated heat change traces of each metal ion titration into ec-SilF1Δ .

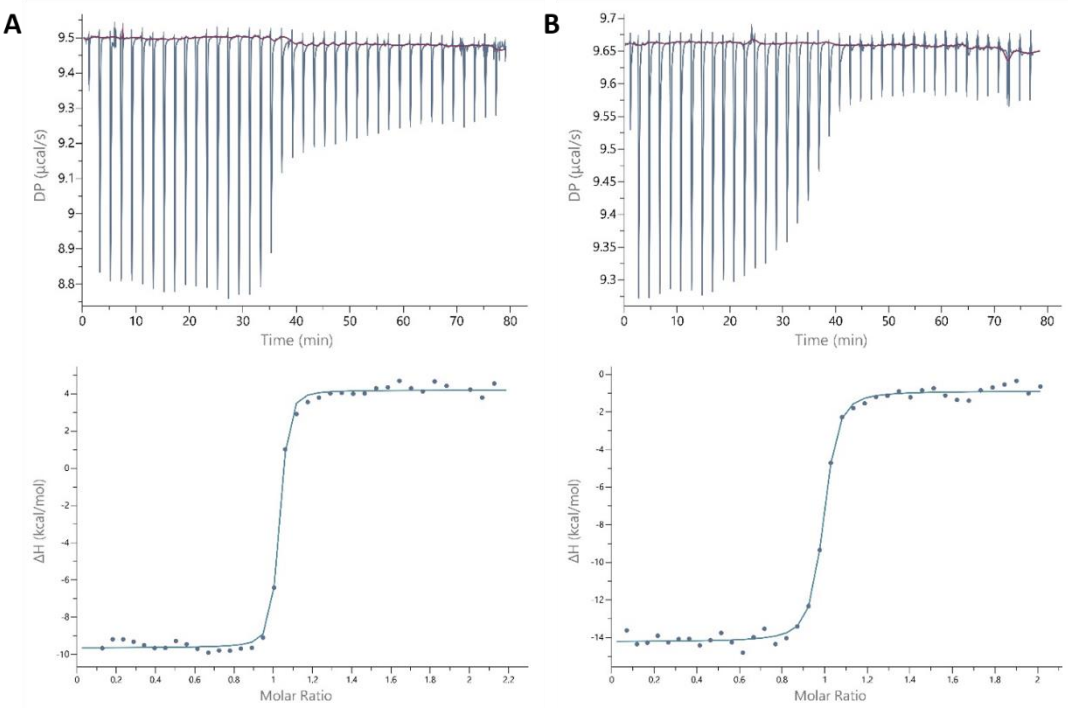

Figure 4.6.1 : ITC heat change traces of ec-SilF1Δ, in both cases 20µM ec-SilF1Δ and 250µM metal was used. **(A)** ec-SilF1Δ with Ag(I) were both in a water only solution, a sharp distinct transition can be observed indicating a 1:1 protein:metal binding event. **(B)** ec-SilF1Δ with Cu(I) were both in a 1M NaCl solution to aid Cu(I) solubility. Again, there is a clear transition to saturation levels however it is not as sharp, but still shows a 1:1 binding event.

4.7 Discussion

Both full-length and truncated forms of *E.coli* SilF have been successfully cloned and expressed in *E.coli* BL21 (DE3) cells. Based on the high expression and purity level (>95%) it was decided that the ec-SilF1Δ construct would be used for characterisation. In addition to this, previous functional and structural analysis of CusF were also conducted using a

similarly truncated form of the protein (Kittleson *et al.,* 2005 & Xue *et al.,* 2008).

As alluded to in Section 4.4.1, all the full-length constructs of SilF contain a N-terminal signal peptide sequence that informs the cell that the protein is bound for the periplasm (Denks *et al.,* 2014). The signal peptide, although part of the expressed protein is not part of the mature protein, therefore the anticipated Mw for SilF is 11.58 kDa and not the 13.85 kDa which the sequence would suggest. The presence of the signal peptide and its subsequent cleavage site was predicted by the programme SignalP v5.0 (Almagro *et al.,* 2019) analysing the SilF sequence.

The expression and purification of the full-length construct showed that a reasonable amount of the protein could be produced, however the purity of the protein (~<60%) was not sufficient enough for characterisation due to the presence of the contaminants. The lack of ability to cleave the C-terminal His-tag meant that a reverse IMAC could not be conducted, which would of have aided in purifying the protein further. However as this was not an option, and based on the purity of the truncated form of ec-SilF1Δ, the phasing out of the full-length construct was decided and the focus switched to the truncated construct.

The ability to cleave the N-terminal His-tag from the truncated ec-SilF1Δ led to a highly pure sample (~95%), as seen in Figure 4.4.7-A. The ability to produce a pure protein sample is necessary for both the biophysical characterisation, as it eliminates any contaminants affecting any interactions and measurements. In addition to this it is essential for crystallisation as it improves the chances of crystal contacts forming, leading to better diffracting crystals. Structure determination of the

homolog CusF structure was also solved using a truncated protein, with the purpose of truncating being to remove long flexible N-terminal region to allow crystal contacts to form more easily (Loftin *et.al,* 2005). The purpose of truncating SilF was also to achieve this same outcome (See Chapter 5).

The production of the ec-SilF1Δ protein was further characterised using several biophysical techniques.

Initial confirmation that the protein produced was as expected was achieved through mass spectroscopy. As shown in section 4.5.1 the protein Mw estimation was determined to be 9151 Da. From the Mw estimation two conclusions can be made, firstly that the Mw is slightly lower than anticipated and secondly that even with the slightly lower Mw estimation the protein is present and cleaved.

Addressing the first conclusion, the anticipated Mw of cleaved ec-SilF1Δ is 9156 Da therefore it can be seen that the mass spectroscopy Mw is 5 Da lighter. The lower Mw does not suggest that an amino acid is missing from the sequence, this would be a shown as a minimum difference of 57 Da (Mw of glycine). Therefore, two possibilities arise to explain this difference. The first is that there is an error in the Mw determination by the software used. However, the system is calibrated with myoglobin prior to sample addition, this calibration gave the correct Mw for myoglobin suggesting there was no error in the system. The second possibility is that a modification to the protein has occurred which has results in the lower Mw. What this modification is was not measurable with the scope of equipment at hand, however conducting native mass spectroscopy may of shed light on this (Loo, J.A., 1998) but was not a

conceivable option due to time. Subsequent structure determination (Chapter 5) showed that there were no obvious modifications to the amino acid sequence, however modifications such as the deprotonation of certain residues such as histidine's, aspartates and glutamates may result in the lower molecular weight. These would not be noticeable in the structure but may be present still.

The second conclusion, made about the protein being cleaved, is based on the fact that although the Mw estimation is slightly lower than anticipated, it is close enough to the cleaved Mw that it is evident that cleavage has occurred (full-length Mw is 10857 Da).

Confirmation of the presence of ec-SilF1Δ through mass spectroscopy led to further examination of the oligomeric state of ec-SilF1Δ in solution, SEC-MALLS and AUC.

The results from SEC-MALLS showed a single monodispersed peak with a Mw of 8.7 kDa, close to the anticipated Mw, suggesting ec-SilF1Δ was monomeric in solution. The variance from the true Mw value is attributed to the unknown refractive index increment (dn/dc) of ec-SilF1Δ. Due to the large concentration and volumes required to measure this it was not feasible to accurately calculate, therefore a protein average value of 0.185 mL/g (Zhao *et al.,* 2011) was used in the analysis.

To further corroborate this result AUC of the apo ec-SilF1Δ was conducted. This also showed a single monodispersed peak that, when corrected for the buffer density and viscosity and the protein $\bar{v}$, gave a molecular weight estimation that was exceptionally close to the anticipated, average value 9.01 kDa. The addition of Ag(I) and Cu(I) to the samples did not change the oligomeric state of ec-SilF1Δ, however the Mw estimations were considerably higher than the apo state. The

increased molecular weight estimations were attributed to ec-SilF1Δ having a different partial specific volumes ($\bar{v}$) when the metal is bound. The presence of the large metal ion changes the volume of the protein component and thus its interaction with the solvent (buffer) (Murphy *et al.,* 1998). If the accurate $\bar{v}$ of the protein-ligand complex isn't known then the sedimentation coefficient and Mw estimations, calculated through AUC, will not be accurate and variation in the value will be observed (see Equation 2.12 in section 2.7.3.1). This was seen when comparing the Mw estimations and the sedimentation coefficients of the apo and holo bound forms. In order to determine an accurate $\bar{v}$ for each metal, density measurements need to be collected over a larger concentration range (0.25 – 30 mg/mL) (Stothart, 1984). This is not feasible with ec-SilF1Δ therefore the apo $\bar{v}$ was used, and thus why the Mw's are higher than anticipated.

The thermostability of ec-SilF1Δ was analysed using nano-DSF and used to investigate the effect, if any, of metal ions. The assays showed that in general ec-SilF1Δ is a stable protein in all samples, with an onset temperature (temperature at which unfolding starts) range of between 56 - 64 °C (see Table 4-2). SilF is thought to have a similar structure to CusF, and as seen in Chapter 5 is confirmed, therefore it should adopt a β-barrel conformation with hydrogen bonds forming between the peptide backbone of each strand. Studies have shown that β-barrel like protein have high melting temperatures due to the large number of hydrogen bonds present (Naveed & Liang, 2014).

The T_m of ec-SilF1Δ however varies between both sample buffer types but shows a similar trend between the apo and holo bound forms.

The T_m of apo ec-SilF1Δ was shown to be 72.7 °C indicating a very stable protein as expected. The addition of Ag(I) to the protein however seems to stabilise the protein further with the T_m increasing by 1.2 °C to 78.9 °C. This increase in T_m suggests that an interaction between ec-SilF1Δ and Ag(I) is occurring, thus presumably binding. Further support of this was based upon the quenching of the tryptophan fluorescence at 330/350nm, the low signal of the 330/350 ratio meant that the T_m was calculated using the scattering data. In CusF the metal binding site contains a tryptophan residue which aids in the coordination of both Ag(I) and Cu(I) (Loftin *et.al,* 2005), sequence alignments of SilF to CusF have shown that there is a conserved metal binding motif (Figure 4.7.1) of which a tryptophan is also preserved. The lack of Trp fluorescence upon the addition of Ag(I) can be explained through the binding Ag(I) blocking any fluorescence from being detected.

```
SilF MRNSLKAVLFGAFSVMFSAGLHAET--HQHGDMNAASDASVQQVIRGSGVVKAIDMNSKK 58
CusF MKKALQVAMFSLFTV---IGFNAQANEHHHETM----SEAQPQVISATGVVKGIDLESKK 53
      *:::*:..:*. *:*    *::*:: *:* *      . :  *** .:****.**::***
SilF ITISHEAIPAVGWPAMTMRFTFVNADDAIDAINALKTGNHVDFSFIQQGNISLLKSINVT 118
CusF ITIHHDPIAAVNWPEMTMRFTITPQT----KMSEIKTGDKVAFNFVQQGNLSLLQDIKVS 109
     *** *: * **.** ******:.        :. :***::* *.*:****:***:.*:*:
SilF QS 120
CusF Q- 110
     *
```

Figure 4.7.1: Sequence alignment of SilF and CusF with the metal binding site highlighted in yellow as determined from the CusF structure (Loftin *et al.,* 2005)

In comparison the T_m of apo ec-SilF1Δ in the 1M NaCl used for Cu(I) studies showed a very significant drop compared to the water dialysed ec-SilF1Δ, the T_m dropped to 65.4 °C in the apo form a 7.3 °C difference. This suggests that two things, firstly that the high salinity of the buffer has a small destabilising effect on the protein resulting in the lowered T_m. However, the second conclusion is that although the buffer destabilises

the protein it is not enough to cause denaturing of the protein as it is still a reasonably high T_m. As with the addition of Ag(I) to ec-SilF1Δ the addition of Cu(I) also seems to cause a stabilisation of the protein, with the T_m shown to be 67.3 °C. This difference of 1.9 °C is slightly larger than the addition of Ag(I), however it would suggest binding is also occurring between the protein and the metal ion. There was also tryptophan quenching observed in the Cu(I) added ec-SilF1Δ, therefore the scattering data was used to determine the onset and T_m.

The apparent binding of Ag(I) and Cu(I) to ec-SilF1Δ suggests that ITC should be able to detect this and get a binding affinity, see Section 4.6.

The ITC binding studies observed in section 4.6 show that ec-SilF1Δ does bind to both Ag(I) and Cu(I), with a potent interaction shown with low nM affinity.

The results from the ITC show that both metals bind tightly to ec-SilF1Δ (Figure 4.6.1) with a low nano molar dissociation constants (K_d) observed, (see Table 4-4 & 4-5).

Table 4-5: Binding affinities of SilF and CusF to Ag(I) and Cu(I) as determined through ITC. Cu(I) data taken from Kittleson *et.al*, 2005.

Complex	**K_d (nM)**	**Stoichiometry**
SilF - Ag(I)	7.55 (±1.25)	0.987 (±0.026)
SilF – Cu(I)	30.00 (±6.53)	0.960 (±0.22)
CusF – Ag(I)	38.5	0.520 (±0.08)
CusF – Cu(I)	495	0.820 (±0.09)

The tight binding affinity of ec-SilF1Δ to Ag(I) and Cu(I) is further supported by the free energy (ΔG) and enthalpy (ΔH) changes (Table 4-4). Both values are negative for both metals, a negative enthalpy change suggests that the bonds being made on binding energetically favourable to the system. The large negative free energy shows the high affinity of the metal ions for SilF (Bastos & Velazquez-Campoy, 2021; Krainer *et al.,* 2012 & Velazquez-Campoy & Freire, 2006).

Both metals were observed to bind at a 1:1 ratio , this is expected as there is notionally one binding site based on homology to CusF (Figure 4.7.1) (Loftin *et al.,* 2007).

Binding studies of CusF to Cu(I) and Ag(I), observed by Kittleson *et al.,* (2005), showed that CusF bound to both metals with a higher affinity to Ag(I), than the SilF system. Kittleson *et.al* (2005)*,* postulated that the lower affinity to Cu(I) is due to the *cus* system (copper resistance) somehow taking into account that some cellular processes need copper (mainly Cu(II) rather than Cu(I)) (Solomon *et al.,* 2014), whereas Ag(I) is toxic and needs to be removed immediately. Therefore, having a lower affinity to Cu(I) may allow the metal to be oxidised and incorporated into a designated cell system. It is plausible to assume that the same theory is true here, with the *sil* system evolving to bind tighter to Ag(I) due to its high toxicity and facilitate its immediate excision from the cell (see Section 1.3.2).

In addition, it has been observed that Cu(I) resistance can be observed in bacteria without the *sil* system present. (Hooton *et al.,* 2021).

In addition to the conclusions made by Kittleson *et.al,* (2005), it should be noted that their data does lead to questions which the author addressed and may need to be replicated the SilF ITC. The first being that the best fit stoichiometry for Ag(I) was calculated to 0.5:1 rather that the 1:1 which it is known to be through the crystal structure (Kittleson *et.al,* 2005 & Xue *et.al,* 2008). This suggests that either the metal ion or protein concentration was calculated incorrectly. This would result in a reasonably accurate K_d, however the enthalpy, entropy and free energy of the reactions would not be accurate. The second observation is their difficulty in obtaining Cu(I) data, something which was observed in our own initial data collection. Kittleson *et al.,* ran several preliminary ITC runs with just Cu(I) to look at the effect of oxidation of Cu(I) to Cu(II) over a period of time. This was conducted for SilF however a similar effect was not observed as with the CusF data.

As some similar observations were seen in the SilF data that were present in the CusF data, closer inspection into the method was conducted. The literature on Ag(I) and Cu(I) binding studies showed that buffer components can have a serious effect on these transition metals. In both cases a buffering agent (HEPES) was initially used, as to ensure the system was buffered. However, studies suggested that buffers such as HEPES, MOPS, MES, CHES, etc. show coordinating effects on these metal ions (Babel *et al.,* 2020; Mash *et al.,* 2003). Buffers such as HEPES are amino sulfonic buffers containing amide and sulphide groups, when in the presence of Ag(I) and Cu(I) interactions between the metal ions and the amide groups leads to complexes forming which would affect the ITC results (Tan *et al.,* 2007). Therefore, in our studies we opted not to use buffering agents, rather for Ag(I) studies the components were made in

water, and for Cu(I) 1 M NaCl was used. The high salinity of Cu(I) samples was also to primarily aid the solubility of Cu(I) as it is only soluble in concentrated HCl or ammonia otherwise (Fritz, J., 2002), these were originally used however caused problem in ITC measurements. The use of high salt concentrations within the experiments could potentially lead to disruptions within the metal coordination, possibly through disruption of the water molecule coordination. It is also possible that the protein could crash out of solution in high salt concentrations, this is sometime seen in proteins, however this was not observed in this case. As binding was still observed, both these impacts were deemed minimal and acceptable as it was the only realistic method of Cu(I) solubilisation.

4.8 Conclusion and Future work

The production and characterisation of SilF has been successfully carried out, with SilF shown to be a small periplasmic metal binding protein. The protein has been shown to be produced in sufficient quantity and purity as to allow biophysical characterisation and subsequent crystallographic analysis (Chapter 5) to be conducted. The biophysical analysis has shown that the protein is monomeric in solution with a high affinity for both Ag(I) and Cu(I) as determined through ITC.

In addition to the biophysical methods carried out within this chapter further biophysical studies could look at any conformational changes that occur when metals bind, this could be achieved through circular dichroism and SAXS.

One of the main aims going forward is to determine the structure of the protein in either its apo and/or holo bound forms to both Ag(I) and Cu(I). This should allow us to determine the residues involved in binding and

the mechanism as well. Understanding the residues involved will also allow for mutagenesis studies to be conducted as to ascertain which are the crucial residues. Another future investigation is to look at the potential of SilF binding to other metal ions to see if the SilF has acquired affinity to other toxic metal ions.

5 Structure Determination of ec-SilF1Δ

5.1 Introduction

ec-SilF1Δ can be produced in sufficient quantities and of a quality that allows structural characterisation to be conducted, as shown in Chapter 4. Biophysical characterisation of ec-SilF1Δ showed that ec-SilF1Δ binds tightly to both Ag(I) and Cu(I), with a Kd of 7.55 and 30 nM respectfully. The high affinity of ec-SilF1Δ to both metal leads to the possibility of solving the structure of both the apo and holo bound forms of the protein. Determining the structure of ec-SilF1Δ will lead to comparisons with CusF to be made and also an understanding of how ec-SilF1Δ binds more tightly to Ag(I) and Cu(I) in comparison to CusF. In order to ascertain the structures of ec-SilF1Δ X-Ray crystallography will be conducted, along with other synchrotron based biophysical techniques which were not available in the previous chapter.

5.2 Aims

Following the biophysical and biochemical characterisation of SilF in chapter 4, aim of this chapter is to determine the structure of SilF. This will be achieved by:

I. Confirming that the protein produced in the previous chapter is of sufficient quality for structural studies.
II. Crystallise SilF in both its apo and holo bound forms.
III. Determine the X-ray crystal structure of apo SilF

5.3 Secondary Structure Determination through Circular Dichroism (CD)

Prior to crystallisation of ec-SilF1Δ an initial characterisation of the secondary structure of the protein was determined through synchrotron radiation circular dichroism (SR-CD). The analytical use of CD is to determine the α-helical and β-sheet content of proteins using the differential absorption of left and right circularly polarised light. In addition, CD is a quality control method for ensuring the protein product is not denatured (Whitmore & Wallace, 2008). Measurements of CD are taken at two regions of the UV spectra, the far (180-260 nm) and the near-UV (250-330 nm), using the method outlined in Section 2.7.6. Far-UV measurements pertain to the peptide backbone, this gives information on the secondary structure, with α-helices and β-sheets differing in the absorption. Whereas the near-UV is used to look at aromatic residues within the protein (Greenfield, 2006). All data was processed using CDApps data processing software (Hussain *et al.,* 2015; Hussain *et al.,* 2012).

The far-UV region (180-260 nm) results, measuring the peptide backbone (see Figure 5.3.1); of the native apo ec-SilF1Δ shows a CD spectrum dominated by the β-sheets. The Secondary Structure Estimation (SSE) analysis of the spectrum confirms this, also indicating the presence of unordered regions (Figure 5.3.1-B), SSE is an auto fitting programme that utilises various references from other dataset libraries of known structures. The addition of metals showed an increase in the α-helical content at the expense of the unordered regions. However, the β-sheet remained the dominant structural component (Figure 5.3.1).

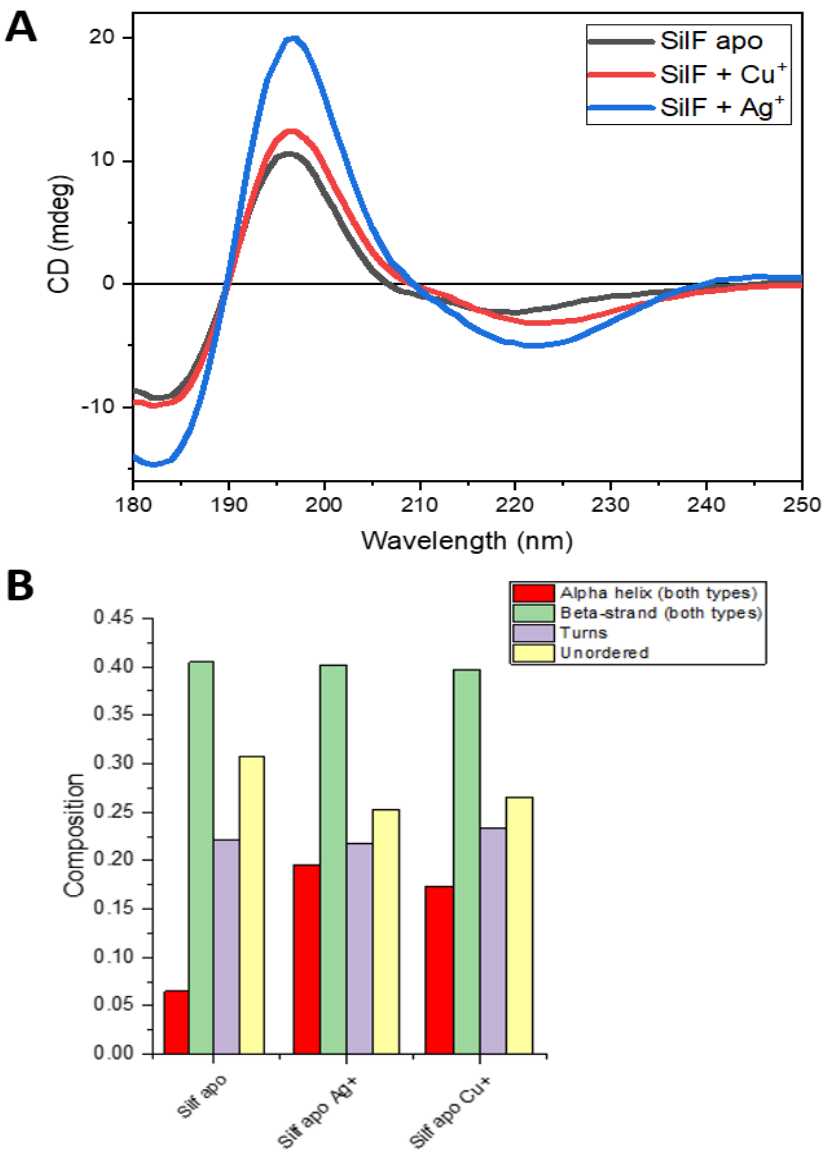

Figure 5.3.1: (A) The far-UV CD spectra of native ec-SilF1Δ at 500 μM concentration (Black), of Cu(I)-ec-SilF1Δ complex (Red) and of Ag(I)-ec-SilF1Δ complex (Blue). Metal concentrations were 5 mM, a 1:10 protein:metal ratio. **(B)** SSE of ec-SilF1Δ with and without metals, showing the increase in α-helical content at the expense of unordered protein when metals are present.

All the far-UV spectra were normalised at 190 nm in terms of UV absorption and the SSE rerun for the normalised CD spectra. Measurements at the near-UV region (250-330 nm) were also recorded, looking at the aromatic residues, checking on the influence of the metal ions on the aromatic side chains. Both the CD and absorption spectra

confirmed that there was a strong influence of the metal ions on the CD associated to the aromatic side chain residues, with CD and absorption spectral features changing drastically (Figure 5.3.2). Furthermore, there was scattering in the case of Cu^{+} complex possibly due to the oxidation of Cu^{+} to Cu^{2+} and aggregation of Cu^{+} ions in aqueous solution.

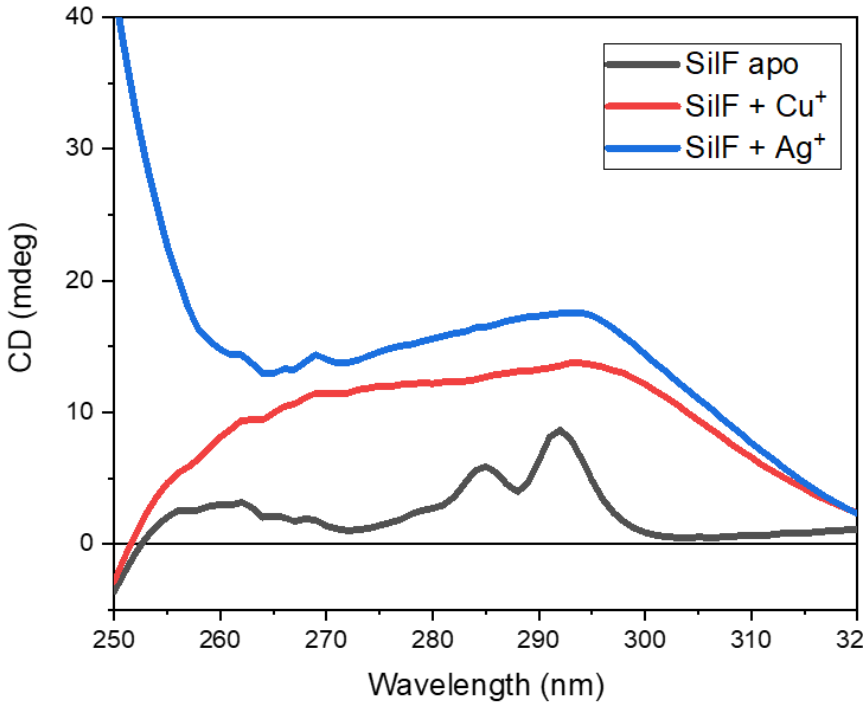

Figure 5.3.2: The near-UV CD spectra of native ec-SilF1Δ (Black), of Cu(I) ec-SilF1Δ complex (Red) and of Ag(I) ec-SilF1Δ complex (Blue).

5.4 Crystallisation of apo and holo ec-SilF1Δ

5.4.1 Apo ec-SilF1Δ

Structural analysis of ec-SilF1Δ was conducted through X-Ray crystallography, owing to the proteins small size eliminating the possibility of Cryo-EM. NMR was an additional possibility however due to lack of time labelled SilF was not feasible, also crystals formed quickly.

Conditions that produced protein crystals were determined using crystallisation screens. Screens of apo ec-SilF1Δ were prepared (JCSG+,

SG1 and Morpheus II) following the method outlined in Section 2.8.1, with a protein concentration of 20 mg/mL and CrystalQuick-X plates used.

No crystals grew within the Morpheus conditions however, several crystals formed in the SG1 plate condition containing 2 M Ammonium sulphate & 0.1 M sodium HEPES pH 7.5 (E4). The crystals formed within a day and were large rectangular crystals (~500µm x 20µm) with fan like ends. The crystal composition appeared to be a bundle of smaller thinner needles which had come together. Another condition within the SG1 plate, (G3) 0.01 M Zinc sulphate heptahydrate, 0.1 M MES pH 6.5, 25% v/v PEG 550 MME, also produced crystals. The crystals formed in a region of protein precipitate which made it harder to see all the crystals present. The crystals that did form were small rod like crystals measuring approximately 100 x 5 µm, different to those of the previous condition. Figure 5.4.1 shows images of the crystals grown in both conditions.

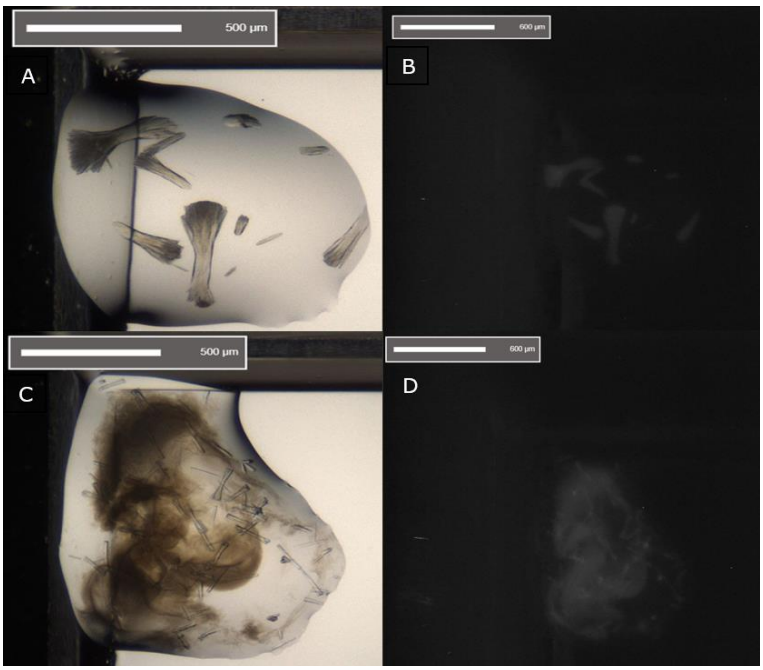

Figure 5.4.1: Crystals of ec-SilF1Δ. A & B show light and UV images of crystals grown after 1 day in condition E4, crystals were large rod like structures with ‘fan-like ends. C & D show light and UV images of crystals grown in condition G3, crystals grew in 3 days.

Prior to mounting the crystals, cryo protectants were made for each condition based on the crystallisation condition (see Table 1-7 in Section 2.8.3). Crystals were mounted following the method outlined in 2.7.3 with initial soaking of the crystal in the cryo-protectant, once mounted samples were stored in pucks in liquid nitrogen until needed for data collection.

5.4.2 Holo ec-SilF1Δ – Ag(I) and Cu(I)

Samples preparation for ligand bound ec-SilF1Δ was carried out the same as in Section 5.4.1 with the protein concentrated to 20 mg/mL, in the presence of Ag(I) and Cu(I). Metal ions were added at a 5x molar excess concentration (10 mM), using $AgNO_3$ and CuCl as a source for the ions. Samples of ec-SilF1Δ with each metal ion were incubated for 30 minutes before dispensing. Samples with CuCl added were incubated in an anaerobic glove box to minimise Cu(I) oxidation.

Crystallisation plates were prepared following the method outline in Section 2.8.1 with JCSG+, SG1 and Morpheus II plates prepared. Crystallisation plates of ec-SilF1Δ with Cu(I) were stored at room temperature in the glove box.

Approximately 2/3 of the screening plate conditions contained protein precipitation. However, SilF-Ag(I) crystals formed in two conditions of the SG1 tray, G9 (0.2 M Ammonium tartrate dibasic, 20% w/v PEG 3350) and D10 (0.2 M $LiSO_4$, 0.1 M Bis Tris pH 6.5, 25% w/v PEG 3350), crystals formed after a week. There were several small crystals in each successful condition. The crystals were imaged using UV optics within the Formulatrix crystallisation imager confirming that they were protein crystals.

As with the Ag(I)-ec-SilF1Δ many of the Cu(I)-ec-SilF1Δ conditions had protein precipitation. SilF-Cu(I) crystals formed after approximately 2 weeks in the SG1 conditions C4 (0.2 M potassium sodium tartrate tetrahydrate & 20% w/v PEG 3350) and G9 (0.2 M ammonium tartrate dibasic & 20% w/v PEG 3350) the crystals were small and rectangular in shape.

Cryo-protectants of crystal producing conditions were prepared based on the condition components with additional glycerol added, see Table 2-7 (Section 2.8.3) for more information on specifics. The cryo-protectants were then used for soaking prior to looping the crystals for imaging following the method outlined in Section 2.8.3.

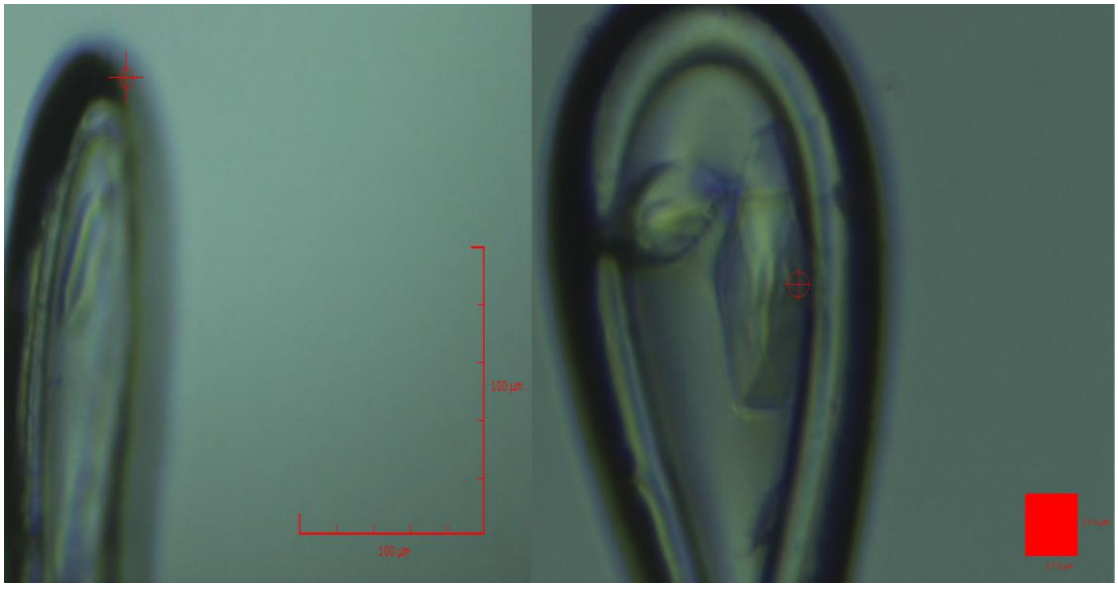

Figure 5.4.2: Looped SilF-Cu^{+} crystals shot on the I24 beamline (17/12/20). Two crystals from condition G9, the larger crystal was used to acquire data from the bottom and middle sections.

5.5 X-Ray Diffraction Collection of ec-SilF1Δ Crystals

All crystals were screened, and data collected using the macromolecular crystallography beamlines at Diamond Light Source on the I24

(Microfocus MX) beamline following the generic screening and data collection method outlined in Section 2.8.5.

Crystals that gave good diffraction in the screening images, that is crystals that gave diffraction spots out to a high resolution on the detector, were then collected off using the optimal collection method outlined in EDNA (see Section 2.8.5). Table 5-1 shows the variable parameters used in the data collection for each resolved structure of ec-SilF1Δ.

Diffraction data, from the collection, that was of sufficient quality, high number of spots and diffraction beyond 4.0 Å, entered the automatic indexing and analysis pipeline within the Diamond servers (see Section 2.8.5). Data sets that showed good statistics, such as resolution, completeness, I/θ (data to noise), etc. were selected for further structure determination, see Table 5-1 for statistics of each data set.

Table 5-1: Collection variables for all ec-SilF1Δ constructs on I24 beamline.

Collection Variables	(G3) Apo ec-SilF1Δ	(D10) Ag(I) ec-SilF1Δ	(C4) Cu(I) ec-SilF1Δ
Wavelength (Å)	0.999	0.999	0.999
Ω oscillation	0.1°	0.1	0.15
Exposure (s)	0.01	0.17	0.01
Beam Energy (keV)	12.6	12.6	12.6
Transmission (%)	20	100	10
No. of Images	2800	1030	1800
Resolution limit (Å)	1.5	1.5	2.1
Indicated Space group	P 65 2 2	P 21 21 21	I 41 2 2

Apo ec-SilF1Δ crystals diffracted in both conditions, however the E4 crystals were poor in quality with low resolution and poor statistics. In comparison, the diffraction data from the G3 crystals was much better, with more favourable statistics. Initial auto-processing of the data confirmed a $P6_522$ space group and a notional resolution of 2.0 Å.

Both sets of crystals of Ag(I) bound ec-SilF1Δ diffracted, with the best data set coming from the D10 condition. The initial screening suggested a $P2_12_12_1$ space group, the auto-processing confirming this, with a notional resolution of 1.8 Å. Finally, the Cu(I) bound ec-SilF1Δ crystals showed diffraction with the best coming from the G9 condition. The crystal had a space group allocation of $I2_12_12_1$ and a notional resolution of 2.2 Å.

5.6 Structure Determination of all ec-SilF1Δ Proteins

The data sets for each crystal collection entered the automatic pipeline within Diamonds servers, following a method outlined in Section 2.8.6 whereby the data is indexed, integrated, scaled and merged. Once this process was applied to the data the resulting structure factors were run through the Matthews programme in CCP4. The subsequent Matthews coefficient indicated the number of molecules within the asymmetric unit of the crystal, this information was used to aid Phaser in conducting molecular replacement.

5.6.1 Apo ec-SilF1Δ

The diffraction data and auto indexing for the apo ec-SilF1Δ crystal showed that the space group was $P6_522$, and that the notional resolution was 2.0 Å. Following the automatic pipeline analysis of the diffraction

data the processed data was analysed in Matthews (CCP4i) to determine the number of molecules within the asymmetric unit (see Section 2.8.6), with a molecular weight of 9100 Da (Mw of monomeric ec-SilF1Δ) used. Based on the Matthews coefficient it was suggested that three molecules of ec-SilF1Δ were present within the asymmetric unit.

Molecular replacement (MR) was subsequently conducted with the data in Phaser, with CusF (PDB; 2VB2) used as the model. The number of molecules within the asymmetric unit were determined to be three, using the Matthews coefficient (see Section 2.8.5). MR was successful in producing a solution of three molecules of ec-SilF1Δ, which fit into the electron density maps at a resolution of 2.0 Å and showed prominent crystal contact regions (see Figure 5.6.1 below).

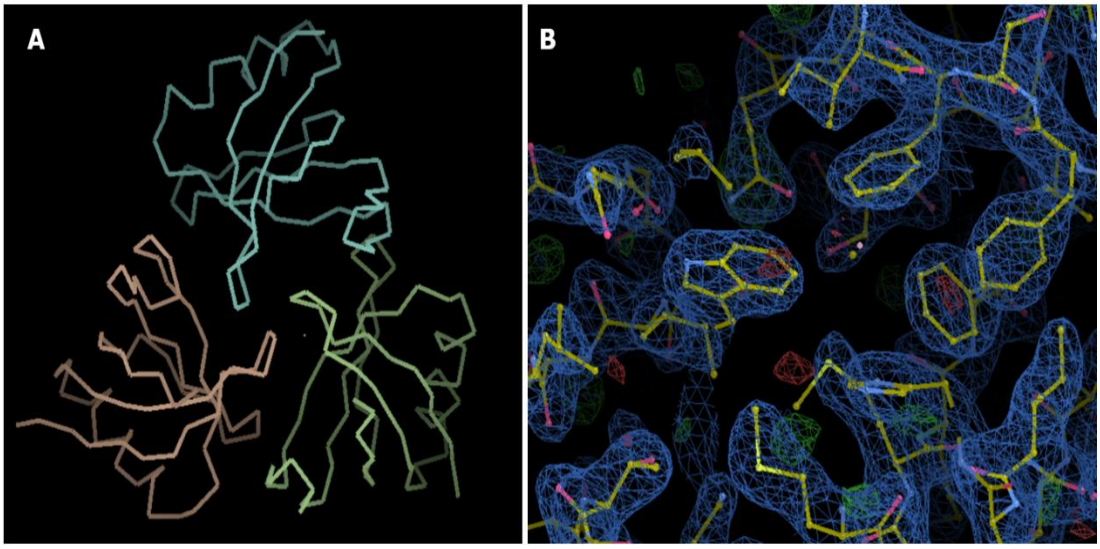

Figure 5.6.1: Crystal packing and electron density maps of apo ec-SilF1Δ. **(A)** Crystal packing, showing the arrangement of ec-SilF1Δ monomers within the crystal. The trimer of molecules shows multiple crystal contact regions essential for crystal formation. **(B)** Electron density map (rmsd 1.09) of one of the ec-SilF1Δ monomers after the final refinement, the resolution is at 2.2 Å. Good density for a couple of phenylalanine and tryptophan residues can be seen easily in the middle.

The model was modified by ensuring the correct amino acid sequence was present, as initially the sequence was CusF, additionally water molecules within the CusF model were also removed. Once the amino acid sequence was changed, refinement was conducted using REFMAC5 (Murshudov *et al.,* 2011), giving a *R* and R_{free} of 0.29 and 0.30. Additional rounds of model correction, refinement and validation (validation through MolProbity (Williams *et al.,* 2018)) were repeated several times with corrections made based on the validation until the *R* and R_{free} no longer changed. The final structure that was resolved to 2.2 Å with the *R* and R_{free} being 0.215 and 0.249 respectfully (see Figure 5.6.2).

Figure 5.6.2: Solved structure of apo ec-SilF1Δ with the secondary structure coloured. The protein consists of a 5 stranded β-barrel core (Yellow) with an α-helix (Red) at one end and an extended loop at the other (Green).

The resolved structure of apo ec-SilF1Δ, Figure 5.6.2, shows a β-barrel composed of 5 β-sheets flanked by an α-helix at one end and an extended loop at the other. The α-helix was slightly disordered at one end to the point it is difficult to say for certainty if it is helical, this structure backs up the results found during CD (Section 5.3), with ~5% of the overall structure being comprised of the α-helix. Based on the homolog structure, CusF, the proposed metal binding site is situated on the extended loop end of the β-barrel. The metal binding site is comprised of a histidine (His63), two methionine's (Met74 & Met76) and a nearby tryptophan residue (Trp71). With the histidine and two methionine's creating a binding crevice for the Ag(I) and Cu(I) ions.

5.6.2 Holo Bound ec-SilF1Δ with Ag(I) and Cu(I)

Analysis of the diffraction data for both metal ion bound forms of ec-SilF1Δ agreed with the initial predictions from EDNA (Section 5.5). Data for Ag(I) bound ec-SilF1Δ indicated that the space group was $P2_12_12_1$ with a notional resolution of 1.7 Å, whereas the Cu(I) bound ec-SilF1Δ had a space group of $I2_12_12_1$ and a resolution of up to 2.2 Å. Table 5.1 shows the data collection statistics.

Analysis of both data sets through Matthews, using CCP4i, suggested six copies were present within the asymmetric unit of both metal conditions.

In both cases, MR was conducted using Phaser (CCP4i) as was used for the apo structure. However, the model used was a monomer of apo ec-SilF1Δ not CusF. The MR for both metals gave successful solutions whereby the models fitted with the electron density maps, with no major variations or non-fitted density. Figure 5.6.3 shows the two structures following MR, with the electron density maps and number of molecules in the asymmetric unit shown.

Initial R and R_{free} values for each construct after MR were 0.45 and 0.45 for Ag(I) bound ec-SilF1Δ and 0.50 and 0.55 for Cu(I) bound ec-SilF1Δ respectfully. As in Section 5.5.1 several rounds of model modifications, refinement and validation were carried out until a final structure was determined. The final structure of Ag(I) bound ec-SilF1Δ was solved to 1.7 Å with an R and R_{free} of 0.20 and 0.23 respectfully. Cu(I) bound ec-SilF1Δ was resolved to a resolution of 2.2 Å with an R and R_{free} of 0.29 and 0.33 respectfully. The final statistics of the apo, Ag(I) and Cu(I) structures are outlined in Table 5-2.

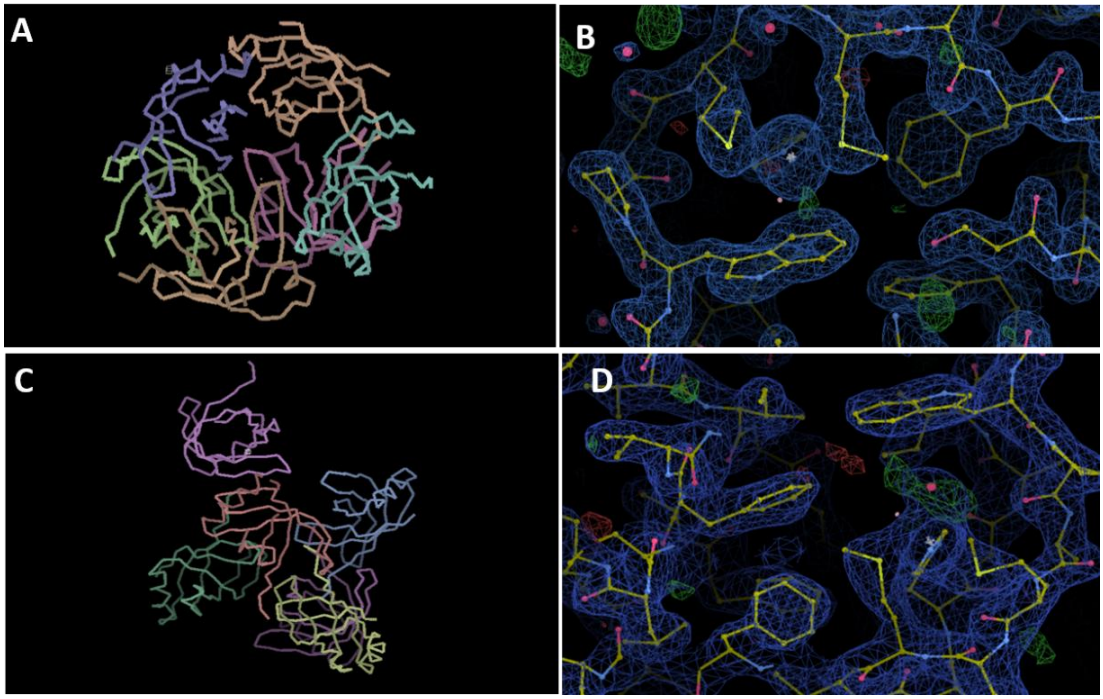

Figure 5.6.3: MR models for ec-SilF1Δ with both metal ions. **(A & C)** showing the number of molecules within the asymmetric unit for Ag(I) and Cu(I) respectfully. **(B & D)** Electron density maps for both bound metals, again respectfully. **(B)** Electron density (rmsd 1.10) for the metal binding site, consisting of two methionine's, a histidine and

Table 5-2: X-Ray diffraction and data analysis statistics of all three SilF structures.

	apo-SilF	Ag(I)-SilF	Cu(I)-SilF
Wavelength	0.999 Å	0.999 Å	0.999 Å
Resolution range	45.95 - 2.2 (2.279 - 2.2)	51.41 - 1.7 (1.761 - 1.7)	46.92 - 2.2 (2.279 - 2.2)
Space group	P 65 2 2	P 21 21 21	I 21 21 21
Unit cell	109.47 109.47 84.59, 90 90 120	60.93 81.59 95.78, 90 90 90	77.29 77.29 187.69, 90 90 90
Total reflections	32682 (1223)	70647 (3492)	35789 (1185)
Unique reflections	15524 (1502)	53221 (5226)	28977 (2855)
Multiplicity	36.9 (31.0)	13.4 (12.5)	24.2 (16.5)
Completeness (%)	98.87 (97.85)	99.95 (100.00)	99.58 (99.88)
Mean I/sigma(I)	15.1	12.8 (0.7)	13.8 (0.5)
Wilson B-factor	46.35	26.62	43.13
CC1/2	1.0 (0.6)	0.998 (0.328)	0.872 (0.432)
Reflections used in refinement	15521 (1502)	53213 (5226)	28904 (2852)
Reflections used for R-free	802 (74)	2618 (274)	1420 (150)
R-work	0.2154 (0.2819)	0.2025 (0.2823)	0.2888 (0.3944)

R-free	0.2493 (0.3449)	0.2335 (0.2584)	0.3312 (0.4058)
Number of non-hydrogen atoms	1805	3790	3656
macromolecules	1792	3563	3634
ligands	2	60	12
solvent	11	167	10
Protein residues	235	469	478
RMS(bonds)	0.014	0.015	0.014
RMS(angles)	1.94	1.84	2.04
Ramachandran favored (%)	98.69	99.78	96.13
Ramachandran allowed (%)	1.31	0.22	3.66
Ramachandran outliers (%)	0.00	0.00	0.22
Rotamer outliers (%)	2.03	0.00	4.25
Molprobity score	1.50	1.21	2.40
Average B-factor	53.13	33.59	54.24

The structure of SilF bound to metal was identical to the apo ec-SilF1Δ construct, with only the metal binding loop differing between the structures. Figure 5.6.4 shows Ag(I) & Cu(I) bound ec-SilF1Δ along with apo ec-SilF1Δ. The overlay of all the structures highlights their high similarities, however it also illustrates the extended loop region which shows the greatest variance in the Cu(I) bound structure.

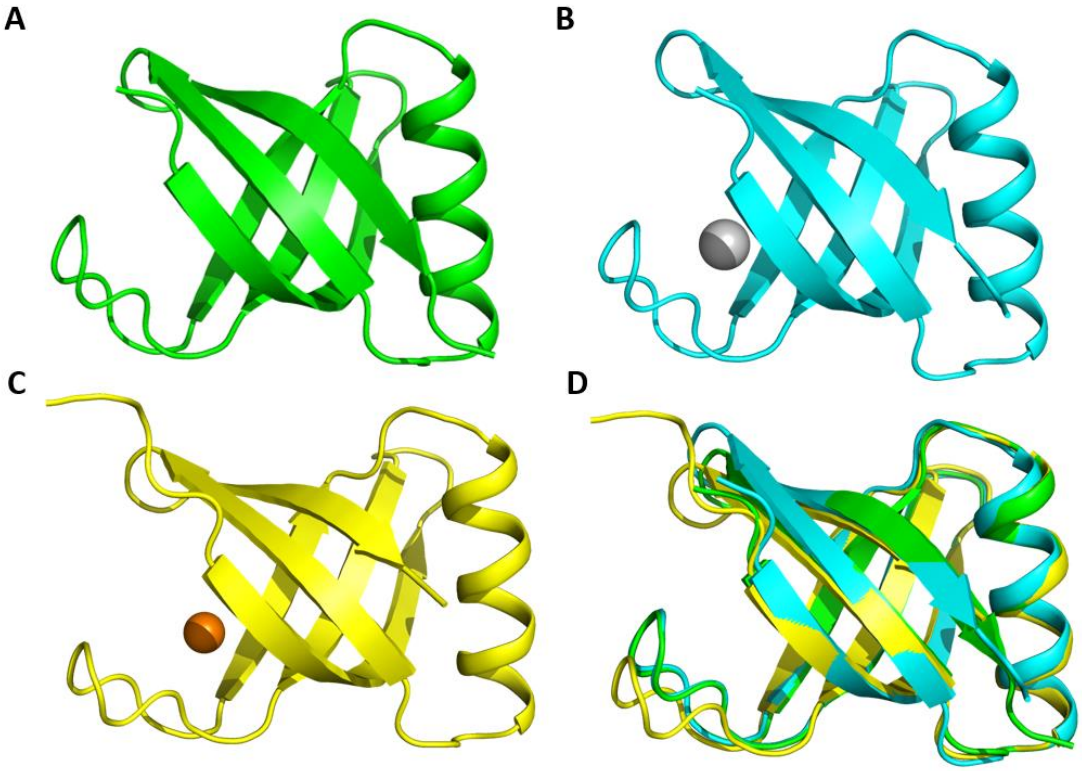

Figure 5.6.4: Structures of SilF in its various states; apo **(A)**, Ag(I) bound **(B)** with Ag(I) in Grey, Cu(I) bound **(C)** with Cu(I) in Orange. **(D)** Overlay of all three structures showing minimal conformational change in the protein other than in the extended loop region where the metal binding site occurs.

Confirmation of the metal ions being present in the binding site was determined through anomalous signal within the collected diffraction data. Reduction of this data showed that there was measurable anomalous signal at the wavelength used for collection. Anomalous difference maps were calculated from these, and the phases derived from

the refined protein model. The resulting maps showed large peaks of electron density in the positions where metal ions were expected in the metal binding site. This is seen in Figure 5.6.5 with the anomalous signal shown as red electron density.

Closer inspection of the metal binding site showed that there were differences in the binding mechanism for Ag(I) and Cu(I), see Figure 5.6.5. The binding of Ag(I) showed that the coordination of the Ag(I) ion occurred through NE2-amide group of the histidine (His63) and the thiol groups of the two methionine's (Met74 & Met76). The nearby tryptophan residue (Trp71) forms a coordination 'cap' through the negatively charged π-orbital of the aromatic ring and the positively charged metal ion.

Whereas the binding of the Cu(I) ion follows the same initial binding mechanism of coordination through the histidine and methionine's, however the difference occurs in tryptophan 'cap'. The coordination of the Cu(I) seems to substitute the tryptophan for a water molecule. The small ion size of the Cu(I), compared to Ag(I), seems to facilitate the access of the water due possibly to the shorter bond length which results in the tryptophan being pushed away from the binding site (Figure 5.6.5-B).

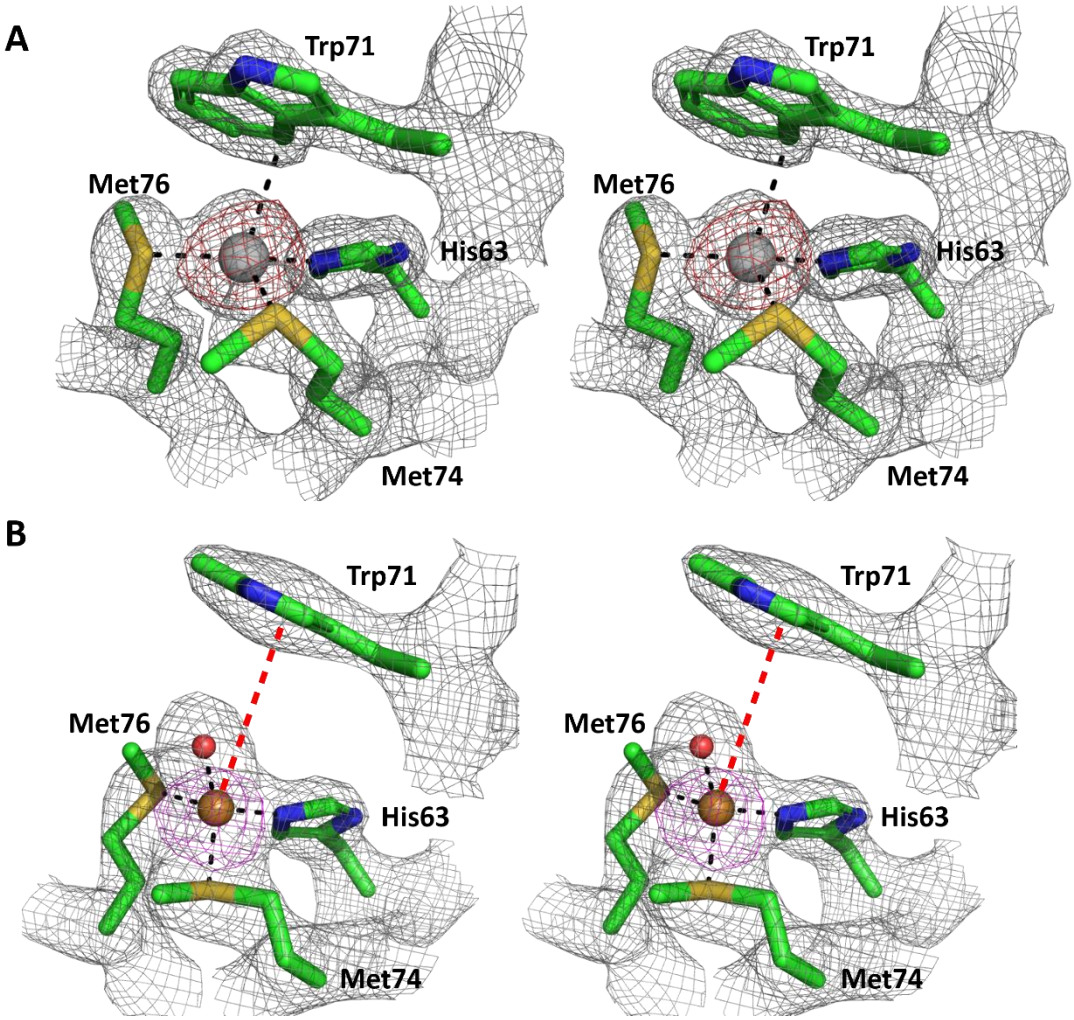

Figure 5.6.5: Stereo-view of the electron density maps (Grey) for **(A)** Ag(I) and **(B)** Cu(I) bound ec-SilF1Δ (rmsd for both 1.08). Ag(I) and Cu(I) ion anomalous density maps are shown in Red and Magenta respectfully, confirming the metals presence. The change in position of Trp71 can clearly be seen through comparison of the two structures, with the Cu(I) bound form no longer showing coordination (Red line). The water molecule (Magenta sphere) can be seen coordinating the Cu(I) directly.

In addition to the main difference in coordination, through the position of Trp71, the position of the coordinating methionine's also varies between Ag(I) and Cu(I) binding based on their rotameric conformer. The bond length observed between Met74 and Ag(I) was shown to be 2.6 Å and for Met76 it was 2.5 Å, however for Cu(I) coordination it was 2.2 Å and 2.3 Å respectfully. Looking at Figure 5.6.5 the subtle differences in the rotameric state can be seen, with Met74 adopting a significantly different rotameric conformer out of the two methionine's.

The coordination length of the π-bond of Trp71 to Ag(I) is 3.8 Å whereas for Cu(I) the coordination length is 5.8 Å, an increase of 2.7 Å which is larger than the accepted length for a π-bond interaction. However, the substituted water molecule has a bond length of 2.4 Å, which is within the normal coordination lengths observed.

The only stable bond length between the two structures is His63 which is 2.3 Å for both metal ions. Table 5-3 shows the bond lengths observed.

Table 5-3: Bond lengths of the four metal binding residues to Ag(I) and Cu(I). Error in measurements is ±0.014Å.

Bond (X = ion)	**SilF-Ag(I) (Å)**	**SilF-Cu(I) (Å)**
N-X (His63)	2.3	2.3
CE3-X (Trp71)	3.1	5.8 (no interaction)
S-X (Met74)	2.6	2.2
S-X (Met76)	2.5	2.3
H_2O-X	-	2.4

5.7 Hydrogen-Deuterium Exchange Mass Spectroscopy (HDX-MS)

Following the determination of the structures of both apo and holo bound ec-SilF1Δ and the results of the CD analysis, HDX-MS was carried out to confirm the metal binding site and assess if any additional metal interaction sites exist. HDX-MS looks at the changes of deuterium uptake between the bound and apo states. Elena Holden and Prof. Justin Benesch (University of Oxford, UK) conducted experiments and analysis. HDX-MS was conducted following the method in Section 2.7.7, whereby the protein was diluted in deuterated buffer, initiating the exchange reaction. Deuterium exchanges onto the backbone amides of the protein at various rates depending on the individual amide's solvent accessibility and inter/intramolecular bonds. Ligand binding to the protein masks the binding site and blocks the site from deuterium exchange, comparing mass spectra with and without a ligand present identifies binding sites. In the case of this study only Ag(I) was used and non-aerobic conditions had to be used meaning that Cu(I) would readily be oxidised to Cu(II).

The initial mapping experiment, or 0s time point, where no deuterium is incorporated, produced peptides covering 88.9% of the protein amino acid sequence, see Figure 5.7.1.

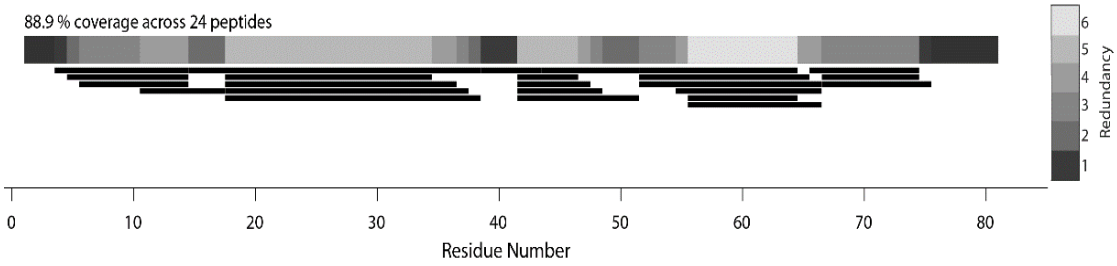

Figure 5.7.1: Initial HDX digestion map of apo ec-SilF1Δ showing approximately 89 % of coverage of the peptide sequence.

The addition of Ag(I) showed an increased protection (reduced deuterium exchange) for a 25 amino acid sequence that included the metal binding site (IDMNSKKITIS**H**EAIPAVG**W**PA**M**T**M**) see Figure 5.7.2. The region in question showed a 16% reduction in deuterium uptake, suggesting Ag(I) interacts within the region as expected. Changes in deuterium uptake were deemed significant by a Students T test at 99.9% confidence.

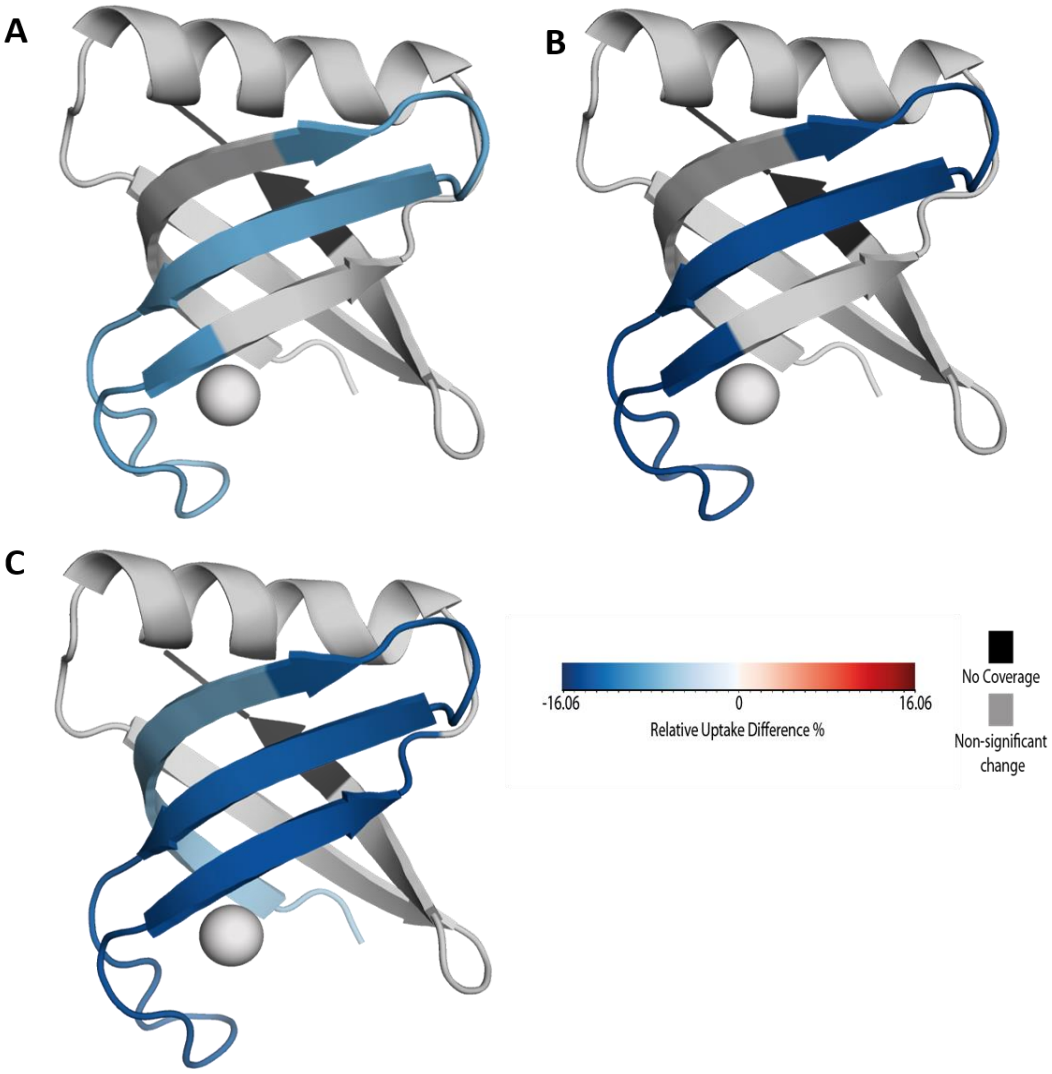

Figure 5.7.2: HDX of SilF in its Ag(I) bound form compared to its apo form. **(A)** 30s incubation, **(B)** 5 minute incubation & **(C)** 30 minute incubation. The Blue colouring illustrates the amount of protection deuterium protection over time.

5.8 Discussion

The ability to produce the protein to this level has led to in depth characterisation of the protein within this chapter.

5.8.1 Crystallisation of ec-SilF1Δ

Crystallisation of ec-SilF1Δ in its apo and Ag(I) bound state yielded crystals within a few days. The crystallisation of ec-SilF1Δ with Cu(I) was not as straight forward, as the biggest issue was maintaining the oxidation state of Cu(I). As highlighted in Sections 2.8.1 and 5.4.2 ec-SilF1Δ was incubated with Cu(I) in an anaerobic glove box, ensuring the Cu(I) did not oxidise, before being removed as to allow the protein to be dispensed using the Mosquito. It was hoped that by being bound to the protein, oxidation of Cu(I) to Cu(II) would not occur as it would be protected. Once dispensed the protein crystallisation trays were returned to the anaerobic conditions to minimise any further oxidation.

The formation of crystals followed the standard protocol of cryo-protecting if necessary. With regard to the holo bound forms there was substantial evidence to add each metal ion into the condition to maintain the equilibrium of bound and unbound protein (Hassell *et al.,* 2006), as essentially the protein crystals would be diluted into a new condition all be it the same condition with glycerol added in. However, as Ag(I) is insoluble in a lot of conditions, trial cryo-protectants were prepared which all showed upon addition of $AgNO_3$ the Ag(I) crashed out of solution, turning milky white. A similar observation was seen in the Cu(I) trial protectants, with the solution turning cloudy and opaque. Therefore, it was decided that no metal would be added to the cryo-protectants. It was hoped that the tight binding of the metal ions, seen in ITC from

Chapter 4, would minimise the effects of the equilibrium change and maintain complex of ec-SilF1Δ-metal ion.

5.8.2 The Structure of ec-SilF1Δ

Initial structural characterisation of ec-SilF1Δ was based off the homolog CusF (PDB 2VB2), of which there is approximately 47% sequence homology. The structure of CusF is that of a five stranded β-barrel with two extended loops on each end, of which the metal binding site is on one of them (Xue *et al.,* 2008). Therefore ,it was assumed that ec-SilF1Δ would also adopt a very similar structure.

Structural analysis of ec-SilF1Δ through CD (Section 5.3) gave an idea of the secondary structures present, with the predicted β-barrel being the predominant component and an unordered region (Figure 5.3.1). However, unlike CusF there was evidence of α-helical content within the protein as well. Subsequent structure determination in Section 5.6.1/2 showed that the actual structure of ec-SilF1Δ was a five stranded β-barrel with a α-helix at one end and an extended loop at the other, where the metal binding site is situated similarly to CusF (See Figure 5.8.1).

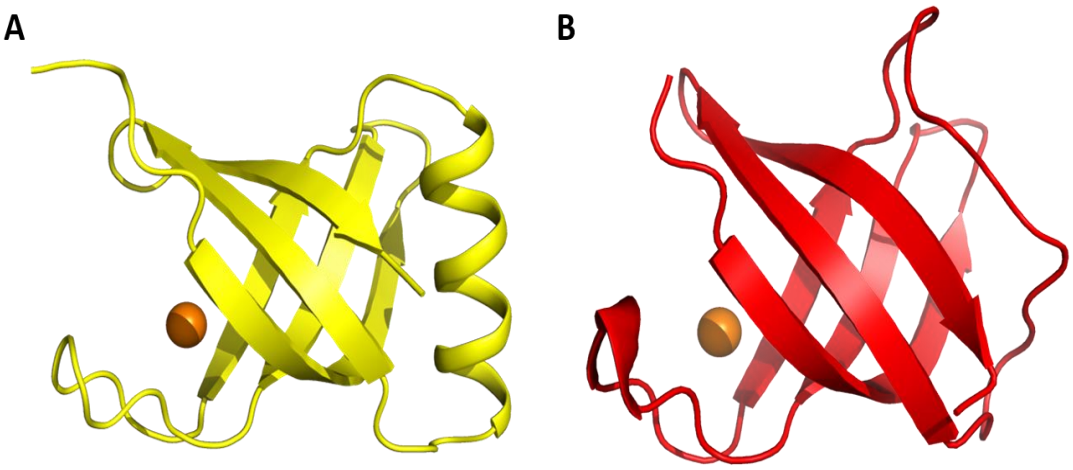

Figure 5.8.1: Comparison of ec-SilF1Δ (Yellow) and CusF (Red), both structures bound to Cu(I). Structurally there are many similarities between the two with a β-barrel core and an extended loop where the metal binding site occurs at one end. The other end however is where the differences occur, with ec-SilF1Δ presenting an α-helix whereas CusF has another extended loop

Interestingly the CD analysis showed that the α-helical content of ec-SilF1Δ increased upon addition of both Ag(I) and Cu(I) ions, suggesting that the binding of the metal ion stabilises the protein. However, the crystal structures do not show any major differences in the α-helix between the apo and holo forms. Although no overall major change was observed in the α-helix, the model of the apo structure showed that the α-helix N-terminal end did show variability in its position of the amino acids between the three molecules (see Figure 5.8.2). This suggests that there is flexibility within the α-helix resulting in the differences, which may suggest that the α-helix is unstable in solution but within the crystal the packing has stabilised enough to not be noticeable.

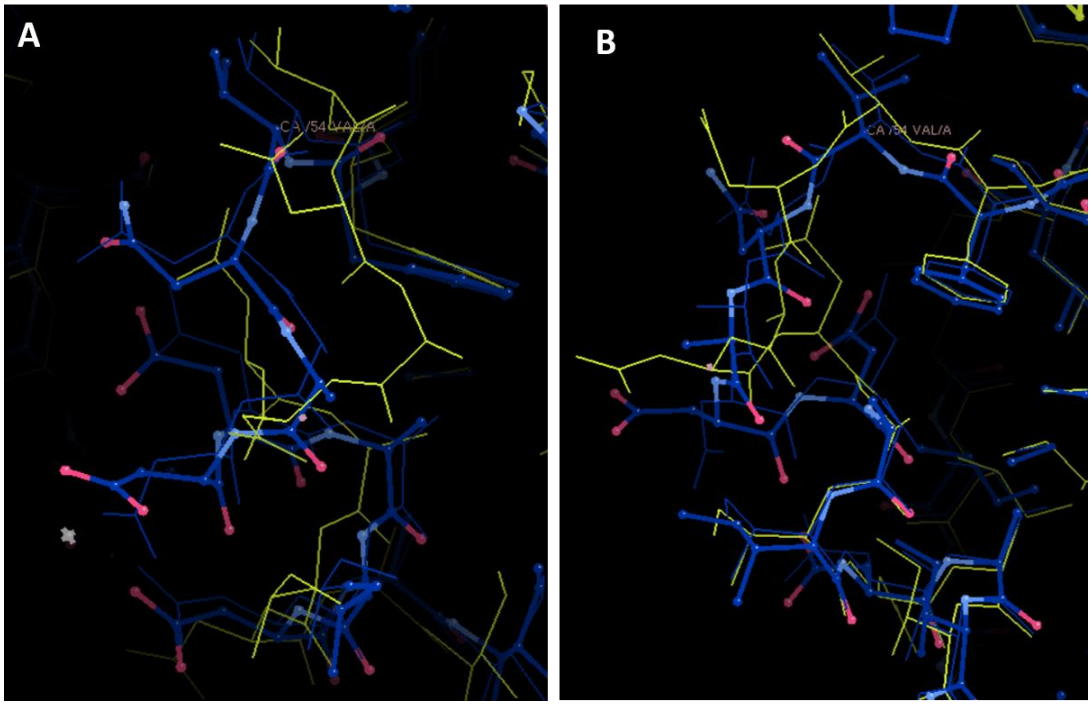

Figure 5.8.2: Overlay of the α-helix region of apo ec-SilF1Δ showing the 3 chains present. The two Blue chains some consistency with each other,, however the Yellow chain shows a drastic difference in its position. This highlights the flexibility within this region of the protein.

5.8.3 The Metal Binding Site of ec-SilF1Δ

The metal binding site of ec-SilF1Δ is formed from strictly conserved residues His63, Trp71, Met74 and Met76 and is located on the extended loop end of the β-barrel, see Figure 5.8.3.

Upon Ag(I) binding the histidine and methionine residues occupy three of the coordination sites of the bound metal. The coordination sphere is completed by the indole ring of Trp71, which forms a π-cation interaction to complete the tetrahedral coordination sphere (Allen *et al.,* 1991). However, Cu(I) binding adopts a distorted trigonal coordination geometry through His63, Met74 and Met76, but the fourth coordination site is occupied by a water molecule not the tryptophan (see Figure 5.6.5). The presence of the water molecule prevents the formation of the π-cation

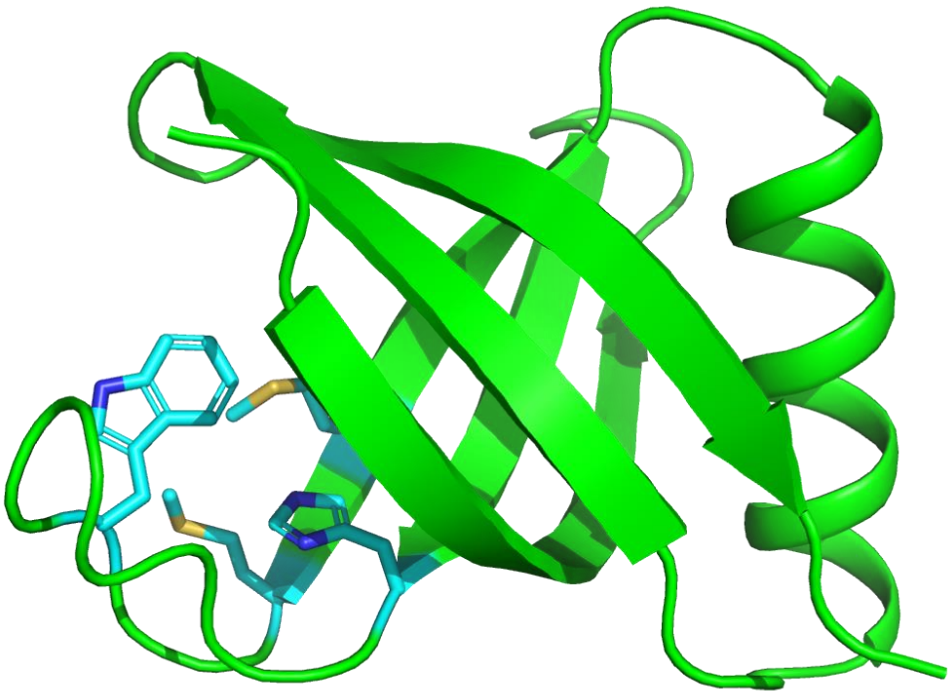

Figure 5.8.3: Structure of ec-SilF1Δ with the metal binding site residues coloured in Cyan. Their position is situated at the extended loop end of the protein.

interaction between Cu(I) ion and the indole ring of Trp71. The interaction was observed in all molecules within the crystal, this persistence suggests that Cu(I) to water binding is stronger and more favourable than to Trp71. It also suggests that the Ag(I)-Trp71 binding is stronger than presumably an Ag(I)-water interaction as this is not observed.

Comparisons to the CusF system shows that there more differences than just those observed between the two ion binding conformations. The high-resolution (1.0 Å) structure of CusF with Ag(I) bound (Loftin et al, 2007) shows that the position of all the binding residues are relatively similar, with the coordinating methionine's adopting the greatest variance (Figure 5.8.4-A). However, with this said the overall binding site shows minimal differences. Whereas when comparing CusF to Cu(I) bound ec-SilF1Δ there is much more variance. Firstly, the coordinating

methionine's, there is substantially different rotamers found within the binding of Ag(I) and Cu(I) to ec-SilF1Δ and also to CusF (see Figure 5.8.4-B). The varied position of the methionine's within Cu(I)-ec-SilF1Δ may be a result of the mobile water molecule, with the position adopted being the most thermodynamically favourable. However, a more plausible explanation is that the smaller ionic radius of Cu(I) (0.60-0.74 Å) relative to Ag(I) (1.0-1.14 Å) constrains the geometry of the coordinating methionine's, resulting in them tucking into the binding site more to interact with the metal (Shannon, 1976). A similar observation is seen in the CusF structure supporting this hypothesis, as a water molecule is not present within the binding of Cu(I) to CusF.

In addition, the position of the tryptophan residue (Trp71) has already been shown to have a large conformational change, based on the presence of a water molecule within ec-SilF1Δ. The lack of a water molecule within CusF is an interesting one, with no real explanation as to why it occurs in ec-SilF1Δ and not CusF. However, its presence would explain why a lower binding affinity was observed compared to Ag(I) binding. Stabilisation of Cu(I) via a π-cation interaction has previously been demonstrated for Cu(I) binding to CusF (Xue et al 2008). The lack of coordination through this bond is likely the main cause for such a vast difference in binding affinities.

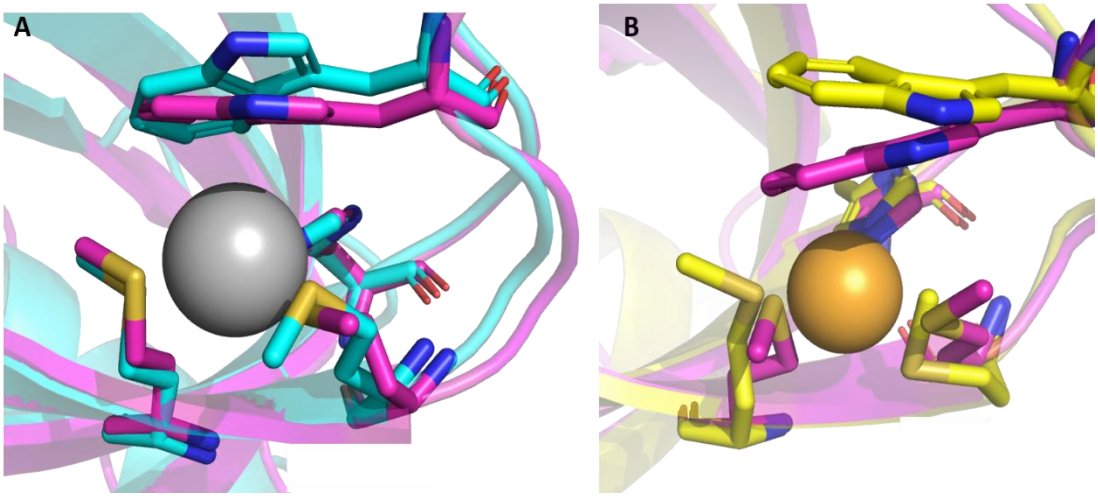

Figure 5.8.4: Comparison of the metal binding site of CusF and ec-SilF1Δ. **(A)** ec-SilF1Δ (Cyan) and CusF (Magenta) binding to Ag(I), the position of all the residues is relatively constant with the methionine's showing the greatest difference. **(B)** ec-SilF1Δ (Yellow) and CusF (Magenta) binding to Cu(I). There is much greater variance between the two compared to when Ag(I) is bound. The two methionine and tryptophan residues show large differences in conformations.

In addition to the lack of a π-cation interaction with Cu(I) resulting in lower binding affinity, further reductions can be predicted based on the preference of sulphurous ligands to bind Ag(I) relative to Cu(I) (Nies, 2003). The results of the ITC studies (Chapter 4.6) show that there was a small reduction in the binding enthalpy observed between ec-SilF1Δ and Cu(I) when compared to Ag(I) binding, with an overall lower binding affinity as predicted as well.

The fact that both SilF and CusF both bind Ag(I) and Cu(I), but exhibit a preference for the former, may reflect a more general biological need of copper for some cellular systems. Whereas some periplasmic proteins, for example, the zinc-copper superoxide dismutase (SODC) require copper for activity, and it is advantageous to maintain non-harmful level of copper in the periplasm (Rensing and Grass, 2003). The results of the structural characterisation of ec-SilF1Δ, combined with the binding

studies in Chapter 4, gives no explanation on the evolution of the system nor why ec-SilF1Δ has a tighter overall affinity to both Ag(I) and Cu(I). However, it does show why there are differences in affinity between Ag(I) and Cu(I) binding within ec-SilF1Δ.

Finally based on the structures of the Ag(I) and Cu(I) bound ec-SilF1Δ there was conjecture on whether more than one binding site was present. In both structures there was the traditional metal binding site with the metal ion clearly present. However, there was also anomalous density present at another site (Histidine 98) that was clearly an electron dense rich atom which must have been another Ag(I)/Cu(I) ion.

Two proposals were put forward, the first being that this was another metal binding site that had previously not been observed. The other, and more likely was that this was a crystal contact point that utilised the metal ion for binding.

Based on the ITC results (Chapter 4.6) there was clearly only evidence for one Ag(I)/Cu(I) per ec-SilF1Δ, however, to make sure this was absolute HDX was conducted (Section 5.7). HDX shows areas of the peptide backbone that are protected or not protected from deuterium exchange, ligand binding results in protection. The results of the HDX (Figure 5.7.2) showed that the main metal binding site showed large levels of deuterium protection, as a result of the metal ion binding. The region relating to His98 however did not show any protection, suggesting that this was not a true metal binding site. Therefore, it would suggest that the binding of a second metal ion was a crystal contact artefact.

5.8.4 Comparison of the structure of ec-SilF1Δ

The structure of ec-SilF1Δ shows many similarities to its homolog CusF as well as some differences, namely the presence of the α-helix (see Figure 5.8.1). Further structural comparison of ec-SilF1Δ through several structural and functional servers, including MetalPDB (Putignano *et al.,* 2018) and Dali (Holm, 2020), indicated several other similar proteins were identified.

Through the metal PDB, which looks at the metal binding sites of proteins and compares them to other known structures, only CusF was identified as a similar protein. The analysis highlighted the histidine and methionine residues as the predominant metal coordinators, leaving out the tryptophan highlighting that it may not be essential for metal binding of which the Cu(I) ec-SilF1Δ would support.

Structures from the Dali servers, based on a Z-score between 8.6-7.2, showed that in addition to CusF, subunit S1 of Pertussis toxin (PDB; 1PRT), a domain from pro-protein glutaminase (PDB; 3A54), and subunit B of subtilase cytotoxin (PDB; 3DWA) showed the greatest similarities in structure to ec-SilF1Δ. The identified structures are either protein domains or small proteins that fall under a family of proteins designated oligonucleotide binding (OB) fold proteins. As suggested by their name they predominantly bind to nucleotide sequences. The Dali server showed that one of these proteins, ModE (Z-score 3.2), is a molybdenum sensor that regulates transcription of several genes involved in cellular molybdenum control by binding to ssDNA, however to do so it must bind to molybdenum (Schuttelkopf, 2003). To date this is the only partial metal binding OB-fold protein (Gourely *et al.,* 2001), however it could be that ec-SilF1Δ also falls into this category of proteins.

The family of OB fold proteins show a structure composed of 5 stranded (or sometimes more) β-barrel interlinked with an evolving definition of either an α-helix, extended loop or three-helix bundle between strands β_3-β_4 (Arcus, 2002; Bochkarev & Bochkareva, 2004; Murzin, 1993). Since their discovery in 1993 there have been over 1500 structures containing OB-folds deposited within the PDB, Figure 5.8.5 shows several structures OB-fold proteins with a comparison to ec-SilF1Δ.

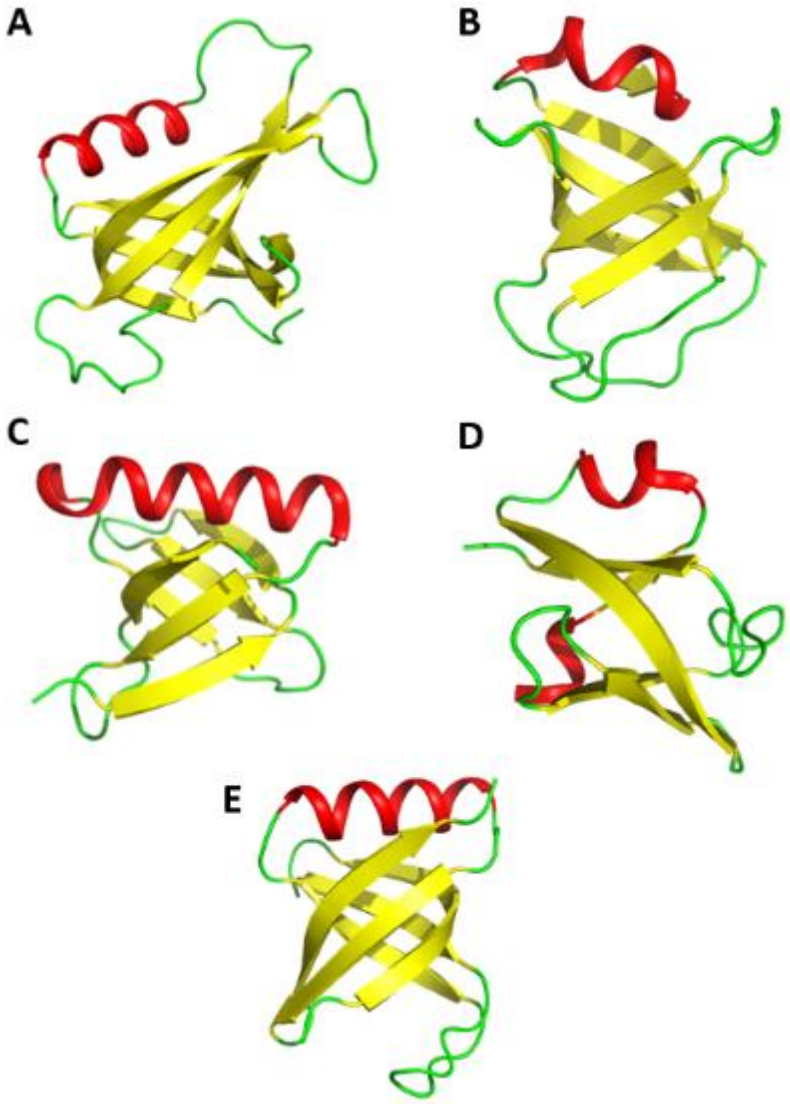

Figure 5.8.5: Comparison of several OB-fold proteins and domains including ec-SilF1Δ. (A) Pertussis toxin domain (1PRT), (B) RPA domain (1L1O), (C) pro-protein glutaminase domain (3A54), (D) ModE (1O71) and (E) ec-SilF1Δ.

The binding regions of OB-fold proteins vary with no singular defined binding region identified. However, from the deposited structures of OB-fold proteins with their ligands many of the interactions occur in the extended loop regions between the β-sheets, with many utilising the α-helix/extended loop region (Flynn & Zul, 2010; Theobald *et al.,* 2003).

Interaction studies between the CusF and CusB (CusB is a fusion protein of the CusCBA complex, homologous to SilB), have shown that through cross-linking, of lysine residues, two regions of CusF interact with CusB (Mealman *et al.,* 2011). The cross-linked regions occur towards the N-terminal (CusF Lys18) and C-terminal (CusF Lys45) sides of the metal binding site, however both are parallel to each other in the structure. The study proposed that the Lys18 forms the main interaction between the proteins and the latter (Lys45) is involved in specificity to CusB, giving an overall dual recognition mechanism. The basis of this conclusion was that studies whereby CusF was substituted with SilF, the result was that no interaction occurred between SilF and CusB (Bagai *et al.,* 2008). Closer inspection of the sequences around the cross-linked regions (see Figure 5.8.6) showed that there is high conservation around the K18 residue in both species. Whereas the Lys45 shows virtually no conservation between the species, with ec-SilF1Δ showing a greater charge difference in the region. The charge difference is a result of several aspartic acid residues being present giving a negative charge. Therefore, based on the conservation of the Lys18 region it would suggest that it is involved in the interface of metal transition between CusF/SilF and CusB/SilB. Whereas the varied region of Lys45 suggests that it is a regulatory role, whereby CusB/SilB can distinguishes between

the target chaperone. This theory is given support by the fact that the *cus* system can occur on its own but when the *sil* system is present the *cus* system is always present as well (Hooton *et al.,* 2021).

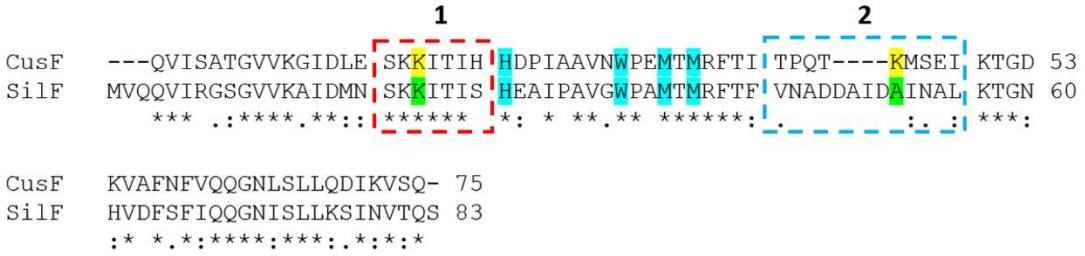

Figure 5.8.6: Sequence alignment of CusF and ec-SilF1Δ, with a number of key residues highlighted from Mealman *et al.,* (2006). Highlighted in Yellow are the two lysine (K18 & K45) residues that were cross-linked, in Green are their counterparts in ec-SilF1Δ. Conservation of K18 in SilF is seen however not for K45. The residues within the Red box (1) are the immediate residues next to K18, they are highly conserved between the species. Residues highlighted in the Blue box (2) however show very little conservation, this is the region which corresponds to the extended loop of CusF and the α-helix of ec-SilF1Δ.

As started earlier in the section, sole metal binding OB-fold proteins are virtually unheard of, with only ModE shown to interact with a metal ion of which this is not the main function of the protein. Although no studies have been conducted to look at an interaction between oligonucleotides and oligosaccharides with either CusF or ec-SilF1Δ, it is possible that this may occur, although what function this would provide is unknown. The evolution of CusF and ec-SilF1Δ, if any, from this family of proteins is intriguing, especially when looking at such a large change in target ligand going from sugars/nucleotides to metals.

5.9 Conclusion and Future Work

Overall, the successful structural characterisation of ec-SilF1Δ in its apo and holo bound states to Ag(I) and Cu(I) were solved demonstrating the

structural basis for difference observed in the affinities SilF for Ag(I) and Cu(I). The proteins show large structural homology to its homolog CusF, however contains some structural differences namely the presence of a α-helix at one end of the protein.

The binding mechanism of ec-SilF1Δ was also shown to be the same as CusF, whereby the main coordination of the metal ions occurs through a histidine and two methionine residues. However, differences lay in the position of the tryptophan (Trp71) residue, for Ag(I) binding the tryptophan residue forms a coordinating π-cation bond the same as in CusF-Ag(I). However, with regard to Cu(I) binding to ec-SilF1Δ the tryptophan is displaced by a water molecule which coordinates the Cu(I) ion instead. The displacement of the tryptophan lends support to the ITC results observed in Chapter 4 which showed a lower affinity of ec-SilF1Δ to Cu(I) over Ag(I).

Finally, the exploration of ec-SilF1Δ protein family was investigated, with the ec-SilF1Δ belonging to the oligonucleotide/saccharide fold family. However, ec-SilF1Δ, and by extension CusF, form a sub-family of OB-fold proteins that bind to metal ions over the traditional ligand for this family.

Going forward with SilF the main areas of interest lie within the metal binding site and the interaction of SilF with other members of the sil family.

One area of interest is to look at mutating residues within the metal binding site, specifically His63, Met74 and Met76 as they are directly involved in coordination. Mutating these residues one at a time may affect the binding affinities of the protein and/or the specificity to Ag(I) and Cu(I). In conjunction with the metal binding site is the investigation to see if SilF binds other metal ions. The binding mechanism of SilF to

Cu(I) leads to the possibility of other small, similarly coordinated metal ions to bind to the protein.

Another main priority going forward would be to investigate the interaction of SilF with SilB through cross-linking studies as was conducted for CusF-CusB, as well as obtaining a structure to assess the actual residues involved in the interaction and the mechanism of how SilF off loads the metal ion to SilB. Additionally looking at the substitution of SilF with CusF to see if the system can still work, or as in the CusF substitution with SilF the system fails, and no interaction is observed.

6 Outer Membrane Protein SilC

6.1 Introduction

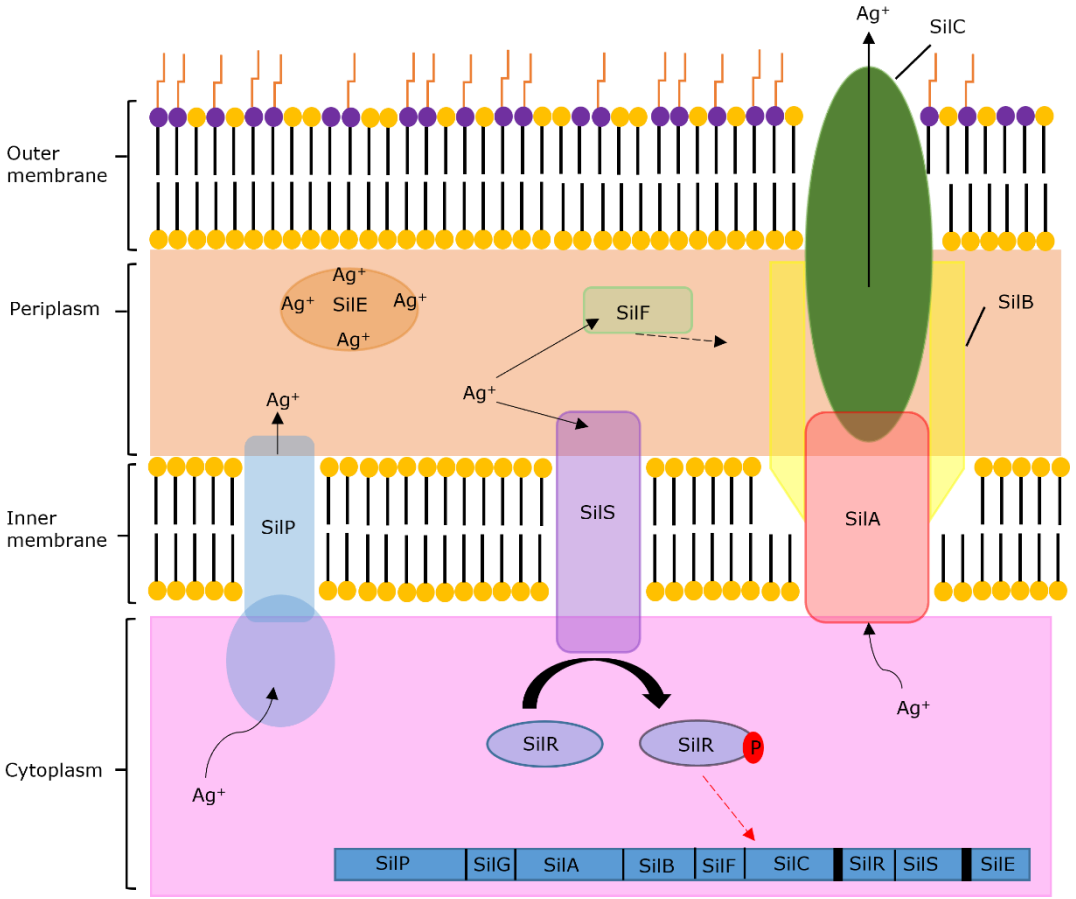

Figure 6.1.1.: Sil system overview with SilC highlighted (Dark Green) in the outer membrane.

The largest component of the *sil* system is the SilCBA efflux complex (see Figure 6.1.1) and based on its homology to the CusCBA complex the three proteins that appear to have similar putative role in metal ion efflux. The complex consists of an inner membrane RND pump, SilA, which is proposed to use a proton gradient to transport its target ligand into the periplasm. The second protein is a proposed membrane fusion protein, SilB, which links SilA to the outer membrane component SilC: this final protein is an outer membrane protein (OMP) which forms a porin like structure that is proposed to facilitate Ag(I)) to exit the cell

(Franke *et.al.,* 2003). This chapter focuses on the characterisation of the outer membrane factor SilC.

OMP's such as CusC, TolC and OprM, of which SilC is homologous to, are trimeric assemblies whose monomer contain four β-strands and up to twelve α-helices (Figure 6.1.2-B). The active trimeric complex has a membrane embedded β-sheet porin-like channel structure on the surface and a predominately α-helical domain within the periplasm (Koronakis *et al.,* 2000; Kulathalia *et al.,* 2011). Figure 6.1.2-B shows the structure of CusC in its monomeric form and in its trimeric barrel form.

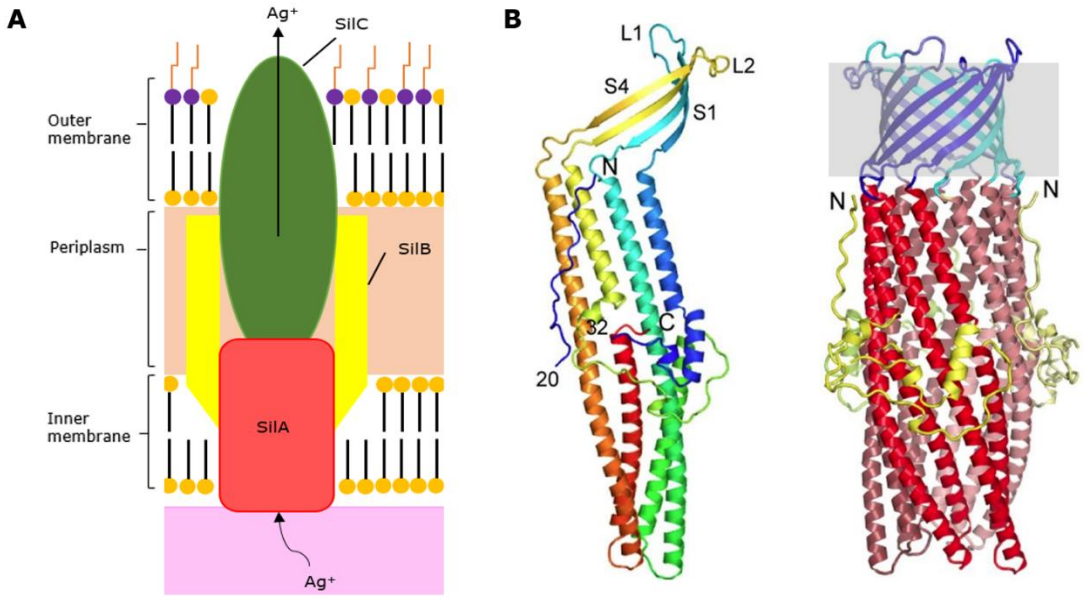

Figure 6.1.1: (A) Basic overview of the makeup of the membrane spanning SilCBA complex and the proposed method of Ag(I) transportation. **(B)** CusC monomer (Left) comprised of 4 β-strands and 12 α-helices. (Right) CusC trimer with the outer membrane bound β-barrel (grey) and the periplasmic α-helical barrel now formed. (Images of CusC modified from Kulathila *et al.,* 2011 (PDB; 3PIK))

6.2 Aims

SilC is an essential component of the SilCBA system that is expected to play a key role in the control of silver efflux. To this end I will aim to

I. Express and purify SilC and enable both biophysical and structural analysis can be conducted.

II. Determine the structure of SilC using crystallography. Comparing any structure to other known outer membrane factor proteins

III. Understand the relationship between SilC and the metal ions Ag(I) and Cu(I)

6.3 Expression and Purification

Over expression plasmid constructs for SilC were previously designed and assembled by Dr. Karishma Asiani and the Oxford Protein Production Facility (OPPF) (now Protein Production UK (PPUK), RCaH, Harwell Campus, Oxfordshire, UK). Two full length constructs were designed, with either a C-terminal 6His or GFP-6His-tag (pOPINE-GFP).

6.3.1 Expression

The expression plasmid with a C-terminal 6xHis-tag were transformed in C43 *E.coli* cells (according to section 2.2.1). Expression followed the protocol outlined in section 2.6.1. Cell pellets were either used for purification straight away or were stored at -80 °C.

6.3.2 Purification

Purification of SilC with a C-terminal 6xHis-tag followed the protocol outlined in section 2.6.2. Solubilised samples of SilC in LDAO were run down a HisTrap column and eluted using an imidazole gradient following the protocol in 2.6.2). Fractions containing a 280 nm absorbance were analysed by SDS-PAGE gel (Figure 6.3.1-A).

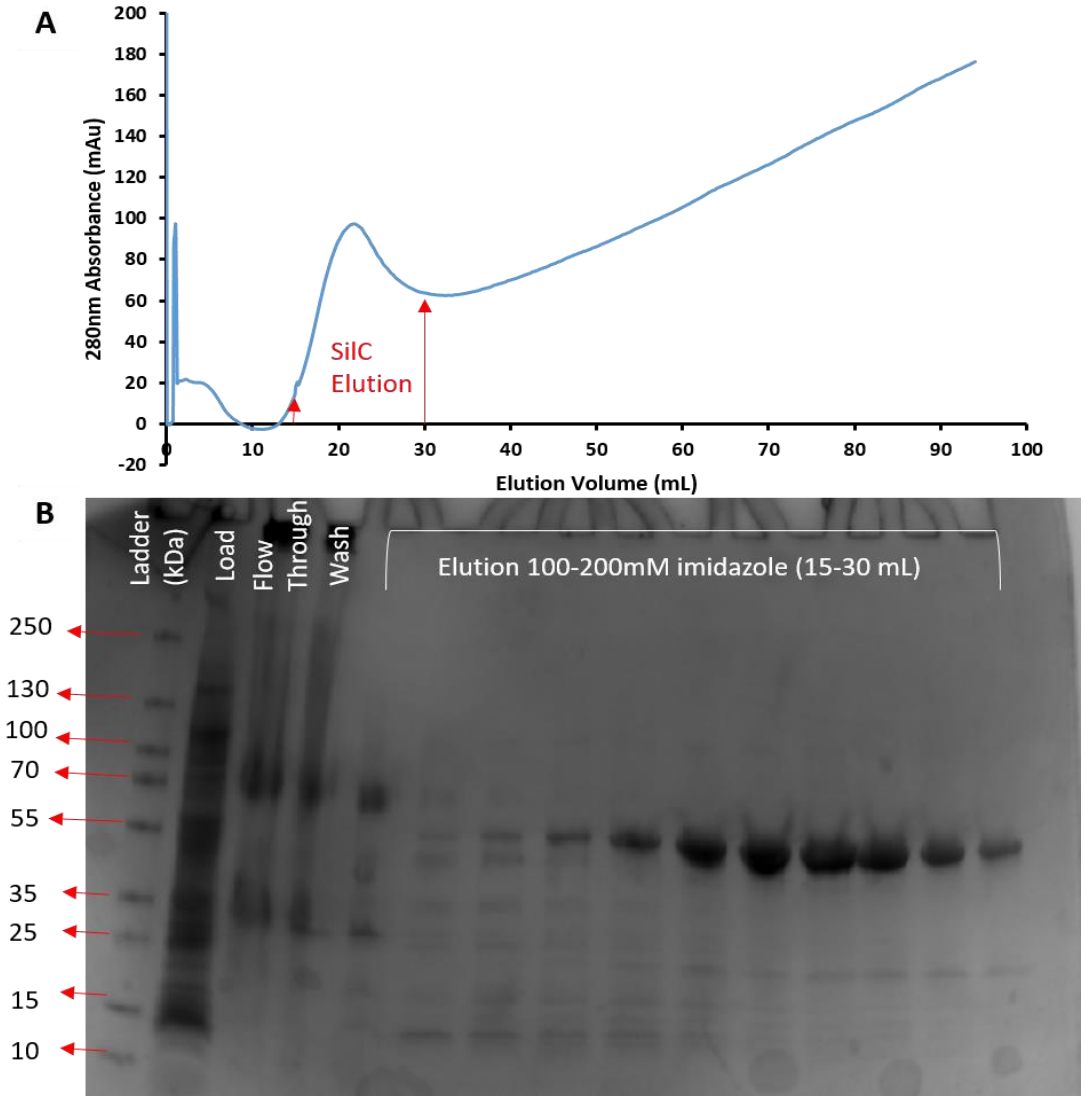

Figure 6.3.1: (A) Absorbance (280 nm) trace of SilC during HisTrap gradient elution, with the protein eluting between 100-200 mM imidazole. **(B)** SDS-PAGE of SilC post HisTrap gradient elution. The majority of SilC eluted between 150-200 mM imidazole (15-30 mL).

Fractions of SilC (expected Mw = 55 kDa) were pooled and concentrated to 5 mL for buffer exchange. Buffer exchanged entailed using SEC Buffer 3 (2.6.2) to pre-equilibrate two desalting PD10 columns (Cytiva, UK). Once equilibrated, 2.5 mL of the pooled SilC was applied to the column followed by 3 mL of SEC Buffer 3 to elute the protein from the column. The resulting two 3 mL samples were collected and concentrated down to 350 µL for SEC as outlined in 2.6.2.

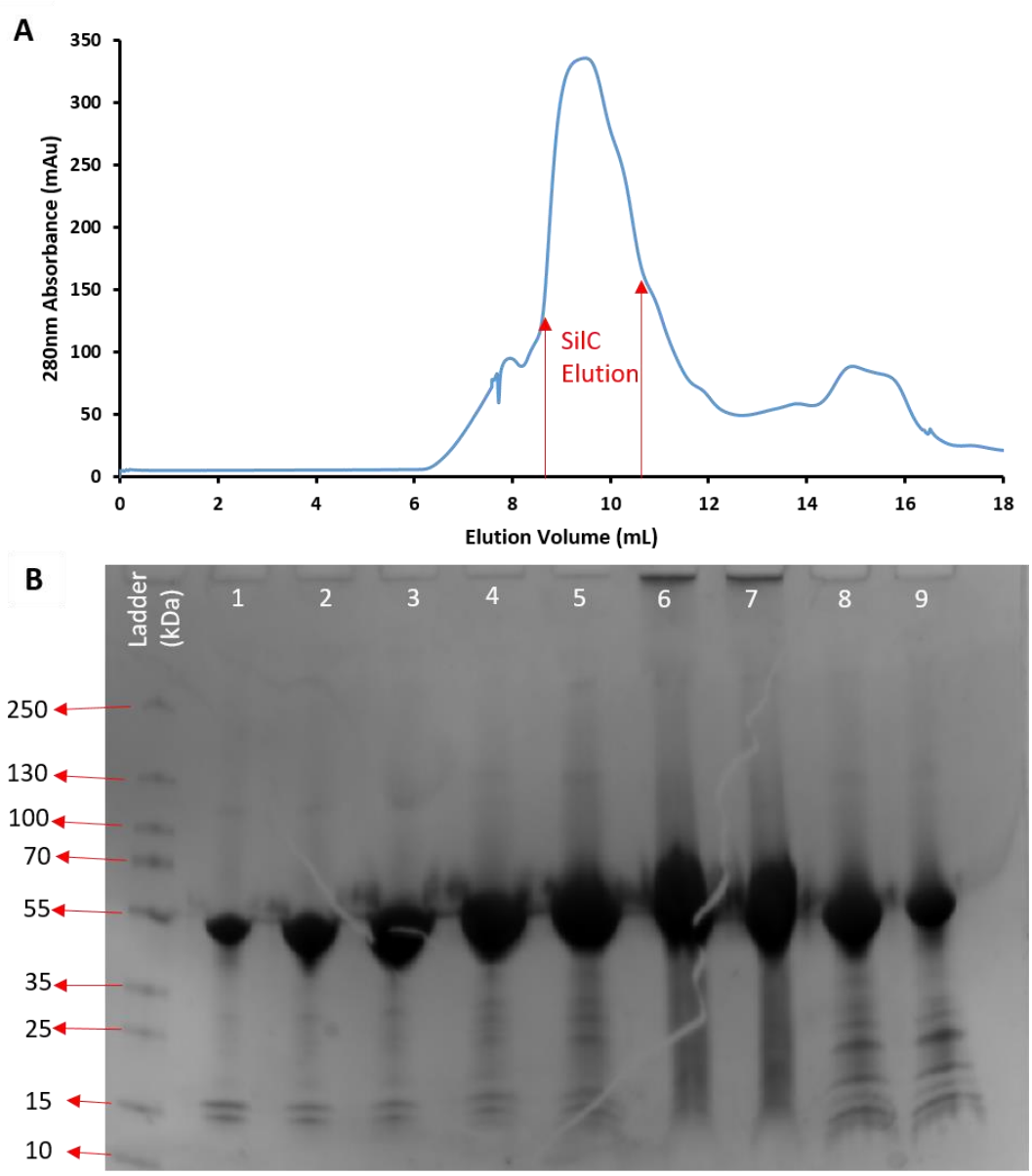

Figure 6.3.2: (A) 280 nm absorbance of SilC after SEC with a Superdex S200 10/300 column, elution point of SilC is marked with red arrows. **(B)** SDS-PAGE of SilC after SEC. Lanes 1-3 correspond to a small peak occurring at 8 mL, while lanes 4-7 correspond to the large peak at 9.5 mL which contains most of SilC. Lanes 8-9 correspond to the fractions between 11-12 mL.

Fractions from SEC that corresponded to the 280 nm peak were analysed by SDS-PAGE gel electrophoresis, and the results are shown in Figure 6.3.2-B. Fractions of SilC were concentrated to 13 mg/mL for immediate

structural and biophysical characterisation or were snap frozen for storage. Typically, it was found that a total yield of 1 mg of SilC was produced per 1 L of TB media.

6.4 Biophysical Characterisation

6.4.1 SEC-MALLS

Following purification, the stoichiometry of SilC was characterised by SEC-MALLS following the method outlined in section 2.7.2 with the results shown in Figure 6.4.1 below.

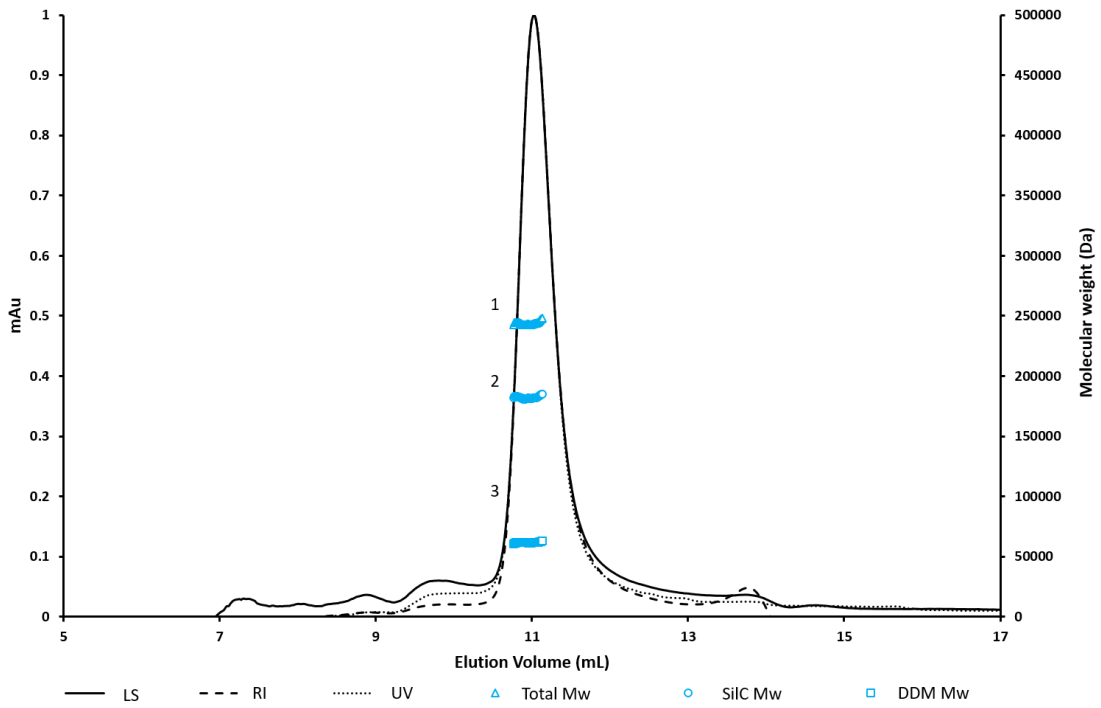

Figure 6.4.1: SEC-MALLS trace of SilC showing Light Scattering (LS), refractive index (RI) and Ultraviolet 280 nm (UV) absorbance's. (1) Indicates the molecular weight estimation of the entire complex, (2) the molecular weight of the protein component and (3) the molecular weight of the detergent component.

Careful analysis of the SEC-MALLS data was conducted using conjugate analysis to distinguish between two components (see section 2.7.2 for

the method), in this case protein and detergent, showed that the protein molecular weight component of the main peak was 169.3 kDa, with the detergent content of approximately 74.7 kDa and an overall molecular weight 244 kDa. The molecular weight of the protein component suggests that stoichiometry of 3 monomers per Mw estimation (3:1) is present (169 kDa / 52 kDa = 3.25), thus showing that SilC is trimeric in solution.

Table 6-1: SEC-MALS data for SilC, showing the Mw of the complex, protein and detergent components.

SEC-MALS Output	Values
Co-polymer Mw (kDa)	244 (±1.3%)
Protein Mw (kDa)	169.3 (±6.7%)
DDM Detergent Mw (kDa)	74.7 (±4.2%)
Polydispersity (Mw/Mn)	1.001

6.4.2 Nano-DSF Stability Assay

Now that the oligomeric state of SilC has been shown to be trimeric from the SEC-MALLS analysis, we next analysed the stability of the complex using nano-DSF performed on the Prometheus NT.48 (Section 2.7.4). Assays were carried out using the method outlined in section 2.6.3, with an optimal protein concentration of 1 mg/mL. The results can be seen in Figure 6.4.2 and Table 6.2.

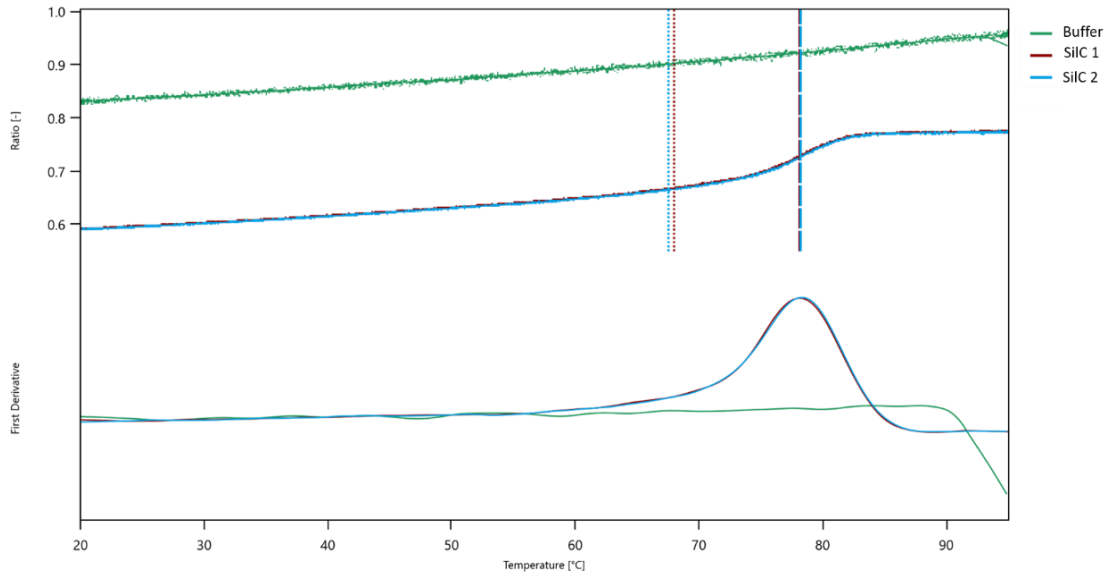

Figure 6.4.2: Thermal stability profile of SilC measuring the 330/350 fluorescence ratio. SilC (red and blue) shows a *T*m of approx. 78°C, while a buffer blank (green) was also run as a control.

The results of the assay show that SilC has a mean onset temperature of 67.7°C and a mean T_m of 78.2°C, both of which are reasonably high but commonly seen in outer membrane factor proteins such as OmpC which has a T_m of 75°C (Agarwal *et al.,* 2014 & Keegan *et al.,* 2010).

Table 6-2: Nano-DSF thermal unfolding results of SilC using Prometheus NT.48. The results show that SilC has a T_m of 78.2 °C

Temperature Point	Run 1 (°C)	Run 2 (°C)	Average (°C)
Onset	68.0	67.5	67.75
Inflection (T_m)	78.1	78.3	78.20

6.5 Crystallisation of SilC

SilC was concentrated to 13 mg/mL and dispensed into 3 well Swissci sitting drop plates following the method in section 2.8.1 with trays stored at both 20 °C and 4 °C. The screens used were Molecular Dimensions MemGold, MemGold-2, MemChannel, and MemStart/MemSys.

Crystals grew readily in two conditions: 0.1 M $MgCl_2 \bullet 6H_2O$, 0.1 M sodium citrate (pH 5) & 11% PEG 4000 (MemChannel B12, 4 and 20 °C at a 1:2 ratio of protein:matrix) and 0.12 M Lithium sulphate, 0.02 M Tris (pH 7.5), 0.1 M sodium citrate (pH 5) & 20% v/v PEG 300 (MemGold F2, 20 °C at a ratio of 1:1 protein:matrix). Crystals grew within 5 Days for MemChannel and MemGold conditions respectfully. Crystals in both MemChannel B12 conditions were small in size, measuring approximately 10 µm in size, with a plate like morphology. Crystals that grew in the MemGold F2 condition differed in size and shape, the crystals were approximately 50 µm in size with an octahedral morphology. Figure 6.5.1 shows the crystals that grew in each condition.

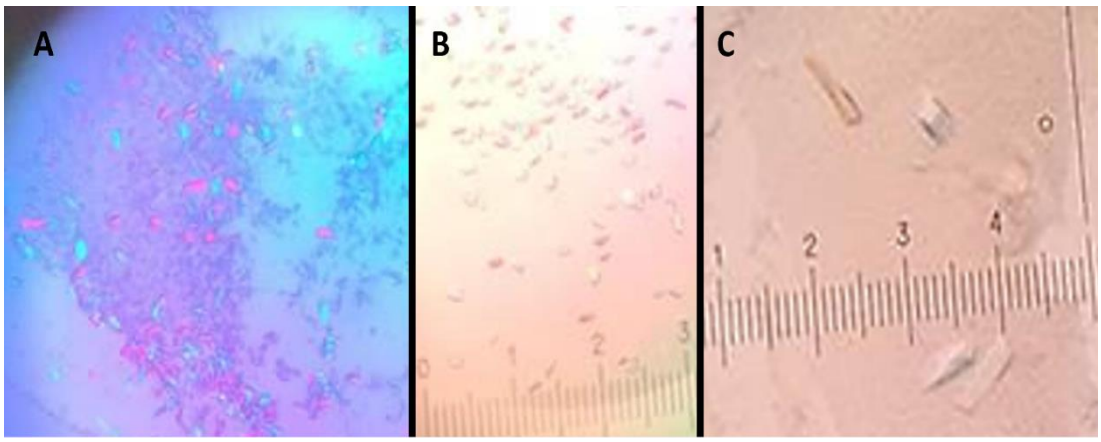

Figure 6.5.1: (A & B) Crystals of SilC grown in MemChannel B12 conditions at 4 °C **(A)** and 20 °C **(B)**, crystals were plate like measuring ~10 µm in length. **(C)** Crystals of SilC grown in MemGold F2 conditions at 20 °C measured ~50 µm in length and ~10 µm in width.

UV images of the crystals were taken in the Formulatrix to determine if the crystals were protein, with protein crystals showing up as white outlines of the crystal shape. Protein crystals of SilC from both conditions were mounted into crystallisation loops following the method outlined in section 2.8.4. Crystals in the MemChannel B12 condition needed additional cryo-protecting prior to freezing, the conditions are outlined in Table 2-7 in the same section.

6.6 Structure Determination of SilC

6.6.1 X-Ray Diffraction Data Collection

Due to the small size of the crystals, all X-ray diffraction data for the SilC crystals were collected on I24 (Microfocus MX) beamlines at Diamond Light Source with a Pilatus3 6M detector. Diffraction Crystals from the MemChannel B12 (4 °C) and MemGold F2 conditions diffracted to ~3.0 Å. Given this, and that the respective space group ($P6_322$) was readily assignable, the data was able to be entered into the automatic indexing and analysis pipeline on the Diamond servers (see section 2.8.6 for more information). The results of the automatic data processing showed that the data set processed in Dials had the best statistics compared to the other processes, the statistics are shown in Table 6-3.

Table 6-3: Initial SilC B12 X-Ray data collection variables and Dials analysis statistics. Values in brackets denote outer shell variables

Collection Variables	
Wavelength (Å)	0.999
Ω oscillation	0.1°

Exposure (s)	0.01
Beam Energy (keV)	12.6
Transmission (%)	20
No. of Images	2800
Resolution limit (Å)	2.2

Dials Statistics	
Space group	$P6_322$
Unit dimensions (A B C, α β γ	87.99 87.99 326.52, 90 90 120
Resolution range (Å)	326.52 – 2.69
Observations	674276 (30944)
Unique Observations	23142 (1018)
Multiplicity (%)	29.1 (30.4)
I/θ	3.3 (0.4)
CC 1/2	1.0 (0.2)
Completeness	99.7 (89.9)

The automatic processing assigned a $P6_322$ space group and a notional resolution of 2.7 Å to the data, however suggested that there was potentially some radiation damage to the data set. Further inspection of the data showed that radiation damage started to occur after approximately 1800 images (180° rotation), however data processing continued.

6.6.2 Structure Solution of SilC

The processed data was then subjected to the manual pipeline outlined in section 2.8.6, using the CCP4 interface first in Matthews and then Phaser for molecular replacement (MR). The Matthews coefficient suggested that

within the asymmetric unit there was one molecule of SilC, similar to that found with CusC (Kulathila, *et al.,* 2011). Molecular replacement of the SilC data was carried out using Phaser, with the CusC structure (PDB: 3PIK) used as the model (72% sequence identity, see Figure 6.5.4) and one molecule assigned to the asymmetric unit which was successful in providing a structure for SilC. MR was successful with a structure determination solved. Viewing the coordinates in Coot from MR, along with the density maps, showed that both corroborated with each other for the most part, with the β-sheet region showing minimal density matching. In addition, by loading the symmetry mates of the monomer showed that the protein was in its trimeric state, arranged as a hexamer plates within the crystal packing (see Figure 6.6.1).

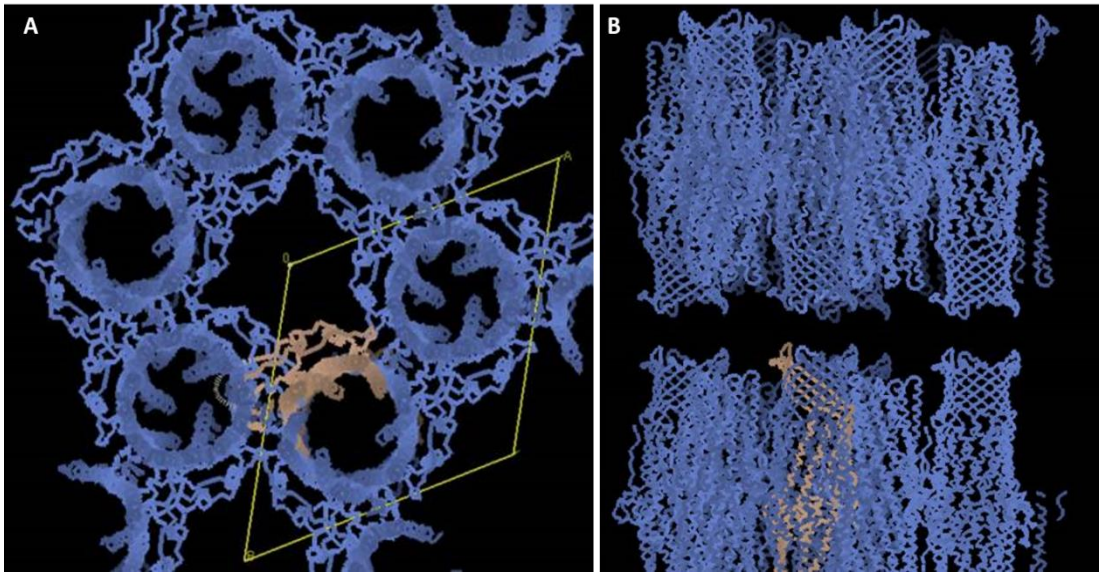

Figure 6.6.1: (A) Top down view of SilC (along unit cell, yellow) with its symmetry mates shown (blue) in its $P6_322$ space group, showing a hexamer of trimers present. **(B)** Side on view of SilC hexamer illustrating the large gap between the next SilC hexamer.

Further analysis of the crystal packing showed that the hexamer plates had large gaps between them, effectively resulting in no crystal contacts forming. It was then assumed that the wrong space group had been assigned to the data, in order to ascertain this the data was run through

the space group validator programme Zanuda, discussed later in section 6.7.2, (Lebedev, A.A. & Isupov, M.N., 2014). The output from Zanuda suggested that the space group $P6_322$ was incorrect and that the space group was actually $P12_11$ (hereafter $P2_1$). The outcome of this suggests that pseudo symmetry was occurring, whereby the crystal seemed to have a higher degree of symmetry than was actually there. This is discussed further in the discussion (section 6.7.2.1).

Reprocessing the data in Dials in a $P2_1$ space group and with a resolution cut back to 3.2 Å gave better statistics than the previous space group. The resolution reduction was due to radiation damage occurring after 180° of collection, the data to this point was acceptable and had a resolution of 3.2 Å. A new Matthews coefficient was determined using the monomer molecular weight, this suggested the presence of 6 molecules per asymmetric unit suggesting 2 trimers. Molecular replacement was carried out with a CusC trimer (based of PDB; 3PIK) used as a model instead of a monomer.

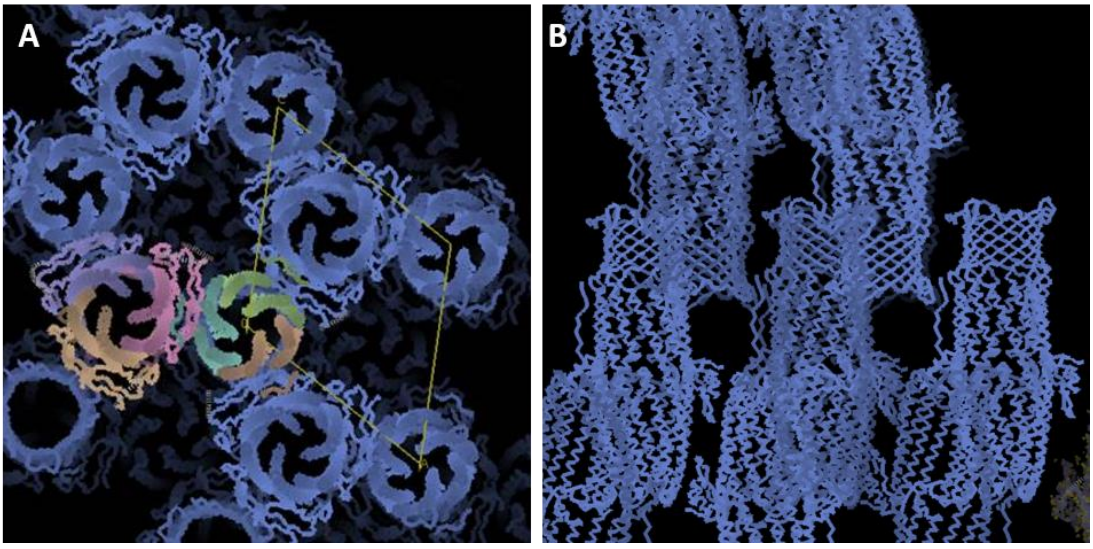

Figure 6.6.2: (A) Top down view of SilC (along unit cell, yellow) with its symmetry mates shown (blue) in its $P12_11$ space group. A hexamer distribution can still be seen in this orientation. **(B)** Side on view of SilC crystal packing, compared to Figure 6.6.1 there is no longer hexamer plates rather an interconnecting system of alternating SilC conformers.

A successful model was determined for the data, with a different crystal packing observed (Figure 6.6.2). The alterations made to the MR model are discussed further in section 6.7.2.1.

6.6.3 Model Building, Refinement and Validation of SilC

Closer inspection of the models to the electron density maps showed no obvious errors with the positioning of α-helices and β-sheets. However, as CusC was used as the model the sequence of amino acids was incorrect, therefore changes to the amino acid sequence were made prior to refinement. Changes to the amino acid sequence were made based on the sequence alignment, see Figure 6.6.3, of CusC to SilC in coot. Once the correct sequence was present the first round of refinement in Refmac5 was conducted with 10 cycles carried out (Section 2.8.5). The *R* and R_{free} produced were 0.280 and 0.306 respectively.

```
CusC      MSPCKLLPFCVALALTGC-SLAPDYQRPAMPVPQQFSLSQNGLVNAADNYQNAGWRTFFV  59
SilC      MFKLKLLSISTIFILAGCVSLAPEYQRPPAPVPQQFSLSKNSLTPAVNSYQDTGWRNFFV  60
          *   *** :.. : *:** ****:****  *********:*.*. *.:.**::***.***

CusC      DNQVKTLISEALVNNRDLRMATLKVQEARAQYRLTDADRYPQLNGEGSGSWSGNLKGNTA  119
SilC      DPQVSRLIGEALNNNRDLRMAALKVEEARAQFNVTDADRYPQLNASSGITYNGGLKGDKP  120
          * **. **.*** ********:***:*****:.:**********.... ::.*.***:.

CusC      TTREFSTGLNASFDLDFFGRLKNMSEAERQNYLATEEAQRAVHILLVSNVAQSYFNQQLA  179
SilC      TTQEYDAGLELSYELDFFGKLKNMSEADRQNYFASEEARRAVHILLVSNVSQSYFSQQLA  180
          **:*:.:**: *::*****:*******:****:*:***:***********:****.****

CusC      YAQLQIAEETLRNYQQSYAFVEKQLLTGSSNVLALEQARGVIESTRSDIAKRQGELAQAN  239
SilC      YEQLRIARETLKNYEQSYAFVEQQLVTGSTNVLALEQARGQIESTRAEIAKREGDLAQAN  240
          * **:**.***:**:*******:**:***:********** *****::****:*:*****

CusC      NALQLLLGSYGKLPQAQTVNSDSLQSVKLPAGLSSQILLQRPDIMEAEHALMAANANIGA  299
SilC      NALQLVLGTYRAVPSEKGIKGGEIAPVKLPPNLSSQILLQRPDIMEAEYQLKAADANIGA  300
          *****:**:*  :*. : ::...:  **** .**************: * **:*****

CusC      ARAAFFPSISLTSGISTASSDLSSLFNASSGMWNFIPKIEIPIFNAGRNQANLDIAEIRQ  359
SilC      ARAAFFPSITLTSGLSSSSTELSSLFTSGSGMWNFIPKIEIPIFNAGRNKANLKLAEIRQ  360
          *********:****:*::*::*****.:.********************:***.:*****

CusC      QQSVVNYEQKIQNAFKEVADALALRQSLNDQISAQQRYLASLQITLQRARALYQHGAVSY  419
SilC      QQSVVNYEQKIQSAFKDVSDTLALRDSLSQQLESQQRYLDSLQITLQRARGLYASGAVSY  420
          ************.***:*:*:****:**.:*:.:***** **********.**  *****

CusC      LEVLDAERSLFATRQTLLDLNYARQVNEISLYTALGGG---     457
SilC      IEVLDAERSLFATQQTILDLTYSRQVNEINLFTALGGGWVE     461
          :************:**:***.*:******.*:******
```

Figure 6.6.3: Sequence alignment of CusC (PDB; 3PIK) and SilC showing 72% identity to each other. Identical residues denoted with (*), semi-conservative (.), conservative mutations (:).

Following the first refinement, changes were made to the SilC model, such as amending chain shifts and twisted peptide backbones. Following this, the SilC model was refined using Phenix with several rounds of refinement, modification and validation conducted. The change was based on the number of molecules to amend (6) and the number of residues per chain, Phenix automatically produces a MolProbity report, which CCP4i does not, which is easier to work with.

The final SilC structure was refined to a resolution of 3.2 Å with an R and Rfree of 0.236 and 0.279 respectively, electron density maps can be seen in Figure 6.6.4. The full list of statistics can be seen in Table 6-4.

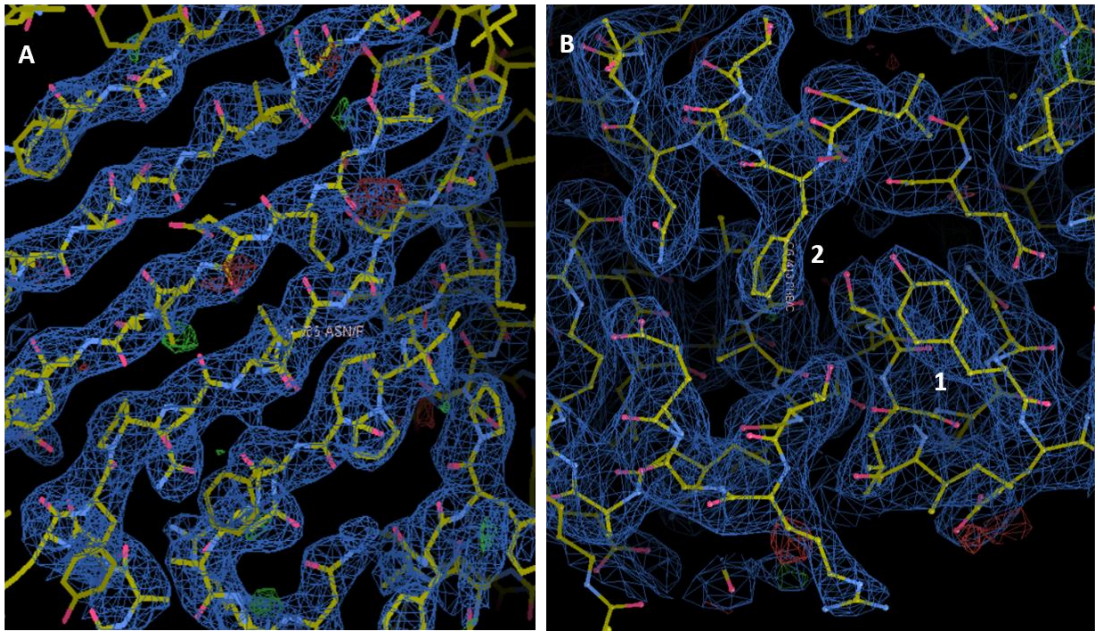

Figure 6.6.4: Electron density maps with model of SilC shown. **(A)** Region of β-sheet in SilC, showing the typical parallel strands. **(B)** α-helical region of SilC, with clear density seen for a tyrosine (1) and phenylalanine (2) residues for example.

Table 6-4: Statistics for final SilC model after refinements.

Statistic	Value
Wavelength	0.999 Å
Resolution range	44.29 - 3.203 (3.317 - 3.203)
Space group	P 1 21 1
Unit cell	88.05 326.79 88.10 90 120.26 90
Total reflections	236917 (15386)
Unique reflections	70140 (4668)
Multiplicity	3.4 (3.3)
Completeness (%)	99.35 (97.91)
Mean I/sigma(I)	3.5 (1.5)
Wilson B-factor	46.16
R-merge (%)	24.2 (89.8)
R-pim (%)	17.9 (66.9)
CC1/2	0.94 (0.418)
Reflections used in refinement	69912 (6893)
Reflections used for R-free	3469 (368)
R-work	0.2361
R-free	0.2799
Number of non-hydrogen atoms	20501
macromolecules	20501
Protein residues	2616
RMS(bonds)	0.011
RMS(angles)	1.28
Ramachandran favored (%)	96.53
Ramachandran allowed (%)	3.24
Ramachandran outliers (%)	0.23
Rotamer outliers (%)	0.05
MolProbity score	1.67
Average B-factor	39.20

The finished structure of SilC showed that a monomer was composed of a 4 stranded β-sheet head that is located in the detergent micelle, and 8 α-helices extending down from the head forming two sets of coiled coils, additionally there is a equatorial envelope composed of extended loops (see Figure 6.6.5). Within the structure there was no density for the region corresponding to residues 21-29, therefore these residues were not built into the final structure.

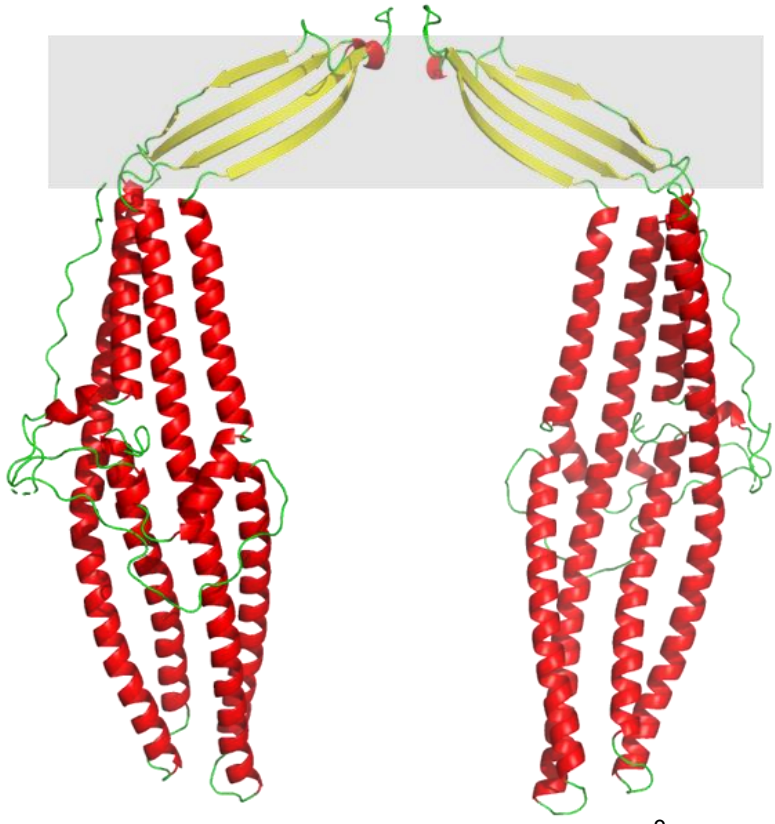

Figure 6.6.5: Structure of SilC monomer (3.2 Å) with the secondary structure coloured, β-sheet head (Yellow), α-helices (Red) and loops (Green) and the outer membrane is denoted in Grey. **(Left)** view of the monomer from outside what would be the β-barrel head. **(Right)** view of monomer looking into the β-barrel head.

SilC was shown to be trimeric within the asymmetric unit (supporting the results in 6.4.1 & 6.4.2). The structure of the trimer is shown in Figure 6.6.6 below. Within the trimer the full β-barrel head and α-helical barrel tail can be seen, with a equatorial envelope consisting of extended loops.

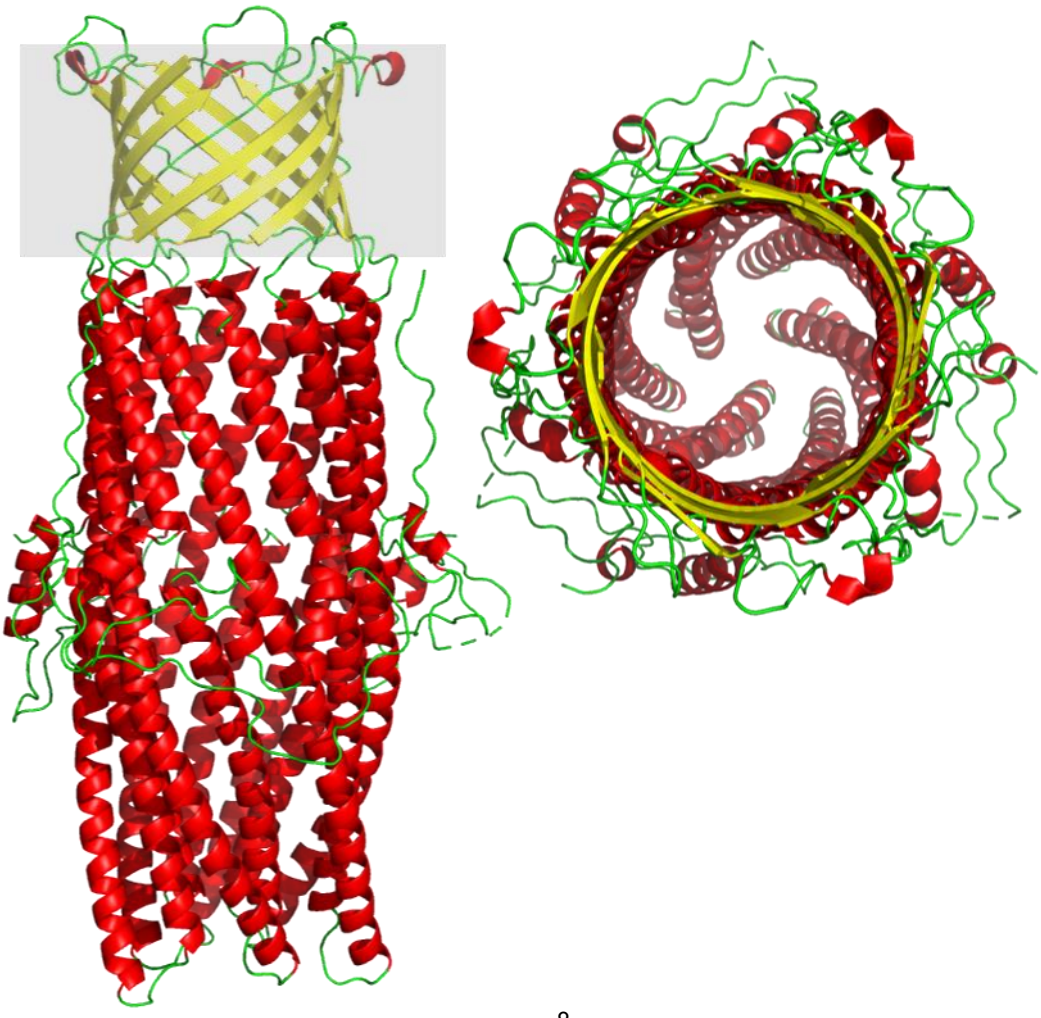

Figure 6.6.6: (Left) SilC trimer (3.2 Å) looking side on, illustrating the β-barrel head (Yellow) and α–helical tail (Red). The grey box denotes the outer membrane and position of the β-barrel head within it. **(Right)** Top down view of the trimer, looking down both the β-barrel and α-helical barrel, this view shows that the protein is in a closed conformation at the base of the α-helical barrel.

Measurements of SilC show that the diameter of the β-barrel is approximately 30.0 Å, which is consistent down the length of the α-barrel until the closed end where upon the diameter of the opening is reduced

to 8.8 Å. The length of SilC was shown to be approximately 126.0 Å, of which the β-barrel and the α-helical barrel constitute 23.0 Å and 91.0 Å respectively, with the remainder of the length made of loops.

6.7 Discussion and Future Work

6.7.1 Purification and Biophysical Characterisation

The expression and purification protocol for SilC followed closely the method outlined in Kulathila *et al.,* 2011 used for CusC. The protocol involved an initial sarcosine solubilisation step after lysis, this solubilisation step removes the inner membrane component of the cell lysate (Filip *et al.,* 1973 & Kropinski *et al.,* 1987). The removal of the inner membrane also reduces the possibility of contaminating proteins such as AcrB being bought through the purification. AcrB is known to bind to Ni^{2+} affinity columns (Mutakami *et al.,* 2002), therefore as SilC utilises a Ni^{2+} His-tag purification system the use of sarcosine eliminates this common contaminant.

Following sarcosine solubilisation SilC is further solubilised into LDAO before being exchanged into DDM. The purpose of this initial LDAO solubilisation is due to the stability of SilC at pH 7.5, when solubilised in DDM at pH 7.5 SilC crashes out of solution and is only stable at pH 5.0. However, at pH 5 histidine residues within the His-tag become protonated and disrupt their co-ordination of the Ni^{2+} resulting in lower affinity and thus not binding for purification (Bornhorst, J.A. & Falke, J.J., 2000). Therefore, the dual solubilisation allows for the purification and protein stability to be ensured which is essential for later structural studies.

The stability of the protein in these conditions was explored through nano-DSF seen in section 6.4.3. SilC was shown to have a relatively high onset denaturing temperature and a subsequently high melting temperature (T_m) of 78.2°C, the high T_m suggests that the protein is stable in DDM at pH 5.0. Further discussion on the thermal stability of SilC will be discussed later in this section.

The His-tag Ni^{2+} chromatography purification step of SilC yielded a clean protein (Figure 6.3.1-B), with a few lower molecular weight contaminants but an overall purity of ~95%. The imidazole gradient trace (Figure 6.3.1-A) shows the main protein peak followed by a linear increase in the 280 nm absorbance, this is indicative of the absorbance of imidazole as the concentration exceeds 200 mM. Running one of these fractions on a SDS-PAGE gel showed that there was no protein present in these fractions.

The subsequent SEC of the concentrated SilC protein showed a relatively broad peak on the 280 nm trace (Figure 6.3.2-A) with the main peak occurring at an elution position of 10.5 mL. On a Superdex S200 10/300 an eluting protein around that volume has a molecular weight ranging between 400-150 kDa, using the standard protein elution volumes (Cytiva, UK). Therefore, based on the position of the elution peak it can be concluded that the protein is not monomeric in solution but of a higher oligomeric state, possibly, and presumably, as a trimer. However, a limiting factor of S200 columns is that the resolution range for higher Mw proteins is reduced compared to lower Mw proteins, meaning that an accurate Mw cannot be assigned.

Subsequent biophysical characterisation of SilC, through SEC-MALLS, shed more light on the oligomeric state of SilC based on the purification.

SEC-MALLS showed that SilC gave a similar UV trace as in during the purification, however a more defined single peak was present at 10.5 mL (Figure 6.4.1). Initial analysis, using Astra v7 (Wyatt Technologies, UK), of the SilC SEC-MALLS data using conjugate analysis (see section 2.7.2), gave a molecular weight estimation for the protein component of 102 kDa. This molecular weight suggested that the protein was a dimer instead of the anticipated trimer in solution. However, the predicted shape of SilC, based on its homolog CusC and the subsequent structural determination of SilC (see Section 6.6.2), suggested that the shape of SilC was elongated (rod like) rather than globular. Therefore, by factoring in the elongated shape of SilC in the SEC-MALLS conjugated analysis, a different protein molecular weight component (Mw of 169kDa) was obtained. The new Mw is indicative of a trimer (169/52 kDa = 3.25), which was anticipated based on the CusC homolog. The overall Mw of the protein complex was 244 kDa, indicating that the detergent component of the protein was ~75 kDa, this is the anticipated Mw for a DDM micelle (Anatrace, USA).

Actively knowing the trimeric state of SilC is both biophysically important for further experiments, however in terms of solving the structure it is vital for ensuring the most accurate model is used for MR.

Finally, as alluded to earlier in this section, the stability of SilC assessed through nano-DSF showed that the protein is a very stable complex, with an average T_m of 78.2 °C. The 330/350 ratio trace (Figure 6.4.2) shows that there is a flat line for the ratio up to approx. 65.0 °C, suggesting that no unfolding of the protein has occurred up to this point. The onset temperature is shown to be ~68 °C based on the increase in the 330/350

ratio. Studies of outer membrane porins and porin like proteins (of which SilC has structurally been shown to be), have shown that high Tm's are frequently observed an example being the T_m of the porin OmpC was shown to be 75°C (Keegan *et al.,* 2010). Explanations as to these high T_m's is derived from the hydrogen bonding between the β-sheets backbone of the β-barrel, the large number of hydrogen bonds results in a larger amount of energy (higher temperatures) to break (Bannwarth, M. & Schulz, G.E., 2003).

SilC is shown to have a 12 member β-barrel head in its trimeric form (Figure 6.5.7), therefore there are a large number of hydrogen bonds present which would explain why the T_m is high. In addition to this, the α-barrel represents another stabilising aspect of the protein. As discussed in more depth later (Section 6.6.2.1) the α-barrel contains a large number of hydrogen and salt bridges, both of which need larger than normal amounts of energy to break (Thomas *et al.,* 2013). Therefore, the combination of both barrel components of SilC would suggest that a high temperature is needed to denature the protein.

6.7.2 Structure determination and Comparison of SilC structure

6.7.2.1 Structure Determination of SilC

As shown in section 6.5.2 the initial space group allocation ($P6_322$) was not correct. Running the data through the Zanuda space group validation programme (Lebedev & Isupov, 2014), a lower symmetry space group was suggested, $P12_11$ (hereafter $P2_1$).

The initial allocation of the $P6_322$ space group was understandable, since the diffraction patterns formed hexagons on the detector with six spots

spaced out at 60° intervals. Therefore, the diffraction suggested a hexagonal unit cell (vectors a=b=c, angles α=β=90° & γ=120°) (International Tables for Crystallography, 2006). The subsequent data processing and molecular replacement showed a model that had one molecule (SilC monomer) within the asymmetric unit, with the model matching large portions of the electron density maps, especially in the α-helix regions however there may be an element of model bias here. The addition of symmetry mates in Coot showed that the protein was trimeric, which is similar to homologs such as CusC and TolC and supportive of the biophysical data. The trimers were arranged in as a hexamer around the c-cell axis, suggestive of 6 fold symmetry, with each trimer alternating in orientation (See Figures 6.6.2 and 6.7.1).

However, on closer inspection there were areas of electron density that did not fit to the model completely around the β-sheet head region. In addition, there was also no obvious or plausible crystal contacts between adjacent hexamer rings (Figure 6.7.1-B).

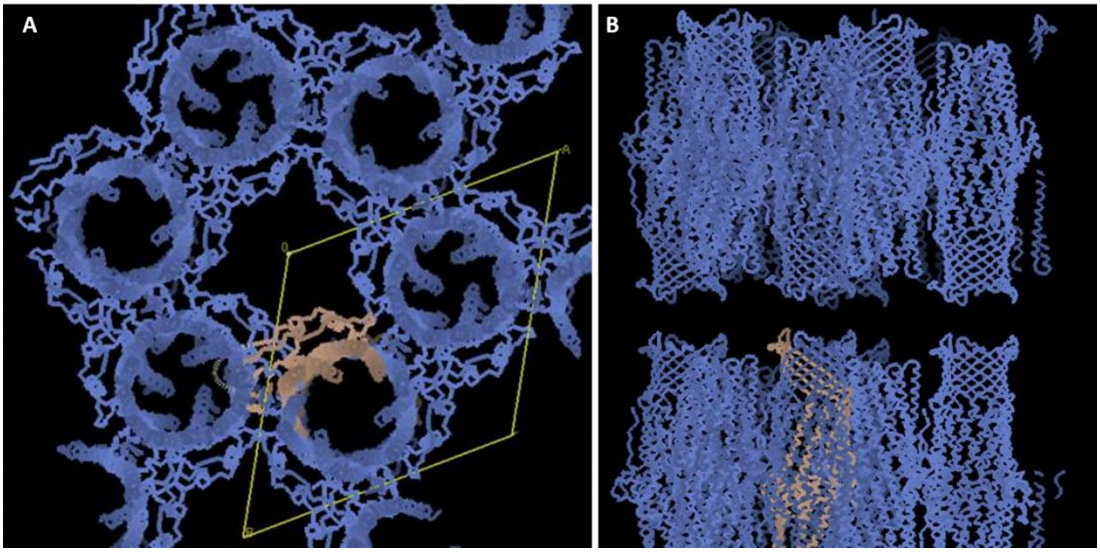

Figure 6.7.1: Ring on SilC trimers arranged in a hexamer ring. Single molecule of SilC shown in orange within the asymmetric unit, the unit cell is also shown.

Two conclusions were drawn from this. Firstly, that the electron density, although it looked correct for the most part with the model, was probably heavily model biased (based on the CusC model) which is why the electron density didn't match completely. The second conclusion is that the space group was incorrect and that the diffraction data contained some form of pseudo-symmetry, whereby the packing of molecules within the crystal give the appearance of a higher degree of symmetry than is actually present within the lattice. This conclusion came about through the large gaps in the crystal lattice between the hexamer rings, however the small difference in model to density matching suggested that the symmetry of the molecules were not quite the same as the crystallographic symmetry (Zwart *et al.,* 2007).

To this end, running the model (.pdb file) and the experimental data (.mtz file) through Zanuda suggested the true space group to be the lower symmetry group of $P2_1$. Zanuda comes to this conclusion through refining the model against the space group already assigned, then expanding the symmetry of the data to all other possible sub-groups. In doing this Zanuda can also change the cell dimensions to accommodate for lower symmetry space groups. In order to determine which solution is the best Zanuda uses the calculated R/Rfree values as an indication of correctness between the model and the data (Lebedev & Isupov, 2014).

As shown in section 6.6.2, the data of SilC suggested that the wrong space group was assigned, the assignment of the new $P2_1$ space group allowed for MR to be carried out. The initial analysis of the data in Matthews suggested that 6 molecules of monomeric SilC were present within the asymmetric unit. Therefore, with this knowledge, coupled with SEC-MALS data and the close homology of CusC to SilC, it confidently

anticipated that SilC was in its trimeric state within the crystal. In order to achieve a more accurate solution the CusC trimer was used as the model for MR, in doing so more of the scattering data would be accounted for within the asymmetric unit. By accounting for more data, a solution is more likely to be found, as well as reducing the time taken for additional model building had a monomer model been used. The successful MR solution was shown through the continuous density of the β-barrel head and α-helical tail of SilC, which was previously broken up in the old space group.

The distribution of the molecules within the $P2_1$ space group show a 2 fold symmetry, as expected. However, looking down the length of the protein the hexamer ring can still be seen (Figure 6.7.2-A), but instead of the trimer molecules lying on the same plane they are now offset by ½ the unit cell (Figure 6.7.2-B). This explains the original, incorrect, assignment of the space group as being hexagonal with 6-fold crystallographic symmetry, but also shows how it was the wrong space group and is now in the correct space group with a 2-fold symmetry. The new space group also displays a much more sensible lattice with clear contacts visible between molecules in a three dimensions throughout the crystal (Figure 6.7.2-B).

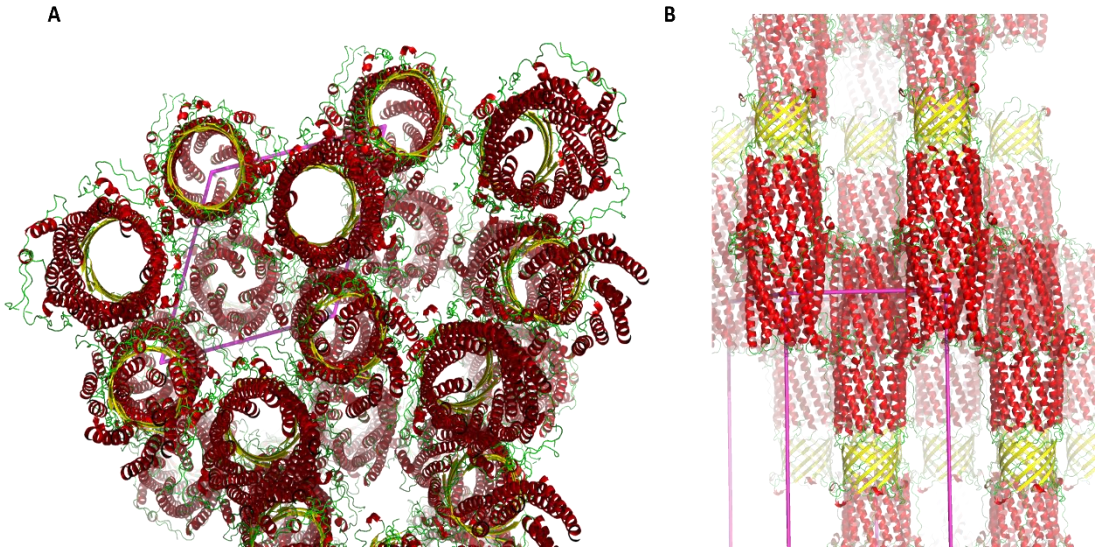

Figure 6.7.2: Structural overview of SilC showing the crystal packing, with the unit cell highlighted in magenta. **(A)** View looking down the length of the crystal, showing the still visible hexagonal packing of the crystal. **(B)** Side on view of the crystal highlighting the offset of ½ the unit cell between each molecule.

6.7.2.2 Comparison of SilC with other Gram-negative Outer Membrane Proteins

The overall solved structure of SilC (Figure 6.6.5) is similar to that of CusC and other outer membrane channel proteins such as TolC and OprM (Akama *et al.,* 2004 & Pei *et al.,* 2011 (PDB TolC; 2XMN & OprM; 1WP1)). As shown in section 6.5.2 the monomer of SilC is composed of a β-sheet head comprised of 4 strands, and 8 α-helices extending down from the head as a tail. The α-helical tail is comprised of 2 long extended α-helices, another 2 long α-helical strands each made by two shorter α-helix chains joined together, the remaining 2 α-helix chains are much shorted and occur in joining regions around the protein (see Figure 6.6.5). The structural layout of SilC is indicative of other outer membrane channel proteins such as TolC and CusC, see Figure 6.7.3. Comparing the three monomeric structures in Figure 6.7.3 the β-sheet head and α-helical tail is conserved across the protein species.

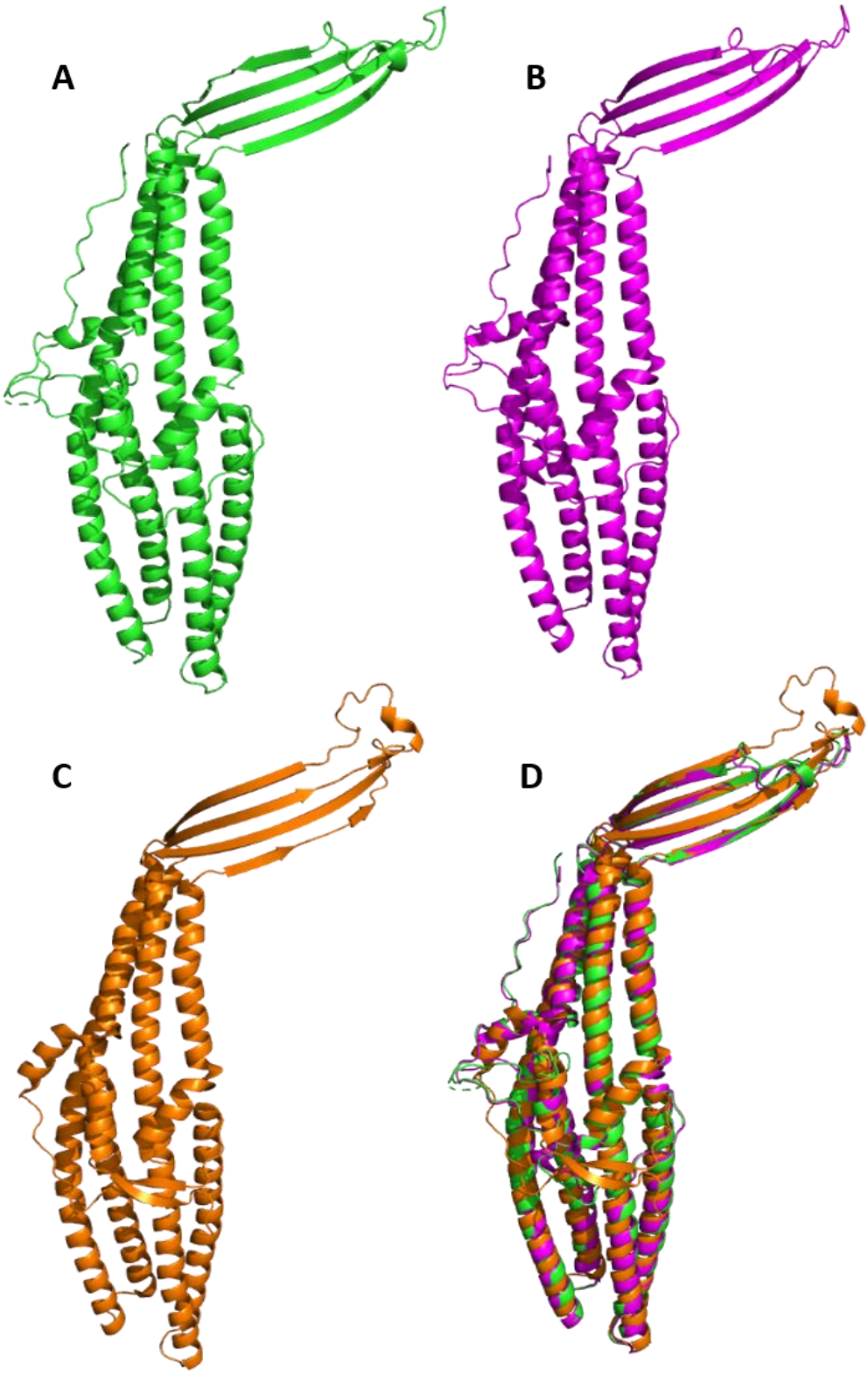

Figure 6.7.3: Comparison of the structures of **(A)** SilC monomer, **(B)** CusC monomer (PDB; 3PIK), **(C)** TolC monomer (PDB; 2XMN). **(D)** Overlay of all three monomers, highlighting the similarities between the structures.

The trimeric structure of SilC (Figure 6.6.6) results in a β-barrel head and α-helical barrel that extends into the periplasm. The β-barrel head of the SilC trimer is ~23 Å in height and measures ~30 Å in diameter, which is comparable to the diameter of CusC (~30 Å) (Kulathila *et al.,* 2011). As seen with CusC, the diameter of the β-barrel is relatively large compared to other outer membrane factor proteins, the TolC structure has a β-barrel diameter of 12 Å which is commonly seen in outer membrane factor proteins (Koronakis *et al.,* 2000). However, when looking at the structure of the TolC monomer there are extended extracellular loops between the β-sheet strands (Figure 6.7.3-C). Subsequently when the trimer forms, these extended loops fold over into the barrel and form a rudimentary 'plug' (Koronakis *et al.,* 2004) (see Figure 6.7.4).

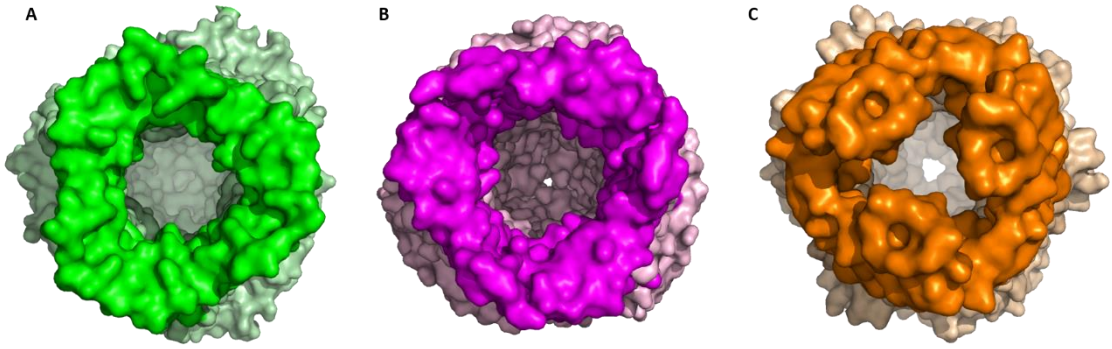

Figure 6.7.4: Structure of the extracellular openings of **(A)** SilC, **(B)** CusC and **(C)** TolC. SilC and CusC show a similar opening, however TolC shows the extended loop 'plug'.

The folding over of the loops in the TolC structure presents a filter mechanism for the type of substrate that can pass through the protein channel, which opens on substrate binding. Whereas CusC, and by extension SilC, lack this filter suggesting that any small substrate can pass through, regardless of the specificity for small molecule substrates seen in CusC (Conroy *et al.,* 2010). This may suggest why in studies

where TolC has been used to replace CusC there is no activity observed (Franke *et al.,* 2003), the assumption would be that a similar effect in seen in SilC.

The other main feature of the SilC trimer is the α-barrel tail, which makes up the Bulk of the protein. The α-barrel is ~91 Å in length, therefore extending ~9.1 nm into the periplasm, and has a uniform diameter of ~30 Å (same as the β-barrel diameter) down the barrel length. The length of the SilC α-barrel is consistent with other homologs such as TolC which is ~100 Å (10 nm) (Koronakis et al 2000). The barrel is composed of six sets of coiled coils with two sets coming from each SilC monomer, this is seen in CusC, TolC and OprM. The coils are composed of one long extended α-helix and another long α-helix made from two smaller α-helices joined together (Koronakis et al 2000, Kulathila et al 2011)., see Figure 6.7.5.

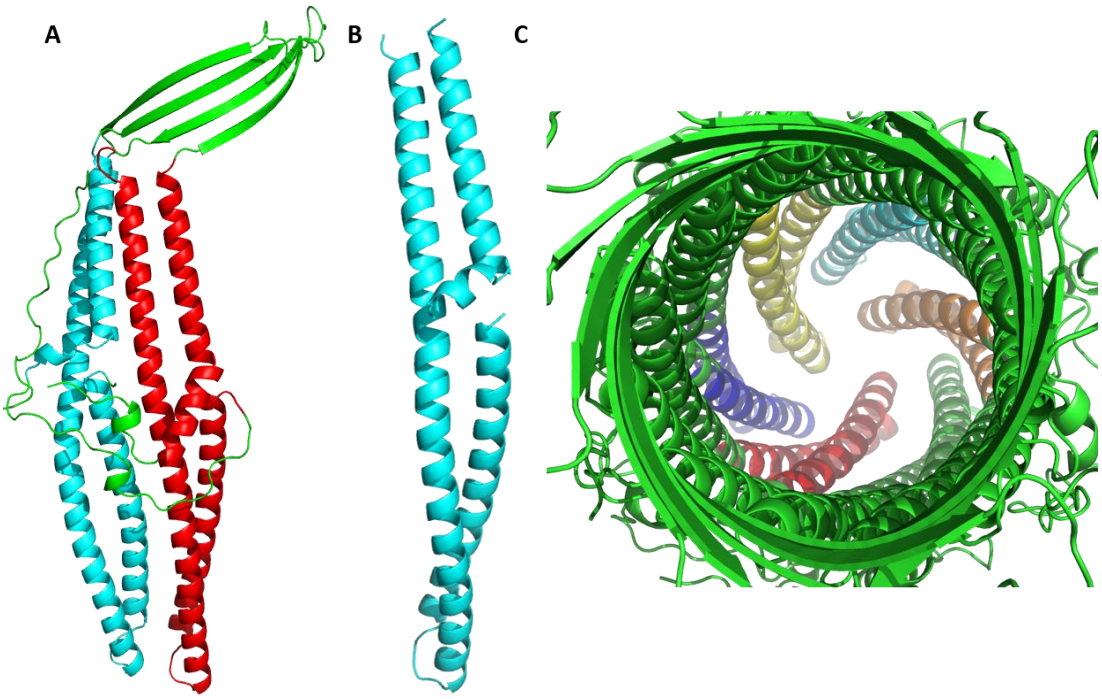

Figure 6.7.5: Structural view of SilC coiled coils. **(A)** SilC monomer showing the two coiled coil sets (Cyan and Red). **(B)** A single coiled coil pair from a SilC monomer. **(C)** Longitudinal view of SilC looking from the extracellular end to the periplasmic end. Showing in different colours are the six coiled coils that form the closed state of SilC.

The coiled coils form the closed conformation of the protein at the periplasmic end (Figure 6.7.5-C). This closure seems logical as with the SilC β-barrel head providing no filtering system, an open protein structure at both ends would allow any number of small substrate molecules to pass through into the periplasm. The formation of the closed coiled coil 'plug' is thought to form in the same way as TolC, whereby hydrogen bonding and salt bridges formed between the amino acid side chains of two adjacent coiled coils (Bavro et al 2008). Studies looking at disrupting these interactions, through mutagenesis and cross-linking, showed detrimental effects with a permanent open conformation maintained resulting in permeability to ions and antibiotics (Andersen *et at*., 2002 & Eswaran *et al.,* 2003).

The main roles of the α-barrel within SilC seems to be as a connector to the SilAB complex and as a facilitator for allowing ions to pass through, this role is assumed when comparing to SilC to the TolC-AcrAB and CusCBA complexes.

Within the TolC-AcrAB complex, TolC performs the role of SilC, AcrB is homologous to SilA (efflux pump) and AcrA is a membrane fusion protein similar to SilB. AcrAB and CusAB readily form complexes on the periplasmic side of the inner membrane, however the full complex with the outer membrane protein does not form unless the substrate is present (Su *et al.,* 2012 and Zgurskaya & Nikaido, 2000), see Figure 6.7.6-A. TolC interacts with AcrA directly upon substrate binding (Figure 6.7.6-B). The formation of the complex is stabilised through energetically favourable interactions with the side chains of the TolC coiled coils and the loops between the α-helices of AcrA (see Figure 6.7.6-C) (Lobedanz *et al.,* 2007).

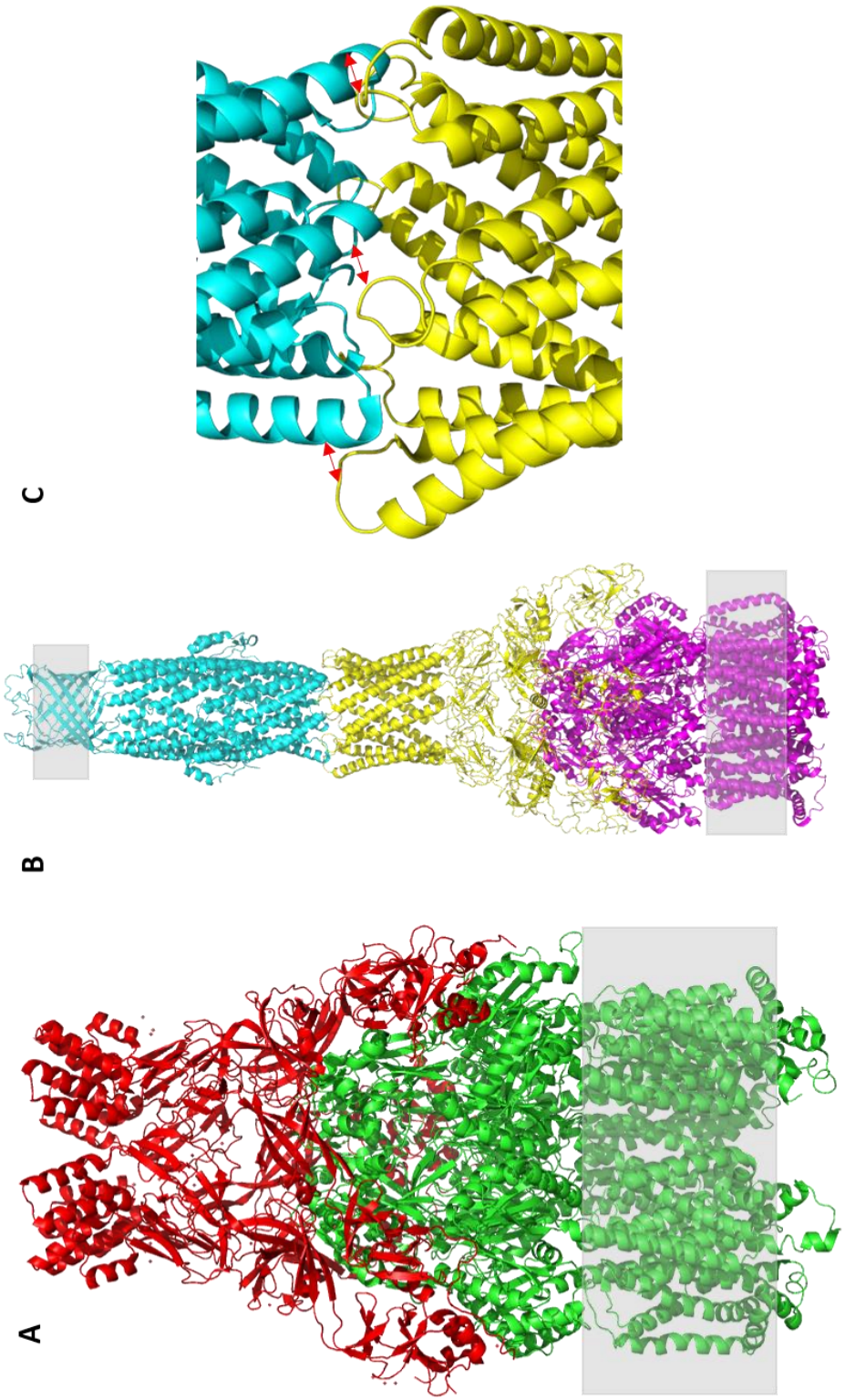

The energetically favourable interactions that occur between TolC and AcrA have been shown, in the presence of the substrate, to result in the opening of the periplasmic 'plug' of TolC and allow the substrate to pass through (Wang *et al.,* 2017).

It is assumed that SilC will form part of the overall SilCBA complex when the substrate (Ag(I)/Cu(I)) binds to the SilA/B proteins. Subsequent interactions between SilB and SilC, similar to those observed in the TolC/ArcA system, will facilitate the conformational change that allows the metal ions to be transported out of the cell.

The final observation made from the SilC structure is the variation of the amino acids in equatorial envelope region when compared to CusC (see Figure 6.7.7). As can be seen from the sequence alignment in Figure 6.7.7 the equatorial region is split into two main region (1) and (2). Region 1 contains many conserved residues between the two proteins with a reasonable amount of conservative mutations as well. In comparison the region with the greatest diversity is region 2, here we see a lot of either semi- or non-conservative mutation. An initial explanation for the variation in amino acids between SilC and CusC was for specificity reasons to the membrane fusion protein, for SilC this is SilB. However, drawing comparisons to the TolC-AcrAB complex structure by Wang *et al* (2017), as alluded to earlier in the section, the binding region of ArcA (SilB homolog) to TolC occurs at the top of ArcA and the bottom of the α-barrel of TolC. Therefore, if this structure is assumed to be similar to the SilCBA complex, which through homology modelling of the system is plausible, the equatorial region of SilC plays no direct role in interacting with SilB.

Figure 6.7.7: (Left) Structural comparison of SilC (Green) and CusC (Magenta) with differences in amino acids between the two protein highlighted in Blue. **(Right)** Sequence alignment of SilC and CusC with the equatorial envelope regions highlighted in red boxes. Identical residues denoted with (*), semi-conservative (.), conservative mutations (:) and non-conservative mutations are left blank. Region 2 shows the greatest variability between the two proteins.

Additional research into the homologs of SilC, mainly TolC, showed that the equatorial region and coiled-coil ends of TolC, along with the loops at the top of AcrA, interact with the peptidoglycan layer of the periplasm (Chen *et al.,* 2022 & Shi *et al.,* 2019). Peptidoglycan is composed of repeating sugar units (see Section 1.1.2) therefore giving a polar element to the layer. The amino acid makeup of the SilC equatorial region contains polar or charged residues which may be involved in forming hydrogen bonds with the peptidoglycan, this would stabilise SilC in complex with SilAB. In order to test this theory *in vivo* studies of the SilCBA system, whereby the equatorial region of SilC is comprised of non-polar or uncharged amino acids may result in a less stable complex resulting in cell death on exposure to Ag(I) or Cu(I).

A final possible explanation of the varied equatorial region of SilC is that it facilitates specificity to other periplasmic sil proteins, SilF or SilE. However, further investigation is needed into this.

6.7.3 Conclusion and Future Work

The production of SilC, combined with the biophysical and structural characterisation, has been successfully carried out, with the several key outcomes obtained. Firstly, the production of SilC to a quantity and purity level that enables both biophysical and structural characterisation to be conducted. Secondly, through the biophysical characterisation, confirmation that SilC forms stable trimers in solution, which supports the assumption based off the homolog CusC. Stability of SilC, assessed through nano-DSF, showed that the trimers had a high Tm, which through the literature and the structure are affiliated to the hydrogen bonding of the α and β-barrel.

Finally the structure determination of SilC to a resolution of 3.2 Å. The structure shows the main features affiliated with outer membrane factor proteins, namely the β-barrel head and the α-barrel tail. Based on the structure and its close homology to other systems, such as TolC, it is assumed that SilC behave like these other systems in the formation of the SilCBA complex.

Going forward some future avenues to explore with SilC would be to look at any possible binding to Ag(I) or Cu(I). This would clarify if SilC directly interacts with the ions in exporting them, or confirm that SilC allows for the passive diffusion of the ions out of the cell.

In conjunction with the binding studies, looking at *in vivo* studies of bacterial cells with and without SilC expressed along with the SilAB proteins. Additionally, substituting SilC with CusC or TolC to asses cell survival. This would give an insight into the specificity of the β-barrel heads in terms of substrate extrusion, as they differ between the proteins (see section 6.6.2.2). It would also give an indication of the types of interactions occurring at the periplasmic end of the α-barrel with SilB. If no or limited reduction in cell survivability it would suggest that SilC can easily be substituted without a detrimental effect to the system.

Another avenue of interest will be to mutate the residues of the coiled-coils involved in the interactions with SilB to determine how easy it is to disrupt the formation of the complex. It may also affect the size of the pore which may effect the exportation of Ag(I)/Cu(I) through the complex.

Finally looking to obtain the overall SilCBA complex structure, with all components present. Based off literature studies the most plausible way of achieving this would be through Cryo-EM (Wang *et al.,* 2017). Obtaining the complete complex structure, the specific interactions between the constituent components can be reviewed and a mechanism for ion exportation can be surmised. Direct comparison to systems such as the TolC-AcrAB, would highlight any intricate differences that may explain the specificity to monovalent ions. In terms of SilC the main area of interest would be between the top of SilB and the coiled coil ends of SilC.

7 General Discussion

This chapter looks more closely at the relationship between the proteins investigated in this research and their role within the sil system. The aims of the project, as outlined in Section 1.8, are also discussed.

7.1 The Sil System Background

Presently the *sil* system has not been investigated in great depth structurally, as shown in Section 1.4. At the time of writing, the only protein that has been extensively characterised was SilE, which was shown to be a periplasmic metalloprotein capable of binding up to eight Ag(I) ions (Asiani *et al.,* 2016). The other proteins within the system have been given putative roles based on their homology to proteins found within the cus and cue systems, which are involved in bacterial copper homeostasis.

In total the *sil* system is comprised of nine proteins; SilS and SilR, a two component system comprised of a histidine sensor kinase (SilS) and a response regulator (SilR). SilP a inner membrane metal exporting P1B-ATPase. SilCBA a transmembrane RND efflux pump system comprised of SilA an inner membrane efflux pump, SilB a membrane fusion protein and SilC an outer membrane factor protein. Two periplasmic proteins SilE a metalloprotein and SilF a metallochaperone that forms part of the SilCBA system. Finally, SilG a protein of unknown function as no homologs can be found (Gupta *et al.,* 1999). Figure 7.1.1 shows an overview of the sil system with no structural information regarding each constituent protein.

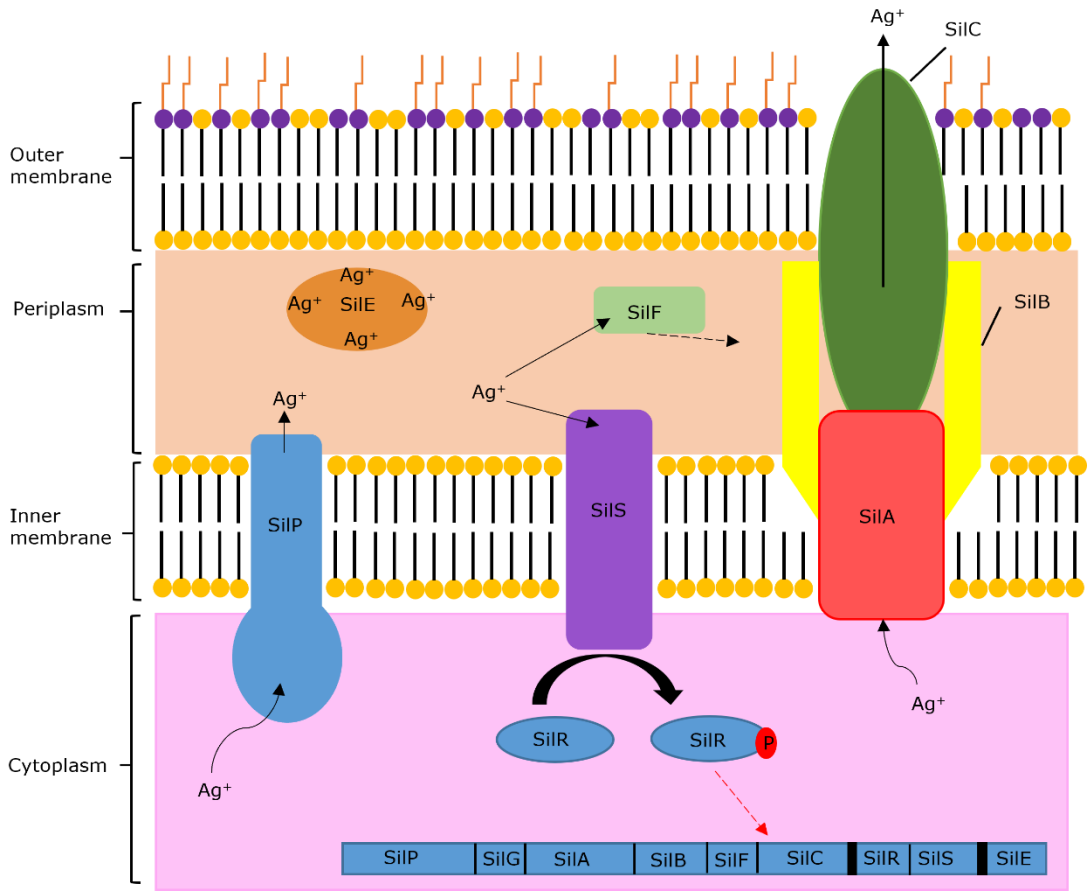

Figure 7.1.1: Overview of the sil system with their putative roles shown based on homology to the cus and cue proteins.

This work focuses on three of the proteins within the system; SilP, SilF and SilC, with the main objectives being the functional biophysical and structural characterisation. Understanding the function of each protein, coupled with structural information, will give a better understanding of the sil system as a whole and potentially lead the design of future inhibitors.

7.2 Functional characterisation of the sil proteins

7.2.1 SilP a metal ion exporting pump

SilP is a P1B-ATPase, which falls into the family of metal ions exporters. The enzymes use ATP to export metal ions out of the cytoplasm and into the periplasm. The mechanism by which SilP achieves this is believed to follow the Post-Albers cycle, whereby a number of conformation states lead to various catalytic stages of the protein which hydrolyse ATP and result in metal ion exportation (Albers, 1967; Post *et al*, 1972).

The work of Chapter 3 looked at understanding the Post-Albers cycle with relation to SilP. Structurally it was hoped that one or more of the catalytic states could be acquired, however this ultimately did not happen due to time constraints imposed by the COVID19 pandemic. However, activity assays of the protein shed some light on the catalytic cycle.

ATP assays showed that SilP, in its apo state, is primed for ATP hydrolysis. Whereas the addition of Cu(I) indicates that conformational changes occur prior to the ability to bind and hydrolyse ATP. The implication from the apo data set fits with the standard model of the Post-Albers cycle, whereby the protein fits into the E2 state. However, the data from the Cu(I) does not support this accepted concept, with the data suggesting that a different, unidentified, state is actually present within the system upon addition of Cu(I).

Based on the data, another outcome is that the differences seen between the apo and Cu(I) bound forms of SilP could be explained by the specificity of the protein for said product. As alluded to in Chapter 3,

another interpretation of the data is that SilP may be showing discriminatory tendencies to Cu(I). The lower affinity for ATP when Cu(I) is present, compared to the apo state, may support this and give evidence to suggest that SilP prefers Ag(I) over Cu(I). However more evidence is need for this. If this is the case it would show a considerable difference to those seen in the homolog, CopA, giving support to the sil system evolving from the cus/cue systems to be more specialised in Ag(I) detoxification.

7.2.2 SilF a periplasmic metallochaperone?

The putative role that SilF was given by Gupta *et al.,* (1999) was that of a periplasmic metallochaperone, with a similar function to CusF. Functional studies of SilF, as seen in Chapter 4, showed that this designation was correct. As with CusF, SilF was shown to bind to both Ag(I) and Cu(I) with high affinity, with a preference to the former.

Studies by Kittleson *et al.,* (2006) showed that CusF had mid-nM affinity to Ag(I) over Cu(I), with a ten fold weaker affinity to Cu(I) compared to Ag(I). Based off these results it was suggested that the weaker affinity to Cu(I) was possibly due to the cells need for occasional Cu(I) in some protein complexes, unlike the toxic Ag(I). Observations made within this work show that SilF is not nearly as discriminatory in its target ligands compared to CusF, with ITC studies showing that SilF had low nM affinity to both metal ions. The differences in results leads to the speculation of two possible outcomes; 1) The work conducted by Kittleson *et al.,* (2006) was not as rigorous as our studies, or 2) SilF is a more specialised protein that binds tightly to toxic Ag(I), the result of this high specificity is the additional tight binding of Cu(I).

The work conducted by Kittleson *et al.,* (2006), acknowledged that the results of the ITC studies for the Cu(I) had a lot of error, based on the difficulties of working with Cu(I) in solution. This was an issue as well for these studies however using anaerobic conditions where possible it was possible to maintain Cu(I) for use in these studies.

The issue of SilF being a more specialised protein is up for debate, however prior to the binding studies being conducted it was expected that SilF would bind more tightly to Ag(I) over Cu(I). Being part of the sil, notionally an evolved state of the cus/cue system, it was thought that the protein may have either lost its ability to bind Cu(I) or with a vastly reduced affinity. However, the results of this work showed that the opposite was true and the protein has an enhanced binding affinity to both metal. Suggesting that the protein does not discriminate against either toxic metal and facilitates the immediate eviction of them.

7.3 Structural characterisation of the sil proteins

7.3.1 A solid platform for the determination of SilP through Cryo-EM

Although no atomic resolution structure of SilP was determined in this work through Cryo-EM, a solid foundation was established for future investigations. The ability to express the protein in good quantity and to a high level of purity, gives confidence that whatever is imaged on grids is the protein of choice. In addition the activity of the protein in LMNG, as established in Chapter 3, gives confidence that any future structures of SilP are physiologically relevant.

7.3.2 SilF a metallochaperone like CusF with a twist

Structure determination in Chapter 5 of SilF showed that there were two main differences when compared to CusF. Firstly, the metal binding site, although the same residues were involved in coordinating the metal ions as CusF, the mechanism by which it achieved this was different. In the binding of both metal ions in CusF coordination occurred through direct interaction with the histidine and two methionine residues, and the addition of the π-orbital interaction of the tryptophan. With regard to SilF, the binding of Ag(I) followed the same mechanism as CusF, however when Cu(I) was bound the mechanism was different. Coordination through the histidine and two methionine's was present, however the tryptophan residue was pushed away and instead a water molecule was coordinating. The purpose as to why the tryptophan pi-orbital was not enough to coordinate is still unknown, however its omission from the mechanism does support the difference in affinity seen between Ag(I) and Cu(I) in Chapter 4.

The second observable different between SilF and CusF is the overall structure itself. Both sets of proteins share two common characteristics; a five membered β-barrel core with a loop at one end comprising of the metal binding site. However, the main difference occurs at the opposite end, whereby SilF contains a α-helix region and CusF an extended loop. This leads to two questions. Firstly, why is there a α-helix in SilF but not in CusF? Secondly what is the purpose of the α-helix?

In answering the first question we need to look at the family both these proteins fall under. Structure comparisons with several homology servers showed that SilF and CusF fall into the family of OB-fold proteins, which

typically follow the SilF topology. OB-fold proteins are known to bind to oligonucleotides and/or oligosaccharides, but not commonly metal ions. Therefore it is theorised that SilF and CusF are a new sub-family of these OB-fold proteins. The interesting speculation is that the sil system is thought to have evolved from the amalgamation of the cus and cue systems, therefore if this is the case then SilF should have evolved after CusF. If this was the case then the structure of SilF should be more similar to CusF, yet it is more closely similar to other OB-fold proteins (see Figure 5.8.5) which suggests that it may evolutionarily pre-date CusF. This is mere speculation and further investigation is needed to accurately asses this hypothesis.

The second question regard the purpose of the α-helix is has to date not been fully understood, however it is possible that the α-helix interacts with SilB of the SilCBA complex. This interaction may facilitate the transference of the metal ion between the proteins. To date the mechanism by which CusF off-loads metal ions to CusB so no comparisons can be made between the two system, however it is possible they are different given the fact the binding affinities of each protein to their metal ions is varied as well.

7.3.3 SilC a stable outer membrane protein

Chapter 6 looked at the outer membrane factor protein, SilC, which forms part of the SilCBA complex. The complex is of high importance to the sil system as it is the only method to facilitate the extrusion of metal ions out altogether. Therefore understanding the individual proteins of the complex a insight as to how the complex forms and its mechanism for metal ion exportation.

Structural characterisation of SilC showed that the protein conforms to the highly conserved structure of outer membrane factor proteins, such as TolC and CusC (Akama *et al.,* 2004 & Pei *et al.,* 2011). Further comparisons of the structure showed that SilC, like CusC, has a large channel spanning the length of the protein. This is thought to facilitate the passive diffusion of the metal ions through the protein and out of the cell. Based on this there is no direct evidence to suggest that SilC interacts with either Ag(I) or Cu(I) ions.

There are two main areas of interest with regard to SilC, the coiled-coil ends and the equatorial region of the α-barrel.

The first area of interest is theorised to be directly involved in forming the whole SilCBA complex, through interactions with SilB. The mechanism of interaction is through to be the same as CusC and CusB, with the coiled-coils of CusC interaction with the extended loops of CusB. The structure of SilC supports this hypothesis, however to date there is no SilB structure for confirmation.

The second are of interest is more puzzling, when compared to the same region of the CusC structure there are large differences in amino acids. THe purpose of this is not fully understood, it may be to do with the interactions with the peptidoglycan layer or as a secondary binding site for SilF or SilE potentially, more information is required for this. However it does lead to speculation that the formation of the SilCBA may have subtle differences compared to the CusCBA complex.

7.4 A more in-depth understanding of the sil system

The findings of this work have led to a better understanding of three more proteins involved in bacterial Ag(I) resistance. Functional

characterisation of the three proteins shows that the sil system, like the cus/cue systems, has the ability to transport Ag(I) and Cu(I) with a preference for the former. Lending support to the claim that the sil system is an evolutionary descendent of the cus/cue systems.

Structurally, the two protein structures solved showed that SilC has a very similar structure to CusC, whilst SilF has a major difference in structure when compared to its homolog CusF. The similarities of SilC to CusC leads to the suggestion that the SilCBA complex assembles in the same manner as that of the CusCBA complex. Whereas the interaction of SilF with SilCBA is theorised to be different when compared to CusF and the CusCBA complex. Taking the structures from this work and applying them to Figure 7.1.1 we have built up a better idea of what the sil system looks like, see Figure 7.4.1.

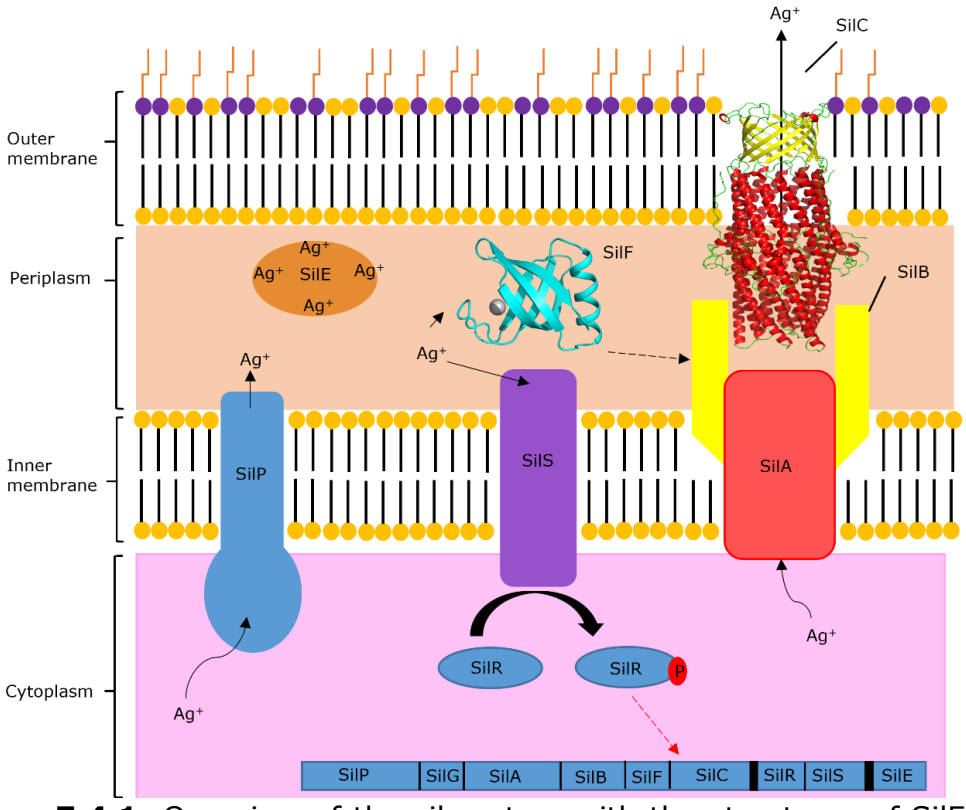

Figure 7.4.1: Overview of the sil system with the structures of SilF and SilC added in. SilF (Cyan) is bound to Ag(I) (Grey) and present in the periplasm. SilC (β-head Yellow, α-barrel Red) can be seen in the outer membrane.

7.5 Future Work

Going forward with the project there are several pieces of research that need to be undertaken to further our understanding of the *sil* system.

Regarding SilP a good foundation has been established in determining the structure, this needs to be taken further with optimal cryo-grid preparation conditions determined. Only once these have been optimised does structure determination stand a reasonable chance of being achieved.

In addition to this the activity assays need to be repeated and expanded on, looking not only at the ATP turnover rate but also the exportation of Cu(I). If possible modify the assay conditions so that Ag(I) can be studied as well. Obtaining more data on activity will give a better understanding of how SilP works, if the Post-Albers cycle is followed, and look at any co-operativity is taking place.

Further work on SilF will focus on the phenotypic effect of silver resistance when knocked out, this will give a better idea of the role of SilF in the *sil* system. In addition to this looking at the substitution of SilF with CusF and vice versa. Another area will be to look at mutating the residues involved in metal coordination to see which mutations stop or reduce metal affinity.

Finally the immediate future work on SilC will look at obtaining the overall SilCBA complex structure, this will give a better understanding of how the complex forms and also where metal ions pass through. In conjunction with this studies looking at the *in vivo* effects of SilC being substituted with TolC/CusC, this will give information on the potential compatibility, and possible evolution, of these systems.

8 References

A, S., JD, D., & TM, P. (2002). Vancomycin resistance in staphylococci. Clinical Microbiology Reviews, 15(3), 430–438.

Affandi, T., Issaian, A. V., & McEvoy, M. M. (2016). The Structure of the Periplasmic Sensor Domain of the Histidine Kinase CusS Shows Unusual Metal Ion Coordination at the Dimeric Interface. Biochemistry, 55(37), 5296–5306.

Afzal, A. M., Rasool, M. H., Waseem, M., & Aslam, B. (2017). Assessment of heavy metal tolerance and biosorptive potential of Klebsiella variicola isolated from industrial effluents. AMB Express, 7(1).

Agarwal, R., Zakharov, S., Hasan, S. S., Ryan, C. M., Whitelegge, J. P., & Cramer, W. A. (2014). Structure-function of cyanobacterial outer-membrane protein, Slr1270: Homolog of Escherichia coli drug export/colicin import protein, TolC. FEBS Letters, 588(21), 3793–3801.

Albers, R. W. (1967). Biochemical Aspects of Active Transport. Annual Review of Biochemistry, 36(1), 727–756.

Allen, F. H., Davies, J. E., Galloy, J. J., Johnson, O., Kennard, O., Macrae, C. F., Mitchell, E. M., Mitchell, G. F., Smith, J. M., & Watson, D. G. (1991). The Development of Versions 3 and 4 of the Cam

Almagro Armenteros, J. J., Tsirigos, K. D., Sønderby, C. K., Petersen, T. N., Winther, O., Brunak, S., von Heijne, G., & Nielsen, H. (2019). SignalP 5.0 improves signal peptide predictions using deep neural networks. Nature Biotechnology 2019 37:4, 37(4), 420–423.

Alquethamy, S. F., Khorvash, M., Pederick, V. G., Whittall, J. J., Paton, J. C., Paulsen, I. T., Hassan, K. A., McDevitt, C. A., & Eijkelkamp, B. A.

(2019). The role of the copA copper efflux system in acinetobacter baumannii virulence. International Journal of Molecular Sciences, 20(3).

American Society of Biological Chemists., Rockefeller Institute for Medical Research., & American Society for Biochemistry and Molecular Biology. (n.d.). The Journal of biological chemistry. American Society for Biochemistry and Molecular Biology. Retrieved August 28, 2018.

Andersen, C., Koronakis, E., Bokma, E., Eswaran, J., Humphreys, D., Hughes, C., & Koronakis, V. (2002). Transition to the open state of the TolC periplasmic tunnel entrance. Proceedings of the National Academy of Sciences, 99(17), 11103–11108.

Andersson, M., Mattle, D., Sitsel, O., Nielsen, A. M., White, S. H., Nissen, P., & Gourdon, P. (2014). Copper-transporting P-type ATPases use a unique ion-release pathway. Nature Structural & Molecular Biology, 21(1), 43–48.

Andrade, L. N., Siqueira, T. E. S., Martinez, R., & Darini, A. L. C. (2018). Multidrug-Resistant CTX-M-(15, 9, 2)- and KPC-2-Producing Enterobacter hormaechei and Enterobacter asburiae Isolates Possessed a Set of Acquired Heavy Metal Tolerance Genes Including a Chromosomal sil Operon (for Acquired Silver Resistance). Frontiers in Microbiology, 9(MAR), 539.

Anraku, Y. (1988). Bacterial Electron Transport Chains. Annual Review of Biochemistry, 57(1), 101–132.

AP, J. (2011). Methicillin-resistant Staphylococcus aureus: the European landscape. The Journal of Antimicrobial Chemotherapy, 66 Suppl 4(SUPPL. 4).

Apell, H. J. (2004). How do P-Type ATPases transport ions? Bioelectrochemistry, 63(1–2), 149–156.

Arakawa, H., Neault, J. F., & Tajmir-Riahi, H. A. (2001). Silver(I) Complexes with DNA and RNA Studied by Fourier Transform Infrared Spectroscopy and Capillary Electrophoresis. Biophysical Journal, 81, 1580–1587.

Arcus, V. (2002). OB-fold domains: A snapshot of the evolution of sequence, structure and function. In Current Opinion in Structural Biology (Vol. 12, Issue 6, pp. 794–801). Elsevier Ltd.

Argüello, J. M. (2003). Identification of Ion-Selectivity Determinants in Heavy-Metal Transport P1B-type ATPases. Journal of Membrane Biology, 195(2), 93–108.

Argüello, J. M., Eren, E., & González-Guerrero, M. (2007). The structure and function of heavy metal transport P1B-ATPases. BioMetals, 20(3–4), 233–248.

Argüello, J. M., Raimunda, D., & Padilla-Benavides, T. (2013). Mechanisms of copper homeostasis in bacteria. Frontiers in Cellular and Infection Microbiology, 4(NOV).

Argüello, J. M., González-Guerrero, M., & Raimunda, D. (2011). Bacterial transition metal P(1B)-ATPases: transport mechanism and roles in virulence. Biochemistry, 50(46), 9940–9949.

Arnesano, F., Banci, L., Bertini, I., Ciofi-Baffoni, S., Molteni, E., Huffman, D. L., & O'Halloran, T. V. (2002). Metallochaperones and metal-transporting ATPases: A comparative analysis of sequences and structures. Genome Research, 12(2), 255–271.

Arnesano, F., Banci, L., Bertini, I., Mangani, S., & Thompsett, A. R. (2003). A redox switch in CopC: An intriguing copper trafficking protein that binds copper(I) and copper(II) at different sites. Proceedings of the National Academy of Sciences, 100(7), 3814–3819.

Asiani, K. R., Williams, H., Bird, L., Jenner, M., Searle, M. S., Hobman, J. L., Scott, D. J., & Soultanas, P. (2016). SilE is an intrinsically disordered periplasmic "molecular sponge" involved in bacterial silver resistance. Molecular Microbiology, 101(5), 731–742.

AT, B. (1992). Free R value: a novel statistical quantity for assessing the accuracy of crystal structures. Nature, 355(6359), 472–475.

Atiyeh, B. S., Costagliola, M., Hayek, S. N., & Dibo, S. A. (2007). Effect of silver on burn wound infection control and healing: Review of the literature. Burns, 33(2), 139–148.

Axelsen, K. B., & Palmgren, M. G. (1998). Evolution of Substrate Specificities in the P-Type ATPase Superfamily. Journal of Molecular Evolution, 46, 84–101.

BA, C. (1995). Vancomycin. The Medical Clinics of North America, 79(4), 817–831.

Babel, L., Bonnet-Gómez, S., & Fromm, K. M. (2020). Appropriate Buffers for Studying the Bioinorganic Chemistry of Silver(I). Chemistry 2020, Vol. 2, Pages 193-202, 2(1), 193–202.

Bagai, I., Rensing, C., Blackburn, N. J., & Mcevoy, M. M. (2008). Direct Metal Transfer between Periplasmic Proteins Identifies a Bacterial Copper Chaperone †. Biochemistry, 47, 11408–11414.

Bannwarth, M., & Schulz, G. E. (2003). The expression of outer membrane proteins for crystallization. Biochimica et Biophysica Acta (BBA) - Biomembranes, 1610(1), 37–45.

Bannwarth, M., & Schulz, G. E. (2003). The expression of outer membrane proteins for crystallization. Biochimica et Biophysica Acta (BBA) - Biomembranes, 1610(1), 37–45.

Bartolommei, G., Moncelli, M. R., & Tadini-Buoninsegni, F. (2013). A Method to Measure Hydrolytic Activity of Adenosinetriphosphatases (ATPases). PLOS ONE, 8(3), e58615.

Bastos, M., & Velazquez-Campoy, A. (2021). Isothermal titration calorimetry (ITC): a standard operating procedure (SOP). European Biophysics Journal 2021 50:3, 50(3), 363–371.

Bavro, V. N., Pietras, Z., Furnham, N., Pérez-Cano, L., Fernández-Recio, J., Pei, X. Y., Misra, R., & Luisi, B. (2008). Assembly and Channel Opening in a Bacterial Drug Efflux Machine. Molecular Cell, 30(1), 114.

Bayr, H. (2005). Reactive oxygen species. Critical Care Medicine, 33(Suppl), S498–S501.

Beneš, V., Leonhardt, T., Sácký, J., & Kotrba, P. (2018). Two P1B-1-ATPases of Amanita strobiliformis With Distinct Properties in Cu/Ag Transport. Frontiers in Microbiology, 9, 747.

Berrow, N. S., Alderton, D., Sainsbury, S., Nettleship, J., Assenberg, R., Rahman, N., Stuart, D. I., & Owens, R. J. (2007). A versatile ligation-independent cloning method suitable for high-throughput e

Bertani, G. (1951). STUDIES ON LYSOGENESIS I. : The Mode of Phage Liberation by Lysogenic Escherichia coli1. Journal of Bacteriology, 62(3), 293.

Bertini, I., Gray, H. B., Lippard, S. J., Selverstone Valentine, J., Lippard, S., & Valentine, J. (1994). BIOINORGANIC CHEMISTRY.

Bharti, R., Wadhwani, K., Tikku, A., & Chandra, A. (2010). Dental amalgam: an update. Journal of Conservative Dentistry, 13(4), 204–208.

Birch, J., Cheruvara, H., Gamage, N., Harrison, P. J., Lithgo, R., & Quigley, A. (2020). Changes in Membrane Protein Structural Biology. Biology, 9(11), 1–31.

Bloch, M., Santiveri, M., & Taylor, N. M. I. (2020). Membrane Protein Cryo-EM: Cryo-Grid Optimization and Data Collection with Protein in Detergent. Methods in Molecular Biology, 2127, 227–244.

Bochkarev, A., & Bochkareva, E. (2004). From RPA to BRCA2: Lessons from single-stranded DNA binding by the OB-fold. In Current Opinion in Structural Biology (Vol. 14, Issue 1, pp. 36–42). Elsevier Ltd.

Bond, C. S. (2003). TopDraw: a sketchpad for protein structure topology cartoons. Bioinformatics, 19(2), 311–312.

Bondarczuk, K., & Piotrowska-Seget, Z. (2013). Molecular basis of active copper resistance mechanisms in Gram-negative bacteria. In Cell Biology and Toxicology (Vol. 29, Issue 6, pp. 397–405). Springer.

Borjigin, J., Payne, A. S., Deng, J., Li, X., Wang, M. M., Ovodenko, B., Gitlin, J. D., & Snyder, S. H. (1999). A novel pineal night-specific ATPase encoded by the Wilson disease gene. Journal of Neuroscience, 19(3), 1018–1026.

Bornhorst, J. A., & Falke, J. J. (2000). Purification of Proteins Using Polyhistidine Affinity Tags. Methods in Enzymology, 326, 245.

Bragg, P. D., & Rainnie, D. J. (1974). The effect of silver ions on the respiratory chain of Escherichia coli. Canadian Journal of Microbiology, 20(6), 883–889.

Broecker, J., Eger, B. T., & Ernst, O. P. (2017). Crystallogenesis of Membrane Proteins Mediated by Polymer-Bounded Lipid Nanodiscs. Structure, 25(2), 384–392.

Brown, N. L., Barrett, S. R., Camakaris, J., Lee, B. T. O., & Rouch, D. A. (1995). Molecular genetics and transport analysis of the copper-resistance determinant (pco) from Escherichia coli plasmid pRJ1004. Molecular Microbiology, 17(6), 1153–1166.

Bublitz, M., Morth, J. P., & Nissen, P. (2011). P-type ATPases at a glance. Journal of Cell Science, 124(124), 2515–2519.

Bublitz, M., Nass, K., Drachmann, N. D., Markvardsen, A. J., Gutmann, M. J., Barends, T. R. M., Mattle, D., Shoeman, R. L., Doak, R. B., Boutet, S., Messerschmidt, M., Seibert, M. M., Williams, G. J., Foucar, L., Reinhard, L., Sitsel, }} Oleg, Gregersen, J. L., Clausen, J. D., Boesen, T., … Schlichting, I. (2015). Structural studies of P-type ATPase–ligand complexes using an X-ray free-electron laser. IUCrJ, 2, 409–420.

Bublitz, M., Poulsen, H., Preben Morth, J., Nissen, P., Christopher Tate, B., & Stevens, R. (2010). In and out of the cation pumps: P-Type ATPase structure revisited. Current Opinion in Structural Biology, 20, 431–439.

Butler, K. S., Peeler, D. J., Casey, B. J., Dair, B. J., & Elespuru, R. K. (2015). Silver nanoparticles: correlating nanoparticle size and cellular uptake with genotoxicity. Mutagenesis, 30(4), 577–591.

C, L., M, R., W, W., E, G., M, H., D, L., JM, R., K, G., & CE, B. (1996). ATPase activity of the cystic fibrosis transmembrane conductance regulator. The Journal of Biological Chemistry, 271(45), 28463–28468.

Carlson, M. L., Young, J. W., Zhao, Z., Fabre, L., Jun, D., Li, J., Li, J., Dhupar, H. S., Wason, I., Mills, A. T., Beatty, J. T., Klassen, J. S., Rouiller, I., & Duong, F. (2018). The peptidisc, a simple method for stabilizing membrane proteins in detergent-free solution. ELife, 7.

Caroff, M., & Karibian, D. (2003). Structure of bacterial lipopolysaccharides. In Carbohydrate Research (Vol. 338, Issue 23, pp. 2431–2447). Elsevier BV.

Cha, J.-S., & Cooksey, D. A. (1991). Copper resistance in Pseudomonas syringae mediated by periplasmic and outer membrane proteins (copper-binding proteins/blue copper proteins). In Proc. Nati. Acad. Sci. USA (Vol. 88).

Chabert, V., Hologne, M., Sénèque, O., Crochet, A., Walker, O., & Fromm, K. M. (2017). Model peptide studies of Ag + binding sites from the silver resistance protein SilE. Chemical Communications, 53(45), 6105–6108.

Chaga, G., Hopp, J., & Nelson, P. (1999). Immobilized metal ion affinity chromatography on Co^{2+}-carboxymethylaspartate–agarose Superflow, as demonstrated by one-step purification of lactate dehydrogenase from

chicken breast muscle. Biotechnology and Applied Biochemistry, 29(1), 19–24.

Chalk, R., Berridge, G., Shrestha, L., Strain-Damerell, C., Mahajan, P., Yue, W., Gileadi, O., & Burgess-Brown, N. (2014). High-Throughput Mass Spectrometry Applied to Structural Genomics. Chromatography, 1(4), 159–175.

Chen, C., & Wang, J. (2007). Influence of metal ionic characteristics on their biosorption capacity by Saccharomyces cerevisiae. Applied Microbiology and Biotechnology, 74(4), 911–917.

Chen, D., Zhao, Y., Qiu, Y., Xiao, L., He, H., Zheng, D., Li, X., Yu, X., Xu, N., Hu, X., Chen, F., Li, H., & Chen, Y. (2020). CusS-CusR Two-Component System Mediates Tigecycline Resistance in Carbapenem-Resistant Klebsiella pneumoniae. Frontiers in Microbiology, 10.

Chen, V. B., Arendall, W. B., III, Headd, J. J., Keedy, D. A., Immormino, R. M., Kapral, G. J., Murray, L. W., Richardson, J. S., & Richardson, D. C. (2010). MolProbity: all-atom structure validation for macromolecular crystallography. Acta Crystallographica Section D: Biological Crystallography, 66(Pt 1), 12.

Choi, Y., Kim, H. A., Kim, K. W., & Lee, B. T. (2018). Comparative toxicity of silver nanoparticles and silver ions to Escherichia coli. Journal of Environmental Sciences, 66, 50–60.

Chojnacka, K. (2010). Biosorption and bioaccumulation – the prospects for practical applications. Environment International, 36, 299–307.

Cizmar, P., & Yuana, Y. (2017). Detection and Characterization of Extracellular Vesicles by Transmission and Cryo-Transmission Electron Microscopy. Methods in Molecular Biology (Clifton, N.J.), 1660, 221–232.

Conroy, O., Kim, E.-H., McEvoy, M. M., & Rensing, C. (2010). Differing ability to transport non-metal substrates by two RND-type metal exporters. FEMS Microbiology Letters, 308(2), 115.

Cook, G., Costerton, J. W., & Darouiche, R. O. (2000). Direct confocal microscopy studies of the bacterial colonization in vitro of a silver-coated heart valve sewing cuff. International Journal of Antimicrobial Agents, 13(3), 169–173.

Cooksey, D. A. (1994). Molecular mechanisms of copper resistance and accumulation in bacteria. FEMS Microbiology Reviews, 14(4), 381–386.

Cowan, S. W., Garavito, R. M., Jansonius, J. N., Jenkins, J. A., Karlsson, R., König, N., Pai, E. F., Pauptit, R. A., Rizkallah, P. J., Rosenbusch, J. P., Rummel, G., & Schirmer, T. (1995). The structure of OmpF porin in a tetragonal crystal form. Structure, 3(10), 1041–1050.

Cross, R. L., & Müller, V. (2004). The evolution of A-, F-, and V-type ATP synthases and ATPases: reversals in function and changes in the H + /ATP coupling ratio. FEBS Letters, 576(1–2), 1–4.

Dakal, T. C., Kumar, A., Majumdar, R. S., & Yadav, V. (2016). Mechanistic Basis of Antimicrobial Actions of Silver Nanoparticles. Frontiers in Microbiology, 7, 1831.

D'Arcy, A., Mac Sweeney, A., Stihle, M., Haber, A., & IUCr. (2003). The advantages of using a modified microbatch method for rapid screening of protein crystallization conditions. Urn:Issn:0907-4449, 59(2), 396–399.

Denisov, I. G., & Sligar, S. G. (2016). Nanodiscs for structural and functional studies of membrane proteins. Nature Structural & Molecular Biology 2016 23:6, 23(6), 481–486.

Denks, K., Vogt, A., Sachelaru, I., Petriman, N.-A., Kudva, R., & Koch, H.-G. (2014). The Sec translocon mediated protein transport in prokaryotes and eukaryotes.

Dibrov, P., Dzioba, J., Gosink, K. K., & Häse, C. C. (2002). Chemiosmotic mechanism of antimicrobial activity of Ag+ in Vibrio cholerae. Antimicrobial Agents and Chemotherapy, 46(8), 2668–2670.

Diep, P., Mahadevan, R., & Yakunin, A. F. (2018). Heavy metal removal by bioaccumulation using genetically engineered microorganisms. In Frontiers in Bioengineering and Biotechnology (Vol. 6, Issue OCT, p. 157). Frontiers Media S.A.

Drees, S. L., Beyer, D. F., Lenders-Lomscher, C., & Lübben, M. (2015). Distinct functions of serial metal-binding domains in the E scherichia coli P 1 B -ATPase CopA. Molecular Microbiology, 97(3), 423–438.

Drew, D., Lerch, M., Kunji, E., Slotboom, D.-J., & de Gier, J.-W. (2006). Optimization of membrane protein overexpression and purification using GFP fusions. Nature Methods, 3(4), 303–313.

Du, D., Wang, Z., James, N. R., Voss, J. E., Klimont, E., Ohene-Agyei, T., Venter, H., Chiu, W., & Luisi, B. F. (2014). Structure of the AcrAB–TolC multidrug efflux pump. Nature, 509(7501), 512–515.

Ducheyne, P., Grainger, D. W., Healy, K. E., Hutmacher, D. W., & Kirkpatrick, C. J. (C. J. (n.d.). Comprehensive biomaterials II.

Ebel, C. (2011). Sedimentation velocity to characterize surfactants and solubilized membrane proteins. Methods, 54(1), 56–66.

Eckhardt, S., Brunetto, P. S., Gagnon, J., Priebe, M., Giese, B., & Fromm, K. M. (2013). Nanobio Silver: Its Interactions with Peptides and Bacteria, and Its Uses in Medicine. Chemical Reviews, 113(7), 4708–4754.

Edwards-Jones, V. (2009). The benefits of silver in hygiene, personal care and healthcare. Letters in Applied Microbiology, 49(2), 147–152.

Elkrewi, E., Randall, C. P., Ooi, N., Cottell, J. L., & O'Neill, A. J. (2017). Cryptic silver resistance is prevalent and readily activated in certain Gram-negative pathogens. *Journal of Antimicrobial Chemotherapy*, *72*(11), 3043–3046.

Emsley, P., & Cowtan, K. (2004). Coot: model-building tools for molecular graphics. Acta Crystallographica. Section D, Biological Crystallography, 60(Pt 12 Pt 1), 2126–2132.

Esmann, M. (1988). ATPase and phosphatase activity of Na+,K+-ATPase: Molar and specific activity, protein determination. Methods in Enzymology, 156, 105–115.

Eswaran, J., Hughes, C., & Koronakis, V. (2003). Locking TolC Entrance Helices to Prevent Protein Translocation by the Bacterial Type I Export Apparatus. Journal of Molecular Biology, 327(2), 309–315.

Evans, P. R. (2006). Scaling and assessment of data quality. Acta Crystallographica. Section D, Biological Crystallography, 62(Pt 1), 72–82.

Evans, P. R., & Murshudov, G. N. (2013). How good are my data and what is the resolution? Acta Crystallographica. Section D, Biological Crystallography, 69(Pt 7), 1204–1214.

Evans, P., & McCoy, A. (2008). An introduction to molecular replacement. Acta Crystallographica Section D: Biological Crystallography, 64(Pt 1), 1.

F, G. (2015). The MORPHEUS II protein crystallization screen. Acta Crystallographica. Section F, Structural Biology Communications, 71(Pt 7), 831–837.

Fairhead, M., & Howarth, M. (2015). Site-specific biotinylation of purified proteins using BirA. Methods in Molecular Biology, 1266, 171–184.

Fan, B., & Rosen, B. P. (2002). Biochemical characterization of CopA, the Escherichia coli Cu(I)-translocating P-type ATPase. Journal of Biological Chemistry, 277(49), 46987–46992.

Fazio, V. J., Peat, T. S., & Newman, J. (2014). A drunken search in crystallization space. Acta Crystallographica. Section F, Structural Biology Communications, 70(Pt 10), 1303.

Feng, Q. L., Wu, J., Chen, G. Q., Cui, F. Z., Kim, T. N., & Kim, J. O. (2000). A mechanistic study of the antibacterial effect of silver ions on Escherichia coli and Staphylococcus aureus. Journal of Biomedical Materials Research, 52(4), 662–668.

Filip, C., Fletcher, G., Wulff, J. L., & Earhart, C. F. (1973). Solubilization of the Cytoplasmic Membrane of Escherichia coli by the Ionic Detergent Sodium-Lauryl Sarcosinate. JOURNAL OF BACTERIOLOGY, 115(3), 717–722.

Finley, P. J., Norton, R., Austin, C., Mitchell, A., Zank, S., & Durham, P. (2015). Unprecedented Silver Resistance in Clinically Isolated Enterobacteriaceae: Major Implications for Burn and

Wound Management. *Antimicrobial Agents and Chemotherapy*, *59*(8), 4734.

Fleming, A. (1929). On the antibacterial action of cultures of a penicillium, with special reference to their use in the isolation of b. influenzae.

Flynn, R. L., & Zou, L. (2010). Oligonucleotide/oligosaccharide-binding fold proteins: A growing family of genome guardians. In Critical Reviews in Biochemistry and Molecular Biology (Vol. 45, Issue 4, pp. 266–275). NIH Public Access.

Fomina, M., & Gadd, G. M. (2014). Biosorption: Current perspectives on concept, definition and application. Bioresource Technology, 160, 3–14.

Fox, B. G., & Blommel, P. G. (n.d.). Autoinduction of Protein Expression.

Fox, B. S., Beyer, M. K., & Bondybey, V. E. (2002). Coordination chemistry of silver cations. Journal of the American Chemical Society, 124(45), 13613–13623.

Fox, C. L., & Modak, S. M. (1974). Mechanism of Silver Sulfadiazine Action on Burn Wound Infections. In Antimicrobial Agents and Chemotherapy (Vol. 5, Issue 6).

Franke, S., Grass, G., Rensing, C., & Nies, D. H. (2003). Molecular analysis of the copper-transporting efflux system CusCFBA of Escherichia coli. Journal of Bacteriology, 185(13), 3804–3812.

Frauenfeld, J., Löving, R., Armache, J.-P., Sonnen, A., Guettou, F., Moberg, P., Zhu, L., Jegerschöld, C., Flayhan, A., Briggs, J. A. G., Garoff, H., Löw, C., Cheng, Y., & Nordlund, P. (2016). A novel lipoprotein

nanoparticle system for membrane proteins. Nature Methods, 13(4), 345.

Fritz, J. J. (2002). Solubility of cuprous chloride in various soluble aqueous chlorides. Journal of Chemical and Engineering Data, 27(2), 188–193.

Fu, Y., Tsui, H. C. T., Bruce, K. E., Sham, L. T., Higgins, K. A., Lisher, J. P., Kazmierczak, K. M., Maroney, M. J., Dann, C. E., Winkler, M. E., & Giedroc, D. P. (2013). A new structural paradigm in copper resistance in Streptococcus pneumoniae. Nature Chemical Biology, 9(3), 177–183.

Gadd, G. . (2009). Biosorption: critical review of scientific rationale, environmental importance and significance for pollution treatment. Journal of Chemical Technology & Biotechnology, 84(1), 13–28.

Gadd, G. . (1990). Heavy metal accumulation by bacteria and other microorganisms. Experientia, 46, 834–840.

Gallenito, M. J., Irvine, G. W., Zhang, L., Meloni, G., Li, R., Chemcomm, /, & Communication, C. (2019). Coordination promiscuity guarantees metal substrate selection in transmembrane primary-active Zn 2+ pumps †. Chem. Commun, 55, 10844.

Geoff, T., Battye, G., Kontogiannis, L., Johnson, O., Powell, H. R., & Leslie, A. G. W. (2011). Biological Crystallography iMOSFLM: a new graphical interface for diffraction-image processing with MOSFLM. Research Papers Acta Cryst, 67, 271–281.

Ghandour, W., Hubbard III, J. A., Deistung, J., Hughes, M. N., & Poole, R. K. (1988). The uptake of silver ions by Escherichia coli K12: toxic

effects and interaction with copper ions. In Appl Microbiol Biotechnol (Vol. 28).

Gibson, D. G., Young, L., Chuang, R. Y., Venter, J. C., Hutchison, C. A., & Smith, H. O. (2009). Enzymatic assembly of DNA molecules up to several hundred kilobases. Nature Methods, 6(5), 343–345.

Giner-Lamia, J., López-Maury, L., Reyes, J. C., & Florencio, F. J. (2012). The CopRS two-component system is responsible for resistance to copper in the cyanobacterium Synechocystis sp. PCC 6803. Plant Physiology, 159(4), 1806–1818.

Gonzalez-Flecha, B., & Demple, B. (1995). Metabolic sources of hydrogen peroxide in aerobically growing Escherichia coli. Journal of Biological Chemistry, 270(23), 13681–13687.

González-Guerrero, M., & Argü, J. M. (2008). Mechanism of Cu-transporting ATPases: Soluble Cu chaperones directly transfer Cu to transmembrane transport sites. Proc. Nati. Acad. Sci. USA, 105(16), 5992–5997.

Gordon, O., Slenters, T. V., Brunetto, P. S., Villaruz, A. E., Sturdevant, D. E., Otto, M., Landmann, R., & Fromm, K. M. (2010). Silver coordination polymers for prevention of implant infection: Thiol interaction, impact on respiratory chain enzymes, and hydroxyl radical induction. Antimicrobial Agents and Chemotherapy, 54(10), 4208–4218.

Gourdon, P., Liu, X.-Y., Skjørringe, T., Morth, J. P., Møller, L. B., Pedersen, B. P., & Nissen, P. (2011). Crystal structure of a copper-transporting PIB-type ATPase. Nature, 475(7354), 59–64.

Gourley, D. G., Schüttelkop, A. W., Anderson, L. A., Price, N. C., Boxer, D. H., & Hunter, W. N. (2001). Oxyanion binding alters conformation and quaternary structure of the C-terminal domain of the transcriptional regulator ModE. Implications for molybdate-dependent regulation, signaling, storage, and transport. Journal of Biological Chemistry, 276(23), 20641–20647.

Gram, & C. (1884). Ueber die isolirte Farbung der Schizomyceten in Schnitt-und Trockenpraparaten. Fortschritte Der Medicin, 2, 185–189.

Grass, G., & Rensing, C. (2001). CueO is a multi-copper oxidase that confers copper tolerance in Escherichia coli. Biochemical and Biophysical Research Communications, 286(5), 902–908.

Greenfield, N. J. (2006). Using circular dichroism spectra to estimate protein secondary structure. Nature Protocols, 1(6), 2876.

Grieben, M., Pike, A. C. W., Shintre, C. A., Venturi, E., El-Ajouz, S., Tessitore, A., Shrestha, L., Mukhopadhyay, S., Mahajan, P., Chalk, R., Burgess-Brown, N. A., Sitsapesan, R., Huiskonen, J. T., & Carpenter, E. P. (2016). Structure of the polycystic kidney disease TRP channel Polycystin-2 (PC2). Nature Structural & Molecular Biology 2016 24:2, 24(2), 114–122.

GS, A., CC, W., T, C., & DL, S. (2011). The architecture of CopA from Archeaoglobus fulgidus studied by cryo-electron microscopy and computational docking. Structure (London, England : 1993), 19(9), 1219–1232.

Guangyong, J. I., & Silver, S. (1995). Bacterial resistance mechanisms for heavy metals of environmental concern. In Journal of Industrial Microbiology (Vol. 14).

Gupta, A., Phung, L. T., Taylor, D. E., & Silver, S. (2001). Diversity of silver resistance genes in IncH incompatibility group plasmids. Microbiology, 147(12), 3393–3402.

Gupta, A., Maynes, M., & Silver, S. (1998). Effects of halides on plasmid-mediated silver resistance in Escherichia coli. Applied and Environmental Microbiology, 64(12), 5042–5045.

Gupta, A., Matsui, K., Lo, J.-F., & Silver, S. (1999). Molecular basis for resistance to silver cations in Salmonella. Nature Medicine, 5(2), 183–188.

Gwin, C. A., & Gunsch, C. K. (2018). Examining relationships between total silver concentration and Sil silver resistance genes in domestic wastewater treatment plants. Journal of Applied Microbiology, 124(6), 1638–1646.

H, A., M, K., M, Y., T, T., T, K., H, Y., S, N., A, N., & T, N. (2004). Crystal structure of the drug discharge outer membrane protein, OprM, of Pseudomonas aeruginosa: dual modes of membrane anchoring and occluded cavity end. The Journal of Biological Chemistry, 279(51), 52816–52819.

Hancock, R. E. W. (1984). Alterations in outer membrane permibabilty. Annual Review of Microbiology, 38(237–264).

Hassell, A. M., An, G., Bledsoe, R. K., Bynum, J. M., Carter, H. L., Deng, S. J. J., Gampe, R. T., Grisard, T. E., Madauss, K. P., Nolte, R. T.,

Rocque, W. J., Wang, L., Weaver, K. L., Williams, S. P., Wisely, G. B., Xu, R., & Shewchuk, L. M. (2006). Crystallization of protein-ligand complexes. Acta Crystallographica Section D: Biological Crystallography, 63(1), 72–79.

Hauer, F., Gerle, C., Fischer, N., Oshima, A., Shinzawa-Itoh, K., Shimada, S., Yokoyama, K., Fujiyoshi, Y., & Stark, H. (2015). GraDeR: Membrane Protein Complex Preparation for Single-Particle Cryo-EM. Hauer, F., Gerle, C., Fischer, N., Oshima, A., Shinzawa-Itoh, K., Shimada, S., Yokoyama, K., Fujiyoshi, Y., & Stark, H. (2015). GraDeR: Membrane Protein Complex Preparation for Single-Particle Cryo-EM. Structure, 23(9), 1769–1775.

Hauer, F., Gerle, C., Fischer, N., Oshima, A., Shinzawa-Itoh, K., Shimada, S., Yokoyama, K., Fujiyoshi, Y., & Stark, H. (2015). GraDeR: Membrane Protein Complex Preparation for Single-Particle Cryo-EM. Structure, 23(9), 1769–1775.

Hayyan, M., Ali Hashim, M., & AlNashef, I. M. (2016). Superoxide Ion: Generation and Chemical Implications. Chemical Reviews, 116(3029–3085).

Hernández-Montes, G., Argüello, J. M., & Valderrama, B. (2012). Evolution and diversity of periplasmic proteins involved in copper homeostasis in gamma proteobacteria. BMC Microbiology, 12(1), 249.

Higgins, M. K., Eswaran, J., Edwards, P., Schertler, G. F. X., Hughes, C., & Koronakis, V. (2004). Structure of the Ligand-blocked Periplasmic Entrance of the Bacterial Multidrug Efflux Protein TolC.

Hobman, J. L., & Crossman, L. C. (2014). Bacterial antimicrobial metal ion resistance. Jounral of Medical Microbiology, 64, 471–497.

Holdgate, G. A., Tunnicliffe, A., Ward, W. H. J., Weston, S. A., Rosenbrock, G., Barth, P. T., Taylor, I. W. F., Pauptit, R. A., & Timms, D. (1997). The Entropic Penalty of Ordered Water Accounts for Weaker Binding of the Antibiotic Novobiocin to a Resistant Mutant of DNA Gyrase: A Thermodynamic and Crystallographic Study ‡.

Holm, L. (2020). DALI and the persistence of protein shape. Protein Science, 29(1), 128–140.

Hooton, S. P. T., Pritchard, A. C. W., Asiani, K., Gray-Hammerton, C. J., Stekel, D. J., Crossman, L. C., Millard, A. D., & Hobman, J. L. (2021). Laboratory Stock Variants of the Archetype Silver Resistance Plasmid pMG101 Demonstrate Plasmid Fusion, Loss of Transmissibility, and Transposition of Tn7/pco/sil Into the Host Chromosome. Frontiers in Microbiology, 1, 2339.

Hsu, G. C., Spilburg, C. A., Bull, C., & Hoffman, B. M. (1972). Coboglobins: Heterotropic Linkage and the Existence of a Quaternary Structure Change Upon Oxygenation of Cobaltohemoglobin. Proceedings of the National Academy of Sciences, 69(8), 2122–2124.

Huh, A. J., & Kwon, Y. J. (2011). "Nano antibiotics": A new paradigm for treating infectious diseases using nanomaterials in the antibiotics resistant era. Journal of Controlled Release, 156(2), 128–145.

Hussain, R., Benning, K., Myatt, D., Javorfi, T., Longo, E., Rudd, T.R., Pulford, B., and Siligardi, G. (2015). CDApps: integrated software for

experimental planning and data processing at beamline B23, Diamond Light Source. Corrigendum. J Synchrotron Radiat *22*, 862.

Hussain, R., Jávorfi, T., & Siligardi, G. (2012). Circular dichroism beamline B23 at the Diamond Light Source. Journal of Synchrotron Radiation, 19(1).

Hutchings, M., Truman, A., & Wilkinson, B. (2019). Antibiotics: past, present and future. Current Opinion in Microbiology, 51, 72–80.

I, B., C, R., NJ, B., & MM, M. (2008). Direct metal transfer between periplasmic proteins identifies a bacterial copper chaperone. Biochemistry, 47(44), 11408–11414.

Incardona, M.-F., Bourenkov, G. P., Levik, K., Pieritz, R. A., Popov, A. N., & Svensson, O. (2009). Synchrotron Radiation EDNA: a framework for plugin-based applications applied to X-ray experiment online data analysis. (2009). Journal of Synchrotron Radiation, 16, 827-879.

Inesi, G., Lewis, D., Ma, H., Prasad, A., & Toyoshima, C. (2006). Concerted Conformational Effects of Ca 2+ and ATP Are Required for Activation of Sequential Reactions in the Ca 2+ ATPase (SERCA) Catalytic Cycle †, ‡. Biochemistry, 45, 13769–13778.

Inesi, G., Pilankatta, R., & Tadini-Buoninsegni, F. (2014). Biochemical characterization of P-type copper ATPases. In Biochemical Journal (Vol. 463, Issue 2, pp. 167–176). Portland Press Ltd.

International Tables for Crystallography. (2006). International Tables for Crystallography.

Jardetzky, O. (1966). Simple allosteric model for membrane pumps. In Nature (Vol. 211, Issue 5052, pp. 969–970). Nature Publishing Group.

Jimenez, J., Chakraborty, I., Cid, A. M. Del, & Mascharak, P. K. (2017). Five- and Six-Coordinated Silver(I) Complexes Derived from 2,6-(Pyridyl)iminodiadamantanes: Sustained Release of Bioactive Silver toward Bacterial Eradication. Inorganic Chemistry, 56(9), 4784–4787.

Jones, C. E., Daly, N. L., Cobine, P. A., Craik, D. J., & Dameron, C. T. (2003). Structure and metal binding studies of the second copper binding domain of the Menkes ATPase. Journal of Structural Biology, 143(3), 209–218.

Joshi, N., Ngwenya, B. T., Butler, I. B., & French, C. E. (2015). Use of bioreporters and deletion mutants reveals ionic silver and ROS to be equally important in silver nanotoxicity. Journal of Hazardous Materials, 287, 51–58.

Kabsch, W. (1988). Automatic Indexing of Rotation Diffraction Patterns. J. Appl. Cryst, 21, 67–71.

Kaduková, J., & Virčíková, E. (2004). Comparison of differences between copper bioaccumulation and biosorption. Environment International, 31, 227–232.

Kantardjieff, K. A., & Rupp, B. (2003). Matthews coefficient probabilities: Improved estimates for unit cell contents of proteins, DNA, and protein–nucleic acid complex crystals. Protein Science : A Publication of the Protein Society, 12(9), 1865.

Kawate, T., & Gouaux, E. (2006). Fluorescence-Detection Size-Exclusion Chromatography for Precrystallization Screening of Integral Membrane Proteins. Structure, 14(4), 673–681.

Keegan, N., Ridley, H., & Lakey, J. H. (2010). Discovery of Biphasic Thermal Unfolding of OmpC with Implications for Surface Loop Stability. Biochemistry, 49(45), 9715–9721.

Kittleson, J. T., Loftin, I. R., Hausrath, A. C., Engelhardt, K. P., Rensing, C., & Mcevoy, M. M. (2006). Periplasmic Metal-Resistance Protein CusF Exhibits High Affinity and Specificity for Both Cu I and Ag I †. Biochemistry, 45, 11096–11102.

Koronakis, V., Eswaran, J., & Hughes, C. (2004). structure and function of tolc: The Bacterial Exit Duct for Proteins and Drugs. Annual Review of Biochemistry, 73, 467–489.

Koronakis, V., Sharff, A., Koronakis, E., Luisi, B., & Hughes, C. (2000). Crystal structure of the bacterial membrane protein TolC central to multidrug efflux and protein export. Nature, 405(6789), 914–919.

Krainer, G., Broecker, J., Vargas, C., Fanghänel, J., & Keller, S. (2012). Quantifying High-Affinity Binding of Hydrophobic Ligands by Isothermal Titration Calorimetry. Analytical Chemistry, 84(24), 10715–10722.

Kramer, J., Özkaya, Ö., & Kümmerli, R. (2019). Bacterial siderophores in community and host interactions. Nature Reviews Microbiology 2019 18:3, 18(3), 152–163.

Krebs, H. A., & Johnson, W. A. (1980). The role of citric acid in intermediate metabolism in animal tissues. *FEBS Letters*, *117 Suppl*, 383–390.

Krissinel, E., & Henrick, K. (2007). Inference of Macromolecular Assemblies from Crystalline State. Journal of Molecular Biology, 372(3), 774–797.

Kropinski, A. M., Parr, T. R., Angus, B. L., Hancock, R. E. W., Ghiorse, W. C., & Greenberg3, E. P. (1987). Isolation of the Outer Membrane and Characterization of the Major Outer Membrane Protein from Spirochaeta aurantia. Journal of Bacteriology, 169(1), 172–179.

Kühlbrandt, W. (2004). Biology, structure and mechanism of P-type ATPases. In Nature Reviews Molecular Cell Biology (Vol. 5, Issue 4, pp. 282–295). Nature Publishing Group.

Kulathila, R., Kulathila, R., Indic, M., & van den Berg, B. (2011). Crystal structure of Escherichia coli CusC, the outer membrane component of a heavy metal efflux pump. PLoS ONE, 6(1).

Le Roy, A., Wang, K., Schaack, B., Schuck, P., Breyton, C., & Ebel, C. (2015). AUC and Small-Angle Scattering for Membrane Proteins. Methods in Enzymology, 562, 257–286.

Lebedev, A. A., & Isupov, M. N. (2014). Space-group and origin ambiguity in macromolecular structures with pseudo-symmetry and its treatment with the program Zanuda. Acta Crystallographica Section D: Biological Crystallography, 70(9), 2430–2443.

Ledin, M. (2000). Accumulation of metals by microorganisms - processes and importance for soil systems. Earth Science Reviews, 51(1–4), 1–31.

Leekha, S., Terrell, C. L., & Edson, R. S. (2011). General Principles of Antimicrobial Therapy. Mayo Clinic Proceedings, 86(2), 156–167.

Lekeux, G., Crowet, J.-M., Nouet, C., Joris, M., Jadoul, A., Bosman, B., Carnol, M., Motte, P., Lins, L., Galleni, M., & Hanikenne, M. (2019). Homology modeling and in vivo functional characterization of the zinc

permeation pathway in a heavy metal P-type ATPase. Journal of Experimental Botany, 70(1), 329–341.

León-Torres, A., Arango, E., Castillo, E., & Soto, C. Y. (2020). CtpB is a plasma membrane copper (I) transporting P-type ATPase of Mycobacterium tuberculosis. Biological Research, 53(1), 6.

Li, W. R., Xie, X. B., Shi, Q. S., Zeng, H. Y., Ou-Yang, Y. S., & Chen, Y. Ben. (2010). Antibacterial activity and mechanism of silver nanoparticles on Escherichia coli. Applied Microbiology and Biotechnology, 85(4), 1115–1122.

Liebschner, D., Afonine, P. V., Baker, M. L., Bunkóczi, G., Chen, V. B., Croll, T. I., Hintze, B., Hung, L.-W., Jain, S., McCoy, A. J., Moriarty, N. W., Oeffner, R. D., Poon, B. K., Prisant, M. G., Read, R. J., Richardson, J. S., Richardson, D. C., Sammito, M. D., Sobolev, O. V., … Adams, P. D. (2019). Macromolecular structure determination using X-rays, neutrons and electrons: recent developments in Phenix. Acta Crystallographica. Section D, Structural Biology, 75(Pt 10), 861.

Liu, W., Chun, E., Thompson, A. A., Chubukov, P., Xu, F., Katritch, V., Han, G. W., Roth, C. B., Heitman, L. H., IJzerman, A. P., Cherezov, V., & Stevens, R. C. (2012). Structural Basis for Allosteric Regulation of GPCRs by Sodium Ions. Science (New York, N.Y.), 337(6091), 232.

Lobedanz, S., Bokma, E., Symmons, M. F., Koronakis, E., Hughes, C., & Koronakis, V. (2007). A periplasmic coiled-coil interface underlying TolC recruitment and the assembly of bacterial drug efflux pumps. Proceedings of the National Academy of Sciences, 104(11), 4612–4617.

Loftin, I. R., Franke, S., Blackburn, N. J., & McEvoy, M. M. (2007). Unusual Cu(I)/Ag(I) coordination of Escherichia coli CusF as revealed by atomic resolution crystallography and X-ray absorption spectroscopy . Protein Science, 16(10), 2287–2293.

Loftin, I. R., Franke, S., Roberts, S. A., Weichsel, A., Héroux, A., Montfort, W. R., Rensing, C., & McEvoy, M. M. (2005). A novel copper-binding fold for the periplasmic copper resistance protein CusF. Biochemistry, 44(31), 10533–10540.

Long, F., Su, C. C., Lei, H. T., Bolla, J. R., Do, S. V., & Yu, E. W. (2012). Structure and mechanism of the tripartite CusCBA heavy-metal efflux complex. In Philosophical Transactions of the Royal Society B: Biological Sciences (Vol. 367, Issue 1592, pp. 1047–1058). Royal Society.

Loo, J. (1997). Studying noncovalent protein complexes by electrospray ionization mass spectrometry. Mass Spectrometry Review, 16, 1–23.

López, M., Quitian, L.-V., Calderón, M.-N., & Soto, C.-Y. (2018). The P-type ATPase CtpG preferentially transports Cd2+ across the Mycobacterium tuberculosis plasma membrane. Archives of Microbiology, 200(3), 483–492.

Lutsenko, S. and Kaplan, J. . (1995). Organization of P-type ATPases: significance of structural diversity. Biochemsitry, 34(48), 15607–15613.

Lutsenko, S., Efremov, R. G., Tsivkovskii, R., & Walker, J. M. (2002). Human Copper-Transporting ATPase ATP7B (The Wilson's Disease Protein): Biochemical Properties and Regulation. In Journal of Bioenergetics and Biomembranes (Vol. 34, Issue 5).

Lutsenko, S., Leshane, E. S., & Shinde, U. (2007). Biochemical basis of regulation of human copper-transporting ATPases. Archives of Biochemistry and Biophysics, 463, 134–148.

Ma, Z., Jacobsen, F. E., & Giedroc, D. P. (2009). Metal Transporters and Metal Sensors: How Coordination Chemistry Controls Bacterial Metal Homeostasis. Chemical Reviews, 109(10), 4644–4681.

MacLennan, D. H., Rice, W. J., & Green, N. M. (1997). The mechanism of Ca2+ transport by sarco(endo)plasmic reticulum Ca2+-ATPases. In Journal of Biological Chemistry (Vol. 272, Issue 46, pp. 28815–28818). American Society for Biochemistry and Molecular Biology.

Mandal, A. K., Yang, Y., Kertesz, T. M., & Argüello, J. M. (2004). Identification of the transmembrane metal binding site in Cu +-transporting PIB-type ATPases. Journal of Biological Chemistry, 279(52), 54802–54807.

Mandal, A. K., & Argüello, J. M. (2003). Functional Roles of Metal Binding Domains of the Archaeoglobus fulgidus Cu^{+}-ATPase CopA †. Biochemistry, 42, 11040–11047.

Mandal, A. K., Cheung, W., & Argüello, J.M. (2002). Characterization of a thermophilic P-type Ag+/Cu+-ATPase from the extremophile Archaeoglobus fulgidus. The Journal of Biological Chemistry, 277(9), 7201–7208.

Martin Picard, ‡,§, Tassadite Dahmane, ‡,∥, Manuel Garrigos, §, Carole Gauron, §, Fabrice Giusti, ∥, Marc le Maire, §, Jean-Luc Popot, ∥ and, & Philippe Champeil*, §. (2006). Protective and Inhibitory Effects of

Various Types of Amphipols on the Ca2+-ATPase from Sarcoplasmic Reticulum: A Comparative Study†. Biochemistry, 45(6), 1861–1869.

Mash, H. E., Chin*, Y.-P., Laura Sigg, Renata Hari, A., & Xue, H. (2002). Complexation of Copper by Zwitterionic Aminosulfonic (Good) Buffers. Analytical Chemistry, 75(3), 671–677.

Matias, V. R. F., Al-Amoudi, A., Dubochet, J., & Beveridge, T. J. (2003). Cryo-transmission electron microscopy of frozen-hydrated sections of Escherichia coli and Pseudomonas aeruginosa. Journal of Bacteriology, 185(20), 6112–6118.

Matthew H. Sazinsky, §, Sorabh Agarwal, §, José M. Argüello,‖ and, & Amy C. Rosenzweig*. (2006). Structure of the Actuator Domain from the Archaeoglobus fulgidus Cu^{+}-ATPase. Biochemistry, 45(33), 9949–9955.

Matthews, B. W. (1966). The Determination of the Position of Anomalously Scattering Heavy Atom Groups in Protein Crystals. Acta Cryst, 20, 230.

Matthews, B. W. (1968). Solvent content of protein crystals. Journal of Molecular Biology, 33(2), 491–497.

Mattle, D., Sitsel, O., Autzen, H. E., Meloni, G., Gourdon, P., & Nissen, P. (2013). On Allosteric Modulation of P-Type Cu+ -ATPases. Journal of Molecular Biology, 425, 2299–2308.

Mayer, G., Ludwig, B., Müller, H.-W., Broek, J. A. van den, Friesen, R. H. E., & Schubert, D. (1999). Studying membrane proteins in detergent solution by analytical ultracentrifugation: different methods for density matching. Progress in Colloid and Polymer Science, 113, 176–181.

McAuliffe, C. A., Quagliano, J. V., & Vallarino, L. M. (2002). Metal Complexes of the Amino Acid DL-Methionine. Inorganic Chemistry, 5(11), 1996–2003.

McCoy, A. J., Grosse-Kunstleve, R. W., Adams, P. D., Winn, M. D., Storoni, L. C., Read, R. J., & IUCr. (2007). Phaser crystallographic software. Journal of Applied Crystallography, 40(4), 658–674.

McCoy, A. J., Grosse-Kunstleve, R. W., Adams, P. D., Winn, M. D., Storoni, L. C., Read, R. J., & IUCr. (2007). Phaser crystallographic software. Journal of Applied Crystallography, 40(4), 658–674.

McHugh, G. L., Moellering, R. C., Hopkins, C. C., & Swartz, M. N. (1975). Salmonella typhimurium resistant to silver nitrate, chloramphenicol, and ampicillin. Lancet (London, England), 1(7901), 235–240.

Mcpherson, A. (2001). A comparison of salts for the crystallization of macromolecules. Protein Science : A Publication of the Protein Society, 10(2), 418.

McPherson, A., & Gavira, J. A. (2014). Introduction to protein crystallization. Acta Crystallographica. Section F, Structural Biology Communications, 70(Pt 1), 2.

Mealman, T. D., Bagai, I., Singh, P., Goodlett, D. R., Rensing, C., Zhou, H., Wysocki, V. H., & McEvoy, M. M. (2011). Interactions between CusF and CusB identified by NMR spectroscopy and chemical cross-linking coupled to mass spectrometry. Biochemistry, 50(13), 2559–2566.

Mealman, T. D., Zhou, M., Affandi, T., Chacón, K. N., Aranguren, M. E., Blackburn, N. J., Wysocki, V. H., & McEvoy, M. M. (2012). N-Terminal

Region of CusB Is Sufficient for Metal Binding and Metal Transfer with the Metallochaperone CusF. Biochemistry, 51(34), 6767–6775.

Meis, L., & Vianna, A. L. (1979). Energy Interconversion by the Ca2+-Dependent ATPase of the Sarcoplasmic Reticulum. Annual Review of Biochemistry, 48(1), 275–292.

Mijnendonckx, K., Leys, N., Mahillon, J., Silver, S., Rob, •, & Houdt, V. (2013). Antimicrobial silver: uses, toxicity and potential for resistance. Biometals, 26, 609–621.

Møller, J. V., Juul, B., & Le Maire, M. (1996). Structural organization, ion transport, and energy transduction of P-type ATPases. In Biochimica et Biophysica Acta - Reviews on Biomembranes (Vol. 1286, Issue 1, pp. 1–51). Elsevier B.V.

Morgan, C. T., Tsivkovskii, R., Kosinsky, Y. A., Efremov, R. G., & Lutsenko, S. (2004). The Distinct Functional Properties of the Nucleotide-binding Domain of ATP7B, the Human Copper-transporting ATPase *: analysis of the wilson disease mutations E1064A, H1069Q, R1151H, and C1104F*. Journal of Biological Chemistry, 279(35), 36363–36371.

Mullen, M. D., Wolf, D. C., Ferris, F. G., Beveridge, § T J, Flemming, C. A., & Bailey3, G. W. (1989). Bacterial Sorption of Heavy Metalst. in Applied and Environmental Microbiology (Vol. 55, Issue 12).

Munson, G. P., Lam, D. L., Outten, F. W., & O'Halloran, T. V. (2000). Identification of a copper-responsive two-component system on the chromosome of Escherichia coli K-12. Journal of Bacteriology, 182(20), 5864–5871.

Murakami, S., Nakashima, R., Yamashita, E., & Yamaguchi, A. (2002). Crystal structure of bacterial multidrug efflux transporter AcrB. Nature, 419(6907), 587–593.

Murphy, L. R., Matubayasi, N., Payne, V. A., & Levy, R. M. (1998). Protein hydration and unfolding – insights from experimental partial specific volumes and unfolded protein models. Folding and Design, 3(2), 105–118.

Murshudov, G. N., Skubák, P., Lebedev, A. A., Pannu, N. S., Steiner, R. A., Nicholls, R. A., Winn, M. D., Long, F., Vagin, A. A., & IUCr. (2011). REFMAC5 for the refinement of macromolecular crystal structures. Acta Crystallographica Section D: Biological Crystallography, 67(4), 355–367.

Murzin, A. G. (1993). OB(oligonucleotide/oligosaccharide binding)-fold: common structural and functional solution for non-homologous sequences. In The EMBO Journal vol (Vol. 12, Issue 3).

Naveed, H., & Liang, J. (2014). Weakly Stable Regions and Protein-Protein Interactions in Beta-Barrel Membrane Proteins. Current Pharmaceutical Design, 20(8), 1268–1273.

Newstead, S., Ferrandon, S., & Iwata, S. (2008). Rationalizing α-helical membrane protein crystallization. Protein Science : A Publication of the Protein Society, 17(3), 466.

Newstead, S., Kim, H., Heijne, G. von, Iwata, S., & Drew, D. (2007). High-throughput fluorescent-based optimization of eukaryotic membrane protein overexpression and purification in Saccharomyces cerevisiae. (2007). Proceedings of the National Academy of Science. 104(35), 13936-13941.

Nies, D. H. (2003). Efflux-mediated heavy metal resistance in prokaryotes. FEMS Microbiology Reviews, 27(2–3), 313–339.

Nies, D. H., & Silver, S. (1995). Ion efflux systems involved in bacterial metal resistances. Journa1. Nies, D. H. & Silver, S. Ion Efflux Systems Involved in Bacterial Metal Resistances. J. Ind. Microbiol. 14, 186–199 (1995).l of Industrial Microbiology, 14(2), 186–199.

Norihisa Tamura, Satoshi Murakami, Yoshiaki Oyama, ⊥, Masaji Ishiguro & Akihito Yamaguchi*, ‡,§. (2005). Direct Interaction of Multidrug Efflux Transporter AcrB and Outer Membrane Channel TolC Detected via Site-Directed Disulfide Cross-Linking†. Biochemistry, 44(33), 11115–11121.

Norimatsu, Y., Hasegawa, K., Shimizu, N., & Toyoshima, C. (2017). Protein–phospholipid interplay revealed with crystals of a calcium pump. Nature Publishing Group, 545.

Oh, S. E., Hassan, S. H. A., & Joo, J. H. (2009). Biosorption of heavy metals by lyophilized cells of Pseudomonas stutzeri. World Journal of Microbiology and Biotechnology, 25(10), 1771–1778.

OKAMURA, H., DENAWA, M., OHNIWA, R., & TAKEYASU, K. (2003). P-Type ATPase Superfamily. Annals of the New York Academy of Sciences, 986(1), 219–223.

Okkeri, J., Bencomo, E., Pietilä, M., & Haltia, T. (2002). Introducing Wilson disease mutations into the zinc-transporting P-type ATPase of Escherichia coli. European Journal of Biochemistry, 269(5), 1579–1586.

Olesen, C., Lykke-Møller Sørensen, T., Christina Nielsen, R., Vuust Møller, J., & Nissen, P. (2004). Dephosphorylation of the Calcium Pump

Coupled to Counterion Occlusion Downloaded from. Science, 306, 2251–2255.

Olesen, C., Picard, M., Winther, A. M. L., Gyrup, C., Morth, J. P., Oxvig, C., Møller, J. V., & Nissen, P. (2007). The structural basis of calcium transport by the calcium pump. Nature, 450(7172), 1036–1042.

Outten, F. W., Huffman, D. L., Hale, J. A., & O'Halloran, T. V. (2001). The Independent cue and cus Systems Confer Copper Tolerance during Aerobic and Anaerobic Growth in Escherichia coli. Journal of Biological Chemistry, 276(33), 30670–30677.

Outten, F. W., Outten, C. E., Hale, J., & O'Halloran, T. V. (2000). Transcriptional activation of an Escherichia coli copper efflux regulon by the chromosomal MerR homologue, CueR. Journal of Biological Chemistry, 275(40), 31024–31029.

Pachori, P., Gothalwal, R., & Gandhi, P. (2019). Emergence of antibiotic resistance Pseudomonas aeruginosa in intensive care unit; a critical review. Genes & Diseases, 6(2), 109–119.

Padilla-Benavides, T., Thompson, A. M. G., McEvoy, M. M., & Argüello, J. M. (2014). Mechanism of ATPase-mediated Cu+ export and delivery to periplasmic chaperones: The interaction of Escherichia coli CopA and CusF. Journal of Biological Chemistry, 289(30), 20492–20501.

Palmgren, M. G., & Nissen, P. (2011). P-Type ATPases Phosphorylated intermediate-type ATPase (P-type ATPase): a family of membrane-embedded biological pumps with a single catalytic subunit that form a phosphorylated intermediate during each catalytic cycle. Annu. Rev. Biophys, 40, 243–266.

Park, H.-J., Kim, J. Y., Kim, J., Lee, J.-H., Hahn, J.-S., Gu, M. B., & Yoon, J. (2009). Silver-ion-mediated reactive oxygen species generation affecting bactericidal activity. Water Research, 43(4), 1027–1032.

Parker, J. L., & Newstead, S. (2016). Membrane Protein Crystallisation: Current Trends and Future Perspectives. Advances in Experimental Medicine and Biology, 922, 61–72.

Parker, J. L., & Newstead, S. (2012). Current trends in α-helical membrane protein crystallization: An update. Protein Science : A Publication of the Protein Society, 21(9), 1358.

Payne, A. S., Kelly, E. J., & Gitlin, J. D. (1998). Functional expression of the Wilson disease protein reveals mislocalization and impaired copper-dependent trafficking of the common H1069Q mutation. Proceedings of the National Academy of Sciences of the United States of America, 95(18), 10854–10859.

Pei, X.-Y., Hinchliffe, P., Symmons, M. F., Koronakis, E., Benz, R., Hughes, C., & Koronakis, V. (2011). Structures of sequential open states in a symmetrical opening transition of the TolC exit duct. Proceedings of the National Academy of Sciences of the United States of America, 108(5), 2112.

Percival, S. L., Bowler, P. G., & Russell, D. (2005). Bacterial resistance to silver in wound care. In Journal of Hospital Infection (Vol. 60, Issue 1, pp. 1–7). W.B. Saunders.

Philips, S. J., Canalizo-Hernandez, M., Yildirim, I., Schatz, G. C., Mondragón, A., & O'Halloran, T. V. (2015). Allosteric transcriptional

regulation via changes in the overall topology of the core promoter. Science, 349(6250), 877–881.

Porath, J. (1992). Immobilized metal ion affinity chromatography. Protein Expression and Purification, 3(4), 263–281.

Post, R. L., & Hegyvahy, C. (1972). Activation by Adenosine Triphosphate in the Phosphorylation Kinetics of Sodium and Potassium Ion Transport Adenosine Triphosphatase. Journal of Biological Chemistry, 247(20), 6530–6540.

Postis, V., Rawson, S., Mitchell, J. K., Lee, S. C., Parslow, R. A., Dafforn, T. R., Baldwin, S. A., & Muench, S. P. (2015). The use of SMALPs as a novel membrane protein scaffold for structure study by negative stain electron microscopy. Biochimica et Biophysica Acta (BBA) - Biomembranes, 1848(2), 496–501.

Powell, H. R. (2021). A beginner's guide to X-ray data processing. The Biochemist, 43(3), 46–50.

Powell, H. R., Battye, T. G. G., Kontogiannis, L., Johnson, O., & Leslie, A. G. (2017). Integrating macromolecular X-ray diffraction data with the graphical user interface iMOSFLM. Nature ProtocolsPowell, H. R. (2017). X-ray data processing. Bioscience Reports, 37(5), 20170227.

Puig, S., Rees, E. M., & Thiele, D. J. (2002). The ABCDs of Periplasmic Copper Trafficking. Structure, 10(10), 1292–1295.

Raimunda, D., González-Guerrero, M., Leeber III, B., & Argüello, J. M. (2011). The transport mechanism of bacterial Cu + -ATPases: distinct efflux rates adapted to different function. BioMetals, 24, 467–475.

Randall, C. P., Gupta, A., Jackson, N., Busse, D., & O'Neill, A. J. (2015). Silver resistance in Gram-negative bacteria: a dissection of endogenous and exogenous mechanisms. Journal of Antimicrobial Chemotherapy, 70(4), 1037–1046.

Randall, C. P., Oyama, L. B., Bostock, J. M., Chopra, I., & O'Neill, A. J. (2013). The silver cation (Ag+): antistaphylococcal activity, mode of action and resistance studies. Journal of Antimicrobial Chemotherapy, 68(1), 131–138.

Rensing, C., Fan, B., Sharma, R., Mitra, B., & Rosen, B. P. (2000). CopA: An Escherichia coli Cu(I)-translocating P-type ATPase. Proceedings of the National Academy of Sciences of the United States of America, 97(2), 652–656.

Rensing, C., & Grass, G. (2003). Escherichia coli mechanisms of copper homeostasis in a changing environment. FEMS Microbiology Reviews, 27(2–3), 197–213.

Reynolds, J. A., & Tanford, C. (1976). Determination of molecular weight of the protein moiety in protein-detergent complexes without direct knowledge of detergent binding. Proceedings of the National Academy of Sciences, 73(12), 4467–4470.

Riggle, P. J., & Kumamoto, C. A. (2000). Role of a Candida albicans P1-type ATPase in resistance to copper and silver ion toxicity. Journal of Bacteriology, 182(17), 4899–4905.

Robinson, N. (2011). A platform for copper pumps.

Rubino, J. T., Riggs-Gelasco, P., & Franz, K. J. (2010). Methionine motifs of copper transport proteins provide general and flexible thioether-only

binding sites for Cu(I) and Ag(I). JBIC Journal of Biological Inorganic Chemistry, 15(7), 1033–1049.

Russell, A. D., & Hugo, W. B. (1994). Antimicrobial activity and action of silver. Progress in Medicinal Chemistry, 31, 351–370.

Ruud, M., Bruseth, L. J., Kleivdal, H., Høgh, B. T., Benz, R., & Jensen, H. B. (2002). Structural characterization of the fusobacterial non-specific porin FomA suggests a 14-stranded topology, unlike the classical porins. Microbiology, 148, 3395–3403.

S, S., J, L., C, L., A, H., M, K., M, S., D, D., DJ, S., & JW, de G. (2012). Optimizing membrane protein overexpression in the Escherichia coli strain Lemo21(DE3). Journal of Molecular Biology, 423(4), 648–659.

Salvay, A. G., Santamaria, M., Le Maire, M., Ebel, C., Salvay, A. G., Ebel, C., & Santamaria, M. (2007). Analytical Ultracentrifugation Sedimentation Velocity for the Characterization of Detergent-Solubilized Membrane Proteins Ca ++-ATPase and ExbB. J Biol Phys, 33, 399–419.

Sazinsky, M. H., Mandal, A. K., Argüello, J. M., & Rosenzweig, A. C. (2006). Structure of the ATP binding domain from the Archaeoglobus fulgidus Cu^{+}-ATPase. Journal of Biological Chemistry, 281(16), 11161–11166.

Scheres, S. H. W. (2019). Single-particle processing in relion-3.1.

Schreurs, W. J. A., & Rosenberg, H. (1982). Effect of Silver Ions on Transport and Retention of Phosphate by Escherichia coli. In Journal of Bacteriology.

Schüttelkopf, A. W., Boxer, D. H., & Hunter, W. N. (2003). Crystal structure of activated ModE reveals conformational changes involving

both oxyanion and DNA-binding domains. Journal of Molecular Biology, 326(3), 761–767.

Seddon, A. M., Curnow, P., & Booth, P. J. (2004). Membrane proteins, lipids and detergents: not just a soap opera. Biochimica et Biophysica Acta (BBA) - Biomembranes, 1666(1–2), 105–117.

Semeykina, A. L., & Skulachev, V. P. (1990). Submicromolar Ag+ increases passive Na+ permeability and inhibits the respiration-supported formation of Na+ gradient in Bacillus FTU vesicles. FEBS Letters, 269(1), 69–72.

Sengupta, S., Chattopadhyay, M. K., & Grossart, H.-P. (2013). The multifaceted roles of antibiotics and antibiotic resistance in nature. Frontiers in Microbiology, 4(MAR).

Shannon, R. D. (1976). Revised Effective Ionic Radii and Systematic Studies of Interatomie Distances in Halides and Chaleogenides. In Acta Cryst (Vol. 32), 751.

Shen, H.-H., Lithgow, T., & Martin, L. L. (2013). Reconstitution of Membrane Proteins into Model Membranes: Seeking Better Ways to Retain Protein Activities. International Journal of Molecular Science, 14(1), 1589

Shi, X., Chen, M., Yu, Z., Bell, J. M., Wang, H., Forrester, I., Villarreal, H., Jakana, J., Du, D., Luisi, B. F., Ludtke, S. J., & Wang, Z. (2019). In situ structure and assembly of the multidrug efflux pump AcrAB-TolC. Nature Communications, 10(1), 1-6.

Shikanai, T., Müller-Moulé, P., Munekage, Y., Niyogi, K. K., & Pilon, M. (2003). PAA1, a P-Type ATPase of Arabidopsis, Functions in Copper Transport in Chloroplasts. The Plant Cell, 15, 1333–1346.

Sievers, F., Wilm, A., Dineen, D., Gibson, T. J., Karplus, K., Li, W., Lopez, R., McWilliam, H., Remmert, M., Söding, J., Thompson, J. D., & Higgins, D. G. (2011). Fast, scalable generation of high-quality protein multiple sequence alignments using Clustal Omega. Molecular Systems Biology, 7(1), 539.

Silhavy, T. J., Kahne, D., & Walker, S. (2010). The Bacterial Cell Envelope. Cold Spring Harbor Perspectives in Biology, 2(5).

Siliu Tan, Melek Erol, Athula Attygalle, Henry Du, and, & Svetlana Sukhishvili*. (2007). Synthesis of Positively Charged Silver Nanoparticles via Photoreduction of AgNO3 in Branched Polyethyleneimine/HEPES Solutions. Langmuir, 23(19), 9836–9843.

Silver, S. (2003). Bacterial silver resistance: molecular biology and uses and misuses of silver compounds. FEMS Microbiology Reviews, 27(2–3), 341–353.

Silver, S. (1981). Mechanisms of Plasmid-Determined Heavy Metal Resistances. In Molecular Biology, Pathogenicity, and Ecology of Bacterial Plasmids (pp. 179–189). Springer US.

Silver, S., Gupta, A., Matsui, K., & Lo, J. F. (1999). Resistance to Ag(I) cations in bacteria: Environments, genes and proteins. Metal-Based Drugs, 6(4–5), 315–320.

Silver, S., Nucifora, G., & Phung, L. T. (1993). Human Menkes X-chromosome disease and the staphylococcal cadmium-resistance

ATPase: a remarkable similarity in protein sequences. Molecular Microbiology, 10(1), 7–12.

Silver, S., & Phung, L. T. (1996). Bacterial heavy metal resistance: New Surprises. In Annu. Rev. Microbiol (Vol. 50).

Silver, S., Phung, L. T., & Silver, G. (2006). Silver as biocides in burn and wound dressings and bacterial resistance to silver compounds. J Ind Microbiol Biotechnol, 33, 627–634.

Singh, S. K., Grass, G., Rensing, C., & Montfort, W. R. (2004). Cuprous oxidase activity of CueO from Escherichia coli. Journal of Bacteriology, 186(22), 7815–7817.

Sitsel, O., Grønberg, C., Autzen, H. E., Wang, K., Meloni, G., Nissen, P., & Gourdon, P. (2015). Structure and Function of Cu(I)-and Zn(II)-ATPases. Biochemistry, 12, 1.

Sivashanmugam, A., Murray, V., Cui, C., Zhang, Y., Wang, J., & Li, Q. (2009). Practical protocols for production of very high yields of recombinant proteins using Escherichia coli. Protein Science, 18(5), 936–948.

Sjöstrand, D., Diamanti, R., Lundgren, C. A. K., Wiseman, B., & Högbom, M. (2017). A rapid expression and purification condition screening protocol for membrane protein structural biology. Protein Science : A Publication of the Protein Society, 26(8), 1653.

Skjørringe, T., Amstrup Pedersen, P., Salling Thorborg, S., Nissen, P., Gourdon, P., & Birk Møller, L. (2017). Characterization of ATP7A missense mutants suggests a correlation between intracellular trafficking and severity of Menkes disease. Scientific Reports, 7(1), 757.

Slawson, R. M., Lee, H., & Trevors, J. T. (1990). Mini review Bacterial interactions with silver. In Biol Metals (Vol. 3).

Slotboom, D. J., Duurkens, R. H., Olieman, K., & Erkens, G. B. (2008). Static light scattering to characterize membrane proteins in detergent solution. Methods, 46(2), 73–82.

Smith, A. T., Smith, K. P., & Rosenzweig, A. C. (2014). Diversity of the metal-transporting P1B-type ATPases. JBIC Journal of Biological Inorganic Chemistry, 19(6), 947–960.

Smith, A. T., Ross, M. O., Hoffman, B. M., & Rosenzweig, A. C. (2017). Metal Selectivity of a Cd-, Co-, and Zn-Transporting P 1B-type ATPase. Biochemistry, 56, 95.

Solioz, M., & Vulpe, C. (1996). CPx-type ATPases: a class of P-type ATPases that pump heavy metals. Trends in Biochemical Sciences, 21(7), 237–241.

Solomon, E. I., Heppner, D. E., Johnston, E. M., Ginsbach, J. W., Cirera, J., Qayyum, M., Kieber-Emmons, M. T., Kjaergaard, C. H., Hadt, R. G., & Tian, L. (2014). Copper Active Sites in Biology. Chemical reviews, 114(7), 3659

Sonnenfeld, E. M., Beveridge, T. J., Koch, A. L., & Doyle', R. J. (1985). Asymmetric Distribution of Charge on the Cell Wall of Bacillus subtilis. In Journal of Bacteriology (Vol. 163, Issue 3).

Sørensen, T. L. M., Møller, J. V., & Nissen, P. (2004). Phosphoryl transfer and calcium ion occlusion in the calcium pump. Science, 304(5677), 1672–1675.

Staehlin, B. M., Gibbons, J. G., Rokas, A., O'Halloran, T. V., & Slot, J. C. (2016). Evolution of a Heavy Metal Homeostasis/Resistance Island Reflects Increasing Copper Stress in Enterobacteria. *Genome Biology and Evolution*, *8*(3), 811.

Stetsenko, A., & Guskov, A. (2017). An Overview of the Top Ten Detergents Used for Membrane Protein Crystallization. Crystals 2017, Vol. 7, Page 197, 7(7), 197.

Storz, G., & Imlay, J. A. (1999). Oxidative stress. Current Opinion in Microbiology, 2(2), 188–194.

Stothart, P. H. (1984). Determination of partial specific volume and absolute concentration by densimetry. Biochem. J, 219, 1049–1052.

Studier, F. W. (2005). Protein production by auto-induction in high-density shaking cultures.

Su, C.-C., Long, F., Lei, H.-T., Bolla, J. R., Do, S. V., Rajashankar, K. R., & Yu, E. W. (2012). Charged amino acids (R83, E567, D617, E625, R669 and K678) of CusA are required for metal-ion transport in the Cus efflux system. Journal of Molecular Biology, 422(3), 429.

Su, C.-C., Yang, F., Long, F., Reyon, D., Routh, M. D., Kuo, D. W., Mokhtari, A. K., Van Ornam, J. D., Rabe, K. L., Hoy, J. A., Lee, Y. J., Rajashankar, K. R., & Yu, E. W. (2009). Crystal Structure of the Membrane Fusion Protein CusB from Escherichia coli. Journal of Molecular Biology, 393(2), 342–355.

Sweadner, K. J. (2017). Structural biology: An ion-transport enzyme that rocks. Nature, 545(7653), 162–164.

Swiegers*, G. F., & Malefetse†, T. J. (2000). New Self-Assembled Structural Motifs in Coordination Chemistry. Chemical Reviews, 100(9), 3483–3537.

Symmons, M. F., Bokma, E., Koronakis, E., Hughes, C., & Koronakis, V. (2009). The assembled structure of a complete tripartite bacterial multidrug efflux pump. Proceedings of the National Academy of Sciences, 106(17), 7173–7178.

Tanford, C., Nozaki, Y., Reynolds, J. A., & Makino, S. (1974). Molecular characterization of proteins in detergent solutions. Biochemistry, 13(11), 2369–2376.

Tartoff, K.D. and Hobbs, C. A. (1987). Improved Media for Growing Plasmid and Cosmid Clones. Bethesda Research Laboratories Focus, 9(12).

Theobald, D. L., Mitton-Fry, R. M., & Wuttke, D. S. (2003). Nucleic acid recognition by OB-fold proteins. In Annual Review of Biophysics and Biomolecular Structure (Vol. 32, pp. 115–133). Annual Reviews 4139 El Camino Way, P.O. Box 10139, Palo Alto, CA 94303-0139, USA .

Thever, M. D., & Saier, M. H. (2009). Bioinformatic Characterization of P-Type ATPases Encoded Within the Fully Sequenced Genomes of 26 Eukaryotes. Journal of Membrane Biology 2009 229:3, 229(3), 115–130.

Thomas, F., Boyle, A. L., Burton, A. J., & Woolfson, D. N. (2013). A Set of de Novo Designed Parallel Heterodimeric Coiled Coils with Quantified Dissociation Constants in the Micromolar to Sub-nanomolar Regime. J. Am. Chem. Soc, 135, 19.

Thomas, K. J., & Rice, C. V. (2015). Equilibrium binding behavior of magnesium to wall teichoic acid. Biochimica et Biophysica Acta - Biomembranes, 1848(10), 1981–1987.

Tobin, E. J., & Bambauer, R. (2003). Silver Coating of Dialysis Catheters to Reduce Bacterial Colonization and Infection. Therapeutic Apheresis and Dialysis, 7(6), 504–509.

Toyoshima, C., & Mizutani, T. (2004). Crystal structure of the calcium pump with a bound ATP analogue. Nature, 430(6999), 529–535.

Toyoshima, C., & Nomura, H. (2002). Structural changes in the calcium pump accompanying the dissociation of calcium. Nature, 418(6898), 605–611.

Toyoshima, C., Nomura, H., & Sugita, Y. (2003). Structural basis of ion pumping by Ca 2+ -ATPase of sarcoplasmic reticulum. FEBS Letters, 555(1), 106–110.

Toyoshima, C., Nomura, H., & Tsuda, T. (2004). Lumenal gating mechanism revealed in calcium pump crystal structures with phosphate analogues. Nature, 432(7015), 361–368.

Tribet, C., Audebert, R., & Popot, J.-L. (1996). Amphipols: Polymers that keep membrane proteins soluble in aqueous solutions. Proceedings of the National Academy of Sciences of the United States of America, 93(26), 15047.

Ucisik, M. N., Chakravorty, D. K., & Merz, K. M. (2015). Models for the Metal Transfer Complex of the N-Terminal Region of CusB and CusF. Biochemistry, 54, 50.

V, P., A, R., L, B., & C, A. (2018). MetalPDB in 2018: a database of metal sites in biological macromolecular structures. Nucleic Acids Research, 46(D1), D459–D464.

Valls, M., & de Lorenzo, V. (2002). Exploiting the genetic and biochemical capacities of bacteria for the remediation of heavy metal pollution. FEMS Microbiology Reviews, 26(4), 327–338.

Velásquez, L., & Dussan, J. (2009). Biosorption and bioaccumulation of heavy metals on dead and living biomass of Bacillus sphaericus. Journal of Hazardous Materials, 167, 713–716.

Velazquez-Campoy, A., & Freire, E. (2006). Isothermal titration calorimetry to determine association constants for high-affinity ligands. NATURE PROTOCOLS, 1(1).

Vergalli, J., Bodrenko, I. V., Masi, M., Moynié, L., Acosta-Gutiérrez, S., Naismith, J. H., Davin-Regli, A., Ceccarelli, M., van den Berg, B., Winterhalter, M., & Pagès, J.-M. (2019). Porins and small-molecule translocation across the outer membrane of Gram-negative bacteria. Nature Reviews Microbiology 2019 18:3, 18(3), 164–176.

Vergis, J. M., & Wiener, M. C. (2011). The variable detergent sensitivity of proteases that are utilized for recombinant protein affinity tag removal. Protein Expression and Purification, 78Vijayaraghavan, K., & Yun, Y. S. (2008). Bacterial biosorbents and biosorption. Biotechnology Advances, 26(3), 266–291.

Vijayaraghavan, K., & Yun, Y. S. (2008). Bacterial biosorbents and biosorption. Biotechnology Advances, 26(3), 266–291.

Vollmer, W., Blanot, D., & De Pedro, M. A. (2008). Peptidoglycan structure and architecture. In FEMS Microbiology Reviews (Vol. 32, Issue 2, pp. 149–167). John Wiley & Sons, Ltd.

WA, K. (2007). OligoCalc: an online oligonucleotide properties calculator. Nucleic Acids Research, 35(Web Server issue).

Wang, K., Sitsel, O., Meloni, G., Autzen, H. E., Andersson, M., Klymchuk, T., Nielsen, A. M., Rees, D. C., Nissen, P., & Gourdon, P. (2014). Structure and mechanism of Zn2+-transporting P-type ATPases. Nature, 514(7253), 518–522.

Wang, H., Yan, A., Liu, Z., Yang, X., Xu, Z., Wang, Y., Wang, R., Koohi-Moghadam, M., Hu, L., Xia, W., Tang, H., Wang, Y., Li, H., & Sun, H. (2019). Deciphering molecular mechanism of silver by integrated omic approaches enables enhancing its antimicrobial efficacy in E. coli. *PLOS Biology*, *17*(6).

Wang, Y., Branicky, R., Noë, A., & Hekimi, S. (2018). Superoxide dismutases: Dual roles in controlling ROS damage and regulating ROS signaling. Journal of Cell Biology, 217(6), 1915–1928.

Wang, Z., Fan, G., Hryc, C. F., Blaza, J. N., Serysheva, I. I., Schmid, M. F., Chiu, W., Luisi, B. F., & Du, D. (2017). An allosteric transport mechanism for the AcrAB-TolC multidrug efflux pump. ELife, 6.

Wen, J., Lord, H., Knutson, N., & Wikström, M. (2020). Nano differential scanning fluorimetry for comparability studies of therapeutic proteins. Analytical Biochemistry, 593.

Whitmore, L., & Wallace, B. A. (2008). Protein secondary structure analyses from circular dichroism spectroscopy: Methods and reference databases. Biopolymers, 89(5), 392–400.

Wilcox, D. E. (2008). Isothermal titration calorimetry of metal ions binding to proteins: An overview of recent studies. Inorganica Chimica Acta, 361(4), 857–867.

Williams, C. J., Headd, J. J., Moriarty, N. W., Prisant, M. G., Videau, L. L., Deis, L. N., Verma, V., Keedy, D. A., Hintze, B. J., Chen, V. B., Jain, S., Lewis, S. M., Arendall, W. B., III, Snoeyink, J. (2018). MolProbity: More and better reference data for improved all-atom structure validation. Protein Science: A Publication of the protein society, 27(1), 293

Winn, M. D., Ballard, C. C., Cowtan, K. D., Dodson, E. J., Emsley, P., Evans, P. R., Keegan, R. M., Krissinel, E. B., Leslie, A. G. W., McCoy, A., McNicholas, S. J., Murshudov, G. N., Pannu, N. S., Potterton, E.A. (2011). Overview of the CCP4 suite and current developments. Acta Crystallographica Section D, 67(4), 235

Wright, J. B., Lam, K., & Burrell, R. E. (1998). Wound management in an era of increasing bacterial antibiotic resistance: A role for topical silver treatment. American Journal of Infection Control, 26(6), 572–577.

Xu, W., Barrientos, T., & Andrews, N. C. (2013). Iron and copper in mitochondrial diseases. In Cell Metabolism (Vol. 17, Issue 3, pp. 319–328). Cell Press.

Xue, Y., Davis, A. V., Balakrishnan, G., Stasser, J. P., Staehlin, B. M., Focia, P., Spiro, T. G., Penner-Hahn, J. E., & O'Halloran, T. V. (2008).

Cu(I) recognition via cation-π and methionine interactions in CusF. Nature Chemical Biology, 4(2), 107–109.

Y, H., E, M., T, T., & C, T. (2007). Domain organization and movements in heavy metal ion pumps: papain digestion of CopA, a Cu+-transporting ATPase. The Journal of Biological Chemistry, 282(35), 25213–25221.

Yin, I. X., Zhang, J., Zhao, I. S., Mei, M. L., Li, Q., & Chu, C. H. (2020). The Antibacterial Mechanism of Silver Nanoparticles and Its Application in Dentistry. *International Journal of Nanomedicine*, *15*, 2555–2562.

Z, Z., Y, W., Y, D., & M, H. (2020). Structure-based engineering of anti-GFP nanobody tandems as ultra-high-affinity reagents for purification.

Zegzouti, H., Zdanovskaia, M., Hsiao, K., & Goueli, S. A. (2009). 560 ASSAY and Drug Development Technologies.

Zgurskaya, H. I., & Nikaido, H. (2000). Cross-Linked Complex between Oligomeric Periplasmic Lipoprotein AcrA and the Inner-Membrane-Associated Multidrug Efflux Pump AcrB from Escherichia coli. Journal of Bacteriology, 182(15), 4264.

Zhao, H., Brown, P. H., & Schuck, P. (2011). On the Distribution of Protein Refractive Index Increments. Biophysical Journal, 100(9), 2309.

Zhitnitsky, D., & Lewinson, O. (2014). Identification of functionally important conserved trans-membrane residues of bacterial P IB -type ATPases. Molecular Microbiology, 91(4), 777–789.

Zielazinski Evanston, E. L. (2013). Substrate Specificity of P 1B -type ATPases.

Zimmermann, M., Clarke, O., Gulbis, J. M., Keizer, D. W., Jarvis, R. S., Cobbett, C. S., Hinds, M. G., Xiao, Z., & Wedd, A. G. (2009). Metal

Binding Affinities of Arabidopsis Zinc and Copper Transporters: Selectivities Match the Relative, but Not the Absolute, Affinities of their Amino-Terminal Domains,. Biochemistry, 48(49), 11640–11654.

Zimmermann, M., Clarke, O., Gulbis, J. M., Keizer, D. W., Jarvis, R. S., Cobbett, C. S., Hinds, M. G., Xiao, Z., & Wedd, A. G. (2009). Metal Binding Affinities of Arabidopsis Zinc and Copper Transporters: Selectivities Match the Relative, but Not the Absolute, Affinities of their Amino-Terminal Domains. Biochemistry, 48, 48.

Zoroddu, M. A., Aaseth, J., Crisponi, G., Medici, S., Peana, M., & Nurchi, V. M. (2019). The essential metals for humans: a brief overview. Journal of Inorganic Biochemistry, 195, 120–129.

Zuckerman, M. (2019). More Harm than Healing? Investigating the Iatrogenic Effects of Mercury Treatment on Acquired Syphilis in Post-medieval London. Open Archaeology, 2, 42–55.

Zwart, P. H., Grosse-Kunstleve, R. W., Lebedev, A. A., Murshudov, G. N., & Adams, P. D. (2008). Surprises and pitfalls arising from (pseudo)symmetry. Acta Crystallographica Section D: Biological Crystallography, 64(Pt 1), 99.

9 Appendix

9.1 PIPs Reflective Statement

Note to examiners: This statement is included as an appendix to the thesis in order that the thesis accurately captures the PhD training experienced by the candidate as a BBSRC Doctoral Training Partnership student.

The Professional Internship for PhD Students is a compulsory 3-month placement which must be undertaken by DTP students. It is usually centred on a specific project and must not be related to the PhD project. This reflective statement is designed to capture the skills development which has taken place during the student's placement and the impact on their career plans it has had.

PIPS Reflective Statement

Due to the COVID 19 pandemic my PIPs placement entailed a two month placement at Gyreox Limited, a start-up company based at the Rutherford Appleton Laboratories which looks at the development of peptide macrocycles as drug targets.

During my time at the company, I was tasked with several aims. One of these was the production and purification of the enzymes involved in the catalysis of linear peptides. However, the main focus of the placement was synthesising and purifying the linear peptides, before analysing they were the correct sequence using LCMS. I then had to carry out assays with the enzymes the company uses to turn the linear peptides into cyclic peptides. These cyclic peptides were then analysed for their cell permeability properties for future use.

The main outcomes of the PIPs placement were to successfully produce the enzymes required, synthesise the necessary linear peptides and

conduct assays on them. This was achieved with several new targets identified which the company would work on to assess their viability for their main project aims.

During my time at Gyreox I learnt several new lab based techniques that my PhD does not encompass. The highly sensitive analytical technique of LCMS played a major role in the company, being used for determining the status of the start and end products. Other skills that were learnt during my time was the necessity for inter-departmental meetings, whereby the work conducted by one department affects the other. In addition, the development of my laboratory note taking. I am used to making lab notes however within a company these need to be meticulous. There are several reasons for this, firstly so that the work can be repeated by other, and secondly it is important for patents and intellectual property, the main purpose of companies.

Another area of development was understanding how team working works in industry. It was apparent that everyone has their main individual roles, however when results are needed everyone chips in to get the results and analyse them for major presentations.

By carrying out my PIPs placement I now have a better understanding how start up companies work, in comparison to larger established companies. Based on this I like how in a start up company there is more chance of being involved in several areas of research, whereas in larger companies you tend to be more secular and less involved in the overall project. Based on this I feel that upon finishing the PhD I would like to work in a start up company focusing on Biotech.